

NORTHWESTERN UNIVERSITY

Connecting Spin Dynamics and Electron Transfer Reactions in Organic Molecules with Multiple  
Unpaired Electrons

A DISSERTATION

SUBMITTED TO THE GRADUATE SCHOOL IN PARTIAL FULFILLMENT OF THE  
REQUIREMENTS

for the degree

DOCTOR OF PHILOSOPHY

Field of Chemistry

By

Noah Elliott Horwitz

EVANSTON, ILLINOIS

December 2017

Chapter 3 is a derivative of work copyright © Wu, Y. L.; Horwitz, N. E.; Chen, K. S.; Gomez-Gualdron, D. A.; Luu, N. S.; Ma, L.; Wang, T. C.; Hersam, M. C.; Hupp, J. T.; Farha, O. K.; Snurr, R. Q.; Wasielewski, M. R., and first published in *Nature Chemistry*, Macmillan Publishers Limited 2016

Chapters 4 and 5, Appendices C and D, and relevant material in Appendix B copyright © American Chemical Society. Noah E. Horwitz and the American Chemical Society agree that each has unlimited use of the Supporting Information in Appendices B, C, and D

Chapters 1, 2, 6, 7, and all other material are released under a Creative Commons Attribution 4.0 International License.



## ABSTRACT

### **Connecting Spin Dynamics and Electron Transfer Reactions in Organic Molecules with Multiple Unpaired Electrons**

Noah E. Horwitz

The work presented in this dissertation examines the interplay between electron transfer reactions and electron spin in photoactive organic molecules. Organic compounds that undergo electron transfer reactions after absorbing light are important in natural photosynthesis, photobiology, and synthetic photovoltaics. These electron transfer reactions depend on the spin states of the electrons involved, and in turn influence these spin states. In this thesis, the design and synthesis of several molecules to investigate these relationships are described. Electron paramagnetic resonance (EPR) and transient optical absorption (TA) spectroscopies are used to examine the spin states and movements of electrons following photoexcitation.

Systems containing a single unpaired electron are investigated in Chapter 2. Upon photoexcitation, this electron moves between different sites in the molecule. We study the dependence of the electron transfer rates on solvent parameters, and perform preliminary EPR experiments towards using similar systems for spin coherence transfer.

In Chapter 3, EPR spectroscopy and time-resolved microwave conductivity are used to investigate a photoactive organic framework material. We show that these guanine-quadruplex frameworks generate spin-correlated radical pairs upon photoexcitation, and the resulting radical ions are delocalized and mobile within the framework. These results suggest that this new class of materials may be useful for photovoltaics and batteries.

In Chapters 4 and 5, radical-donor-acceptor molecules that form a triradical state upon photoexcitation are investigated. In Chapter 4, the additional radical is found to induce intersystem crossing on a timescale much faster than in similar systems. In Chapter 5, small differences in the rates of electron transfer processes are found to induce significant changes in the spin polarization of the stable radical. In Chapter 6, a molecule containing two stable radicals coupled to a donor-acceptor system is studied by EPR to examine spin polarization and coherence transfer between the four radicals following photoexcitation.

Finally, in Chapter 7, a new experimental technique is proposed and tested for measuring the spin states of photogenerated radical pairs with high time resolution. While detection of a specific spin state remains challenging, initial experiments show the technique is feasible.

## ACKNOWLEDGEMENTS

It seems somewhat inappropriate that this thesis has only one name on it. The work described herein would not have been possible without the contributions of many other people. More than just facilitating this work, my colleagues have defined it: the course of my graduate career has been shaped by the people in it, perhaps more than by anything else. Beyond the scientific challenges, graduate school is not easy for anyone, and without the support of so many awesome people, I wouldn't have made it through.

First and foremost, I must acknowledge my advisor Prof. Michael Wasielewski. Mike kept the lab well funded and provisioned with state-of-the-art instruments. The only limits to my work were my own creativity and the often-fickle laws of chemistry and physics. Mike also gave me the freedom and support to pursue ideas on my own, and I am grateful for this opportunity to learn by exploring new projects independently. Finally, I was constantly impressed by Mike's ability to recall an obscure piece of data from an old publication, or a small detail crucial to fixing a laboratory instrument. Beyond his guiding the projects I worked on, Mike's little details certainly saved me countless hours throughout my time in the Wasielewski Lab.

I also thank my committee members, Prof. Danna Freedman, Prof. Elad Harel, and Prof. Brian Hoffman, for their feedback and support throughout my graduate career. I am lucky to have had a committee willing to take a critical and thorough look at my work and provide constructive feedback.

Next, I would like to thank the Wasielewski group's A-Team of research faculty, Prof. Yi-lin Wu, Prof. Ryan Young, Dr. Matt Krzyaniak, and Prof. Raanan Carmieli. Raanan

introduced me to EPR spectroscopy and made our spintronics subgroup feel like a real team through our regular meetings and drinking sessions. After Raanan decamped for Israel, Matt settled into this role quickly. Beyond upgrading our EPR hardware and procedures, Matt was always the first person I'd ask about an unexpected EPR result or idea for a new experiment. He also wrote a new fitting program for transient absorption data, without which many of the conclusions of this thesis would have taken much longer to uncover. Yi-lin and Ryan lent their scientific expertise many times when I was having trouble with a difficult synthesis or confusing optical data. But perhaps more importantly, they were always excited to discuss crazy new ideas, and helped foster an atmosphere of creativity in the lab. I also must thank Dr. Sam Chen for helping me get started in the organic synthesis laboratory. Sam's patience and skill in the laboratory were instrumental as I slowly learned the skills required to make the molecules described here.

I've been lucky to have worked with great people in the Wasielewski Group. My cohort in the lab – Patrick Hartnett, Eric Margulies, and Rebecca Lindquist – has been a constant source of help, advice, support, and friendship. The other researchers on our EPR team – particularly Brandon Rugg, Dan Gardner, Jordan Nelson, Scott Dyar, and Yilei Wu – have been a pleasure to work with and have helped me with personal and scientific challenges. Brian Phelan and Leah Shoer were extremely helpful in performing transient absorption experiments for me – often on short notice and with difficult samples! I also need to thank Katie Mauck for providing so much helpful advice and feedback, especially on career-related issues. I'd like to acknowledge the efforts of several people inside and outside the group – among them Jenna Logsdon, Joe Christensen, Dr. Scott Dyar, and Dr. Will Hoffeditz – for going out of their way to organize

social events that helped me get through grad school. My work in the lab was eased by the efforts of our hardworking department staff, in particular our long-serving lab managers, Ben Nelson and Amanda Mahoney. I doubt there's anyone in the group that I haven't leaned on at some point for help.

I have also had the privilege of working on many exciting projects in collaboration with other researchers at Northwestern and beyond. Through these collaborations, I've been able to meet new people, learn about diverse areas of science, and hopefully contribute some useful data. I thank my collaborators for giving me the opportunity to contribute to their work, and for crediting my contributions.

Fellowships from the Department of Energy Office of Science and Northwestern's International Institute for Nanotechnology gave me the freedom to pursue diverse directions in my research and meet other researchers at numerous conferences. I'd especially like to thank Dr. Ping Ge, Carlos Reinhold, and the other staff of the DOE SCGF for their energy, assistance, and flawless organization of the annual meetings, and Margaret Connolly of the IIN for her constant optimism and support.

Lastly but perhaps most importantly, I need to thank my family and friends. My wonderful wife Sherry has been a constant source of support, even when she has been dealing with many of the same challenges in her own work. I have loved discovering Chicago with her, and she has always been there with a more positive take on my (lack of) research progress. My parents, Marshall and Beth, and my sister, Yael, have also supported me not just during graduate school but throughout my whole life. Without them, I wouldn't be the person I am today (and indeed, wouldn't exist at all!).

Beyond these more general acknowledgements, specific credits are due to individual researchers for each chapter:

Chapter 2: Brian T. Phelan, Yi-lin Wu

Chapter 3: Yi-lin Wu, Matthew D. Krzyaniak, Patrick E. Hartnett, Bruker Biospin GMBH

Chapter 4: Brian T. Phelan, Jordan N. Nelson, Matthew D. Krzyaniak, Lukáš Kobr

Chapter 5: Brian T. Phelan, Jordan N. Nelson, Catherine M. Mauck, Matthew D. Krzyaniak

Chapter 6: Matthew D. Krzyaniak, Brian T. Phelan, Brandon K. Rugg

Chapter 7: Brian T. Phelan, Leah E. Shoer, Brandon K. Rugg, Eric A. Margulies, Jordan N. Nelson, Ryan M. Young

## **DEDICATION**

To my family: Mom, Dad, Yael, Sherry, Grandma, Snowflake, Blizzard, Jane, Dian

## TABLE OF CONTENTS

<b>Abstract</b> .....	3
<b>Acknowledgements</b> .....	5
<b>Dedication</b> .....	9
<b>Table of Contents</b> .....	10
<b>List of Figures</b> .....	17
<b>List of Tables</b> .....	27
<b>Chapter 1: Introduction – The Importance of Spin in Electron Transfer Reactions</b> .....	29
1.1 Motivations .....	30
1.2 Systems with One Unpaired Electron and General Techniques .....	31
1.3 Systems with Two Unpaired Electrons.....	35
1.4 Systems with Three and Four Unpaired Electrons .....	40
1.5 Outline.....	42
<b>Chapter 2: Long-Lived Photoproducts in Chemically-Reduced Donor-Acceptor Systems</b> .....	46
2.1 Introduction.....	47
2.2 Experimental .....	49
2.2.1 Synthesis and Chemical Reduction.....	49
2.2.2 Optical Spectroscopy .....	50
2.2.3 EPR Spectroscopy.....	50
2.3 Results and Discussion .....	52
2.3.1 Synthesis .....	52

	11
2.3.2 Steady-state Optical Spectroscopy.....	53
2.3.3 Transient Absorption Spectroscopy.....	54
2.3.4 Solvent Dependence of Electron Transfer Rates .....	56
2.3.5 EPR Spectroscopy.....	59
2.4 Conclusions.....	61
<b>Chapter 3: Charge and Spin Transport in an Organic Molecular Framework .....</b>	<b>63</b>
3.1 Introduction.....	64
3.2 Experimental.....	67
3.3 Results and Discussion .....	70
3.3.1 Steady-state EPR spectroscopy of chemically reduced frameworks .....	70
3.3.2 TRMC .....	72
3.3.3 Time-resolved EPR spectroscopy.....	75
3.4 Conclusions.....	83
<b>Chapter 4: Picosecond Control of Photogenerated Radical Pair Lifetimes Using a Stable Third Radical .....</b>	<b>84</b>
4.1 Introduction.....	85
4.2 Experimental.....	87
4.2.1 Synthesis .....	87
4.2.2 Electrochemistry .....	88
4.2.3 Optical Spectroscopy .....	88
4.2.4 EPR Spectroscopy.....	91
4.3 Results.....	93

	12
4.3.1 Synthesis .....	93
4.3.2 Energetics.....	94
4.3.3 Optical Spectroscopy .....	95
4.3.4 Magnetic Field Effects on the Triplet Yield .....	103
4.3.5 EPR Spectroscopy.....	104
4.4 Discussion.....	108
4.4.1 Charge Separation and Recombination in the Presence of a Third Spin .....	108
4.4.2 Rapid Intersystem Crossing of 4.1b in Benzene.....	110
4.4.3 Photophysical Processes at Low Temperature.....	111
4.4.4 Magnetic Coupling Between BDPA and <sup>3*</sup> ANI .....	113
4.4.5 Spin Polarization of BDPA.....	115
4.5 Conclusions.....	117
<b>Chapter 5: Spin Polarization Transfer from a Photogenerated Radical Ion Pair to a Stable Radical Controlled by Charge Recombination .....</b>	<b>119</b>
5.1 Introduction.....	120
5.2 Experimental .....	123
5.2.1 Synthesis .....	123
5.2.2 Optical Spectroscopy .....	123
5.2.3 Analysis of Transient Absorption Data .....	125
5.2.4 EPR Spectroscopy.....	125
5.3 Results and Discussion .....	126
5.3.1 Optical Spectroscopy .....	126

	13
5.3.2 Energetics of Electron Transfer Reactions .....	127
5.3.3 Transient Absorption Spectroscopy.....	128
5.3.4 Equilibrium Between the Triplet RP and <sup>3*</sup> NDI.....	130
5.3.5 Magnetic Field Effects on Charge Recombination.....	133
5.3.6 TREPR Spectroscopy .....	135
5.4 Conclusions.....	139
 <b>Chapter 6: Synthesis of a Biradical-Donor-Acceptor System for Investigation of Spin</b>	
<b>Coherence Transfer .....</b>	<b>141</b>
6.1 Introduction.....	142
6.2 Experimental.....	144
6.2.1 Synthesis .....	144
6.2.2 Optical Spectroscopy.....	145
6.2.3 Analysis of Transient Absorption Data .....	146
6.2.4 EPR Spectroscopy.....	146
6.3 Results and Discussion .....	149
6.3.1 Synthesis .....	149
6.3.2 Steady-state characterization .....	150
6.3.3 Transient absorption spectroscopy.....	153
6.3.4 EPR spectroscopy: polarization transfer and spin relaxation .....	158
6.3.5 EPR spectroscopy: coherence transfer experiments .....	162
6.4 Conclusions.....	164

## Chapter 7: Fast Measurement of Radical Pair Spin States by Stimulated Back Electron

<b>Transfer</b> .....	166
7.1 Introduction.....	167
7.1.1 Motivation and Background .....	167
7.1.2 Proposed Spin Measurement Scheme.....	169
7.1.3 Molecules Used in this Study .....	171
7.2 Experimental.....	173
7.2.1 Synthesis .....	173
7.2.2 Optical Absorption Spectroscopy .....	174
7.2.3 EPR Spectroscopy.....	176
7.2.4 Simulations .....	178
7.2.5 Phosphorescence Spectroscopy .....	178
7.3 Results and Discussion .....	179
7.3.1 Steady-state Optical Spectroscopy.....	179
7.3.2 Energetics of Electron Transfer Reactions .....	180
7.3.3 Transient Optical Absorption Spectroscopy Following a Single Pump Pulse.....	181
7.3.4 EPR Spectroscopy Following a Single Pump Pulse .....	187
7.3.5 Simulations of the ZQC Frequencies and Detection Scheme.....	190
7.3.6 Transient Optical Absorption Spectroscopy with Two Pump Pulses .....	191
7.3.7 EPR Spectroscopy with Two Pump Pulses.....	194
7.3.8 Phosphorescence Detection of Triplet Recombination Product .....	202
7.4 Conclusions.....	209

	15
<b>References</b> .....	211
<b>Appendix A: Original Research Proposal: Photophysical Investigation of the Dissociation Mechanism of the Plant Photoreceptor Protein UVR8</b> .....	231
<b>Appendix B: Supplementary Organic Synthesis Information</b> .....	232
B.1 Chapter 2 .....	233
B.2 Chapter 4 .....	236
B.3 Chapter 5 .....	246
B.4 Chapter 6 .....	249
B.5 Chapter 7 .....	253
<b>Appendix C: Supplementary Information for Chapter 4</b> .....	256
C.1 Electrochemistry .....	257
C.2 Reorganization Energy Calculations .....	257
C.3 Electron Transfer Reaction Free Energy Calculations .....	263
C.4 Transient Absorption Spectroscopy .....	265
C.5 Magnetic Field Effects on Transient Absorption Spectra .....	279
C.6 EPR Spectroscopy .....	279
<b>Appendix D: Supplementary Information for Chapter 5</b> .....	282
D.1 Reorganization Energy Calculations .....	283
D.2 Electron Transfer Reaction Free Energy Calculations .....	289
D.3 Transient Absorption Spectroscopy .....	290
D.3.1 Global Fitting of Transient Absorption Data .....	290
D.3.2 Femtosecond Transient Absorption Spectroscopy .....	292

D.3.3 Femtosecond Shortwave Infrared Transient Absorption Spectroscopy.....	296
D.3.4 Nanosecond Transient Absorption Spectroscopy .....	298
D.3.5 Nanosecond Transient Absorption Basis Spectrum Deconvolution.....	303
D.3.6 Fitted Transient Absorption Data.....	305
D.3.7 Nanosecond Transient Absorption Spectroscopy: Magnetic Field Effects .....	306
D.4 Electron Paramagnetic Resonance Spectroscopy .....	307
D.4.1 Echo-detected Field-swept Spectra.....	307
D.4.2 Transient Continuous Wave Spectra.....	308
D.4.3 $T_1$ and $T_2$ measurements .....	308
D.4.4 Fits to Polarization Transfer Kinetics .....	309

## LIST OF FIGURES

**Figure 1.1.** Schematic diagram showing the Zeeman splitting of the two electron spin states  $|\alpha\rangle$  and  $|\beta\rangle$  in an applied magnetic field. The energy of each state ( $E_\alpha$  or  $E_\beta$ ) is a function of the electron g-factor  $g$ , the Bohr magneton  $\beta_e$ , and the magnetic field  $B_0$ . The red rectangle represents the constant microwave photon energy  $h\nu$  used to irradiate the sample as the magnetic field is swept during an EPR experiment, while the position of the red arrow shows the field at which the resonance condition  $\Delta E = h\nu$  is met and an EPR transition is observed.

**Figure 1.2.** (a) Spin states for a weakly-coupled radical pair in a strong magnetic field. Green circles represent population of states following charge separation from a singlet excited state. Arrows represent allowed EPR transitions polarized in absorption (red) and emission (blue). (b) Representative time-resolved EPR spectrum of a photogenerated radical pair showing the four EPR transitions (compound **7.2** in toluene at 85 K).

**Figure 2.1.** Synthesis of **2.1** and **2.2**, the precursors to the radical anions used in this study. **2.3**,<sup>68</sup> **2.4**,<sup>69</sup> **2.5**,<sup>70</sup> and **2.8**<sup>71</sup> have been described previously. (a) Pyridine, reflux, 16 h, 19%; (b) 1-butanol, reflux, 17 h, 61%; (c) Pd(PPh<sub>3</sub>)<sub>4</sub>, toluene/EtOH/H<sub>2</sub>O, reflux, overnight, 70%; (d) AcOH, reflux, 17 h, 38%.

**Figure 2.2.** UV-visible absorption spectra of **2.1**<sup>•-</sup> and **2.2**<sup>•-</sup> prepared by chemical reduction in DMF.

**Figure 2.3.** Femtosecond transient absorption spectra of chemically-reduced (a) **2.1**<sup>•-</sup> and (b) **2.2**<sup>•-</sup> in DMF following excitation at 605 nm.

**Figure 2.4.** Echo-detected EPR spectra from **2.2**<sup>•-</sup> in DMF at room temperature, following excitation by (a) a 480 nm or (b) a 605 nm laser pulse.

**Figure 3.1.** Structures of the molecules used in this study: the framework materials **G<sub>2</sub>NDI** and **G<sub>2</sub>PDI**, and the monomeric standards **NDI** and **PDI**. Adapted from Wu et al.<sup>53</sup>

**Figure 3.2.** CW-EPR spectra at X-band (9.5 GHz) of chemically reduced (a) **NDI** and **G<sub>2</sub>NDI** and (b) **PDI** and **G<sub>2</sub>PDI** at room temperature. **NDI** and **PDI** radical anions are dispersed in polystyrene films, while partially-reduced **G<sub>2</sub>NDI** and **G<sub>2</sub>PDI** are suspended in CH<sub>2</sub>Cl<sub>2</sub>.

**Figure 3.3.** TRMC kinetic traces from (a) **G<sub>2</sub>NDI** and (b) **G<sub>2</sub>PDI** under vacuum at room temperature, following excitation by a 416 nm or 500 nm laser pulse respectively.

**Figure 3.4.** TRMC kinetics of (a) **G<sub>2</sub>NDI** and (b) **G<sub>2</sub>PDI** under nitrogen and dry air. Background subtraction was not successful for the data in (a), causing the difference in shape versus Figure 3.3.

**Figure 3.5.** X-band (9.5 GHz) TR-EPR spectra (a) **G<sub>2</sub>NDI** following excitation at 416 nm and (b) **G<sub>2</sub>PDI** following excitation at 500 nm, at room temperature (295 K) and 85 K.

**Figure 3.6** Schematic diagrams showing the radical pair spin levels for (a)  $2J \ll B_0$  and (b)  $2J \approx B_0$ . Green circles represent population of states following charge separation from a singlet excited state. Arrows represent allowed EPR transitions polarized in absorption (red) and emission (blue).

**Figure 3.7.** TR-EPR spectra (a) **G<sub>2</sub>NDI** following excitation at 420 nm and (b) **G<sub>2</sub>PDI** following excitation at 500 nm, at room temperature at Q-band (34 GHz).

**Scheme 4.1.** (a) Bis(pinacolato)diboron, Pd(dppf)Cl<sub>2</sub>, KOAc, 1,4-dioxane, 75 °C, 2d, 88%. (b) 3-bromo-5-iodo-N,N-dimethylaniline, Pd(PPh<sub>3</sub>)<sub>4</sub>, K<sub>2</sub>CO<sub>3</sub>, toluene, EtOH, H<sub>2</sub>O, reflux, 2d, 30%. (c) N-Boc-piperazine, Pd<sub>2</sub>(dba)<sub>3</sub>, P(tBu)<sub>3</sub>, NaOtBu, toluene, 100 °C, overnight, 73%. (d) HCl, EtOH, reflux, 1h, *quant.* (e) 4-bromo-N-(2,5-dimethylphenyl)-1,8-naphthalimide, 2-methoxyethanol, reflux, 2d, 32%. (f) MnO<sub>2</sub>, DBU, THF, rt, 15 min, *quant.*

**Figure 4.1.** UV-visible absorption spectrum of **4.1a** and **4.1b** in toluene.

**Figure 4.2.** Transient absorption spectra in benzene at 295K: (a) **4.1a**, (b) **4.1b**. The species-associated spectra obtained by global fitting of the fsTA data for **4.1a** and **4.1b** are given in (c) and (d), respectively. Sharp features at early times are artifacts due to Raman scattering of the pump laser by the solvent.

**Figure 4.3.** Transient absorption spectra in THF at 295 K: (a) **4.1a**, (b) **4.1b**. The species-associated spectra obtained by global fitting of the fsTA data for **4.1a** and **4.1b** are given in (c) and (d), respectively. Sharp features at early times are artifacts due to Raman scattering of the pump laser by the solvent.

**Figure 4.4.** Transient absorption spectra in PrCN at 295K: (a) **4.1a** and (b) **4.1b**. The species-associated spectra obtained by global fitting of the fsTA data for **4.1a** and **4.1b** are given in (c) and (d), respectively. Sharp features at early times are artifacts due to Raman scattering of the pump laser by the solvent.

**Figure 4.5.** Transient absorption spectra in PrCN at 105K: (a) **4.1a** and (b) **4.1b**. The species-associated spectra obtained by global fitting of the fsTA data for **4.1a** and **4.1b** are given in (c) and (d), respectively.

**Figure 4.6.** CW-EPR signals from **4.1a** and **4.1b** in toluene at room temperature.

**Figure 4.7.** Field-swept, echo-detected EPR spectra of **4.1b** in (a) benzene, (b) THF, and (c) PrCN collected before and after photoexcitation.

**Figure 4.8.** Kinetics of the echo-detected EPR signal following photoexcitation, both without (a) and with (b) a  $\pi$  pulse before the echo sequence. The initial slight decrease around 150 ns is due to the laser pulse occurring during the pulse sequence.

**Figure 4.9.** (a) TCW-EPR spectra of **4.1b** in PrCN at 105 K following photoexcitation. (b) Echo-detected EPR spectrum of **4.1b** in PrCN at 10 K following photoexcitation. Triangles indicate field positions at which the transient nutation experiment was conducted. (c) Transient nutation spectra at different field positions. Blue traces indicate field positions corresponding to the new, transient signal, while red traces correspond to unexcited BDPA.

**Scheme 4.2.** Schematic diagram showing the relative energy levels of the singlet excited state, RP, and triplet excited state for (left) **4.1a** and (right) **4.1b**. Mixing between the singlet and triplet RP levels is forbidden in **4.1a**, but not in **4.1b**.

**Figure 5.1.** Structures of the molecules used in this study.

**Figure 5.2.** UV-visible absorption spectra of **5.1a** and **5.1b** in benzene.

**Figure 5.3.** fsTA spectra in benzene following excitation with 414 nm laser pulse: (a) **5.1a**; (b) **5.1b**.

**Figure 5.4.** Nanosecond transient absorption spectra normalized at different times following photoexcitation in benzene: (a) **5.1a**; (b) **5.1b**. Raw data is presented in Appendix D.

**Figure 5.5.** Contributions from RP and  $^3\text{NDI}$  states as a function of time for (a) **5.1a** in benzene; (b) **5.1a** in 10% fluorobenzene/benzene; (c) **5.1b** in benzene; (d) **5.1b** in 10% fluorobenzene/benzene. Raw data, reference spectra, and fitting details are presented in Appendix D.

**Figure 5.6.** (a) Schematic showing dependence of the RP state energies on external magnetic field, with  $2J < 0$ . (b) Population of these states following S- $T_{+1}$  mixing at  $B = 2J$  and S- $T_0$  mixing at  $B \gg 2J$ , denoted by size of filled circles.  $\Psi_A$  and  $\Psi_B$  are the new eigenstates resulting from S-T mixing. (c) Long-lived (1  $\mu\text{s}$ ) nsTA signal at 473 nm as a function of magnetic field for **5.1a** in de-aerated toluene at 295 K. The peak is fit to a Gaussian centered at 19.2 mT. (d) Relative contributions from RP and  $^3\text{NDI}$  states as a function of time at 473 nm for **5.1a** in benzene at  $B = 0$  mT and 19 mT. The raw data are presented in Figure D.16.

**Figure 5.7.** Time-resolved EPR on **5.1b**: (a) steady-state spectrum in benzene in the absence of photoexcitation; (b) kinetic traces at the maximum field position for samples in benzene and mixed solvents.

**Figure 5.8.** Schematic diagram (not to scale) showing changes in the RP spin state populations over time, and the influence of solvent polarity on the total RP population. This model is proposed to account for the observed inversion of the BDPA<sup>•</sup> polarization with time, and the solvent dependence of the polarization rates.

**Figure 6.1.** Synthetic scheme for synthesis of **6.1** and **6.2**. a) DMF, reflux, 19 h, not isolated. b) 2-methoxyethanol, reflux, 18 h, 21%. c) 2-methoxyethanol, reflux, 2 d, ~2%. d) DBU, MnO<sub>2</sub>, THF, 15 min, quant. e) Pd(PPh<sub>3</sub>)<sub>4</sub>, K<sub>2</sub>CO<sub>3</sub>, toluene/EtOH/H<sub>2</sub>O, reflux, 20 h, 67%. f) Pd<sub>2</sub>(dba)<sub>3</sub>, P(tBu)<sub>3</sub>, NaOtBu, toluene, 100 °C, 15 h, 36%. g) 12 M HCl, EtOH, reflux, 100 min, quant. h) 2-methoxyethanol, reflux, 16 h.

**Figure 6.2.** UV-visible absorption spectra of **6.1** and **6.2** in toluene solution at room temperature.

**Figure 6.3.** CW-EPR spectra of **6.2** in benzene and **6.1** in toluene at room temperature.

**Figure 6.4.** DEER modulations (a) and fitted distance distribution (b) for **6.1** in toluene at 85 K.

**Figure 6.5.** Femtosecond transient absorption spectra (a) of **6.1** in airfree toluene following excitation at 414 nm. Spectra were fitted to a species-associated kinetic model (b). Species spectra (c) and populations over time (d) are shown.

**Figure 6.6.** Femtosecond transient absorption spectra (a) of **6.2** in airfree toluene following excitation at 414 nm. Spectra were fitted to a species-associated kinetic model (b). Species spectra (c) and populations over time (d) are shown.

**Figure 6.7.** Nanosecond transient absorption spectra of (a) **6.1** and (b) **6.2** in toluene at room temperature following excitation at 414 nm. Contributions of the ion pair and <sup>3</sup>\*NDI in these spectra over time, as derived from basis spectrum fitting, are shown for (c) **6.1** and (d) **6.2**.

**Figure 6.8.** fsTA (a) and nsTA (b) spectra of **6.1** in PrCN at 105 K, following excitation at 414 nm. A Savitsky-Golay filter with a 5 nm window has been applied to the nsTA data in the wavelength domain.

**Figure 6.9.** Contour plots showing time-resolved EPR signals from (a) **5.1b** in toluene, (b) **6.2** in benzene, and (c) **6.1** in toluene, all at room temperature following 416 nm excitation.

**Figure 6.10.** Changes in the spin echo EPR signal from BDPA<sup>•</sup> following inversion of (a) BDPA<sup>•</sup> or (b) one hyperfine line of TEMPO<sup>•</sup>.

**Figure 6.11.** Results of coherence transfer experiment performed with (a)  $\pi/2$ -pulse resonant with BDPA<sup>•</sup> or (b)  $\pi/2$ -pulse resonant with TEMPO<sup>•</sup>. Inset: field-swept spin echo detected spectrum of **6.1** in toluene, collected with the selective microwave pulses used for the coherence transfer experiment.

**Figure 7.1.** Molecules **7.1**, **7.2**, and **7.3** used in this study.

**Figure 7.2.** UV-visible absorption spectra of **7.1**, **7.2**, and **7.3** in THF at room temperature.

**Figure 7.3.** fsTA spectra (a) of **7.1** in toluene at room temperature following excitation at 414 nm. Spectra were fitted to a species-associated kinetic model (b). Species spectra (c) and populations over time (d) are shown.

**Figure 7.4.** nsTA spectra of **7.1** in toluene at room temperature following excitation at 416 nm. Spectra were fitted to a species-associated kinetic model (b). Species spectra (c) and populations over time (d) are shown.

**Figure 7.5.** fsTA spectra (a) of **7.1** in PrCN at 105 K following excitation at 414 nm. Spectra were fitted to a species-associated kinetic model (b). Species spectra (c) and populations over time (d) are shown.

**Figure 7.6.** nsTA spectra (a) of **7.1** in PrCN at 105 K following excitation at 414 nm. Spectra were fitted to a species-associated kinetic model (b). Species spectra (c) and populations over time (d) are shown.

**Figure 7.7.** TR-EPR spectra of (a) **7.1**, (b) **7.2**, and (c) **7.3** in toluene and/or PrCN at 85 K following excitation at 416 nm. Spectra are shown at a fixed time after excitation corresponding to the maximum radical pair signal (if no triplet signal is present) or when both radical pair and triplet signals are strong.

**Figure 7.8.** (a) Electron transfer pathways for the proposed spin measurement scheme, where D is mPD, A<sub>1</sub> is ANI, and A<sub>2</sub> is NDI. Estimated time constants for each step are included for **7.1** in THF at room temperature. <sup>3</sup>\*DA<sub>1</sub>A<sub>2</sub>, highlighted in green, is the final product used to read out the spin state of the D<sup>+</sup>A<sub>1</sub>A<sub>2</sub><sup>-</sup> radical pair. (b) Simulated time evolution of the singlet and triplet radical pair populations in **7.2** in liquid solution due to the ZQC, neglecting dephasing and hyperfine coupling. (c) Kinetic simulation of <sup>3</sup>\*ANI yield following the second laser pulse, using the model in (a). An oscillating triplet radical pair population, also shown, is used as the input signal.

**Figure 7.9.** fsTA spectra (a) of **7.1** in THF at room temperature following excitation by two pump pulses, first at 414 nm and then at 605 nm following a 3.7 ns delay. Kinetic data at two relevant wavelengths were fitted to a species-associated kinetic model (b). Species spectra (c) and populations over time (d) are shown.

**Figure 7.10.** fsTA spectra (a) of **7.2** in toluene at room temperature following excitation by two pump pulses, first at 414 nm and then at 605 nm following a 3.7 ns delay. Kinetic data at two relevant wavelengths were fitted to a species-associated kinetic model (b). Species spectra (c) and populations over time (d) are shown.

**Figure 7.11.** (a) TR-EPR spectra of **7.1** in PrCN at 105 K, following a single 416 nm laser pulse, or 416 nm and 480 nm pulses separated by  $T = 80$  ns. (b) Zoomed view of the signal following two pump laser pulses, with radical pair triplet simulation.

**Figure 7.12.** Echo-detected EPR signals as a function of time after the initial 416 nm pump pulse from (a) **7.1** and (b) **7.3** in PrCN at 85 K. A second pump pulse at 480 nm excites the sample after approximately 200 ns.

**Figure 7.13.** Echo-detected EPR signals as a function of time after the initial 416 nm pump pulse from **7.2** in (a) toluene, (b) PrCN, and (c) 5CB (aligned parallel to  $B_0$ ) at 85 K. A second pump pulse at 480 nm excites the sample after approximately 200 ns.

**Figure 7.14.** Triplet EPR signal as a function of the delay between pump pulses, collected for **7.1** in PrCN (a) by TCW-EPR at 105 K and (b) by echo detection at 85 K. The small change in temperature between these measurements is not expected to have a large effect on the data.

**Figure 7.15.** Triplet EPR signal as a function of the delay between pump pulses, collected for **7.2** (a) in toluene at 85 K by TCW-EPR detection, (b) in aligned 5CB at 85 K by TCW-EPR detection, (c) in toluene at 85 K by echo detection, and (d) in aligned 5CB at 85 K by echo detection.

**Figure 7.16.** EPR data from **7.3** in PrCN at 85 K. (a) TCW spectrum 160 ns after 416 nm pulse and 80 ns after 480 nm pulse, showing triplet and radical pair signals. Red and blue arrows denote magnetic field positions for ZQC detection experiments based on the radical pair signal (red) and the triplet signal (blue). Spectrometer artifacts are present on the high-field edge of the spectrum. (b) Comparison of echo-detected kinetics measured from the radical pair signal after a single laser pulse (416 nm), as a function of time after the laser pulse, and those measured from the triplet signal after two laser pulses (416 nm, 480 nm) as a function of the spacing between the two pulses.

**Figure 7.17.** Magnetic field effects on triplet yields, as measured by phosphorescence, for (a) **7.2** in toluene with 1% pyridine, (b) **7.2** in PrCN with 1% pyridine, and (c) **7.3** in PrCN. Relative triplet yields are reported as  $T/T_0$ , the ratio of the phosphorescence signal at a given magnetic field to that measured with zero applied magnetic field. All samples are measured at 77 K.

**Figure 7.18.** Phosphorescence signal versus the spacing in time between 416 nm and 480 nm pulses, for (a) **7.2** in toluene, (b) **7.2** in PrCN, (c) **7.2** in 5CB, and (d) **7.3** in PrCN, all measured at 77 K. The data in (d) is compared to EPR-detected data measured on **7.3** in PrCN at 85 K.

**Figure A.1.** Amino acid residues involved in UVR8 photodissociation. Salt bridge interactions between arginines R286 and R338 and aspartates D107 and D44 are responsible for holding monomers A and B together. Tryptophan residues W285, W233, and W337 are involved in absorption of UV-B light by UVR8. Adapted from Voityuk et al.<sup>254</sup>

**Figure A.2.** Representative TR-EPR spectra of (a) a radical pair and (b) a triplet state showing polarization resulting from radical pair recombination, with fit (red). Author's own work; unpublished.

**Figure A.3.** Transient absorption spectra of tryptophan in phosphate buffer at pH 7.4 following excitation at 292 nm. The spectra show a long-lived singlet excited state  $^1\text{TrpH}$ . Figure from Kandori et al.<sup>285</sup>

**Figure B.1.** Outline of synthetic route to final products **5.1a**, **5.1b**, and **5.2**. Compounds **5.3**, **5.4**, and **4.6** were synthesized as previously described.<sup>45, 70, 300</sup>

**Figure B.2.** Outline of synthetic scheme for **7.1**. **7.4** was prepared as previously described.<sup>235</sup>

**Figure C.1.** a) Comparison of cyclic voltammograms (CVs) for **4.5a** and **4.5b**. b) CV for **4.5b** showing oxidation and reduction features. c) Differential pulse voltammograms for **4.5a** and **4.5b**.

**Figure C.2.** Structures of molecular fragments for which energies were computed.

**Figure C.3.** **4.1a** in benzene at 295 K, 414 nm exc., fsTA. a) fsTA spectra; b) fitting parameters; c) fitted species spectra; d) fitted kinetics.

**Figure C.4.** **4.1a** in benzene at 295 K, 414 nm exc., nsTA. a) nsTA spectra; b) fitting parameters; c) fitted species spectra; d) fitted kinetics.

**Figure C.5.** **4.1a** in THF at 295 K, 414 nm exc., fsTA. a) fsTA spectra; b) fitting parameters; c) fitted species spectra; d) fitted kinetics.

**Figure C.6.** **4.1a** in PrCN at 295 K, 414 nm exc., fsTA. a) fsTA spectra; b) fitting parameters; c) fitted species spectra; d) fitted kinetics.

**Figure C.7.** **4.1b** in benzene at 295 K, 414 nm exc., fsTA. a) fsTA spectra; b) fitting parameters; c) fitted species spectra; d) fitted kinetics.

**Figure C.8.** **4.1b** in benzene at 295 K, 414 nm exc., nsTA. a) nsTA spectra; b) fitting parameters; c) fitted species spectra; d) fitted kinetics.

**Figure C.9.** **4.1b** in THF at 295 K, 414 nm exc., fsTA. a) fsTA spectra; b) fitting parameters; c) fitted species spectra; d) fitted kinetics.

**Figure C.10.** **4.1b** in THF at 295 K, 414 nm exc., nsTA. a) nsTA spectra; b) fitting parameters; c) fitted species spectra; d) fitted kinetics.

**Figure C.11.** **4.1b** in PrCN at 295 K, 414 nm exc., fsTA. a) fsTA spectra; b) fitting parameters; c) fitted species spectra; d) fitted kinetics.

**Figure C.12.** **4.1b** in PrCN at 295 K, 414 nm exc., nsTA. a) nsTA spectra; b) fitting parameters; c) fitted species spectra; d) fitted kinetics.

**Figure C.13.** **4.1a** in PrCN at 105 K, 414 nm exc., fsTA. a) fsTA spectra; b) fitting parameters for model with stretched exponential decay between A and B; c) fitted species spectra; d) fitted kinetics.

**Figure C.14.** **4.1a** in PrCN at 105 K, 414 nm exc., nsTA. a) nsTA spectra; b) fitting parameters; c) fitted species spectra; d) fitted kinetics.

**Figure C.15.** **4.1b** in PrCN at 105 K, 414 nm exc., fsTA. a) fsTA spectra; b) fitting parameters; c) fitted species spectra; d) fitted kinetics.

**Figure C.16.** **4.1b** in PrCN at 105 K, 414 nm exc., nsTA. a) nsTA spectra; b) fitting parameters; c) fitted species spectra; d) fitted kinetics.

**Figure C.17.** **4.1b** in a) benzene, b) THF, and c) PrCN at 295 K, 502 nm exc., fsTA. Scattered excitation light near 500 nm has been removed from the spectra.

**Figure C.18.** Magnetic field effect on  $^3\text{ANI}$  yield in **4.1a** following 416 nm excitation, measured at room temperature in an air-free toluene solution. Triplet yield is reported relative to the average value over several measurements at zero field.

**Figure C.19.** Echo-detected EPR spectra of **4.1a** in a) benzene, b) THF, and c) PrCN at 295 K with 416 nm excitation.

**Figure C.20.** Echo-detected EPR spectra of **4.1b** in a) benzene, b) THF, and c) PrCN at 295 K with 500 nm excitation selective for BDPA.

**Figure C.20.** Echo-detected EPR spectra of **4.1b** in a) benzene, b) THF, and c) PrCN at 295 K with 500 nm excitation selective for BDPA.

**Figure C.22.** Simulation of the EPR spectrum from a system with weak coupling between  $S = \frac{1}{2}$  and  $S = 1$  species, compared to the spectrum of **4.1b** at 105 K in PrCN at 472 ns after excitation.

**Figure D.1.** Structures of molecular fragments for which energies were computed.

**Figure D.2.** Femtosecond transient absorption spectra (a) of **5.2** in airfree toluene following excitation at 414 nm. Spectra were fitted to a species-associated kinetic model (b). Species spectra (c) and populations over time (d) are shown.

**Figure D.3.** Femtosecond transient absorption spectra (a) of **5.1a** in airfree benzene following excitation at 414 nm. Spectra were fitted to a species-associated kinetic model (b). Species spectra (c) and populations over time (d) are shown.

**Figure D.4.** Femtosecond transient absorption spectra (a) of **5.1b** in airfree benzene following excitation at 414 nm. Spectra were fitted to a species-associated kinetic model (b). Species spectra (c) and populations over time (d) are shown.

**Figure D.5.** Femtosecond transient absorption spectra (a) of **5.1b** in airfree tetrahydrofuran following excitation at 414 nm. Spectra were fitted to a species-associated kinetic model (b). Species spectra (c) and populations over time (d) are shown. Sharp features in the fitted spectrum of species A are artifacts due to the similarity of the charge separation rate and the instrument response function.

**Figure D.6.** Femtosecond transient absorption spectra in the NIR region (a) of **4.1a** in airfree toluene and (b) **4.1b** in airfree THF, following excitation at 414 nm. These compounds have previously been shown to form  $mPD^{+}$  upon photoexcitation. The  $mPD^{+}$  feature near 1600 nm is clearly visible in (a), and possibly present in (b).

**Figure D.7.** Shortwave infrared transient absorption spectra (top) and kinetics (bottom) of (a) **4.1a** in benzene, (b) **4.1b** in tetrahydrofuran, and (c) **5.1b** in benzene.

**Figure D.8.** Nanosecond transient absorption spectra (a) of **5.2** in airfree toluene following excitation at 414 nm. Spectra were fitted to a species-associated kinetic model (b). Species spectra (c) and populations over time (d) are shown.

**Figure D.9.** Nanosecond transient absorption spectra (a) of **5.1a** in airfree benzene following excitation at 414 nm. Fitting to a species-associated kinetic model (b) including recombination to triplet was attempted. Species spectra (c) and populations over time (d) are shown.

**Figure D.10.** Nanosecond transient absorption spectra (a) of **5.1a** in airfree benzene following excitation at 414 nm. A kinetic trace at 476 nm was fitted to a biexponential decay with a Gaussian IRF (b).

**Figure D.11.** Nanosecond transient absorption spectra (a) of **5.1b** in airfree benzene following excitation at 414 nm. Fitting to a species-associated kinetic model (b) including recombination to triplet was attempted. Species spectra (c) and populations over time (d) are shown.

**Figure D.12.** Nanosecond transient absorption spectra (a) of **5.1b** in airfree benzene following excitation at 414 nm. A kinetic trace at 476 nm was fitted to a biexponential decay with a Gaussian IRF (b).

**Figure D.13.** Nanosecond transient absorption spectra of (a) **5.1a** and (b) **5.1b** in airfree 10% fluorobenzene/benzene (v/v), at 295 K following excitation at 414 nm. These data were fit using the basis spectrum deconvolution described below.

**Figure D.14.** Normalized triplet and radical ion pair basis spectra used in the nanosecond transient absorption fitting procedure.

**Figure D.15.** Individual nanosecond transient absorption spectra with fits and residuals, used to check goodness of fit: **5.1a** in benzene at 4 ns (a) and 80 ns (b) after pump pulse; **5.1b** in benzene at 4 ns (c) and 20 ns (d). (a) and (d) are the time points with the largest residuals (as sum of squared errors) in their respective datasets. The relatively large residual in (d) near the BDPA ground state absorption is due to a change in the Stark shift features that may be related to conformational change over time.

**Figure D.16.** Nanosecond transient absorption spectra of **5.1a** in airfree toluene at 295 K following excitation at 416 nm with (a) 0 mT and (b) 19 mT applied magnetic field.

**Figure D.17.** Echo-detected EPR spectra of **5.1b** in (a) benzene, (b) 5% fluorobenzene/95% benzene (v/v), and (c) 10% fluorobenzene/90% benzene (v/v) at 295 K.

**Figure D.18.** Transient continuous wave detected EPR spectra of **5.1b** in toluene at 295 K following excitation at 416 nm. (a) Contour plot showing initial positive then negative polarization of BDPA'. (b) Two time points showing that positive and negative features are confined to the BDPA' line.

**Figure D.19.** Saturation recovery measurement of  $T_1$  (a) and  $T_2$  measurement (b) for **5.1b** in benzene at 295 K.

**Figure D.20.** Saturation recovery measurement of  $T_1$  (a) and  $T_2$  measurement (b) for **5.1b** in 5:95 fluorobenzene:benzene at 295 K.

**Figure D.21.** Saturation recovery measurement of  $T_1$  (a) and  $T_2$  measurement (b) for **5.1b** in 10:90 fluorobenzene:benzene at 295 K.

**Figure D.22.** EPR signal of **5.1b** in benzene as a function of time following excitation at 416 nm, with kinetic fit.

**Figure D.23.** EPR signal of **5.1b** in 5% fluorobenzene/benzene as a function of time following excitation at 416 nm, with kinetic fit.

**Figure D.24.** EPR signal of **5.1b** in 10% fluorobenzene/benzene as a function of time following excitation at 416 nm, with kinetic fit.

## LIST OF TABLES

**Table 2.1.** Time constants for forward ( $\tau_{\text{FET}}$ ) and back ( $\tau_{\text{BET}}$ ) electron transfer reactions obtained from species-associated fits to the femtosecond and nanosecond transient absorption data.

**Table 2.2.** Estimated free energy changes ( $\Delta G$ ) and reorganization energies ( $\lambda$ ) for forward (FET 1 = NDI $^{\cdot-}$  to NMI; FET 2 = NMI $^{\cdot-}$  to PI) and back electron transfer (BET 1 = NMI $^{\cdot-}$  to NDI; BET 2 = PI $^{\cdot-}$  to NDI) reactions in **2.1 $^{\cdot-}$**  and **2.2 $^{\cdot-}$** . Static ( $\epsilon_s$ ) and high frequency/optical ( $\epsilon_{\text{op}}$ ) dielectric constants for the solvents are included.<sup>67, 79-81</sup> Within the model used, the parameters for the single forward electron transfer reaction in **2.1 $^{\cdot-}$**  are the same as for the first forward electron transfer reaction in **2.2 $^{\cdot-}$** ; this latter reaction is therefore not reported separately.

**Table 4.1.** Experimental redox potentials of **4.5a** and **4.5b**, literature potentials for ANI (V vs. SCE), and free energies of charge separation (CS) and charge recombination to the singlet ground state (CRS) and  $^3$ \*ANI (CRT).

**Table 4.2.** Time constants for charge separation (CS), charge recombination (CR), and  $^3$ \*ANI decay at room temperature, obtained from fits to transient absorption data.

**Table 5.1.** Estimated free energy changes ( $\Delta G$ ) and reorganization energies ( $\lambda$ ) in eV for charge separation (“CS1”), charge shift (“CS2”), and singlet (“CRS”) and triplet (“CRT”) charge recombination reactions in **5.1a** and **5.1b**.

**Table 5.2.** Polarization transfer time constants and relative amplitudes for **5.1b**.

**Table 6.1.**  $T_1$  relaxation time constants and extrapolated cross-relaxation time constants for  $\sim 10^{-4}$  M solutions of **5.1b**, **6.2**, and **6.1** in toluene at room temperature.

**Table 7.1.** Free energy changes for recombination of the specified radical ion pairs to the singlet ground state or to the lowest energy triplet state,  $^3$ \*NDI at 2.03 eV.

**Table 7.2.** Time constants for charge separation ( $\tau_{\text{CS1}}$ ), charge shift ( $\tau_{\text{CS2}}$ ), and singlet ( $\tau_{\text{CRS}}$ ) and triplet ( $\tau_{\text{CRT}}$ ) charge recombination for **7.1-7.3** at room temperature, obtained from species-associated fits to transient absorption measurements on **7.1-7.3** or their D-ANI model compounds. Due to the model used for fitting,  $\tau_{\text{CS2}}$  also contains a contribution from recombination of the primary radical pair, which is significant for data in THF.

**Table 7.3.** On/off ratios of phosphorescence following excitation by 416 nm and 480 nm pulses, measured as the ratio of integrated kinetics at delays of +50 ns (near the maximum signal) and -10 ns (with the 480 nm pulse coming before the 416 nm pulse). All samples were measured at 77 K,  $B_0 = 0$  mT.

**Table A.1.** Summary of species expected from each proposed mechanism. TrpH denotes a tryptophan residue in its native state, while Trp denotes a tryptophan residue in which the indole ring has been deprotonated. Likewise, ArgH<sup>+</sup> denotes a protonated arginine residue, as it exists at physiological pH.

**Table A.2.** Optical absorption of species that may be detected during transient absorption spectroscopy measurements on UVR8.

**Table C.1.** Energies of neutral and charged mPD and ANI obtained via DFT (B3LYP / 6-31G\* in vacuum)

**Table C.2.** Optimized coordinates for neutral mPD.

**Table C.3.** Optimized coordinates for mPD radical cation.

**Table C.4.** Optimized coordinates for neutral ANI.

**Table C.5.** Optimized coordinates for ANI radical anion.

**Table C.6.** Fitting parameters for BDPAH-mPD-<sup>3\*</sup>ANI spectrum from **4.1a** in toluene (Figure C.21a).

**Table C.7.** Simulation parameters for Figure C.22. Hyperfine coupling was not treated explicitly and is assumed to contribute to the broadening.

**Table D.1.** Energies of neutral and charged mPD and NDI obtained via DFT (B3LYP / 6-31G\* in vacuum). Vibrational frequencies were calculated for all optimized structures and no imaginary frequencies were found.

**Table D.2.** Optimized coordinates for neutral NDI.

**Table D.3.** Optimized coordinates for NDI radical anion.

**Table D.4.** Optimized coordinates for triplet NDI.

**Table D.5.** Optimized coordinates for neutral ANI.

**Table D.6.** Optimized coordinates for ANI radical cation.

# CHAPTER 1

## Introduction – The Importance of Spin in Electron Transfer Reactions

## 1.1 Motivations

Modern electronics technologies are essential components of today's world. By carefully controlling how electric charges move through a circuit, scientists and engineers have revolutionized fields ranging from power generation to information processing. While the charge of electrons is central to these technologies, the electron's intrinsic magnetic moment – imparted by its spin – is often overlooked. Focusing on electron spin opens the door to a wide range of interesting physics with a multitude of potential applications. This rapidly-developing field of spintronics can potentially enable faster, more efficient, and smaller information processing devices.<sup>1</sup> Additionally, electron spins are promising qubits for quantum computation,<sup>2-5</sup> potentially offering access to much faster algorithms for certain tasks.

This thesis is focused on the study of electron spins in organic molecules and materials. Organic compounds have attracted much research for potential uses in electronics, solar photovoltaics, and other functional materials, thanks to desirable properties including flexibility, ease of processing, and the ability to tune properties through synthetic chemistry.<sup>6</sup> Information processing devices with extremely small components could be enabled by organic single-molecular electronics or spintronics.<sup>7-10</sup> Despite this promise, the development of organic materials towards these applications, particularly in spintronics, is still in its infancy. As such, this dissertation is directed towards understanding some of the basic charge and spin transport processes that can occur in these compounds, as well as the interplay between them.

Most known organic molecules are unsuitable for the study of spin phenomena for a simple reason. In most molecules containing an even number of electrons, each electron is

tightly paired in an orbital with another electron having opposing spin. Interesting spin phenomena occur only in molecules containing unpaired electrons. Such systems include both persistent radicals generated through chemical synthesis as well as transient states resulting from photoexcitation. Many interactions of closed-shell organic molecules with light involve the creation of pairs of radicals, triplet excited states, or other paramagnetic species. These paramagnetic species are not just bystanders, but often essential intermediates, including in photosynthesis and photobiology,<sup>11-14</sup> organic photovoltaics,<sup>15-17</sup> organic light-emitting diodes,<sup>18-19</sup> and photodynamic therapy.<sup>20-21</sup> Thus, achieving a full understanding of these important processes and devices provides another motivation for studying electron spins in organic materials, including the work in this thesis. As one example, study of the spin states of radical pairs and triplets created during natural photosynthesis has been instrumental in understanding this process.<sup>14</sup> The close connection between spin and photoinduced processes such as electron transfer also raises the possibility that by manipulating the spin dynamics in photoactive molecules their suitability for certain applications could be improved. This topic is explored in more depth later in this thesis, for the case of organic photovoltaics.

## **1.2 Systems with One Unpaired Electron and General Techniques**

The work in this thesis spans systems containing one, two, three, and four unpaired spins. It is useful to review the processes and interactions that can affect charges and spins in each such system. It is also necessary to introduce the techniques that can be used to follow and measure

these processes. We start by considering an organic radical with a single unpaired electron. Such a system has two electron spin states, which can be separated in energy by an applied magnetic field according to Figure 1.1.

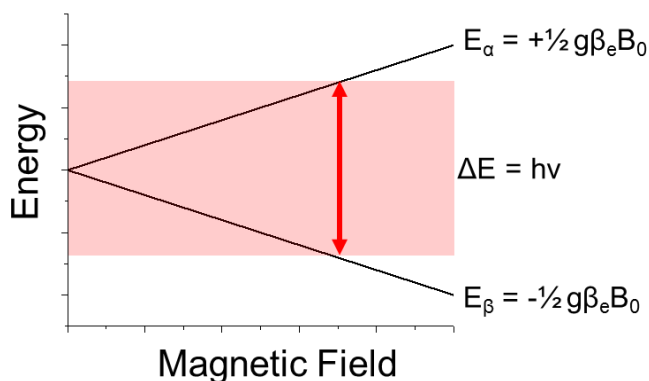


**Figure 1.1.** Schematic diagram showing the Zeeman splitting of the two electron spin states  $|\alpha\rangle$  and  $|\beta\rangle$  in an applied magnetic field. The energy of each state ( $E_{\alpha}$  or  $E_{\beta}$ ) is a function of the electron  $g$ -factor  $g$ , the Bohr magneton  $\beta_e$ , and the magnetic field  $B_0$ . The red rectangle represents the constant microwave photon energy  $h\nu$  used to irradiate the sample as the magnetic field is swept during an EPR experiment, while the position of the red arrow shows the field at which the resonance condition  $\Delta E = h\nu$  is met and an EPR transition is observed.

This energy gap is at the heart of the main technique used to study electron spin states, electron paramagnetic resonance (EPR) spectroscopy. A sample containing paramagnetic species is placed in an applied magnetic field, and electromagnetic radiation (typically in the microwave region) excites a transition between these spin states. Depending on the relative populations of these states in the ensemble, absorption or stimulated emission of microwave radiation occurs, which can be detected by the EPR spectrometer. In a typical experiment on a stable radical at thermal equilibrium, these populations are determined by the Boltzmann distribution, and an absorptive line is observed. This population difference is referred to as the

spin polarization, and systems in which the populations differ from thermal equilibrium are referred to as spin polarized. In this way, the intensity and sign of the EPR line give information on the populations of spin states that is difficult to measure by other techniques.

Further information is included in the EPR spectrum when the unpaired electron couples to other magnetic particles, including nuclei. The hyperfine coupling between electrons and magnetic nuclei splits the EPR line into multiple transitions, according to a selection rule that only the electron spin flips during EPR transitions.<sup>22</sup> Through the hyperfine coupling, the EPR spectrum also provides information on the magnetic environment of the unpaired electron. Similar to the chemical shift in NMR, the  $g$ -factor also contains information about the environment of the unpaired electron. Deviations in the  $g$ -factor from the value for a free electron are primarily due to coupling between spin and orbital angular momentum. Since spin-orbit coupling tends to be weak in organic radicals composed of light atoms, the main effect of this variable  $g$ -factor in the systems studied here is to induce a small shift in the EPR line between different radicals, which becomes important during study of multi-spin systems.

EPR spectroscopy offers tools to manipulate the spin state of a system, in addition to measuring it. By using microwave pulses of specific duration and power, the initial spin polarization can be inverted, or converted into a superposition between the two spin states. This superposition, also called a coherence, is central to many of the spin information operations that would be required for a quantum computer. In summary, EPR spectroscopy provides the ability to manipulate and measure electron spin states, an essential requirement for the work in this thesis.

To measure the movement of electrons, additional techniques are useful. Transient absorption (TA), a time-resolved optical spectroscopy, is the main technique used in this thesis to follow electron movement between different parts of a molecule. Different chemical species tend to have different electronic absorption spectra, including compounds that are oxidized or reduced due to loss or gain of an electron. As an electron is transferred between different parts of a molecule, the overall spectrum will change. In this technique, the molecule is initially excited by a pump laser pulse. Sometime later, a probe pulse is passed through the sample. By monitoring the near-ultraviolet, visible, and/or near-infrared absorption spectrum as a function of the time between these pulses, the kinetics of electron transfer following the photoexcitation event can be measured.

In solid materials where an electron or hole might be moving between multiple equivalent sites, transient absorption spectroscopy becomes less useful. EPR spectroscopy can provide some information by virtue of the aforementioned coupling between electron and nuclear spins. If the unpaired electron moves between multiple sites on the timescale of the EPR measurement, the hyperfine coupling to any one nucleus will be reduced as detailed by McConnell<sup>23</sup> and Norris.<sup>24</sup> An additional technique – time-resolved microwave conductivity (TRMC) – takes advantage of the increased conductivity of a material containing mobile charge carriers.<sup>25-28</sup> Upon irradiation of such a material with microwaves, the charge carriers will move in response to the oscillating microwave electric field, causing increased absorption of the microwaves by the material. Both of these techniques are exploited in Chapter 3 to probe the movement of charge carriers within an organic framework material.

Techniques to transfer spin information in systems with only one unpaired electron are somewhat limited. However, spin information can be moved from one site to another by simply moving the unpaired electron. With a few exceptions,<sup>29-30</sup> transferring an electron does not change its spin state. This idea underlies many of the projects in this thesis, particularly in Chapter 7. Additionally, there are some techniques in which information can be transferred from the electron to a coupled nucleus,<sup>31</sup> but this thesis is focused on interactions between electron spins.

### 1.3 Systems with Two Unpaired Electrons

In a system with two unpaired electrons, there are now four spin states. Three of these states – the triplet states – have a spin quantum number ( $S$ ) of 1, while the other is a singlet with  $S = 0$ . The two electron spins are also coupled by two interactions. The exchange coupling describes the energy difference associated with exchanging the two electrons. By definition, the exchange coupling determines the energy gap between the singlet state (antisymmetric to exchange of the electrons) and triplet states (symmetric to exchange). Positive exchange coupling, resulting in the triplet states being lower in energy than the singlet, is termed ferromagnetic, while negative exchange coupling is termed antiferromagnetic. For the cases described in this thesis, it is useful to divide systems with even numbers of electrons into two classes based on the magnitude of this exchange interaction. Systems with large exchange couplings have singlet-triplet gaps on the electronic energy scale: molecules in singlet and triplet

ground and excited states fall into this category. For the singlet systems in this category, the energy gap is so large that it no longer makes sense to think of unpaired electrons in these molecules, and their spin dynamics can be ignored. Since the exchange coupling depends on spatial overlap between the wavefunctions of the two electrons, it decays very quickly with the spatial separation between two unpaired electrons. In radical pairs resulting from photoinduced electron transfer, this coupling is therefore much smaller, typically on the order of  $10^{-9}$  to  $10^{-3}$  eV. These more weakly coupled radical pairs comprise the second group of two-spin systems important for this work.

The second interaction between two electron spins is the dipolar coupling, which acts between the magnetic dipoles associated with each electron. This interaction decays inversely with the distance between the electrons. This coupling is dependent on the orientation of the molecules relative to the applied magnetic field, and for molecules in liquid solution, this interaction is averaged to zero by tumbling. By breaking the degeneracy of the three triplet states at zero magnetic field, the dipolar coupling also produces the zero field splitting observed in high spin systems.

By examining photogenerated radical pairs in more detail, the interplay between electron spin states and electron transfer reactions becomes apparent. These states occur in molecules containing electron donor and electron acceptor moieties following photoexcitation. The electron transfer reaction that creates the radical pair proceeds from a singlet or triplet excited state localized to one part of the molecule. Crucially, this electron transfer does not affect the spin state of the electron being transferred. The two newly unpaired electrons maintain their initial singlet or triplet configuration, as a spin-correlated radical pair. However, the two

unpaired electrons are now in different magnetic environments, with different  $g$ -factors and coupled to different nuclei. The initial singlet or triplet state is not an eigenstate of this new system. The preparation of this system therefore generates a coherent superposition between two of the spin states of the radical pair. This process is explained in more detail for a radical pair with weak exchange coupling arising from a singlet excited state.

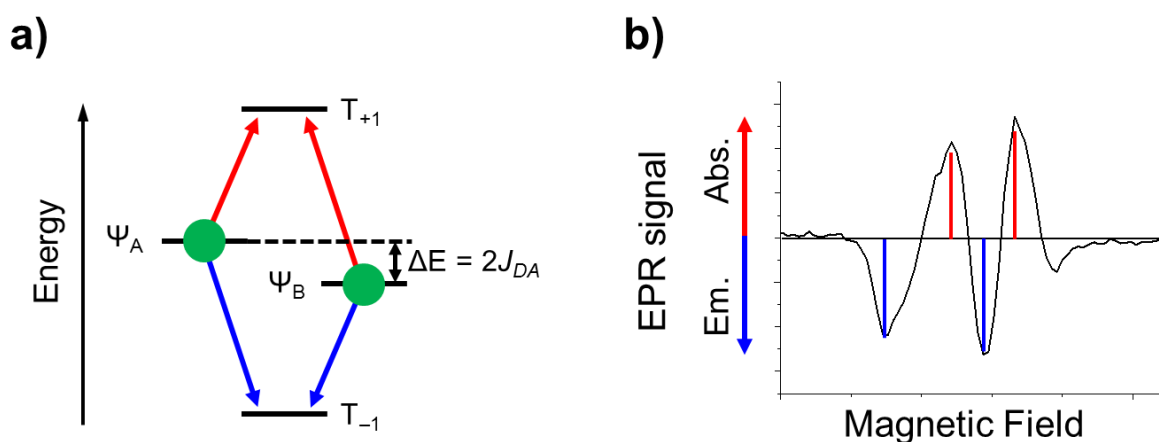


**Figure 1.2.** (a) Spin states for a weakly-coupled radical pair in a strong magnetic field. Green circles represent population of states following charge separation from a singlet excited state. Arrows represent allowed EPR transitions polarized in absorption (red) and emission (blue). (b) Representative time-resolved EPR spectrum of a photogenerated radical pair showing the four EPR transitions (compound **7.2** in toluene at 85 K).

When discussing the EPR spectra of radical pairs, weak exchange coupling is generally considered to be coupling much smaller than the Zeeman splitting of the triplet radical pair states, comparable to or smaller than the electron-nuclear hyperfine coupling. In other words, in the applied magnetic field used for EPR spectroscopy, the triplet states  $T_+$  and  $T_-$  are separated from the two middle states with  $S$  and  $T_0$  character, which are close in energy, as shown in Figure 1.2a. Differences in the magnetic environment between the two radicals are small relative

to the Zeeman energy, and cause mixing only between the S and  $T_0$  states, resulting in the two new eigenstates termed  $\Psi_A$  and  $\Psi_B$ . Following charge separation from a singlet excited state, the radical pair is initialized in a state containing population in  $\Psi_A$  and  $\Psi_B$  as well as a superposition between them: a zero quantum coherence (ZQC). Attempts to measure this ZQC form the basis of Chapter 7. From the energy diagram shown in Figure 1.2a and this initial state, the EPR spectrum of such a radical pair can be predicted. For simplicity, the pair can be considered after the decoherence of the ZQC, such that only  $\Psi_A$  and  $\Psi_B$  are populated. As a consequence of the angular momentum of the photon, the selection rule  $\Delta M_S = \pm 1$  dictates that only the four transitions between  $\Psi_A$  or  $\Psi_B$  and  $T_+$  or  $T_-$  are EPR active. These four transitions are separated by the g-factors of the radicals and the exchange and dipolar coupling between them (and are additionally split by the hyperfine coupling), resulting in a four-line spectrum.<sup>32</sup> As only the two middle energy levels are populated, two of the transitions are absorptive, while two are emissive. In relatively low magnetic field EPR experiments (e.g. at X band), significant overlap of the four lines often occurs, resulting in observation of a two-line spectrum. Radical pairs generated from triplet precursors and those with stronger exchange coupling can exhibit different mixing and EPR spectra. This is discussed in detail in Chapter 3.

Photogenerated radical pairs are eventually destroyed by back electron transfer (recombination) to return the molecule to its ground state. However, the existence of multiple spin states for the radical pair complicates this process. Recombination of a radical pair in a triplet state to a singlet ground state (for example) is a forbidden process. A triplet radical pair can recombine instead to another triplet excited state in the molecule, provided that state is lower in energy than the radical pair. The recombination of radical pairs is spin selective, with singlet

and triplet radical pairs recombining to different products. This spin selectivity has two important consequences. Firstly, the spin state of the radical pair will affect the overall rate of recombination. Recombination is often a limiting factor in potential applications of photoinduced electron transfer reactions, including in organic and dye-sensitized photovoltaics<sup>15, 33-34</sup> and photocatalysts.<sup>35-37</sup> By manipulating the spin state of the electron transfer product, it may be possible to slow this loss process. This idea is explored further in Chapter 4. The second consequence relates to the spin states of any triplet recombination products. As before, moving the electron does not change its spin state, and the spin state of the radical pair will be transferred to the triplet recombination product. Localized triplet states resulting from S-T mixing in a radical pair have unique EPR spectra that can aid in identifying electron transfer processes in unknown systems.

Localized triplet excited states in solids give broad EPR signals, due to the dipolar coupling. A sample in which all of the triplet state molecules are oriented identically relative to the magnetic field (e.g. some single crystals) will give an EPR spectrum consisting of two lines, corresponding to the two allowed transitions between the three triplet sublevels. S-T<sub>0</sub> mixing in a weakly coupled radical pair populates only the middle two energy levels with T<sub>0</sub> character. Because this spin polarization is carried over into a triplet recombination product, localized triplet states arising from radical pair intersystem crossing will only have the middle T<sub>0</sub> state populated. In this case, one of the two lines will show absorption, while the other will show stimulated emission. Adding the signals from all of the molecules in an unoriented sample results in local maxima corresponding to molecules in which one of the principal axes of the zero field splitting tensor is parallel to the applied magnetic field. The sign of the signal – positive

absorption (*a*) or negative stimulated emission (*e*) – at each of these points provides a signature for the triplet formation mechanism. For the aforementioned S-T<sub>0</sub> mixing process, a pattern of *a-e-e-a-a-e* or *e-a-a-e-e-a* is observed across the spectrum from low to high field.<sup>38</sup> Spin-orbit intersystem crossing processes result in other polarization patterns such as *e-a-e-a-e-a*.<sup>39</sup> In this way, EPR signals of triplet states provide information on their origin.

#### 1.4 Systems with Three and Four Unpaired Electrons

Systems with three unpaired electrons include those in which a stable radical is coupled to a photogenerated radical pair or triplet excited state. As with the two-spin systems, these states show different behavior depending on the strength of the exchange coupling with the third spin. In cases where the coupling between all three spins is strong, the system can be described as a single quartet ( $S = 3/2$ ) or doublet ( $S = 1/2$ ) state, depending on the sign of the exchange coupling.<sup>40-41</sup> In other cases, the coupling between the stable radical and one of the unpaired electrons in a radical pair might be stronger than the coupling between the electrons in the photogenerated pair, and the former set of electrons will form a triplet state.<sup>42</sup> Of most relevance for this thesis are molecules in which the coupling to the stable radical is relatively weak compared to the coupling within the photogenerated two-spin system. In these systems, the third spin serves to perturb the spin dynamics of the photogenerated pair, and in simplest terms can be thought of as a bath of extra angular momentum that can enable otherwise forbidden transitions. Chromophores coupled to a stable radical have been found to undergo rapid exchange-induced intersystem crossing (EISC) upon photoexcitation to their singlet excited state, and the resulting

triplet state also exhibits a shortened lifetime compared to the bare chromophore.<sup>40, 43</sup> Similarly, photogenerated radical pairs coupled to stable radicals show faster conversion between their singlet and triplet states. Using a stable radical to perturb the spin dynamics of radical pairs could help extend their lifetime for applications in solar energy conversion, an idea explored in Chapter 4.

The stable radical in these systems is not just a bystander. During EISC and interactions with radical pairs, the stable radical often becomes spin polarized.<sup>44-49</sup> Polarization transfer from a relatively short lived but strongly polarized radical pair or triplet state to a stable radical could make it easier to take advantage of this strongly polarized state in a spintronic device. Additionally, this polarization transfer moves spin information between sites in a molecule in a controllable fashion, which could also be exploited to make spin-based devices. Polarization transfer from a radical pair to a stable radical is investigated in Chapters 4, 5, and 6.

Polarization transfer involves moving populations of spin states between sites. It is also possible to move superposition states, a process termed coherence transfer. The simplest such process would be simply moving a single unpaired electron prepared in a superposition state. This process could be one future direction for the types of molecules investigated in Chapter 2. Additionally, it might be possible to rely on exchange coupling between spins to transfer a coherence between them,<sup>50</sup> a process investigated with a four-spin system in Chapter 6.

## 1.5 Outline

In Chapter 2, two molecules are described that use a chemically-reduced naphthalenediimide (NDI) radical anion as an electron donor. This donor presents new opportunities for both solar energy conversion and spin chemistry. The photoexcited NDI radical anion is a very powerful reducing agent, capable of reducing catalysts for the generation of solar fuels.<sup>51-52</sup> Additionally, moving an unpaired spin allows spin polarization and coherence to be moved from site to site. TA experiments show that some of the same strategies developed for neutral/closed shell donors – namely the use of a secondary acceptor to retard back electron transfer – can be leveraged in these anionic molecules. Photoproduct lifetimes in the microsecond regime are achieved, long enough for photocatalysis applications and EPR investigations of spin phenomena.

In Chapter 3, EPR spectroscopy and TRMC are used to investigate two organic framework materials based on guanine quadruplexes. Steady state EPR spectroscopy on the chemically reduced frameworks proves that electrons are mobile in the materials. TRMC shows a strong photoconductivity signal, suggesting the formation of long-lived charge carriers after photoexcitation. Finally, time resolved EPR spectroscopy provides more detail on the charge separation process, and on the behavior of charge carriers at longer times. These results demonstrate that this novel class of materials may be useful for photovoltaics and photocatalysis. Some of these results were recently published as part of a comprehensive description of these new materials;<sup>53</sup> the goal in this chapter is to go into more depth on the spin dynamics and charge transport processes following photoexcitation.

Chapter 4 describes the synthesis and characterization of a donor-acceptor molecule containing a coupled stable radical. The exchange coupling within the radical pair formed on photoexcitation is much stronger than in previously studied examples of this type of system. The spin dynamics in this molecule are much faster than the time resolution of EPR spectroscopy, but this study highlights that a triplet recombination product can be used to follow the spin dynamics by TA on a much faster timescale. Enhanced formation of triplet radical pairs and the triplet recombination product was found to occur on the picosecond timescale, at least four orders of magnitude faster than the nanosecond rates seen in previous studies. Polarization transfer to the stable radical was also observed by EPR spectroscopy. These results suggest that spin control of radical pair lifetimes can be exploited on a much shorter timescale than previously realized, useful for implementing this strategy in organic photovoltaics.

In Chapter 5, another stable radical – donor – acceptor molecule is prepared and studied by TA and EPR spectroscopies. As expected, polarization transfer from the radical pair to the stable radical is observed. However, in contrast to previously studied systems, multiple rates of polarization transfer are present. The signs, magnitudes, and rates of polarization transfer in this molecule are found to depend sensitively on the polarity of the solvent used for the EPR experiments. Further investigation using TA spectroscopy reveals that an equilibrium between the triplet radical pair and a triplet recombination product controls the spin evolution in this molecule. These results highlight the strong influence of electron transfer rates on spin dynamics in multispin molecules and suggest the importance of optimizing electron transfer parameters when designing molecules for spin transfer processes.

Chapter 6 details the synthesis and characterization of a photogenerated four-spin system, the first such system with a photogenerated radical pair coupled to two stable radicals. This system was designed with the aim of being able to transfer a spin coherence between the two stable radicals by coupling them through the photogenerated radical pair. While preliminary EPR experiments suggest that this coherence transfer process does not occur in the studied molecule, interesting polarization transfer to both radicals is observed.

The work in Chapter 7 pulls together several concepts introduced in the other chapters. The idea of using a second laser pulse to probe the spin state of a photogenerated radical pair on a fast time scale is explored. Excitation of a NDI radical anion in the pair triggers a back electron transfer reaction analogous to that in Chapter 2. Rapid recombination of the high energy radical pair is spin selective, as in Chapter 4, forming a long-lived triplet state that can be measured to determine the triplet character of the original radical pair. This process is demonstrated to work in a number of donor-acceptor molecules, and preliminary efforts to measure zero-quantum coherences with high time resolution are presented.

Finally, a brief note is made on the organization of this thesis as it relates to the intellectual development of the projects described therein. The related molecules in Chapters 4, 5, and 6 are presented from simplest to most complex, but they were not designed or prepared in this order, or for the questions that they ended up answering. The initial versions of the molecules in Chapters 5 and 6 showed a poor yield of the desired radical pair. The molecule studied in Chapter 4 was prepared to investigate this problem, which led to discovery of the fast intersystem crossing that forms the basis for that chapter. Following a redesign to avoid this issue, the molecule examined in Chapter 5 was initially prepared as a model system for Chapter

6, but exhibited unexpected complexity that became interesting in its own right. While I believe that the work in these chapters stands on its own as a contribution to the field, the hidden lesson of this portion of the thesis is that interesting directions can arise from failure and unexpected results.

## CHAPTER 2

# Long-Lived Photoproducts in Chemically-Reduced Donor-Acceptor Systems

Part of a project with Brian Phelan, Prof. Yi-Lin Wu, and Dr. Jinyuan Zhang.

## 2.1 Introduction

Sunlight has the potential to supply an abundant, widespread, and non-polluting energy source. One limitation to widespread utilization of solar energy is the reliance of transportation on fossil fuels. Transportation, accounting for approximately one fifth of global energy use in 2015,<sup>54</sup> requires portable, high density energy sources. While continued improvements in battery technologies provide one means of using renewable energy in transportation, using solar energy to synthesize chemical fuels – a process known as artificial photosynthesis – is also an attractive strategy.

Similar to a photovoltaic cell, artificial photosynthesis uses sunlight to generate high potential electrons and holes.<sup>55-56</sup> These charge carriers are transferred to redox catalysts that act on an abundant starting material – typically water and/or carbon dioxide – to create a reduced chemical fuel at the cathode and oxygen at the anode. Reducing and oxidizing these catalysts requires strong photoreductants or photooxidants to supply the necessary potential. For example, the proton-coupled reduction of CO<sub>2</sub> to CO occurs at a fairly negative -0.77 V vs. SCE,<sup>57</sup> and catalysts for this reaction are somewhat more difficult to reduce. One strategy to enable facile reduction of these catalysts is to use a highly reducing radical anion as the photoreductant. Rylenediimide dyes – namely naphthalenediimide (NDI) and perylenediimide (PDI) – are known to form stable radical anions at mild potentials. These radical anions absorb visible and near infrared light strongly,<sup>58</sup> and following photoexcitation have been shown to be capable of transferring an electron to covalently-attached<sup>59-61</sup> or solution phase electron acceptors.<sup>62</sup> The use of radical anions as electron donors is also interesting from a spin perspective, as these

systems allow movement of a single, unpaired electron. This process could potentially be used to transfer a spin population or coherence between sites in a molecule.

Despite these promising preliminary results, electron transfer systems based on radical anion chromophores are less well studied than those based on neutral, closed-shell chromophores. One challenge in all molecular systems that aim to utilize photoinduced electron transfer is avoiding rapid back electron transfer that returns the system to its ground state.<sup>15, 55, 63-</sup>  
<sup>64</sup> For photocatalysis, electron transfer product lifetimes in the nanosecond to microsecond regime are required to allow enough time for diffusion of reactants to the catalyst.<sup>55</sup> Likewise, investigation of spin phenomena by electron paramagnetic resonance (EPR) spectroscopy requires similar lifetimes. In contrast, most of the dyad systems studied to date have lifetimes in the picosecond or few nanosecond range.<sup>61</sup> In systems based on neutral electron donors and acceptors, two strategies (among others) have proven important in increasing photoproduct lifetimes. Intermediate electron acceptors can be used to provide a barrier to back electron transfer. Additionally, changes in the solvent environment can be used to tune the free energy change for charge recombination, affecting this rate. The first strategy should be applicable to systems based on radical anions. However, a substantially different dependence on solvent polarity is expected in these systems, complicating the second strategy. In a neutral donor-neutral acceptor molecule, electron transfer produces a cation and an anion. The energy of this ion pair state thus contains a Coulombic contribution that is strongly dependent on both the distance separating the charges and the dielectric constant of the medium between them.<sup>65</sup> In contrast, this Coulombic term is not present in a system with only a single (negative) charge. However, differences in solvation of ions between differently sized anions, changes in

reorganization energy, and pairing of dissolved counterions might introduce a solvent dependence in these systems.

This study aims to investigate both the solvent dependence and the effects of using an intermediate electron acceptor in radical anion-based molecules, with the aim of guiding the design of similar systems towards photocatalysis and spintronics applications. We report preparation and characterization of a radical anion-acceptor dyad (**2.1<sup>-•</sup>**) and a radical anion-acceptor-acceptor triad (**2.2<sup>-•</sup>**) based on the naphthalenediimide (NDI) radical anion. Naphthalimide (NMI) and pyromellitimide (PI) were chosen as electron acceptors on the basis of their favorable electrochemical potentials and clear optical tags for their photoreduction. Compounds are synthesized as the neutral molecules and chemically or electrochemically reduced to the desired radical anion under inert atmosphere. Transient optical absorption (TA) spectroscopy is used to follow the forward and back electron transfer reactions in these molecules in a variety of solvents.

## **2.2 Experimental**

### **2.2.1 Synthesis and Chemical Reduction**

The synthesis and characterization of compounds **2.1-2.8** is described in detail in Appendix B. Dry N,N-dimethylformamide (DMF) was obtained from a Glass Contour solvent purification system. Butyronitrile (PrCN) was treated with HCl, distilled from K<sub>2</sub>CO<sub>3</sub>, and dried over Al<sub>2</sub>O<sub>3</sub> as described by Armarego and Chai.<sup>66</sup> Pyridine was distilled from CaH<sub>2</sub> before use.

**2.1** and **2.2** were purified by preparative thin layer chromatography on SiO<sub>2</sub> prior to reduction and optical and EPR spectroscopy.

All chemical reductions were carried out in a nitrogen atmosphere glovebox. Separate solutions of **2.1** or **2.2** and of cobaltocene (CoCp<sub>2</sub>) were prepared in the appropriate solvent and mixed. For **2.2**, 0.8 equivalents of CoCp<sub>2</sub> were used per equivalent of **2.2**, to avoid reducing the pyromellitimide (PI) unit.

### 2.2.2 Optical Spectroscopy

Optical measurements were carried out in solutions of DMF ( $\epsilon_S = 38.25^{67}$ ), PrCN ( $\epsilon_S = 24.83^{67}$ ), or pyridine ( $\epsilon_S = 13.26^{67}$ ). Measurements were restricted to relatively polar solvents due to low solubility of **2.1**<sup>•-</sup> and **2.2**<sup>•-</sup> in nonpolar solvents. Toluene ( $\epsilon_S = 2.38^{67}$ ) and 1,4-dioxane ( $\epsilon_S = 2.22^{67}$ ) were found to be unable to dissolve **2.1**<sup>•-</sup> and **2.2**<sup>•-</sup>, while solutions in tetrahydrofuran ( $\epsilon_S = 7.52^{67}$ ) were unstable and prone to spontaneous precipitation of a dark red solid. Anisole was found to form a charge-transfer complex with neutral NDI due to its electron-rich nature and was also excluded from this study. Additionally, halogenated solvents such as dichloromethane, chloroform, and chlorobenzene were avoided due to the possibility of photoreduction of these solvents by photoexcited NDI<sup>•-</sup>.<sup>62</sup>

### 2.2.3 EPR Spectroscopy

EPR measurements were made at X-band (~9.5 GHz) using a Bruker Elexsys E680-X/W EPR spectrometer outfitted with a split ring resonator (ER4118X-MS5). Measurements were performed at room temperature. Sample solutions were prepared in an N<sub>2</sub> glovebox and loaded

into quartz tubes (1.80 mm o.d.  $\times$  1.50 mm i.d.) and affixed to a vacuum adapter before removal from the glovebox. Following one freeze–pump–thaw degassing cycle on a vacuum line ( $10^{-4}$  Torr), samples were sealed under vacuum using an oxy-hydrogen torch.

EPR measurements were collected using electron spin echo (ESE) detection. A 1 kW TWT amplifier (Applied Systems Engineering 117X) was employed to generate high-power microwave pulses. The resonator was partially overcoupled to maximize echo intensity and minimize ringing following microwave pulses. ESE data was obtained with a  $\pi/2$ - $\tau$ - $\pi$  pulse sequence with  $\pi/2 = 16$  ns,  $\pi = 32$  ns, and  $\tau = 120$  ns. The integrated echo intensity was recorded as a function of the magnetic field to yield the spectrum. If the sample is photoexcited at some time  $t$  prior to the  $\pi/2$ - $\tau$ - $\pi$  pulse sequence, spectra can be collected of the transient species as a function of  $t$ .

## 2.3 Results and Discussion

### 2.3.1 Synthesis

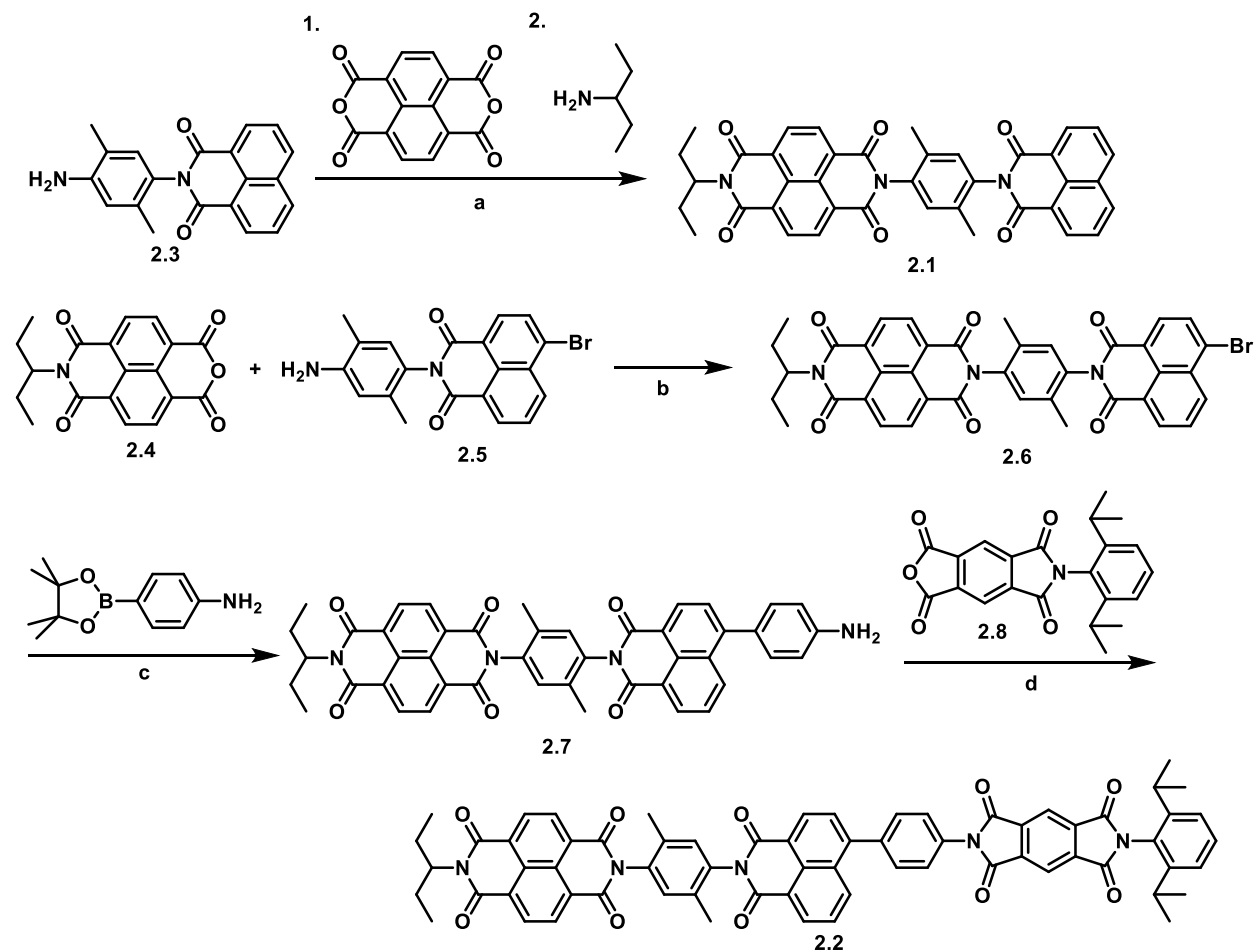


**Figure 2.1.** Synthesis of 2.1 and 2.2, the precursors to the radical anions used in this study. 2.3,<sup>68</sup> 2.4,<sup>69</sup> 2.5,<sup>70</sup> and 2.8<sup>71</sup> have been described previously. (a) Pyridine, reflux, 16 h, 19%; (b) 1-butanol, reflux, 17 h, 61%; (c) Pd(PPh<sub>3</sub>)<sub>4</sub>, toluene/EtOH/H<sub>2</sub>O, reflux, overnight, 70%; (d) AcOH, reflux, 17 h, 38%.

Preparation of **2.1** and **2.2** is outlined in Figure 2.1 and detailed synthetic procedures are given in Appendix B. Synthesis of **2.1** was carried out by a series of condensation reactions from commercially-available precursors to form the three imide linkages present in the structure. **2.6** was prepared analogously, and a Suzuki-Miyaura cross-coupling reaction was used to install an aniline group. A final condensation reaction with **2.8** afforded **2.2**. Following synthesis and purification, one-electron chemical reductions of **2.1** and **2.2** were carried out as described in Section 2.2.1 to prepare **2.1<sup>•-</sup>** and **2.2<sup>•-</sup>** as-needed.

### 2.3.2 Steady-state Optical Spectroscopy

UV-visible absorption spectroscopy was performed on **2.1<sup>•-</sup>** and **2.2<sup>•-</sup>** to confirm selective reduction of the NDI unit. Absorption bands near 475, 605, 700, and 780 nm are characteristic for NDI<sup>•-</sup>. Peaks in the UV region of the spectrum are mostly due to unreduced NDI and NMI. A substoichiometric quantity of cobaltocene reductant was added to ensure that PI would not be reduced; the unreduced **2.1** and **2.2** do not absorb the excitation light used for time resolved optical and EPR spectroscopies.

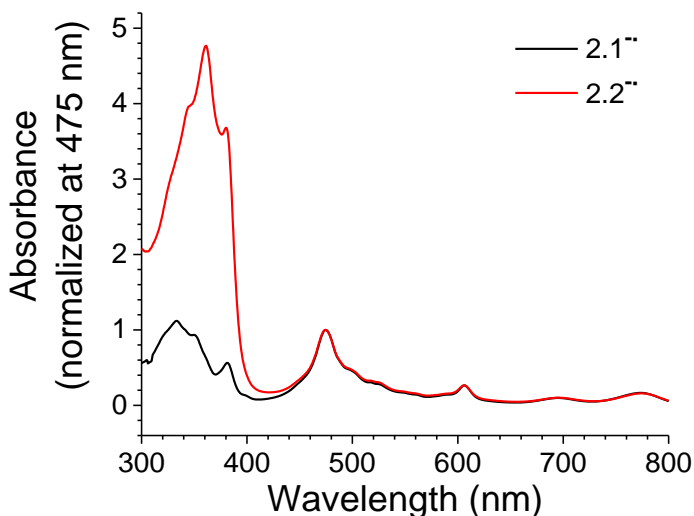


**Figure 2.2.** UV-visible absorption spectra of **2.1<sup>•-</sup>** and **2.2<sup>•-</sup>** prepared by chemical reduction in DMF.

### 2.3.3 Transient Absorption Spectroscopy

Transient absorption spectroscopy was performed on **2.1<sup>•-</sup>** and **2.2<sup>•-</sup>** to follow electron transfer reactions following photoexcitation. Representative femtosecond transient absorption (fsTA) data in DMF are shown in Figure 2.3. At early times after photoexcitation, the fsTA spectrum of **2.1<sup>•-</sup>** shows a strong negative feature near 475 nm, with weaker absorptive features near 430 and 650 nm. These bands are assigned to the ground state bleach and excited state absorption of **NDI<sup>•-</sup>**. Within tens of ps, a strong absorptive band near 420 nm grows in. **NDI<sup>•-</sup>** ground state bleach features at 475 and 700 nm remain. **NMI<sup>•-</sup>** is known to absorb strongly at 420 nm.<sup>58</sup> This process is therefore assigned to electron transfer from **<sup>2\*</sup>NDI<sup>•-</sup>** to **NMI**. At later times, these signals decay together. Fitting to an  $A \rightarrow B \rightarrow \text{GS}$  species-associated kinetic model yields time constants of  $\tau_{A \rightarrow B} = 31$  ps for forward electron transfer, and  $\tau_{B \rightarrow \text{GS}} = 900$  ps for back electron transfer.

**2.2<sup>-</sup>** shows similar features to **2.1<sup>-</sup>** at early times, corresponding to the **2<sup>\*</sup>NDI<sup>-</sup>** excited state. Near 30 ps, a small bump is present near 420 nm (analogous to **2.1<sup>-</sup>**), but this feature quickly disappears as a strong absorptive band grows in near 720 nm. This band is characteristic for **PI<sup>-</sup>**. These spectra suggest electron transfer first from **2<sup>\*</sup>NDI<sup>-</sup>**, and then from **NMI<sup>-</sup>** to **PI**. The **PI<sup>-</sup>** absorptions and **NDI<sup>-</sup>** ground state bleach features persist past the end of the fsTA experiment. Nanosecond transient absorption spectroscopy is used to follow the back electron transfer. Fitting these data to species-associated kinetic models yields time constants of  $\tau_{A \rightarrow B} = 21$  ps for forward electron transfer from **2<sup>\*</sup>NDI<sup>-</sup>** to **NMI**,  $\tau_{B \rightarrow C} = 58$  ps for forward electron transfer from **NMI<sup>-</sup>** to **PI**, and  $\tau_{C \rightarrow GS} = 8.1$   $\mu$ s for back electron transfer. Time constants for the forward and back electron transfer reactions in **2.1<sup>-</sup>** and **2.2<sup>-</sup>** in additional solvents are presented in Table 2.1.

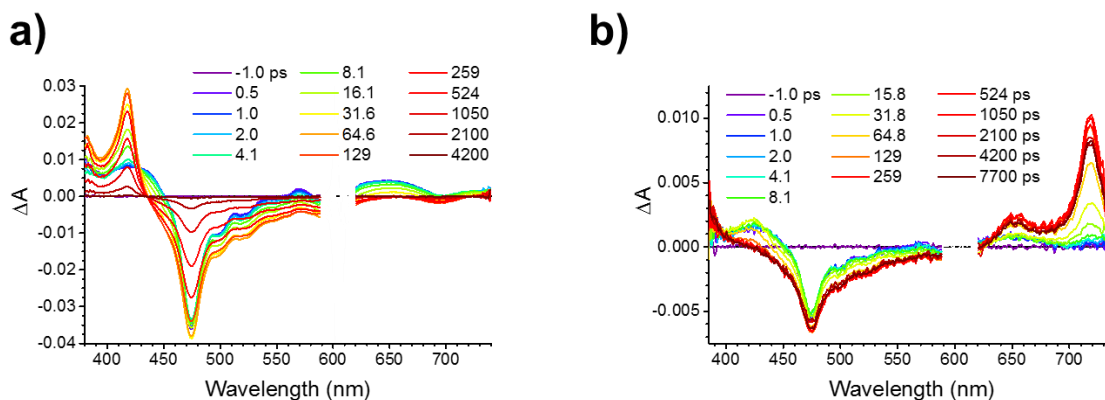


**Figure 2.3.** Femtosecond transient absorption spectra of chemically-reduced (a) **2.1<sup>-</sup>** and (b) **2.2<sup>-</sup>** in DMF following excitation at 605 nm.

Molecule	Solvent	$\epsilon_s$	$\eta$ (cP) <sup>67</sup>	$\tau_{\text{FET1}}$	$\tau_{\text{FET2}}$	$\tau_{\text{BET}}$
<b>2.1<sup>-•</sup></b>	Pyridine	13.26	0.879	16 ps	N/A	520 ps
<b>2.1<sup>-•</sup></b>	PrCN	24.83	0.553	24 ps	N/A	700 ps
<b>2.1<sup>-•</sup></b>	DMF	38.25	0.794	31 ps	N/A	900 ps
<b>2.2<sup>-•</sup></b>	Pyridine	13.26	0.879	10 ps	20 ps	6.5 $\mu$ s
<b>2.2<sup>-•</sup></b>	PrCN	24.83	0.553	15 ps	42 ps	26.8 $\mu$ s
<b>2.2<sup>-•</sup></b>	DMF	38.25	0.794	21 ps	58 ps	8.1 $\mu$ s

**Table 2.1.** Time constants for forward ( $\tau_{\text{FET}}$ ) and back ( $\tau_{\text{BET}}$ ) electron transfer reactions obtained from species-associated fits to the femtosecond and nanosecond transient absorption data.

### 2.3.4 Solvent Dependence of Electron Transfer Rates

As noted previously, because only a single negative charge is present in **2.1<sup>-•</sup>** and **2.2<sup>-•</sup>** and their photoproducts, the energy differences between the ground state, excited state, and photoproduct molecules are not expected to have a strong dependence on solvent dielectric constant. However, in **2.1<sup>-•</sup>**, a clear trend is present in the time constants for the forward and back electron transfer reactions versus solvent polarity: the rates of both reactions slow as the solvent polarity increases. The rates do not correlate with solvent viscosity across the three solvents studied, indicating that the trend is not due to slow motion of the counterion in more viscous solvents. The same trend occurs in **2.2<sup>-•</sup>** for both forward electron transfer reactions. However, the trend is less clear for the back electron transfer reaction in **2.2<sup>-•</sup>**. The rates do correlate with the solvent viscosity, with the more viscous solvents showing faster recombination, but this may be a coincidence.

First we consider the dependence of the forward electron transfer rates on solvent polarity. From Marcus's model of electron transfer reactions,<sup>72</sup> electron transfer rates are determined by the electronic coupling between the reactant and product states, the free energy change associated with the reaction, and the reorganization energy associated with the reaction. Changes in the electronic coupling can be induced by changes in the geometry of the molecule,<sup>73-</sup>

<sup>76</sup> but there is no reason to expect a significant change in the molecular structure when the solvent is changed. While there is no Coulombic contribution to the free energy change, differential solvation of the reactant and product ions may introduce a dependence of this energy change on solvent polarity. However, NDI, NMI, and PI are all similar in size, so such an effect is likely to be small. In contrast, the reorganization energy is expected to show a substantial dependence on solvent polarity: polar solvent molecules will reorient to re-solvate the charge after electron transfer. To test this hypothesis, reorganization energies for forward and back electron transfer reactions were estimated using a dielectric continuum model for solvent reorganization energies<sup>77</sup> and DFT calculations for internal reorganization energies.<sup>45</sup> These results are reported in Table 2.2, along with estimated free energy changes calculated using the Weller equation.<sup>65</sup> Determination of the ion radii is difficult – the Weller model of solid spheres is not completely accurate – and for this estimate, identical radii of 3.5 Å<sup>78</sup> were used for all ions (a simplification that results in no solvent dependence in the free energy estimates).

Compound	Reaction	Solvent	$\epsilon_s$	$\epsilon_{op}$	$\Delta G$ (eV)	$\lambda$ (eV)
<b>2.1<sup>-</sup>/2.2<sup>-</sup></b>	FET 1	Pyridine	13.26	2.27	-0.71	1.45
<b>2.1<sup>-</sup></b>	BET 1	Pyridine	13.26	2.27	-0.89	1.45
<b>2.1<sup>-</sup>/2.2<sup>-</sup></b>	FET 1	PrCN	24.83	1.91	-0.71	1.82
<b>2.1<sup>-</sup></b>	BET 1	PrCN	24.83	1.91	-0.89	1.82
<b>2.1<sup>-</sup>/2.2<sup>-</sup></b>	FET 1	DMF	38.25	2.04	-0.71	1.76
<b>2.1<sup>-</sup></b>	BET 1	DMF	38.25	2.04	-0.89	1.76
<b>2.2<sup>-</sup></b>	FET 2	Pyridine	13.26	2.27	-0.66	1.43
<b>2.2<sup>-</sup></b>	BET 2	Pyridine	13.26	2.27	-0.23	1.68
<b>2.2<sup>-</sup></b>	FET 2	PrCN	24.83	1.91	-0.66	1.77
<b>2.2<sup>-</sup></b>	BET 2	PrCN	24.83	1.91	-0.23	2.09
<b>2.2<sup>-</sup></b>	FET 2	DMF	38.25	2.04	-0.66	1.71
<b>2.2<sup>-</sup></b>	BET 2	DMF	38.25	2.04	-0.23	2.03

**Table 2.2.** Estimated free energy changes ( $\Delta G$ ) and reorganization energies ( $\lambda$ ) for forward (FET 1 = <sup>2\*</sup>NDI<sup>-</sup> to NMI; FET 2 = NMI<sup>-</sup> to PI) and back electron transfer (BET 1 = NMI<sup>-</sup> to NDI; BET 2 = PI<sup>-</sup> to NDI) reactions in **2.1<sup>-</sup>** and **2.2<sup>-</sup>**. Static ( $\epsilon_s$ ) and high frequency/optical ( $\epsilon_{op}$ ) dielectric constants for the solvents are included.<sup>67, 79-81</sup> Within the model used, the parameters for the single forward electron transfer reaction in **2.1<sup>-</sup>** are the same as for the first forward electron transfer reaction in **2.2<sup>-</sup>**; this latter reaction is therefore not reported separately.

From the values in Table 2.2, all of the electron transfer reactions are predicted to be in the Marcus normal region. If the  $\Delta G$  does not change with solvent, then a larger reorganization energy should result in a slower reaction, according to Marcus theory. Somewhat unexpectedly, the estimated reorganization energies cannot completely explain the observed trend in electron transfer rates versus  $\epsilon_s$  of the solvent. The highest reorganization energy is found not for DMF, but for PrCN: since both solvents are fairly polar, the difference in  $\epsilon_{op}$  (refractive index) has a larger effect than the difference in  $\epsilon_s$ . The differences in rates are relatively small, and some of this deviation may be due to experimental error. Alternatively, this may suggest that the assumption of no dependence of  $\Delta G$  on  $\epsilon_s$  is incorrect, due to size differences between the ions. More quantitative estimation of these parameters would require abandoning the simple dielectric continuum model in favor of molecular dynamics simulations.<sup>82-83</sup> Ion pairing between the radical anion and the cobaltocenium counterion could also contribute to the reorganization

energy. This pairing would be more significant in less polar solvents.<sup>84-85</sup> However, this contribution is also difficult to quantify without a more detailed simulation.

For the slowest reaction, the back electron transfer from  $\text{PI}^\bullet$  to NDI in  $\mathbf{2.2}^\bullet$ , the differences in rates may not reflect differences in the solvent environment, but may reflect scavenging of  $\text{PI}^\bullet$  by trace impurities such as  $\text{O}_2$  in the solvent. Consistent with this explanation, some loss of  $\text{NDI}^\bullet$  was observed during these experiments. Additionally a sample prepared by electrochemical reduction of  $\mathbf{2.2}$  in DMF with 0.1 M  $\text{Bu}_4\text{NPF}_6$  showed an even longer photoproduct lifetime of 116  $\mu\text{s}$  (data not shown). While it is tempting to attribute this difference to the presence of the electrolyte, it is also possible that the electrochemical reduction was more effective (than the sub-stoichiometric cobaltocene used for other samples) at scavenging  $\text{O}_2$  and other reactive species from the solution.

### 2.3.5 EPR Spectroscopy

Owing to its long photoproduct lifetime,  $\mathbf{2.2}^\bullet$  is accessible to time-resolved EPR spectroscopy to follow the movement of its unpaired electron between magnetically inequivalent sites. However, two issues limit the sensitivity of EPR spectroscopy to the photoinduced electron transfer in  $\mathbf{2.2}^\bullet$ . Firstly, the EPR signals of  $\text{NDI}^\bullet$  and  $\text{PI}^\bullet$  are similar, with the radicals differing only slightly in g-factor (2.0031 and 2.0025 respectively)<sup>86-87</sup> and linewidth. Secondly, no additional spin polarization is generated by the photoinduced electron transfer process, in contrast to EPR studies of photogenerated radical pairs and triplets, meaning there is no enhancement of the photoproduct EPR signal relative to the  $\mathbf{2.2}^\bullet$  background signal. For these reasons, the transient EPR signals from  $\mathbf{2.2}^\bullet$  are expected to be weak.

The polar solvents required to solvate  $2.2^{\bullet-}$  degrade the  $Q$  factor of the microwave cavity, rendering time-resolved EPR techniques that use continuous wave (CW) microwaves insensitive. For this reason, time-resolved EPR measurements were performed using spin echo detection, which depends less on the cavity  $Q$ . Echo-detected EPR spectra of  $2.2^{\bullet-}$  in DMF at room temperature were collected in the absence of photoexcitation and at 500 ns following a 480 or 605 nm laser pulse (Figure 2.4). Due to the use of relatively short, nonselective microwave pulses, the hyperfine structure of  $NDI^{\bullet-}$  visible in typical CW EPR spectra is not resolved. A slight change in the EPR spectrum is observed upon photoexcitation: the difference spectrum shows increased intensity on the low-field edge of the  $NDI^{\bullet-}$  line and possibly at slightly higher field than this line, and decreased intensity on the high-field edge of the line. While this change is repeatable with both 480 and 605 nm excitation, it is not consistent with the expected change from photoreduction of PI. From the reported  $g$ -factors,  $PI^{\bullet-}$  has a smaller  $g$ -factor than  $NDI^{\bullet-}$  and should give a signal at higher magnetic field. The small increase in signal at higher field than the  $NDI^{\bullet-}$  line may be due to  $PI^{\bullet-}$ , but this signal is very weak and may be an artifact. The apparent shift in the  $NDI^{\bullet-}$  line may be due to a transient change in the microwave cavity resonant frequency due to heating by the excitation laser pulse. It will likely be necessary to repeat this experiment, and include comparison to a  $NDI^{\bullet-}$  control in which no electron transfer is expected.

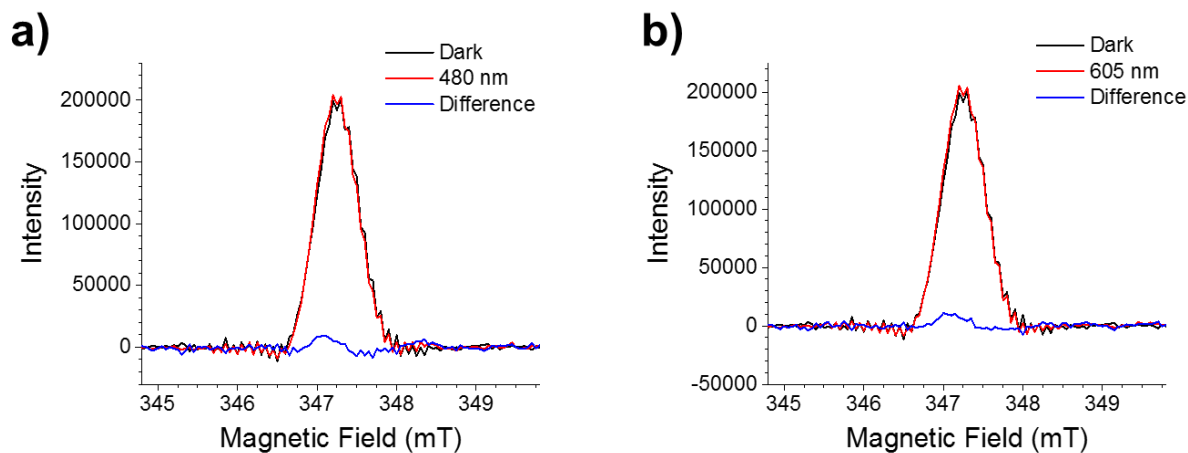


**Figure 2.4.** Echo-detected EPR spectra from  $2.2^{\bullet-}$  in DMF at room temperature, following excitation by (a) a 480 nm or (b) a 605 nm laser pulse.

## 2.4 Conclusions

These results show that some of the same strategies developed to control electron transfer rates in donor-acceptor compounds that form ion pairs can be applied to molecules with a single negative charge. The use of a secondary electron acceptor to form a donor-acceptor-acceptor triad was found to greatly slow the rate of back electron transfer. Photoproduct lifetimes in the microsecond regime were achieved. We also found that the forward electron transfer rates are faster in less polar solvents. The same trend holds for relatively fast back electron transfer reactions (faster than diffusion), but the lifetimes of longer-lived photoproducts may be limited by reactions with impurities. However, this trend is somewhat difficult to explain from estimated free energy changes and reorganization energies associated with these reactions, and more complex methods may be useful to model these reactions.

While the small increase in energy between the starting molecule and the photoproduct in **2.2** precludes the direct use of this system for photocatalysis, these ideas could be applied to the design of radical anion chromophore-catalyst systems for photocatalysis applications. Indeed, our colleagues have been able to build on these ideas to prepare a system capable of reducing a rhenium-based CO<sub>2</sub> reduction catalyst.<sup>51-52</sup>

For future investigations of spin polarization and coherence transfer in these systems, it will be advantageous to use two sites for the unpaired electron that differ in magnetic properties more than NDI<sup>-•</sup> and PI<sup>-•</sup>. One promising avenue is the use of C<sub>60</sub> derivatives as either the radical anion donor<sup>88</sup> or the electron acceptor, as the C<sub>60</sub> radical anion has a much lower g-factor than most organic radicals. Deuteration of rylenediimides can also be used to reduce the EPR linewidth of their radical anions, and we have recently succeeded in perdeuterating NDI using Crabtree's catalyst and D<sub>2</sub>.<sup>89</sup> These strategies should introduce a larger difference in the EPR signals of the starting material and product, simplifying observation of the electron transfer reaction by EPR spectroscopy.

## CHAPTER 3

# Charge and Spin Transport in an Organic Molecular Framework

Adapted in part from Wu, Y. L.; Horwitz, N. E.; Chen, K. S.; Gomez-Gualdron, D. A.; Luu, N. S.; Ma, L.; Wang, T. C.; Hersam, M. C.; Hupp, J. T.; Farha, O. K.; Snurr, R. Q.; Wasielewski, M. R. "G-quadruplex organic frameworks." *Nature Chemistry*, advance online publication, doi:10.1038/nchem.2689 (2016).

### 3.1 Introduction

Most current electronic and spintronic devices are composed of solid, inorganic materials. Replacing some or all of these components with organic solids could provide advantages including flexibility, ease of fabrication, and synthetic tunability.<sup>6</sup> To compete with existing materials, organic materials must allow efficient transport of charge carriers. Achieving high charge carrier mobilities requires careful control of the packing and interactions between adjacent molecules. For this reason, much effort has targeted self-assembled systems in which electron donors and acceptors form ordered,  $\pi$ -stacked arrays.<sup>90-91</sup> Recently, our group has prepared several novel organic framework materials in which guanine quadruplexes serve as an electron donor and as a scaffold for ordering covalently attached electron acceptors.<sup>53</sup> These materials have been shown to undergo photoinduced charge separation, and due to the ordered stacks of donor and acceptor moieties, these materials are expected to show high mobilities for photogenerated holes and electrons. For these reasons, these materials may be useful for applications including organic batteries and photovoltaics.

It is somewhat difficult to measure charge and spin transport processes in these solid materials, and this is a major challenge in developing functional organic materials towards electronic and spintronic applications. The techniques traditionally used for studying these processes in isolated organic molecules – namely transient optical absorption and electron paramagnetic resonance (EPR) spectroscopy – are more challenging to apply in bulk materials with many identical or similar sites. As such, information from several techniques is needed to understand charge and spin transport in these guanine quadruplex frameworks.

Time-resolved microwave conductivity (TRMC) is a technique that allows the photogeneration of mobile charge carriers to be probed, an essential process in organic photovoltaics. Compared with techniques that involve direct measurement of photocurrent generation, it is more difficult to obtain quantitative quantum yields and mobilities from TRMC, but unlike these methods, TRMC does not require attaching electrodes to the sample, and is not dependent on the fabrication parameters required to build a device. TRMC is therefore an ideal technique for rapidly assessing multiple materials for potential application in photovoltaics. In the TRMC experiment, microwave radiation is directed at a sample, usually held in a resonant cavity, and the reflected microwave power is measured as a function of the time after excitation of the sample with a laser pulse. Mobile charge carriers can move in response to the oscillating electric field from the microwave radiation, increasing dielectric loss in the material. While other processes can contribute to the loss in liquid solution, including reorientation of polar molecules, the signal in solid samples is primarily due to free charge carriers.<sup>25, 28</sup>

EPR spectroscopy remains the best technique to understand spin processes following photoexcitation in these frameworks. Photoinduced electron transfer produces a spin-correlated radical ion pair with a unique EPR signal that depends on the coupling between the electron and hole, the magnetic characteristics of the individual polarons, and the singlet or triplet nature of the excited state driving charge separation. However, the interpretation of these spectra is more complicated than for analogous states in small molecules. The exchange and dipolar coupling in the pair can change over time and/or exhibit a wide range across the ensemble, due to migration of the mobile polarons. Several possible explanations must be considered to explain the

observed spectra, and EPR experiments at different magnetic fields are often required to understand the origin of the spectra.<sup>73</sup>

EPR spectroscopy can also provide information on charge transport, as electrons and holes have unpaired spins. In a solid material, only electrons move, while nuclei remain relatively fixed; for this reason, the electron-nuclear hyperfine interaction contains information about the mobility of the unpaired electrons. This relation was originally described by McConnell, who found that as an electron becomes delocalized across additional sites on the EPR time scale, the hyperfine coupling to any given nucleus decreases proportionately to the time spent on that site.<sup>23</sup> This applies quite broadly – both to single molecules in which resonance, rearrangement, or tautomerization delocalizes the unpaired spin, and to bulk materials with movement of the unpaired spin between multiple sites. However, in most solid samples, the hyperfine lines are broadened by anisotropy, and it is very difficult to measure individual coupling constants from the EPR spectrum. Norris extended the McConnell relation to this situation, finding that EPR signals broadened by unresolved hyperfine coupling show a decrease in linewidth of  $1/\sqrt{N}$  for an electron delocalized across  $N$  identical sites.<sup>92</sup> By measuring the linewidth of the EPR signal arising from a charge carrier in a material, its degree of delocalization can be probed.

In this study, we use TRMC and time-resolved EPR spectroscopy to interrogate the charge transport and spin evolution in two guanine quadruplex frameworks, **G<sub>2</sub>NDI** and **G<sub>2</sub>PDI**, following photoexcitation and charge separation. Additionally, steady-state, continuous wave EPR (CW-EPR) spectroscopy is applied to chemically reduced framework materials, demonstrating delocalization of electrons in these compounds. The structures of these

frameworks, as well as the monomeric NDI and PDI standards used for CW-EPR spectroscopy, are given in Figure 3.1. Full details of the synthesis, chemical and structural characterization, and charge separation dynamics have been presented previously.<sup>53</sup>

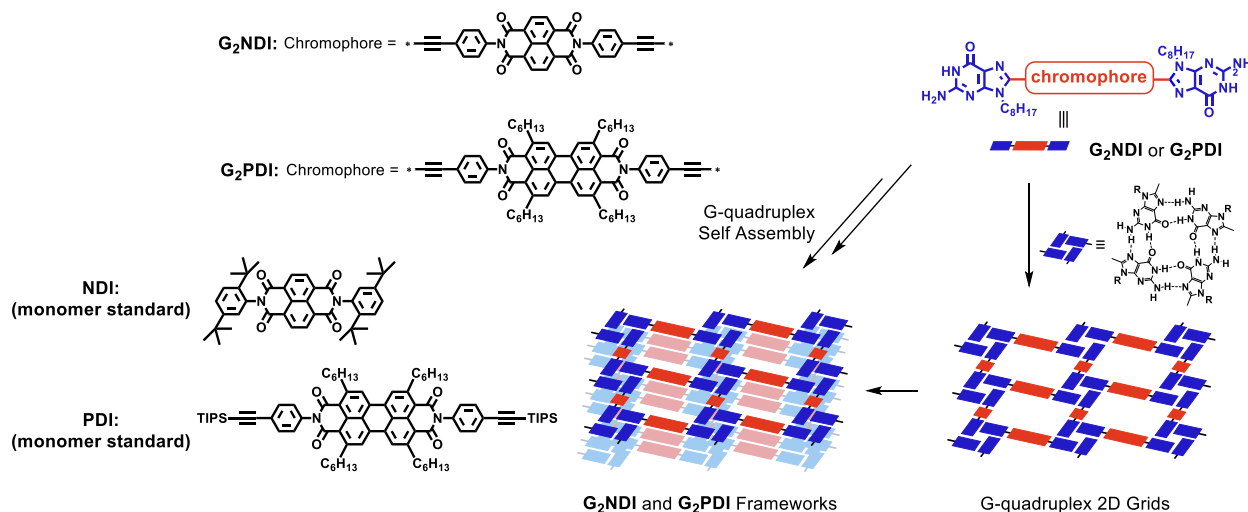


**Figure 3.1.** Structures of the molecules used in this study: the framework materials **G<sub>2</sub>NDI** and **G<sub>2</sub>PDI**, and the monomeric standards **NDI** and **PDI**. Adapted from Wu et al.<sup>53</sup>

### 3.2 Experimental

Electron paramagnetic resonance (EPR) measurements were made at X-band (~9.5 GHz) using a Bruker Elexsys E680-X/W EPR spectrometer outfitted with a split ring resonator (ER4118X-MS5) or a Bruker Elexsys E580 spectrometer with a super high Q resonator (4122 SHQE-W1). The temperature was controlled by an Oxford Instruments CF935 continuous flow cryostat using liquid N<sub>2</sub>.

Continuous wave (CW) EPR spectra were measured using 0.2–0.6 mW microwave power and 0.01–0.1 mT field modulation at 60–100 kHz. Time-resolved EPR measurements

were performed following photoexcitation with 7 ns, 1.8 mJ pulses using the output of an optical parametric oscillator (Spectra-Physics Basi-scan), pumped with the output of a frequency-tripled Nd:YAG laser (Spectra-Physics Quanta-Ray Pro 350). NDI-containing compounds were excited at 416 nm, while PDI-containing samples were excited at 500 nm. Transient CW EPR (TR-EPR) spectra were collected following photoexcitation, and the kinetic traces of the transient magnetization were acquired in quadrature under CW irradiation (2–20 mW). Sweeping the magnetic field gave 2D spectra versus both time and magnetic field. For each kinetic trace, the signal acquired prior to the laser pulse was subtracted from the data. Kinetic traces recorded at magnetic field values off-resonance were considered background signals, whose average was subtracted from all kinetic traces.

Samples for time-resolved measurements were loaded as dry powders into quartz tubes (1.80 mm o.d. × 1.50 mm i.d.), evacuated on a vacuum line ( $10^{-4}$  torr), and sealed under vacuum using an oxy-hydrogen torch. Chemically reduced framework samples were prepared in an N<sub>2</sub> glovebox by adding a solution of cobaltocene (0.07 mol CoCp<sub>2</sub> per mol NDI or PDI) in CH<sub>2</sub>Cl<sub>2</sub> to a stirred suspension of the framework in CH<sub>2</sub>Cl<sub>2</sub>. The resulting reduced suspension was added to quartz tubes (1.80 mm o.d. × 1.50 mm i.d.) and allowed to settle. The tubes were sealed with UV-curing epoxy prior to removal from the glovebox. NDI and PDI anion standards in polystyrene were prepared in an N<sub>2</sub> glovebox by addition of cobaltocene solution in CH<sub>2</sub>Cl<sub>2</sub> to a THF solution of polystyrene ( $M_w = 935$  kDa) and *N,N*-bis(2,5-di-*tert*-butylphenyl)-1,4,5,8-naphthalene diimide (0.1 wt%) or bis(4-((triisopropylsilyl)ethynyl)phenyl)-2,5,8,11-tetrahexylperylene-3,4:9,10-bis(dicarboximides) (0.19 wt%). The solution was then drop cast on glass slides and dried further under vacuum. The resulting polystyrene films were scraped off

and loaded into quartz tubes (4.0 mm o.d. x 3.0 mm i.d.), which were affixed to a vacuum valve and unloaded from the glovebox. The tubes were evacuated ( $10^{-4}$  torr) and sealed under vacuum using an oxy-hydrogen torch.

Time-resolved microwave conductivity (TRMC) measurements were performed using a Bruker Elexsys E680-X/W EPR spectrometer outfitted with a Bruker 4109EF/9102 resonator that maximizes the microwave electric field component ( $E_1$ ) at the sample position. TRMC measurements were performed at X-band (9.7 GHz) using 2.0 mW of microwave power. Resonator Q-values were measured to be between 2000 and 3500, corresponding to an estimated time constant of 60-110 ns.<sup>93</sup> The rise time of the TRMC signal was fit to provide a more accurate estimate of the time resolution of the experiment; typical fit values were near 50 ns. TRMC signals were collected similarly to TR-EPR spectra, with the applied magnetic field turned off to avoid detecting EPR signals. The same laser excitation parameters were used for TRMC and TR-EPR measurements. Blank kinetic traces recorded using an empty quartz tube were subtracted from the experimental data. Signals were detected in quadrature following mixing of the reflected microwaves with a reference arm and then phased into one channel. All TRMC measurements were performed at room temperature under vacuum, with the exception of the air-exposure experiments. Samples for air-exposure TRMC experiments were sealed with epoxy in an N<sub>2</sub>-filled glovebox. Following measurement of the TRMC signal under N<sub>2</sub>, air was allowed to diffuse into the sample through a needle filled with anhydrous CaSO<sub>4</sub> for 30 minutes.

### 3.3 Results and Discussion

#### 3.3.1 Steady-state EPR spectroscopy of chemically reduced frameworks

To investigate the delocalization of electrons in **G<sub>2</sub>NDI** and **G<sub>2</sub>PDI**, these frameworks were partially reduced (~7 mol %) using a solution of cobaltocene. Partial reduction was chosen to approximate conditions in a photovoltaic device, and allow investigation of isolated charge carriers in the absence of spin-spin or Coulombic interactions. Due to the low stability of guanine radical cation, the corresponding experiment with a chemical oxidant to study hole mobility was not performed. For comparison, dilute (0.10-0.19% by weight) samples of chemically reduced NDI and PDI monomer standards in a solid polystyrene matrix were prepared. At higher concentrations, these samples gave broadened lines, presumably due to spin-spin interactions between radicals.

As expected, the CW-EPR spectra of the NDI and PDI standards show single, broad lines with no resolvable hyperfine coupling. In monomeric NDI and PDI radical anions, broad linewidths result from unresolved hyperfine coupling to the four core <sup>1</sup>H and two imide <sup>14</sup>N nuclei, in addition to g-factor anisotropy. Hyperfine anisotropy leads to broad lines when averaging over the multiple orientations in these unoriented solid samples. Because the g-factor anisotropy in these molecules is small (due to the weak spin-orbit coupling common in organic radicals), no distinct features arising from g anisotropy are observed.

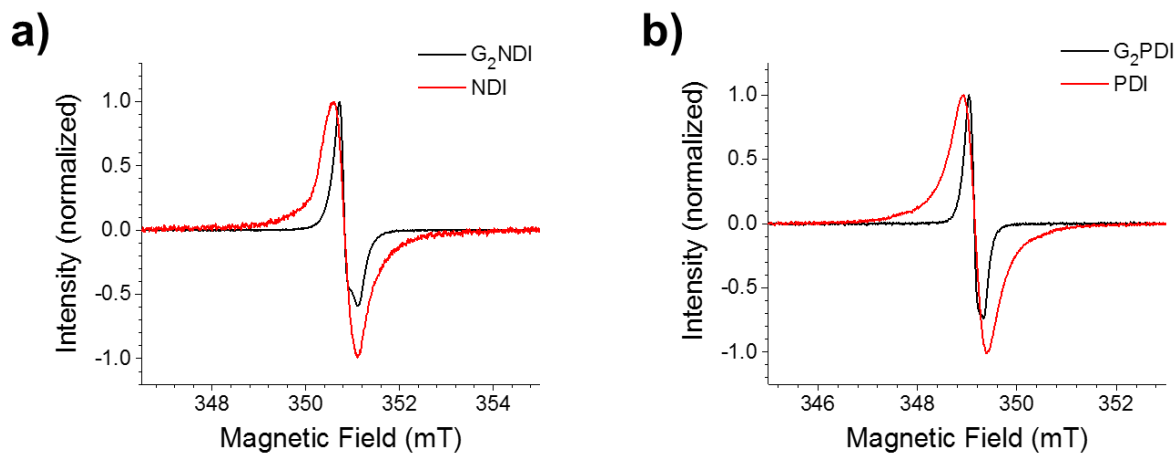


**Figure 3.2.** CW-EPR spectra at X-band (9.5 GHz) of chemically reduced (a) **NDI** and **G<sub>2</sub>NDI** and (b) **PDI** and **G<sub>2</sub>PDI** at room temperature. **NDI** and **PDI** radical anions are dispersed in polystyrene films, while partially-reduced **G<sub>2</sub>NDI** and **G<sub>2</sub>PDI** are suspended in CH<sub>2</sub>Cl<sub>2</sub>.

In contrast, the CW-EPR spectra of chemically-reduced **G<sub>2</sub>NDI** and **G<sub>2</sub>PDI** are much narrower (Figure 3.2). Both spectra show an asymmetry due to *g*-factor anisotropy, particularly pronounced for **G<sub>2</sub>NDI**. Such a reduction in linewidth is well known for systems in which the unpaired electron is delocalized across multiple sites on the EPR timescale.<sup>94-97</sup> Norris et al. have shown that the linewidth of such a spectrum is proportional to  $1/\sqrt{N}$ , where *N* is the number of sites over which the spin is delocalized.<sup>92</sup> For **G<sub>2</sub>NDI**, the full width at half maximum of the integrated CW-EPR spectrum decreases from 0.86 mT to 0.46 mT, corresponding to  $N = 3.5$ . The unpaired electron is therefore delocalized over a lower bound of 3 or 4 NDI units. As this analysis neglects sources of broadening other than hyperfine coupling – including the observed *g*-factor anisotropy – it is likely that the unpaired electron is delocalized over a larger number of sites. For **G<sub>2</sub>PDI**, substantial narrowing of the CW-EPR spectrum is also observed, though the **G<sub>2</sub>PDI** spectrum shows less anisotropy than that of **G<sub>2</sub>NDI**. The full width at half maximum of the integrated CW-EPR spectrum decreases from 0.83 mT to 0.32 mT between the polystyrene

film and the framework, corresponding to  $N = 6.7$  as a lower bound for the number of PDI units over which the spin is delocalized.

The observation of g-factor anisotropy is also informative. For a disordered aggregate, delocalization of the unpaired electron is expected to average over the g-anisotropy, similar to a molecule tumbling in liquid solution. Instead, an anisotropic g-factor is observed for **G<sub>2</sub>NDI**, consistent with the published g-tensor for monomeric NDI anion.<sup>98</sup> This strongly suggests that the delocalization of the unpaired spin occurs over NDI units that are oriented relative to each other, rather than a highly disordered array. Some precedence for this effect can be found in the literature of paramagnetic defects in silicon, in which mobile spins show g-tensor values reflecting an average of the sites occupied by the spin.<sup>99-101</sup> **G<sub>2</sub>PDI** shows similar features, although less pronounced. This is consistent with the powder X-ray diffraction data showing an ordered arrangement of NDI and PDI in these materials.<sup>53</sup> These results suggest a substantial electron mobility over an ordered lattice of electron acceptors in **G<sub>2</sub>NDI** and **G<sub>2</sub>PDI**, an important property for application in photovoltaics and battery cathodes. These results also mean that at least one mobile charge carrier must be considered when interpreting time-resolved EPR spectra and TRMC data.

### 3.3.2 TRMC

TRMC kinetic traces of **G<sub>2</sub>NDI** and **G<sub>2</sub>PDI** under vacuum are presented in Figure 3.3. Solid, polycrystalline samples of **NDI** and **PDI** do not show a strong response, and were subtracted from the **G<sub>2</sub>NDI** and **G<sub>2</sub>PDI** data to remove a background signal caused by light hitting the microwave cavity. Both materials show a rapid rise of the conductivity signal, within

the instrument response of the TRMC experiment. This is consistent with the transient optical absorption data showing picosecond charge separation in both materials.<sup>53</sup> The TRMC signal for both materials is similar, showing an initial decay near 1  $\mu\text{s}$  as well as substantial signal that persists past the 8  $\mu\text{s}$  time window studied. More complex TRMC analysis based on the phase of the signal can also help distinguish between contributions from conductivity due to mobile charge carriers and increases in the polarizability of the sample,<sup>25-26</sup> but our current instrumentation is not amenable to these techniques. Nonetheless, we can be confident that the observed signal is primarily due to mobile charge carriers. In solid samples, pairs of immobile charge carriers cannot reorient in response to the microwave electric field, meaning these species do not contribute to the TRMC signal. Additionally, transient absorption data indicates that geminate recombination of closely-bound ion pairs occurs on the picosecond timescale, completing well within the TRMC instrument response.<sup>53</sup>

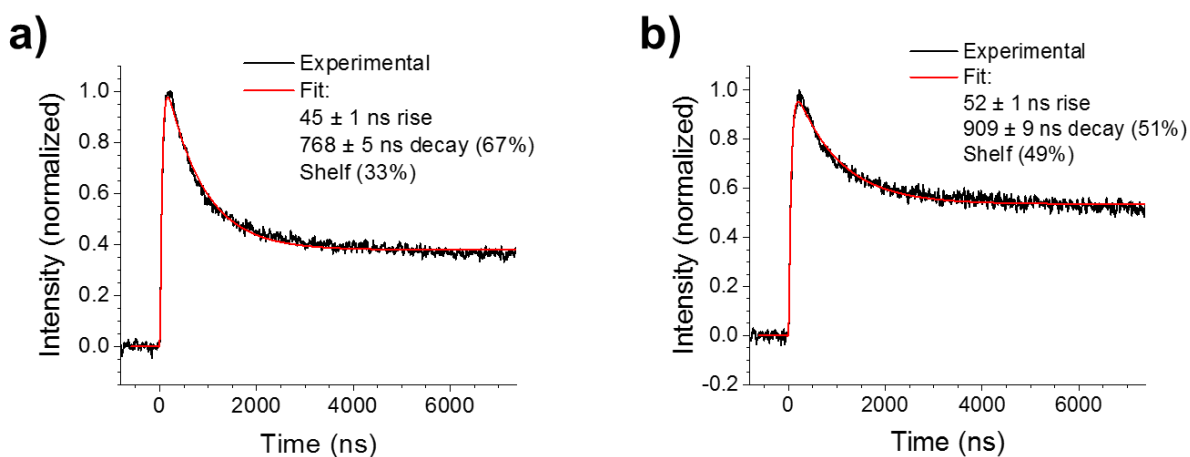


**Figure 3.3.** TRMC kinetic traces from (a) G<sub>2</sub>NDI and (b) G<sub>2</sub>PDI under vacuum at room temperature, following excitation by a 416 nm or 500 nm laser pulse respectively.

It is not immediately clear if the large TRMC signal indicates mobile electrons, holes, or both in the material. From the CW-EPR data, we expect electrons to be highly mobile within **G<sub>2</sub>NDI** and **G<sub>2</sub>PDI**, but the behavior of the holes is less clear. To attempt to gain more information about the carriers responsible for the TRMC signal, we repeated this experiment under both N<sub>2</sub> and dry air (Figure 3.4). O<sub>2</sub> in air is expected to quench electrons (NDI or PDI radical anions) in the material, but is not expected to react as quickly with holes (guanine radical cations). Due to some issues with removing the background signal from these samples, it was not possible to obtain a quantitative fit to this data. Under N<sub>2</sub>, the observed signal is very similar to that measured under vacuum for both **G<sub>2</sub>NDI** and **G<sub>2</sub>PDI**. Under air, the kinetics of the TRMC signal in both **G<sub>2</sub>NDI** and **G<sub>2</sub>PDI** are unchanged, but the magnitude of the signal is reduced. The reduction in signal is more pronounced for **G<sub>2</sub>NDI** than for **G<sub>2</sub>PDI**. A discoloration of **G<sub>2</sub>NDI** upon photoexcitation, attributed to trapped/long lived charge carriers, was observed in samples under vacuum and under N<sub>2</sub>, but not under air, suggesting that O<sub>2</sub> may react with these carriers on a longer timescale (ms to s). This observation and the similarity of the TRMC kinetics under N<sub>2</sub> and under air suggest that quenching of charge carriers by O<sub>2</sub> is mostly occurring in two time regimes: within the instrument response and longer than the TRMC time window. The fast quenching likely occurs when carriers are generated near adsorbed O<sub>2</sub>, while the slow quenching likely occurs following diffusional encounters of O<sub>2</sub> and charge carriers. Consistent with this explanation, **G<sub>2</sub>PDI** shows both a lower porosity by N<sub>2</sub> adsorption measurements<sup>53</sup> and less loss of signal upon introduction of O<sub>2</sub>, as compared to **G<sub>2</sub>NDI**. In the case that the TRMC signal arises from both carriers, preferential quenching of electrons by O<sub>2</sub> would likely lead to a change in the kinetics of the bimolecular decay of the remaining carriers.

Because such a change is not observed, this suggests that either the fast quenching involves the excited chromophore (preventing formation of charge carriers), or that mobile electrons dominate the TRMC signal. These results indicate that long-lived free charge carriers are formed upon photoexcitation of **G<sub>2</sub>NDI** and **G<sub>2</sub>PDI**, a prerequisite for the use of these materials in photovoltaics.

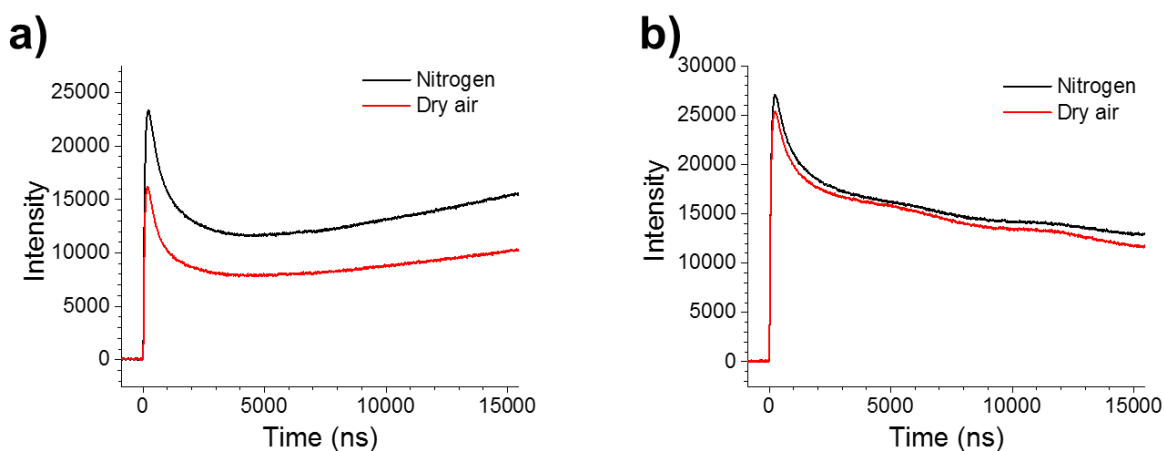


**Figure 3.4.** TRMC kinetics of (a) **G<sub>2</sub>NDI** and (b) **G<sub>2</sub>PDI** under nitrogen and dry air. Background subtraction was not successful for the data in (a), causing the difference in shape versus Figure 3.3.

### 3.3.3 Time-resolved EPR spectroscopy

Time-resolved EPR (TR-EPR) spectra at X-band (9.5 GHz) of **G<sub>2</sub>NDI** and **G<sub>2</sub>PDI** following photoexcitation at room temperature both show narrow, negative signals near  $g = 2$  (Figure 3.5). In the TR-EPR experiment, negative signals occur either by loss of an existing paramagnetic species, or by stimulated emission from a spin polarized species. While a weak CW-EPR background signal is associated with the persistent sample discoloration noted

previously, EPR spectra at higher field also show absorptive features (vide infra), meaning loss of this weak signal is unlikely to account for the observed negative features. Instead, these features are due to a spin-polarized state. The narrow width ( $\sim 3$  mT) of the TR-EPR signal allows assignment of these bands to a photogenerated radical ion pair, rather than the neutral excited triplet states of NDI<sup>102</sup> or PDI<sup>103</sup> (usually  $\sim 100$  mT wide), which supports the assignments in the transient absorption experiments. TR-EPR spectra of photogenerated radical pairs in isolated molecules typically show four overlapping transitions, two absorptive and two in stimulated emission.<sup>104-105</sup> However, spectra showing all transitions polarized in emission or in absorption have been reported from solid materials in which the two radicals can delocalize across different molecules.<sup>106-109</sup>

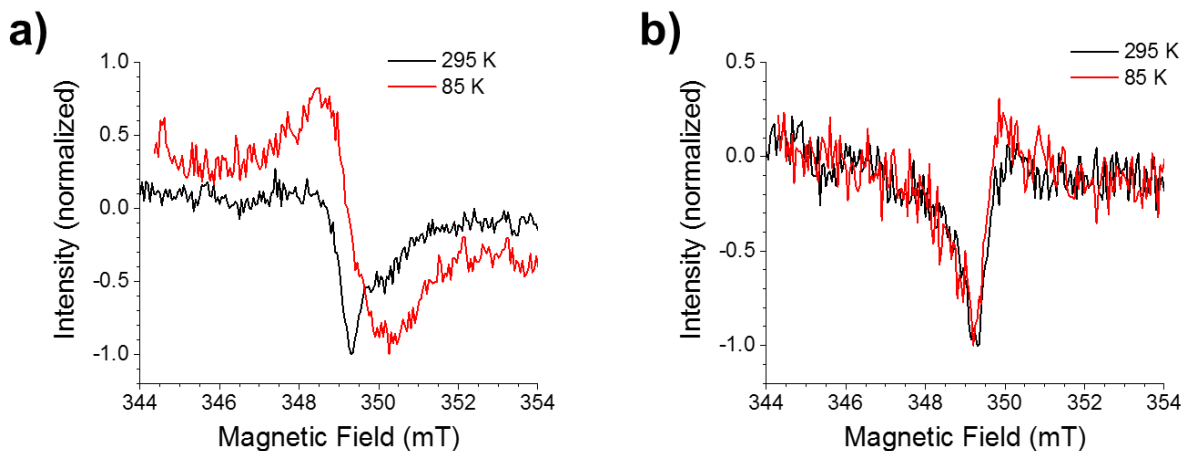


**Figure 3.5.** X-band (9.5 GHz) TR-EPR spectra (a) **G<sub>2</sub>NDI** following excitation at 416 nm and (b) **G<sub>2</sub>PDI** following excitation at 500 nm, at room temperature (295 K) and 85 K.

To understand these signals, it is necessary to examine the spin mixing processes occurring following photoexcitation of **G<sub>2</sub>NDI** and **G<sub>2</sub>PDI**. The spin state of the initial

photoexcited state is carried over into the radical pair. Excitation of **G<sub>2</sub>NDI** at 416 nm and of **G<sub>2</sub>PDI** at 500 nm populates the singlet excited state of NDI or PDI respectively. NDI has been shown to undergo intersystem crossing in <50 ps from its singlet excited state to a triplet state,<sup>110</sup> but transient absorption measurements suggest charge separation in **G<sub>2</sub>NDI** is faster than this process. The radical pairs initially formed from charge separation in **G<sub>2</sub>NDI** and **G<sub>2</sub>PDI** thus have singlet character. Depending on the magnitude and sign of the exchange coupling  $2J$  within the radical pair relative to the applied magnetic field, the singlet radical pair state will mix with one or more of the triplet states. This mixing process results in initial population of multiple eigenstates of the radical pair, which determines the EPR spectrum that will result (Figure 3.6). In the case of  $2J > 0$ , weak exchange coupling ( $2J \ll B_0$ ) results in S-T<sub>0</sub> mixing and four allowed EPR transitions giving rise to an *e-a-e-a* (*a* = absorption, *e* = stimulated emission) spectrum, as described in Chapter 1.3. Exchange coupling approximately equal to the Zeeman interaction results in S-T<sub>+</sub> mixing and the observation of a fully emissive EPR spectrum. If  $2J$  is instead negative, the EPR spectrum will instead show *a-e-a-e* polarization (or *a-e* in the case of overlapping lines) for  $2J \ll B_0$  and all *a* in the case of  $2J \approx B_0$  due to S-T<sub>-</sub> mixing. Likewise, radical pairs derived from triplet excited state precursors will also show this inversion of the EPR spectrum, due to initial population of all three triplet radical pair states.

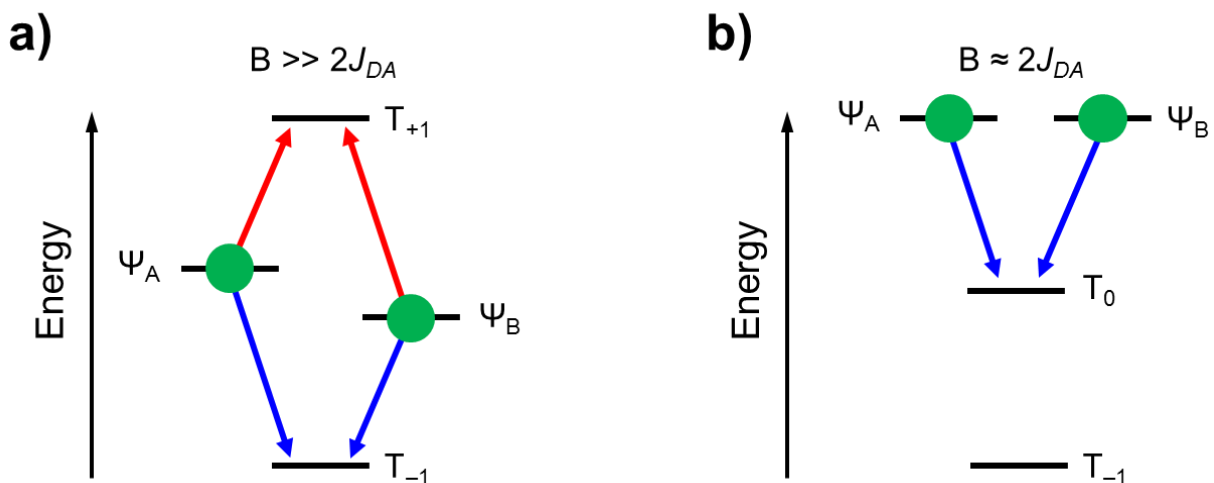


**Figure 3.6** Schematic diagrams showing the radical pair spin levels for (a)  $2J \ll B_0$  and (b)  $2J \approx B_0$ . Green circles represent population of states following charge separation from a singlet excited state. Arrows represent allowed EPR transitions polarized in absorption (red) and emission (blue).

Several different mechanisms – each implying different spin and charge transport properties – have been proposed to account for all-emissive or all-absorptive spectra. Behrends et al. describe growth of an all-absorptive lineshape at late times ( $\sim 10 \mu\text{s}$ ) following the initial observation of an *e-a-e-a* (*a* = absorptive, *e* = emissive) polarization pattern from a conjugated polymer-fullerene blend.<sup>109</sup> They attribute this absorptive polarization to dissociation of the radical ion pair into free polarons and associated spin relaxation. However, such a mechanism is not likely to be the main source of the negative polarization observed for **G<sub>2</sub>NDI** and **G<sub>2</sub>PDI**, as this polarization is present initially, not just at late times. Franco et al. ascribe similar signals in a different polymer-fullerene blend to spin-selective charge recombination in which S-T- or S-T+ mixing occurs in closely-bound, strongly exchange-coupled radical pairs immediately prior to charge recombination.<sup>108</sup> In the case of S-T- mixing, the lowest energy levels are selectively depopulated, leading to emissive polarization of the radical pair EPR transitions. The formation

of these closely-bound pairs depends on delocalization of the radicals throughout the solid material, and Franco et al. also show that as the sample is cooled to 120 K, this process slows and an *a-e-a-e* polarization pattern is recovered. Alternatively, Yonemura et al. show that similar spectra can be obtained from radical pairs in isolated molecules without the need for mobile charge carriers, provided the exchange coupling between the radicals is large enough to allow S-T. or S-T<sub>+</sub> mixing. Under this mechanism, the polarization pattern is observed to change when the EPR experiment is repeated at higher magnetic fields.<sup>73</sup> Both mechanisms involve S-T. or S-T<sub>+</sub> mixing. However, because this mixing selectively populates states in the Yonemura mechanism but depopulates states in the Franco mechanism, the relation of the sign of *J* to the sign of the EPR spectrum is opposite between these mechanisms. The mechanisms also differ in whether this mixing occurs during charge recombination (Franco) or charge separation (Yonemura), and in the implied motions of the unpaired electrons. These studies therefore suggest additional EPR experiments at higher magnetic field and at lower temperatures that can be used to interrogate the mechanism of spin mixing following photoexcitation.

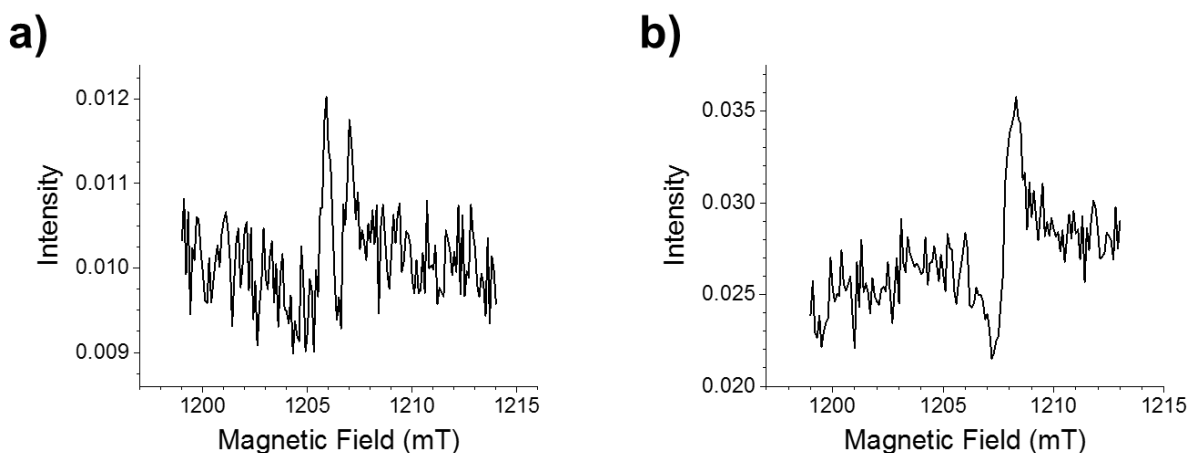


**Figure 3.7.** TR-EPR spectra (a) **G<sub>2</sub>NDI** following excitation at 420 nm and (b) **G<sub>2</sub>PDI** following excitation at 500 nm, at room temperature at Q-band (34 GHz).

TR-EPR spectra of **G<sub>2</sub>NDI** and **G<sub>2</sub>PDI** at room temperature at Q-band (34 GHz) are presented in Figure 3.7. Due to instrumental limitations, the data may contain an arbitrary 180° phase offset, i.e. the absolute sign of the spectrum is arbitrary. Despite this limitation, it is clear that the polarization pattern for **G<sub>2</sub>NDI** changes from all-emissive to *e-a-e-a* (or *a-e-a-e*). For **G<sub>2</sub>PDI**, only two lines can be resolved, giving an *e-a* (or *a-e*) polarization pattern. The TR-EPR experiment at X-band at 85 K shows an *a-e* spectrum from **G<sub>2</sub>NDI** (Figure 3.5a). The spectrum of **G<sub>2</sub>PDI** under these conditions is still mostly emissive, but a weak, absorptive line is observed (Figure 3.5b).

Under the Yonemura mechanism, the emissive nature of the room temperature TR-EPR spectra at X-band, combined with the optical evidence suggesting a singlet excited state precursor, indicates that  $2J > 0$  for both **G<sub>2</sub>NDI** and **G<sub>2</sub>PDI**. In contrast, these observations would be consistent with a value of  $2J < 0$  under the Franco mechanism. Sekiguchi et al. have shown that  $2J > 0$  for radical ion pairs exhibiting charge recombination in the Marcus inverted region<sup>111</sup> (as is likely the case for both **G<sub>2</sub>NDI** and **G<sub>2</sub>PDI**), indicating that the Yonemura mechanism provides a better explanation for this data. In contrast, the TR-EPR spectrum of **G<sub>2</sub>NDI** at 85 K at X-band shows an *a-e* polarization pattern, consistent with either  $2J > 0$  or a triplet excited state precursor. Because **G<sub>2</sub>NDI** and **G<sub>2</sub>PDI** are in the solid state under all conditions studied, neither the free energy change nor the reorganization energy associated with charge recombination are expected to show a large change between 85 K and 295 K; thus, recombination is still expected to be in the Marcus inverted region. This leaves a triplet excited state precursor as the most likely explanation for the polarization pattern of **G<sub>2</sub>NDI** at 85 K. If the charge separation slows at low temperatures, excitation of **G<sub>2</sub>NDI** will initially result in

intersystem crossing of the NDI chromophore (transient absorption measurements could be conducted at 85 K to lend further support to this idea). This explanation is also consistent with the observation of an  $e(-a)$  polarization pattern from **G<sub>2</sub>PDI**, as PDI does not show a high intersystem crossing rate.

When analyzing the TR-EPR data, it is also necessary to consider that not all pairs of charge carriers in these materials will give a strong EPR signal. Thus, it is likely that the observed signals are dominated by a sub-population of radical pairs, and there is likely a range of values of  $2J$  exhibited by the observed radical pairs. The change of the polarization pattern upon performing the TR-EPR experiment at Q-band suggests that at most,  $2J$  is approximately equal to the Zeeman interaction at X-band. At the higher magnetic field used for Q-band measurements, S-T<sub>0</sub> mixing predominates, resulting in the observed polarization. Taken together with the X-band results showing S-T<sub>+</sub> mixing, these results indicate that the range of  $2J$  values for observable radical pairs is small, at least during the spin mixing process. As the exchange coupling decays exponentially with the distance between the radicals, this relatively large value of  $2J$  suggests the observed radical pairs have a short separation distance, on the order of 10 – 20 Å. As this distance is similar to that within **G<sub>2</sub>NDI** and **G<sub>2</sub>PDI** monomers, it is likely that the bulk of the TR-EPR signal derives from Coulombically-trapped short-distance radical ion pairs – or at least from spin mixing that occurs in this regime. Recent work has suggested that in many photovoltaic devices, there is competition between charge separation to localized, Coulombically-trapped ion pairs (often termed a charge transfer or CT state) and to delocalized polaron pairs (often termed a charge-separated or CS state).<sup>112-115</sup> The observation of free charge carriers by TRMC suggests that both CT and CS states are present in **G<sub>2</sub>NDI** and **G<sub>2</sub>PDI** after

photoexcitation. Because geminate recombination of the initial CT states is observed by transient absorption spectroscopy to be much faster than the timescale of TR-EPR spectroscopy, the TR-EPR signal must arise either from CT states trapped at some defect, or from CT states that later dissociate to form free charge carriers.<sup>116-117</sup>

The polarization changes in the X-band TR-EPR spectra at 85 K show that S-T<sub>0</sub> mixing becomes more prominent at low temperatures, suggesting a decrease in the value of  $2J$ . This decrease may be due to conformational changes in the **G<sub>2</sub>NDI** and **G<sub>2</sub>PDI** frameworks that reduce the electronic coupling between radicals,<sup>47, 74</sup> or may reflect different motions of the charge carriers within the solid. Drastic conformational changes seem unlikely given that the materials are already ordered, rigid solids at 295 K. Initially-populated CT states with strong exchange coupling may be unable to dissociate into CS states at low temperatures,<sup>116</sup> resulting in their rapid geminate recombination and precluding them from contributing to the TR-EPR spectra at later times. Any pairs that result from direct population of the CS states would then be the main contributors to the TR-EPR spectra, and spin mixing in these weakly-coupled pairs should be predominated by S-T<sub>0</sub> mixing. Alternatively, the process proposed by Franco et al. in which free charge carriers are thermally detrapped and subsequently encounter to form Coulombically-bound pairs<sup>108</sup> may be contributing to the temperature dependence as well. However, this process seems less likely in these systems given that the TR-EPR data shows the polarization developing much faster ( $\sim 10^1$  ns) than the bimolecular recombination ( $\sim 10^3$  ns) observed by TRMC. Additionally, the relation between the sign of  $J$  and the polarization of the EPR spectrum described earlier are not consistent with the Franco mechanism.

### 3.4 Conclusions

TRMC and EPR measurements of **G<sub>2</sub>NDI** and **G<sub>2</sub>PDI** are able to illuminate the charge transport and spin evolution following photoexcitation of these materials. From these measurements, we propose a likely sequence of events following photoexcitation. Electron transfer from the NDI or PDI excited state results in formation of a closely-bound CT state, possibly in competition with direct formation of a delocalized CS state composed of free charge carriers. At room temperature, dissociation of the CT state can produce additional free charge carriers that preserve the signature of spin mixing in the CT state. Further transient absorption measurements at lower temperatures could help confirm or refute the validity of this model. Understanding the model of charge separation in **G<sub>2</sub>NDI** and **G<sub>2</sub>PDI** is important for potential applications of these materials in photovoltaics, as these models suggest different strategies to favor the formation of free charge carriers. From this work, it is likely that maintaining good ordering of the electron donors and acceptors in guanine quadruplex frameworks is important to obtaining a high yield of CS states,<sup>112</sup> in addition to allowing efficient transport of these charge carriers to the device electrodes.

Taken together, the TRMC and EPR measurements of **G<sub>2</sub>NDI** and **G<sub>2</sub>PDI** show that guanine quadruplex-based framework materials are a promising architecture for organic photovoltaics, batteries, and possibly spintronics. On the basis of these encouraging results, ongoing research is directed at incorporating more electron donors and acceptors into the frameworks, as well as efforts to grow conformal films of these materials for electronic devices.

## CHAPTER 4

# Picosecond Control of Photogenerated Radical Pair Lifetimes using a Stable Third Radical

Adapted from Horwitz, N. E.; Phelan, B. T.; Nelson, J. N.; Krzyaniak, M. D.; Wasielewski, M. R. "Picosecond Control of Photogenerated Radical Pair Lifetimes using a Stable Third Radical." *The Journal of Physical Chemistry A*, 120 (18), 2841–2853 (2016).

## 4.1 Introduction

The ability to control the lifetimes of photogenerated radical ion pairs (RPs) in donor-acceptor systems is important for the design of organic photovoltaics,<sup>63, 118-119</sup> systems for artificial photosynthesis,<sup>55</sup> and molecular spintronics.<sup>120-121</sup> Such control is usually exercised by manipulating the electronic coupling between an electron donor and acceptor and/or the free energy for charge recombination, both of which are key parameters in electron transfer rate theory.<sup>72</sup> A significant body of work has demonstrated that RP spin dynamics can serve as an additional, independent channel through which the charge recombination rate can be controlled.<sup>122-129</sup> Introduction of a stable radical coupled to one or more components of an electron donor-acceptor system can alter these spin dynamics,<sup>122-123, 130-131</sup> and is more amenable to device applications than approaches using static<sup>75, 132-133</sup> or microwave-frequency magnetic fields.<sup>126, 134-136</sup>

In a typical organic electron donor-acceptor system, photo-driven charge separation proceeds rapidly from a singlet excited state to form a singlet RP state. Differences in the magnetic environment between the radicals comprising the RP, mainly *g*-factor and hyperfine coupling differences, drive mixing between the singlet and triplet RP states (S-T mixing).<sup>124, 133, 137-138</sup> Charge recombination is spin selective in that singlet RPs can recombine only to singlet product states, and triplet RPs to triplet states. The rate of S-T mixing can therefore control the overall charge recombination rate.<sup>134, 139</sup> The presence of a third spin in the form of a stable radical has been shown to enhance the S-T mixing rate,<sup>122, 131, 140</sup> leading to an increase or decrease in the overall charge recombination rate constant ( $k_{CR}$ ) that depends on the relative values of the rate constants for singlet ( $k_{CRS}$ ) and triplet ( $k_{CRT}$ ) RP recombination.

Previous studies have largely focused on photosynthetic reaction centers<sup>141-142</sup> and synthetic electron donor-acceptor molecules<sup>143-145</sup> in which the spin-spin exchange ( $J$ ) and dipolar ( $D$ ) interactions within the RPs are weak compared to the electron-nuclear hyperfine interactions within both radicals. The S-T mixing rate depends strongly on the energy gap between these states, which is determined largely by  $J$  and  $D$ .<sup>38, 138</sup> In strongly coupled RPs, the S-T mixing rate is typically slow in the absence of a strong external magnetic field or nearby third radical,<sup>145</sup> and mixing in the presence of an external field may involve different triplet sublevels than for a weakly coupled system.<sup>38, 146</sup> Additionally,  $J$  is related to the electronic coupling matrix element for charge recombination,<sup>75, 147</sup> such that strongly coupled RPs frequently exhibit rapid charge recombination, on the order of picoseconds. For these reasons, the effects of a third spin interacting with a strongly coupled RP may differ from those observed in more weakly coupled systems. While the interactions of freely diffusing radicals with strongly coupled RPs have been studied,<sup>122</sup> there has been little work on covalent or coordinative systems, where the coupling strengths are effectively fixed. Teki and coworkers have presented informative work in this area,<sup>48-49, 148</sup> but their work has focused primarily on the development of spin polarization following charge recombination. Mori et al. have also examined in detail how the presence of a stable radical changes charge recombination rates in different solvents,<sup>124</sup> but they did not measure any spin polarization that may develop in these systems. Determining the relationship between electron transfer kinetics and the development of spin polarization is important for understanding the spin dynamics of these systems and assessing theoretical models for polarization transfer, which have not been tested in the strong RP coupling regime. Systems in which the stable radical becomes strongly polarized following photoexcitation may also be

useful for generating dynamic nuclear polarization (DNP) at ambient temperatures, where the thermal polarization is small,<sup>149</sup> and are potentially applicable to molecular spintronics.<sup>150</sup>

In this work, we report on compound **4.1b** containing the stable radical  $\alpha,\gamma$ -bis(diphenylene- $\beta$ -phenylallyl) (BDPA) covalently attached to an electron donor-acceptor system in which photoinduced electron transfer produces a strongly coupled RP following excitation of the chromophoric electron acceptor 4-amino-1,8-naphthalimide (ANI). An alkylated *meta*-phenylenediamine (mPD) derivative serves as the electron donor. mPD was selected for its mild oxidation potential and its ease of synthetic attachment to BDPA. The corresponding compound **4.1a** containing the diamagnetic precursor to BDPA, termed BDPAH, is used as a reference molecule. Transient optical absorption spectroscopy is used to monitor the radical ions and singlet and triplet recombination products, while electron paramagnetic resonance (EPR) spectroscopy enables measurement of BDPA spin polarization under similar conditions. These experiments were performed in three solvents spanning a range of polarities - benzene ( $\epsilon = 2.28$ ), tetrahydrofuran (THF,  $\epsilon = 7.52$ ), and butyronitrile (PrCN,  $\epsilon = 24.83$ )<sup>151</sup> - in order to modulate the charge separation and recombination energetics.

## 4.2 Experimental

### 4.2.1 Synthesis

The synthesis and characterization of compounds **4.1-4.6** is described in detail in Appendix B. Benzene was distilled before use from CaH<sub>2</sub> and stored in an N<sub>2</sub> glovebox. PrCN

was treated with HCl, distilled from  $K_2CO_3$ , and dried over  $Al_2O_3$  as described by Armarego and Chai.<sup>66</sup> Dry, inhibitor-free THF and dry toluene were used in all other spectroscopic measurements. Compound **4.1a** was purified by preparative thin layer chromatography on  $SiO_2$  prior to EPR and optical spectroscopy, while **4.1b** was prepared from **4.1a** purified in this fashion, then eluted through a  $SiO_2$  plug. Purified **4.1a** was stored in the dark in a  $-20\text{ }^\circ\text{C}$  freezer.

#### 4.2.2 Electrochemistry

Electrochemical measurements were performed on a CH Instruments 660A electrochemical workstation. Samples were measured in a 0.1 M solution of tetra-n-butylammonium hexafluorophosphate ( $TBAPF_6$ ) in dichloromethane purged with Ar to remove oxygen. A 1.0 mm diameter platinum disk electrode, platinum wire counter electrode, and silver wire reference electrode were used. The ferrocene/ferrocenium couple was used as an internal standard.

#### 4.2.3 Optical Spectroscopy

Ground-state absorption measurements were made on a Shimadzu UV-1800 spectrophotometer. Femtosecond visible transient absorption spectroscopy (fsTA) experiments were conducted using a commercial regeneratively amplified Ti:sapphire laser system (Tsunami oscillator/Spitfire amplifier, Spectra-Physics) described previously.<sup>152</sup> Before interaction with the sample, the probe was split using a neutral density filter so that one portion interacted with the sample and one portion provided a reference spectrum. The pump was sent through a commercial depolarizer (DPU-25-A, Thorlabs, Inc.) to suppress the effects of rotational

dynamics and chopped at 500 Hz. The pump was focused to ~0.2-1.0 mm diameter and the probe to ~0.1 mm diameter at the sample. The reference probe and the transmitted probe were coupled into optical fibers and detected using a customized Helios spectrometer and Helios software (Ultrafast Systems, LLC). Nanosecond visible transient absorption spectroscopy (nsTA) experiments were performed using the pump pulse described for the fsTA experiments paired with a photonic crystal fiber ultra-broadband probe generated by a customized EOS spectrometer (Ultrafast Systems, LLC).

Samples for fsTA and nsTA at room temperature were prepared with an optical density between 0.4 and 0.7 at 414 nm in 2 mm quartz cuvettes fused to a quartz bulb for degassing. Samples were subjected to four freeze–pump–thaw degassing cycles on a vacuum line ( $10^{-4}$  Torr) and sealed under vacuum. Samples for low temperature fsTA and nsTA were prepared as dichloromethane solutions with an optical density between 0.4 and 0.7 at 414 nm in 2 mm quartz cuvettes. The dichloromethane was evaporated and the samples reconstituted with an equal volume of PrCN in an N<sub>2</sub>-filled glovebox. The resulting solutions were loaded into an optical sample cell consisting of two quartz windows separated by a 2 mm PTFE spacer, and the cell was sealed under N<sub>2</sub>. Low temperature transient absorption measurements were performed using a Janis VNF-100 cryostat and a Cryo-Con 32B temperature controller. Low temperature samples in PrCN were cooled rapidly to 77 K by flooding the cryostat with liquid N<sub>2</sub> to produce a cracked glass. Samples were then annealed at 120 K to remove cracks and cooled to 105 K (further cooling past the glass transition temperature of 95 K caused the solvent to crack again, precluding optical measurements). At 105 K, PrCN is a viscous, supercooled liquid with a dielectric relaxation time of approximately 10 ms.<sup>153</sup> Since the timescale of solvent motion at

this temperature is much longer than that of the photoinduced processes observed here, PrCN at 105 K can be treated as a solid for the purposes of this study.

The samples were irradiated with 1  $\mu$ J pulses centered at 414 nm or 500 nm and the temporal resolution was  $\sim$ 120 fs to  $\sim$ 280 fs in the fsTA experiments and  $\sim$ 600 ps in the nsTA experiments. Visible fsTA spectra were collected for 3-5 s at each pump-probe time delay; nsTA spectra were collected using similar durations. All datasets were background-subtracted to remove scattered pump light and spontaneous emission and corrected for group delay dispersion and time zero using Surface Explorer (Ultrafast Systems, LLC).

Singular Value Decomposition (SVD) analysis of the transient absorption spectra was performed in Matlab<sup>154</sup> using home written programs. The 2-dimensional spectra were deconvoluted by SVD to produce an orthonormal set of basis spectra which describe the wavelength dependence of the species and a corresponding set of orthogonal vectors which describes the time dependent amplitude of the basis spectra.<sup>155</sup> A species-associated first order kinetic model<sup>156</sup> was fit to a linear combination of the time dependent amplitude vectors and the same linear combination of basis spectra was used to construct the spectra for the chemical species.

Nanosecond transient absorption spectroscopy and corresponding magnetic field effects were measured using the output of a pulsed Continuum 8000 Nd:YAG laser to pump a BBO crystal lasing medium (Continuum Panther EX OPO). The 7 ns, 416 nm pump output was filtered through two dichroic mirrors, focused to a 1.5 mJ, 5 mm diameter spot at the sample, and matched to that of the probe pulse generated using a xenon flashlamp (EG&G Electro-Optics

FX-200). The signal was collected at single wavelengths with a monochromator (HORIBA Triax 180) and detected using a photomultiplier tube (Hamamatsu R926).

Samples with an optical density between 0.4 and 0.7 at 416 nm were placed in a 10 mm quartz cuvette and degassed with up to five freeze-pump-thaw cycles on a vacuum line ( $10^{-4}$  Torr). The cuvette was placed between the poles of an electromagnet (Walker Scientific HV-4W) with a water-cooled power supply (Walker Magnion HS-735). The field strength was measured by a Hall effect probe interfaced with a gaussmeter (Lakeshore 450). The magnetic field effect experiment was performed as previously described.<sup>157</sup> To account for any sample degradation over the several hours of measurements required for each experiment, kinetics at  $B = 0$  mT were measured after every two kinetics measured at specific magnetic fields.

#### 4.2.4 EPR Spectroscopy

EPR measurements were made at X-band ( $\sim 9.5$  GHz) using a Bruker Elexsys E680-X/W EPR spectrometer outfitted with a split ring resonator (ER4118X-MS5). Measurements were performed at room temperature or using an Oxford Instruments CF935 continuous flow cryostat with liquid  $N_2$  or He. Sample solutions (optical density between 0.4 and 0.7 in 2 mm cuvette at 416 nm,  $\sim 10^{-4}$  M) were loaded into quartz tubes (1.80 mm o.d.  $\times$  1.50 mm i.d.), subjected to four freeze-pump-thaw degassing cycles on a vacuum line ( $10^{-4}$  Torr), and sealed under vacuum using an oxy-hydrogen torch. In addition to THF and PrCN, samples were dissolved in benzene instead of toluene as **4.1b** exhibited a greater photostability in benzene. This is likely due to the ability of toluene to donate a hydrogen atom to photoexcited BDPA.<sup>158</sup>

Continuous wave (CW) EPR spectra were measured using 0.6 mW microwave power and 0.01 mT field modulation at 100 kHz. Time-resolved EPR measurements were performed following photoexcitation with 7 ns, 1.8 mJ, 416 nm pulses using the output of an optical parametric oscillator (Spectra-Physics Basi-scan), pumped with the output of a frequency-tripled Nd:YAG laser (Spectra-Physics Quanta-Ray Pro 350).

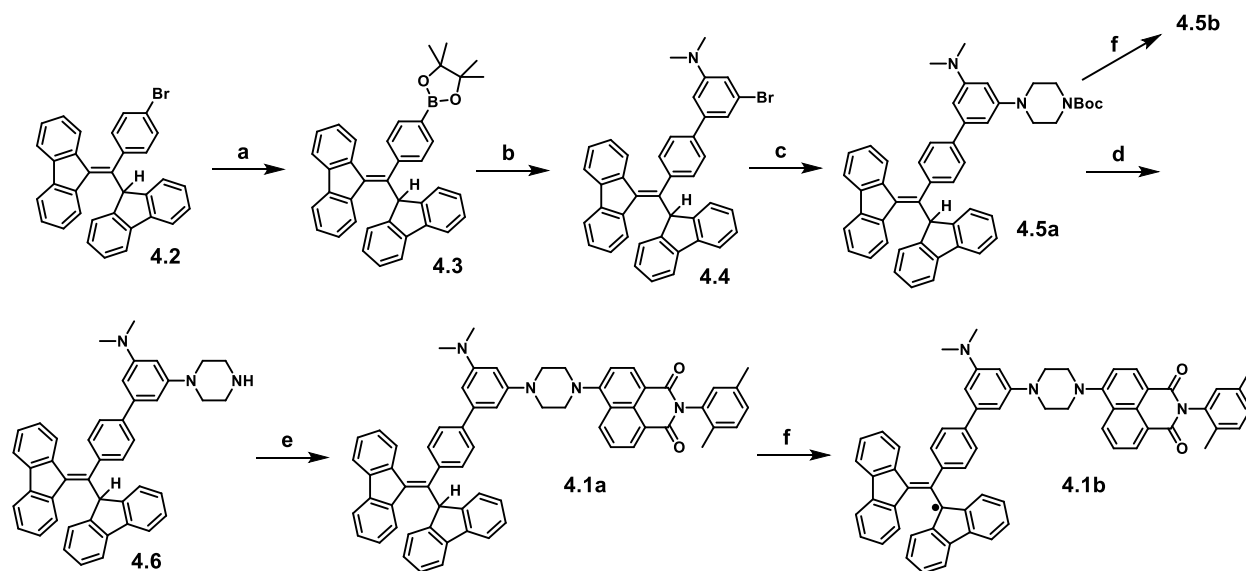
Time-resolved EPR measurements were collected at room temperature using field swept electron spin echo (ESE) detection. For these pulsed experiments, a 1 kW TWT amplifier (Applied Systems Engineering 117X) was employed to generate high-power microwave pulses. The resonator was partially overcoupled to maximize echo intensity and minimize ringing following microwave pulses. ESE data was obtained with a  $\pi/2$ - $\tau$ - $\pi$  pulse sequence with  $\pi/2 = 16$  ns,  $\pi = 32$  ns, and  $\tau = 120$  ns. The integrated echo intensity is recorded as a function of the magnetic field to yield the spectrum. If the sample is photoexcited at some time  $t$  prior to the  $\pi/2$ - $\tau$ - $\pi$  pulse sequence, spectra can be collected of the transient species as a function of  $t$ .

Time-resolved EPR measurements at low temperatures were collected using ESE detection or transient continuous wave (TCW) detection. For TCW-EPR the transient magnetization following photoexcitation was detected in quadrature under CW microwave irradiation (2–20 mW), without field modulation. Sweeping the magnetic field gave 2D spectra versus both time and magnetic field. For each kinetic trace, the signal acquired prior to the laser pulse was subtracted from the data. Kinetic traces recorded at magnetic field values off-resonance were considered background signals, whose average was subtracted from all kinetic traces.

## 4.3 Results

### 4.3.1 Synthesis

The synthesis of **4.1a** and **4.1b** is outlined in Scheme 4.1. Bromo-BDPAH (**4.2**) was synthesized according to the route of Kuhn and Neugebauer.<sup>159</sup> Miyaura borylation of this compound using bis(pinacolato)diboron afforded the corresponding pinacol boronic ester (**4.3**) in high yield. The mPD donor was prepared from 3-bromo-5-iodo-*N,N*-dimethylaniline (see Appendix B) using a Suzuki cross coupling reaction to attach BDPAH (**4.4**) and a Buchwald-Hartwig cross coupling reaction with *N*-Boc-piperazine to introduce the second nitrogen atom (**4.5a**). The Boc protecting group prevents difunctionalization of the piperazine ring and enables purification of the product by silica column chromatography. Compound **4.5a** was deprotected and reacted with 4-bromo-*N*-(2,5-dimethylphenyl)-1,8-naphthalimide (see Appendix B) to afford **4.1a**. Deprotonation and oxidation of **4.1a** with 1,8-diazabicyclo(5.4.0)undec-7-ene (DBU) and MnO<sub>2</sub> resulted in quantitative formation of **4.1b**.<sup>160</sup>



**Scheme 4.1.** (a) Bis(pinacolato)diboron, Pd(dppf)Cl<sub>2</sub>, KOAc, 1,4-dioxane, 75 °C, 2d, 88%. (b) 3-bromo-5-iodo-N,N-dimethylaniline, Pd(PPh<sub>3</sub>)<sub>4</sub>, K<sub>2</sub>CO<sub>3</sub>, toluene, EtOH, H<sub>2</sub>O, reflux, 2d, 30%. (c) N-Boc-piperazine, Pd<sub>2</sub>(dba)<sub>3</sub>, P(tBu)<sub>3</sub>, NaOtBu, toluene, 100 °C, overnight, 73%. (d) HCl, EtOH, reflux, 1h, *quant.* (e) 4-bromo-N-(2,5-dimethylphenyl)-1,8-naphthalimide, 2-methoxyethanol, reflux, 2d, 32%. (f) MnO<sub>2</sub>, DBU, THF, rt, 15 min, *quant.*

### 4.3.2 Energetics

Compounds **4.5a** and **4.5b** were characterized by cyclic voltammetry (CV) and differential pulse voltammetry (DPV) (Figure B.1) and compared to model compounds to determine the free energy changes for photoinduced electron transfer in these compounds (Table 4.1). CV and DPV traces as well as protocols for calculating the free energies for charge separation ( $\Delta G_{CS}$ ), charge recombination to the singlet ground state ( $\Delta G_{CRS}$ ), and charge recombination to <sup>3\*</sup>ANI ( $\Delta G_{CRT}$ ) are given in Appendix C.

Compound	$E_{OX}$	$E_{RED}$	$-\Delta G_{CS}$	$-\Delta G_{CRS}$	$-\Delta G_{CRT}$
<b>4.5a</b>	0.75 (mPD) 1.20 (ANI)	-1.41 (ANI) <sup>161</sup>	0.21 (benzene) 0.38 (THF) 0.43 (PrCN)	2.59 (benzene) 2.42 (THF) 2.37 (PrCN)	0.54 (benzene) 0.37 (THF) 0.32 (PrCN)
<b>4.5b</b>	0.72 (mPD) 0.84 (BDPA) 1.20 (ANI) <sub>161</sub>	-0.44 (BDPA) -1.41 (ANI) <sup>161</sup>	0.24 (benzene) 0.41 (THF) 0.46 (PrCN)	2.56 (benzene) 2.39 (THF) 2.34 (PrCN)	0.51 (benzene) 0.34 (THF) 0.29 (PrCN)

$E_S$  (ANI) = 2.80 eV;  $E_T$  (ANI) = 2.05 eV<sup>161</sup>

**Table 4.1.** Experimental redox potentials of **4.5a** and **4.5b**, literature potentials for ANI (V vs. SCE), and free energies of charge separation (CS) and charge recombination to the singlet ground state (CRS) and <sup>3\*</sup>ANI (CRT).

### 4.3.3 Optical Spectroscopy

The UV-visible absorption spectrum (Figure 4.1) of **4.1a** shows a broad band at 388 nm, corresponding to the charge transfer (CT) absorption of the ANI chromophore,<sup>161</sup> as well as strong bands at 305 and 321 nm from BDPAH. The spectrum of **4.1b** also shows the ANI absorption, but the BDPAH bands are replaced by new features from the BDPA radical at 340, 504, and 874 nm.<sup>162</sup>

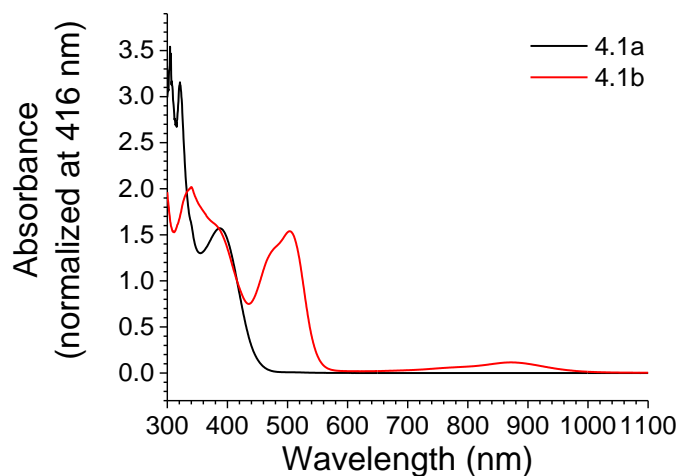


**Figure 4.1.** UV-visible absorption spectrum of **4.1a** and **4.1b** in toluene.

Transient optical absorption (TA) experiments were performed on **4.1a** and **4.1b** to observe the intermediates formed in the electron transfer reactions following photoexcitation. Selected femtosecond transient absorption (fsTA) spectra in benzene, THF, and PrCN at 295 K are shown in Figures 2-4, respectively, while additional nanosecond transient absorption (nsTA) spectra and kinetics fits are given in Appendix C (Figures C.3-C.12). At early times, **4.1a** in benzene (Figure 4.2a,c) shows an absorption near 450 nm and a negative signal near 500 nm, with minor absorptions from 620 to 800 nm. These features correspond to the excited state absorption and stimulated emission from BDPAH-mPD-<sup>1\*</sup>ANI following photoexcitation. At later times, these excited state features decay with  $\tau_{CS} = 13$  ps to yield absorptions at 430 and 500 nm, which are assigned to ANI<sup>\*</sup> based on its known spectrum,<sup>161, 163</sup> and mPD<sup>+</sup>, which absorbs at 490 nm,<sup>164</sup> adding to the total  $\Delta A$  at 500 nm. Subsequent charge recombination of BDPAH- mPD<sup>+</sup>-ANI<sup>\*</sup> occurs in  $\tau_{CR} = 19$  ns to yield a new species that absorbs at 450 and 700 nm and is assigned to BDPAH-mPD-<sup>3\*</sup>ANI,<sup>165</sup> which decays to ground state in  $\tau = 7.0$   $\mu$ s. When the solvent polarity is increased using THF, photoexcitation of **4.1a** results in formation of BDPAH-mPD<sup>+</sup>-ANI<sup>\*</sup> exhibiting sharper absorption bands (Figure 4.3a,c) and a decrease in both the charge separation and recombination time constants to  $\tau_{CS} = 3.3$  ps and  $\tau_{CR} = 270$  ps, respectively (Table 4.2). Similar results are obtained in more polar PrCN, where the time constants for charge separation and recombination decrease further to  $\tau_{CS} = 1.8$  and  $\tau_{CR} = 23$  ps, respectively (Figure 4.4a,c).

<b>Molecule</b>	<b>Solvent</b>	<b><math>\tau_1</math> (CS)</b>	<b><math>\tau_2</math> (CR)</b>	<b><math>\tau_3</math> (<math>^3</math>*ANI decay)</b>
<b>4.1a</b>	Benzene	$13 \pm 2$ ps	$21.3 \pm 0.7$ ns	$7.0 \pm 0.1$ $\mu$ s
<b>4.1a</b>	THF	$3.3 \pm 0.3$ ps	$274 \pm 5$ ps	-
<b>4.1a</b>	PrCN	$1.8 \pm 0.3$ ps	$22.5 \pm 0.4$ ps	-
<b>4.1b</b>	Benzene	$11.9 \pm 0.5$ ps	-	$39.4 \pm 0.8$ ns
<b>4.1b</b>	THF	$1.9 \pm 0.3$ ps	$25.1 \pm 0.5$ ps	$25.9 \pm 0.8$ ns
<b>4.1b</b>	PrCN	$1.8 \pm 0.3$ ps	$28.9 \pm 0.6$ ps	$9.2 \pm 0.9$ ns

**Table 4.2.** Time constants for charge separation (CS), charge recombination (CR), and  $^3$ \*ANI decay at room temperature, obtained from fits to transient absorption data.

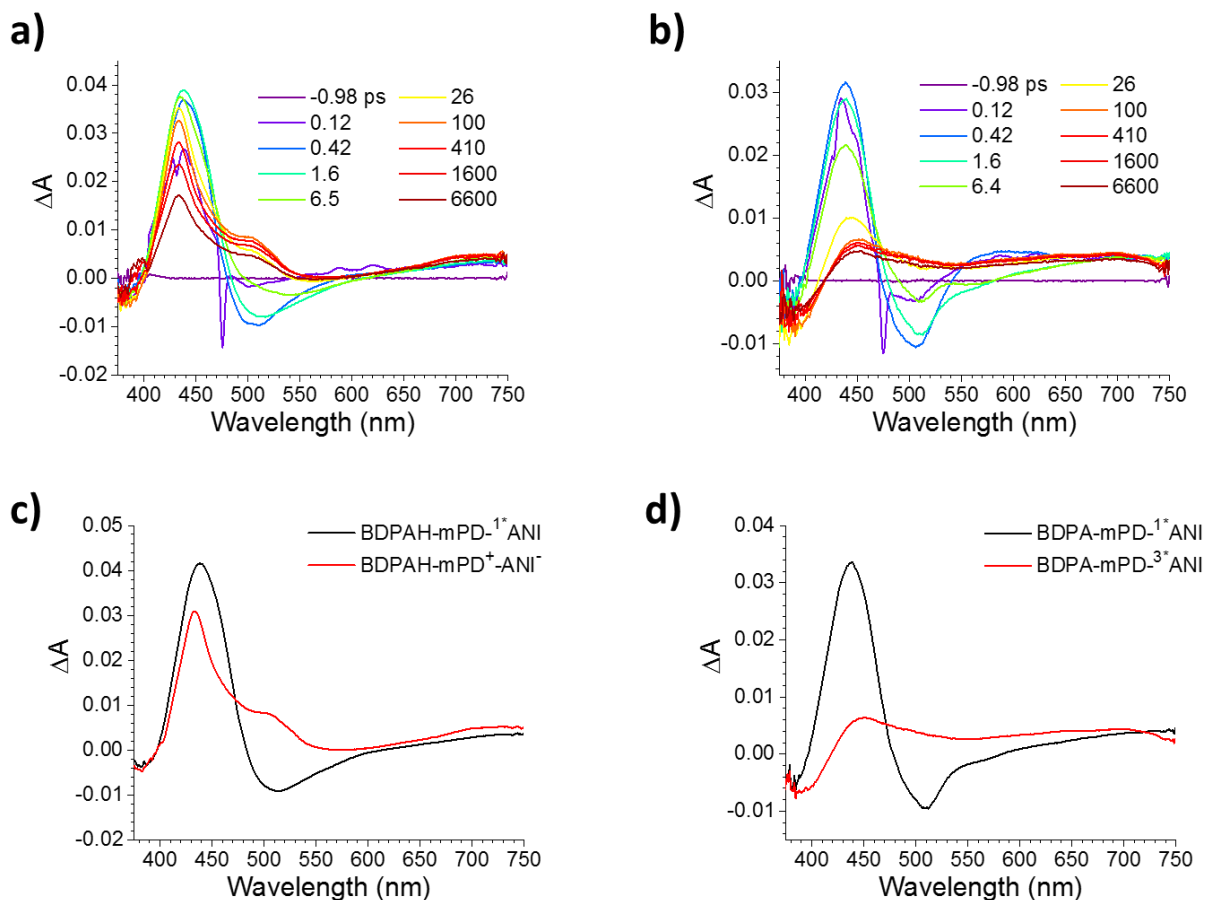


**Figure 4.2.** Transient absorption spectra in benzene at 295K: (a) **4.1a**, (b) **4.1b**. The species-associated spectra obtained by global fitting of the fsTA data for **4.1a** and **4.1b** are given in (c) and (d), respectively. Sharp features at early times are artifacts due to Raman scattering of the pump laser by the solvent.

The fsTA spectra of **4.1b** in benzene (Figure 4.2b,d) at early times display the spectral features characteristic of BDPA-mPD-<sup>1\*</sup>ANI, but the 430 and 500 nm absorptions corresponding to BDPA-mPD<sup>+</sup>-ANI\* formation are never observed. Instead, BDPA-mPD-<sup>1\*</sup>ANI appears to undergo rapid intersystem crossing to form BDPA-mPD-<sup>3\*</sup>ANI in  $\tau = 12$  ps, which decays to ground state in  $\tau = 39$  ns. In contrast, the fsTA spectra of **4.1b** in THF (Figure 4.3b,d) show features similar to those of **4.1a** (Figure 4.3a,c), where the initial formation of BDPA-mPD-

$^1$ \*ANI is followed by charge separation to yield BDPA-mPD<sup>+</sup>-ANI<sup>-</sup> in  $\tau_{CS} = 1.9$  ps. However, compared to **4.1a**, the charge recombination time constant decreases to  $\tau_{CR} = 25$  ps, and a large amount of BDPA-mPD-<sup>3</sup>\*ANI is observed. These results are suggestive of enhanced intersystem crossing in the RP state, forming a large amount of BDPA-<sup>3</sup>(mPD<sup>+</sup>-ANI<sup>-</sup>), which subsequently undergoes rapid charge recombination to yield BDPA-mPD-<sup>3</sup>\*ANI. The fsTA spectra and kinetics of **4.1b** in PrCN (Figure 4.4b,d) are very similar to those in THF and show that charge separation occurs in  $\tau_{CS} = 1.8$  ps, while charge recombination occurs in  $\tau_{CR} = 29$  ps. Both time constants are also similar to those observed for the corresponding processes for **4.1a** in PrCN (Figure 4.4a,c). A smaller yield of BDPA-mPD-<sup>3</sup>\*ANI in **4.1b** following charge recombination is observed in PrCN relative to that in THF. BDPA-mPD-<sup>3</sup>\*ANI decays to ground state in  $\tau = 26$  ns in THF and  $\tau = 9.2$  ns in PrCN, in both cases significantly faster than the  $\tau = 7.0$   $\mu$ s decay observed from **4.1a** in benzene.

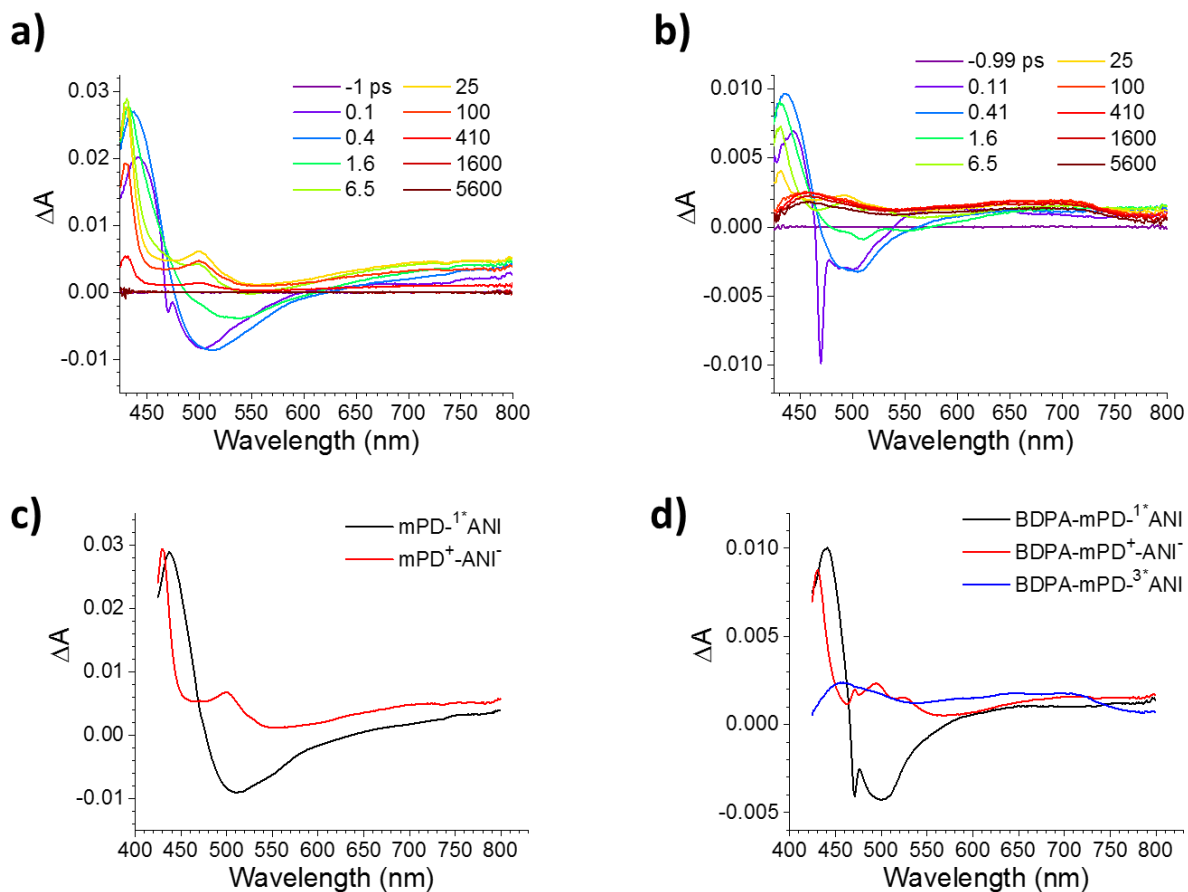


**Figure 4.3.** Transient absorption spectra in THF at 295 K: (a) **4.1a**, (b) **4.1b**. The species-associated spectra obtained by global fitting of the fsTA data for **4.1a** and **4.1b** are given in (c) and (d), respectively. Sharp features at early times are artifacts due to Raman scattering of the pump laser by the solvent.

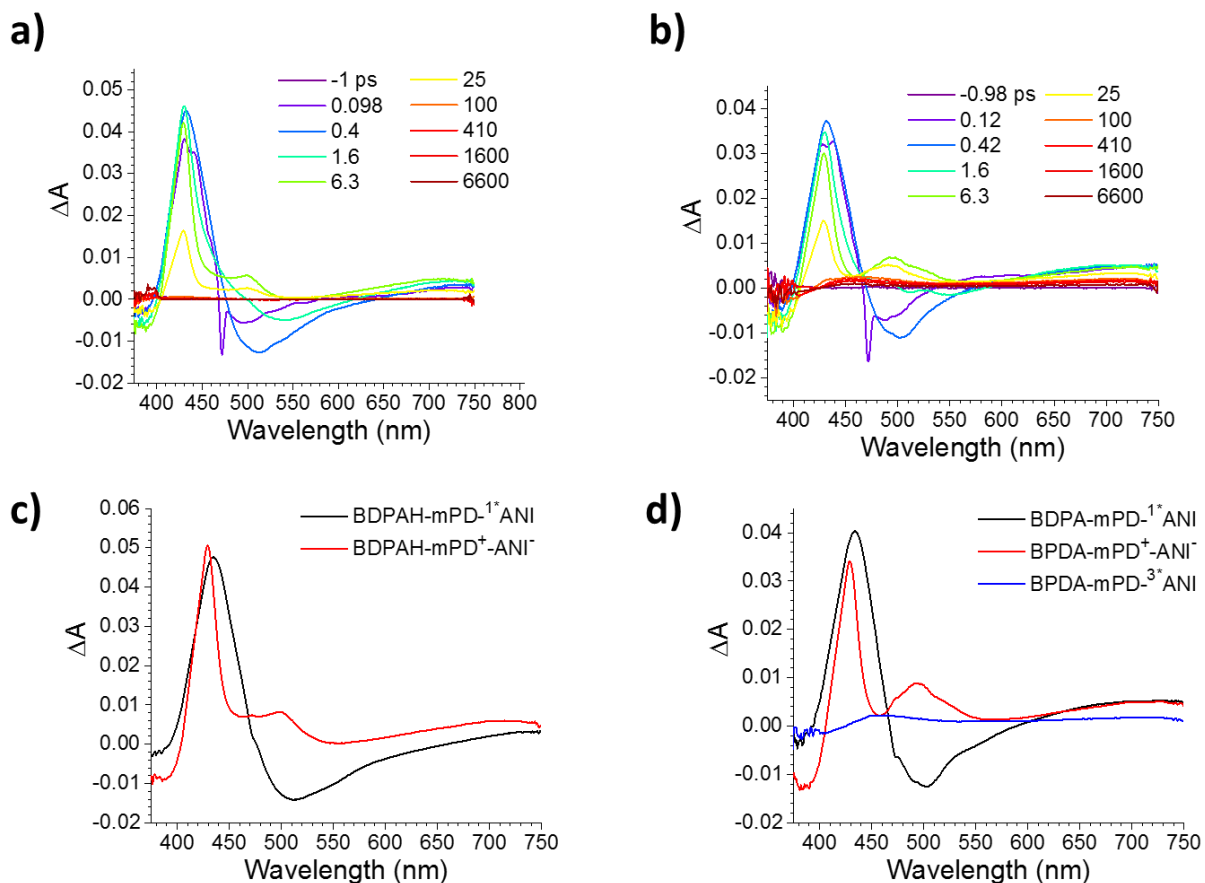


**Figure 4.4.** Transient absorption spectra in PrCN at 295K: (a) **4.1a** and (b) **4.1b** The species-associated spectra obtained by global fitting of the fsTA data for **4.1a** and **4.1b** are given in (c) and (d), respectively. Sharp features at early times are artifacts due to Raman scattering of the pump laser by the solvent.

fsTA experiments on **4.1a** in PrCN at 105 K show the same features observed in PrCN at 295 K (Figures 5a,c; S13), but the rates of the electron transfer processes are substantially different. Charge separation can be fit with a stretched exponential (Kohlrausch-Williams-Watts) function with  $\tau = 74$  ps and  $\beta = 0.21$ , corresponding to an average time constant of  $\tau_{\text{avg}} = 5.3$  ns. In the nsTA spectra (Figure B.14), the charge separated state is already present within the IRF, and some residual excited state is additionally present that decays to form some  $3^*$ ANI that persists beyond the time range of the experiment. Fitting to this model yields a time constant of  $\tau$

= 5.2 ns for intersystem crossing and  $\tau_{\text{CR}} = 54$  ns for charge recombination. The apparent discrepancy between the models used to fit the fs- and nsTA data is addressed in the Discussion. For **4.1b** in PrCN at 105 K, features associated with BDPA-mPD<sup>+</sup>-ANI<sup>•</sup> are never observed, and BDPA-mPD-<sup>1\*</sup>ANI decays to form BDPA-mPD-<sup>3\*</sup>ANI in  $\tau = 24$  ps (Figures 5b,d; S15). The decay of BDPA-mPD-<sup>3\*</sup>ANI can be fit as a stretched exponential with  $\tau = 1.1$   $\mu\text{s}$ ,  $\beta = 0.45$ , and  $\tau_{\text{avg}} = 2.8$   $\mu\text{s}$  (Figure B.16).

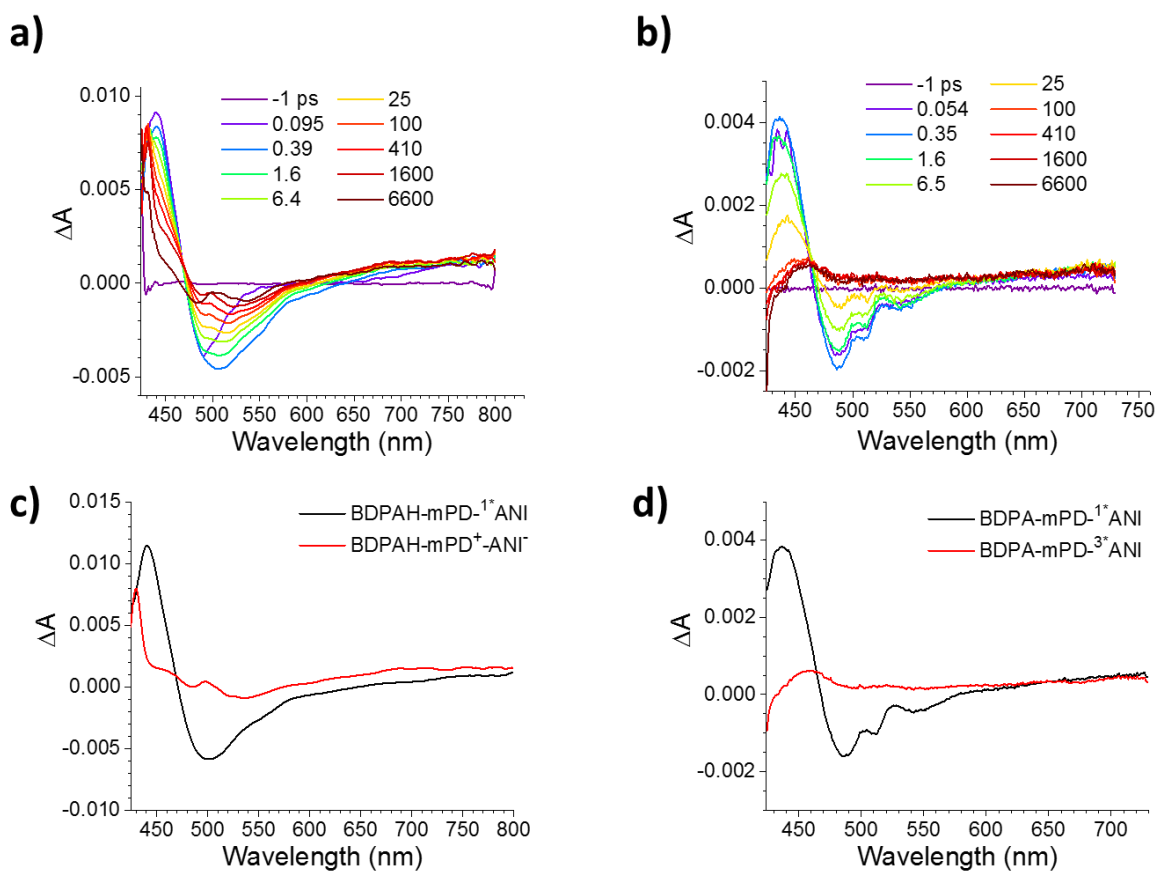


**Figure 4.5.** Transient absorption spectra in PrCN at 105K: (a) **4.1a** and (b) **4.1b**. The species-associated spectra obtained by global fitting of the fsTA data for **4.1a** and **4.1b** are given in (c) and (d), respectively.

To rule out the possibility that features in the transient absorption spectra originate from BDPA excitation, transient absorption spectra were acquired in benzene, THF, and PrCN with 500 nm BDPA-selective excitation (Figure B.17). The fsTA spectra at early times show ground state bleaching around 500 nm with a broad absorptive feature from 550 to 700 nm. This broad absorption decays to a weak absorptive band near 550 nm on a picosecond timescale. This process is assigned to internal conversion of the initially excited doublet state to the lowest excited BDPA doublet state, which is followed by its decay to ground state in tens of picoseconds.

#### 4.3.4 Magnetic Field Effects on the Triplet Yield

The BDPAH-mPD-<sup>3\*</sup>ANI yield produced from charge recombination in **4.1a** in toluene at room temperature shows no dependence on applied magnetic field in the range 0-800 mT (Figure B.18). This indicates that the spin-spin exchange interaction ( $2J$ ) for BDPAH-mPD<sup>+</sup>-ANI<sup>•</sup> in **4.1a** is >800 mT, which greatly exceeds the hyperfine interactions between electron and nuclear spins in the radicals, essentially precluding RP intersystem crossing by S-T mixing. Due to the short BDPA-mPD-<sup>3\*</sup>ANI lifetime in **4.1b**, it is difficult to measure a magnetic field effect on its formation with our equipment. Nevertheless, previous work has shown that  $2J$  of the RP does not depend on the presence of a third spin, so that  $2J$  is most likely >800 mT for BDPA-mPD<sup>+</sup>-ANI<sup>•</sup> in **4.1b** as well.<sup>131, 140</sup>

### 4.3.5 EPR Spectroscopy

Continuous wave (CW) EPR spectroscopy confirms the presence of the BDPA radical in **4.1b** and its absence in **4.1a** (Figure 4.6). The degree of BDPA radical spin polarization following photoexcitation of **4.1b** at room temperature was measured by electron spin echo (ESE) detection. A strong ESE signal was detected from **4.1b** following a  $\pi/2$ - $\tau$ - $\pi$  microwave pulse sequence, even in liquid solvents at room temperature, due to the long spin relaxation times characteristic of BDPA.<sup>166</sup> Samples of **4.1b** in benzene, THF, and PrCN were measured with equal sample volume, concentration, excitation energy, excitation wavelength, and microwave power.

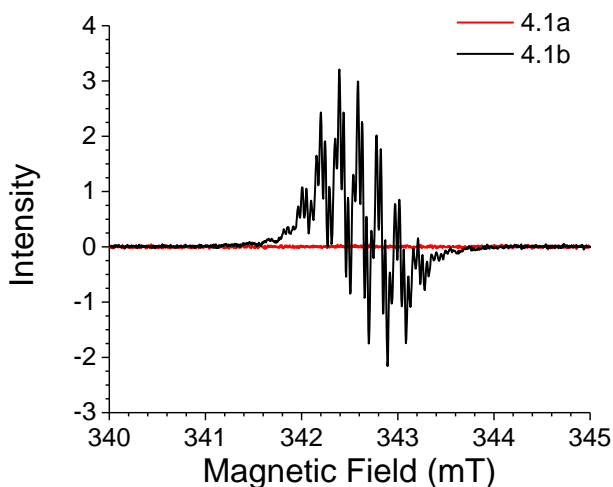


**Figure 4.6.** CW-EPR signals from **4.1a** and **4.1b** in toluene at room temperature.

Field-swept echo-detected spectra collected after photoexcitation were compared to spectra collected without photoexcitation. Compared to the thermal polarization present before the laser pulse, the integrated echo intensity decreased uniformly across the EPR line in all three solvents (Figure 4.7). The intensity at the center of the EPR line decreased to 68% in benzene,

22% in THF, and 80% in PrCN, as measured by averaging several points before and after photoexcitation (Figure 4.8a). Due to difficulties in measuring what fraction of the sample was photoexcited, these values cannot be used as an absolute measure of the degree of polarization, but can be compared to each other. This experiment was also repeated with a  $\pi$  microwave pulse applied before photoexcitation to invert the thermal polarization. In all three solvents, polarization of BDPA following photoexcitation results in the echo amplitude becoming more negative (Figure 4.8b) instead of returning towards zero. Consistent with the transient absorption data, the process producing spin polarization occurs more quickly than the 30-ns time resolution of the EPR experiment. In contrast to **4.1b**, no ESE signals are observed upon photoexcitation of **4.1a** in benzene, THF, or PrCN (Figure B.19).

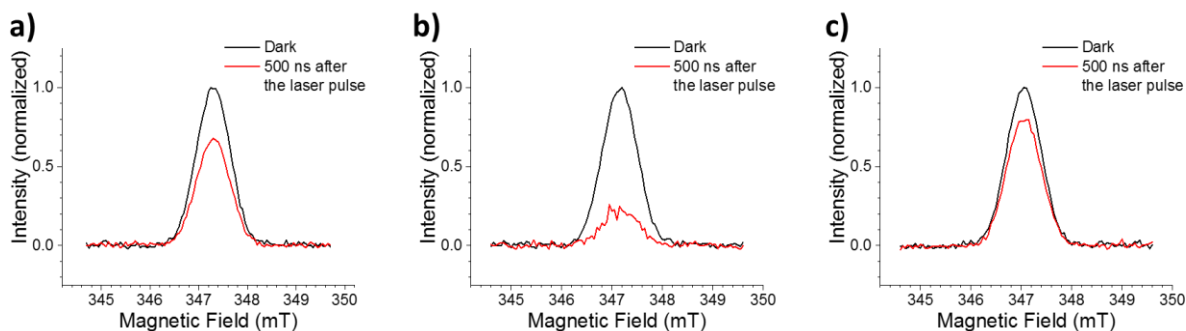


**Figure 4.7.** Field-swept, echo-detected EPR spectra of **4.1b** in (a) benzene, (b) THF, and (c) PrCN collected before and after photoexcitation.

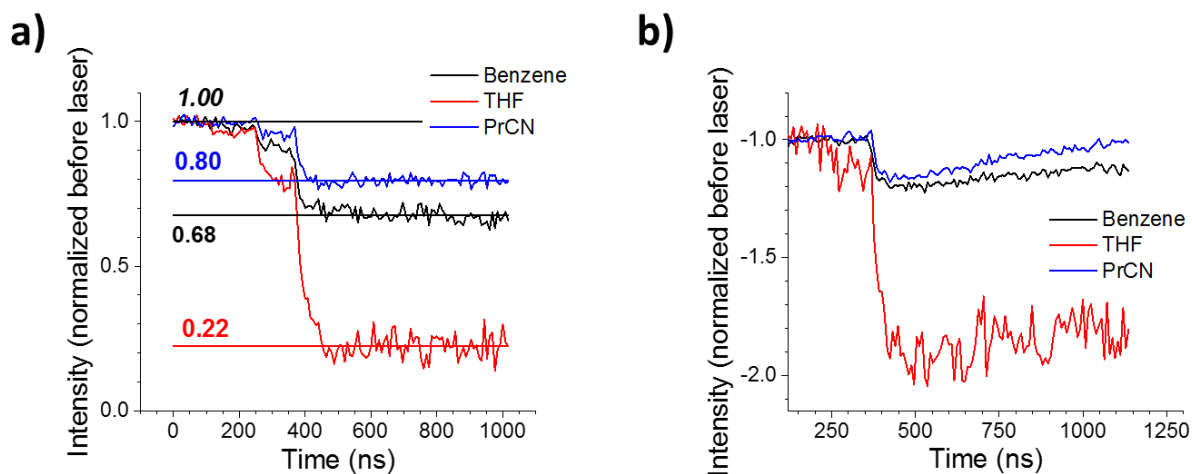


**Figure 4.8.** Kinetics of the echo-detected EPR signal following photoexcitation, both without (a) and with (b) a  $\pi$  pulse before the echo sequence. The initial slight decrease around 150 ns is due to the laser pulse occurring during the pulse sequence.

Once again, to rule out the possibility that features in the transient EPR spectra originate from excitation of BDPA, transient EPR spectra (Figure B.20) were acquired in benzene, THF, and PrCN with excitation at 500 nm, where BDPA is selectively excited. No changes in the BDPA EPR signal are observed upon photoexcitation at 500 nm, indicating that no spin polarization occurs as a result of excitation of BDPA.

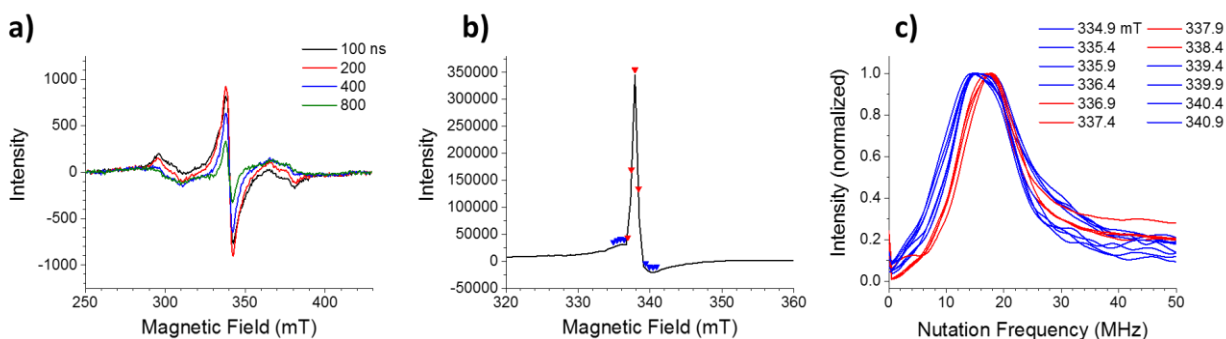


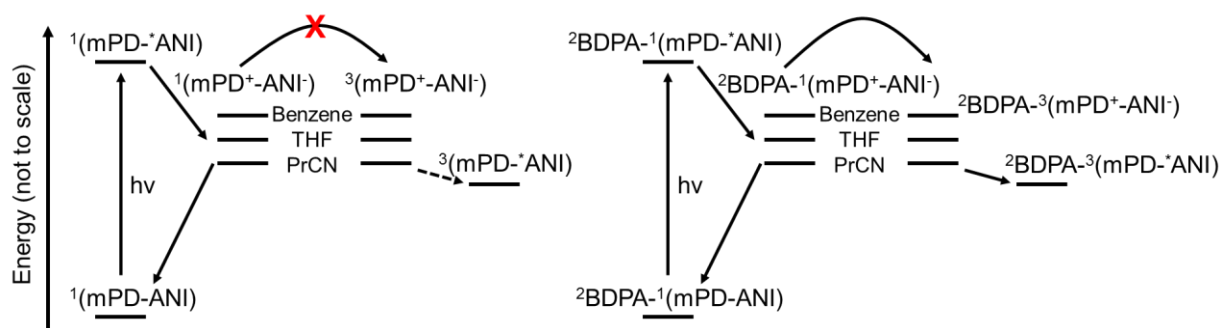
**Figure 4.9.** (a) TCW-EPR spectra of **4.1b** in PrCN at 105 K following photoexcitation. (b) Echo-detected EPR spectrum of **4.1b** in PrCN at 10 K following photoexcitation. Triangles indicate field positions at which the transient nutation experiment was conducted. (c) Transient nutation spectra at different field positions. Blue traces indicate field positions corresponding to the new, transient signal, while red traces correspond to unexcited BDPA.

Time-resolved EPR measurements on **4.1b** at low temperature (Figure 4.9) are strikingly different from those in liquid solution at room temperature. The lack of rotational averaging and slower magnetic relaxation rates in PrCN at 105 K allow observation of several new lines in the transient continuous wave (TCW) EPR spectrum. A broad (~90 mT), polarized set of lines resembling a triplet signal is observed, as well as a narrower (~5 mT) pair of polarized signals. Notably, no very narrow absorptive or emissive feature corresponding to spin-polarized, isolated BDPA is observed. This contrasts with the room temperature spectra, where such a line is the only transient feature observed. The polarization pattern of the triplet-like lines evolves with time, likely due to magnetic relaxation and transitions induced by the CW microwave irradiation. Unlike ESE-detection, the TCW experiment is insensitive to thermally-equilibrated radicals, so that only spin-polarized BDPA is detected following photoexcitation. Thus, time-resolved EPR measurements on **4.1b** were also performed using ESE detection. Field-swept spectra collected both at 105 K and at 10 K show only the narrower 5 mT transient feature and unperturbed BDPA. The 90 mT-wide signal does not produce any detectable echoes, likely due to fast spin relaxation. Transient nutation spectra were collected at 10 K at several field positions on the 5 mT-wide feature and the unperturbed BDPA line, in order to determine the spin quantum number  $S$  for the species giving rise to these features. The unperturbed BDPA signal was used as an internal  $S = 1/2$  standard. The nutation spectra at all measured field positions show a single peak in the region from 15 to 18 MHz consistent with an  $S = 1/2$  species (see below). In contrast to **4.1b**, the EPR spectrum of **4.1a** in PrCN at 105 K shows only a weak signal corresponding to BDPAH-mPD-<sup>3\*</sup>ANI formed through spin-orbit intersystem crossing.

## 4.4 Discussion

### 4.4.1 Charge Separation and Recombination in the Presence of a Third Spin

The fsTA data show that both **4.1a** and **4.1b** undergo photoinduced electron transfer in both polar and nonpolar solvents. Marcus electron transfer theory can be used to analyze the observed solvent dependence of the charge separation and recombination rates.<sup>72</sup> The calculated values of the total reorganization energies ( $\lambda$ ) for charge separation and recombination in benzene, THF, and PrCN are 0.36, 1.03, and 1.18 eV, respectively (see Appendix C). Comparing these values to the free energies for the electron transfer reactions given in Table 4.1, the charge separation reactions to form  $\text{mPD}^+\text{-ANI}^-$  all lie in the Marcus normal region of the  $\ln k$  vs.  $\Delta G$  dependence ( $-\Delta G_{\text{CS}} < \lambda$ ), while the charge recombination reactions of the singlet RP to the singlet ground state all lie in the Marcus inverted region ( $-\Delta G_{\text{CRS}} > \lambda$ ). In addition, the charge recombination reactions of the triplet RP to give  $^3\text{ANI}$  lie in the normal region for THF and PrCN ( $-\Delta G_{\text{CRT}} < \lambda$ ), but the recombination reaction is inverted for benzene ( $-\Delta G_{\text{CRT}} > \lambda$ ).



**Scheme 4.2.** Schematic diagram showing the relative energy levels of the singlet excited state, RP, and triplet excited state for (left) **4.1a** and (right) **4.1b**. Mixing between the singlet and triplet RP levels is forbidden in **4.1a**, but not in **4.1b**.

RP recombination is spin-selective in **4.1a** and **4.1b**, where the singlet RP returns to the singlet ground state, while the triplet RP produces  $^3\text{ANI}$ . For an RP generated from an excited singlet state precursor, weak mixing of the singlet and triplet RP states can be a significant kinetic bottleneck to neutral triplet state formation resulting from charge recombination,<sup>75</sup> particularly in strongly spin coupled RPs. The magnetic field effect data for **4.1a** indicate that  $2J$  within the RP is well in excess of other magnetic interactions such as the hyperfine couplings within the radicals comprising the RP, placing BDPAH-mPD<sup>+</sup>-ANI<sup>•</sup> firmly in the strong coupling regime. The strongly coupled singlet RP produced by photoexcitation of **4.1a** cannot intersystem cross to the triplet RP; thus, charge recombination of BDPAH-mPD<sup>+</sup>-ANI<sup>•</sup> can only occur to the singlet ground state. The large  $\Delta G_{\text{CS}}$  for this process places it in the Marcus inverted region, which is consistent with the observation that  $\tau_{\text{CS}}$  is much faster than  $\tau_{\text{CR}}$  for **4.1a** in all solvents.

The charge separation time constants for **4.1b** are similar to those for **4.1a** in both THF and PrCN (data obtained in benzene will be discussed below); thus, the presence of the BDPA radical does not have a large effect on the energetics of the RP or the electronic coupling between the mPD donor and the excited  $^1\text{ANI}$  acceptor. However, charge recombination of BDPA-mPD<sup>+</sup>-ANI<sup>•</sup> for **4.1b** in THF is more than an order of magnitude faster than BDPAH-mPD<sup>+</sup>-ANI<sup>•</sup> for **4.1a** in THF. This suggests that the difference in recombination rates is due to the effect of the BDPA unpaired spin on the photogenerated RP. The presence of a stable radical coupled to at least one radical of an RP has been shown to accelerate S-T mixing, increasing the triplet RP population, which results in a corresponding increase<sup>131</sup> or decrease<sup>122</sup> in the observed charge recombination rate, depending on the relative rates of singlet and triplet RP

recombination. Thus, the increase in the triplet RP recombination rate for **4.1b** in THF relative to that of **4.1a** can be rationalized by assuming that the presence of the BDPA radical in **4.1b** causes S-T mixing in the photogenerated RP. Given that RP recombination to the singlet ground state is deep in the Marcus inverted region and therefore slow,  $\Delta G_{\text{CRT}}$  for RP recombination to  $^3\text{*ANI}$  (Scheme 4.2) is sufficiently large to result in faster charge recombination via the triplet channel. In PrCN, the charge separation rates for **4.1a** and **4.1b** are both the same ( $\tau_{\text{CS}} = 1.8 \pm 0.3$  ps), while charge recombination is slightly slower for **4.1b** ( $\tau_{\text{CR}} = 28.9 \pm 0.6$  ps) relative to **4.1a** ( $\tau_{\text{CR}} = 22.5 \pm 0.4$  ps). The values of  $\Delta G_{\text{CRS}}$  and  $\Delta G_{\text{CRT}}$  for **4.1a** and **4.1b** in PrCN are less negative than those in THF (Table 4.1). Thus, given that charge recombination to the singlet ground state is in the Marcus inverted region, while charge recombination to  $^3\text{*ANI}$  is in the normal region, it is expected that  $\tau_{\text{CRS}}$  will be shorter and  $\tau_{\text{CRT}}$  will be longer in PrCN relative to THF, which is consistent with our results. Consequently, populating the triplet RP state in **4.1b** in PrCN does not provide a significantly faster charge recombination pathway.

#### 4.4.2 Rapid Intersystem Crossing of **4.1b** in Benzene

In **4.1b**, clear spectroscopic evidence of charge separation is observed in THF and PrCN, but not in benzene. One possibility is that direct intersystem crossing from  $^1\text{*ANI}$  to  $^3\text{*ANI}$  occurs for **4.1b** in benzene at a rate that is competitive with charge separation ( $\tau_{\text{CS}} = 13$  ps). Such rapid triplet formation in radical-chromophore systems is well-documented and is attributed to exchange-induced enhanced intersystem crossing (EISC).<sup>40, 162, 167</sup> Past studies of EISC in other radical-chromophore dyads have shown little solvent dependence in the intersystem crossing rate,<sup>40, 162, 167</sup> making it plausible that this process could be kinetically out-competed in polar

solvents, where charge separation is faster. However, this explanation is difficult to justify in light of the observed kinetics. The rate of charge separation did not differ significantly between **4.1a** and **4.1b** in THF and PrCN, so the difference between BDPA and BDPAH does not seem to affect the energetics or coupling for charge separation. Under the assumption that the intrinsic time constant for charge separation for **4.1b** in benzene remains  $\tau_{CS} = 13$  ps, any EISC process would need to be faster than that to outcompete charge separation. This would necessarily result in loss of  $^1\text{ANI}$  at some combined rate faster than 13 ps, which is not observed.

Another possible explanation is that charge separation does proceed in **4.1b** in benzene at  $\tau_{CS} = 13$  ps, but RP intersystem crossing and recombination to  $^3\text{ANI}$  occur at a faster rate than charge separation, preventing buildup of a significant population of the RP state. This process is consistent with the observed kinetics, and can be justified by solvent effects on the energetics of charge recombination. The higher energy of the RP state in benzene compared to polar solvents makes  $\Delta G_{\text{CRT}}$  more negative for  $^3\text{ANI}$  formation, which places  $\Delta G_{\text{CRT}}$  (-0.51 eV) closer to the maximum of the  $\ln k$  vs.  $\Delta G_{\text{CRS}}$  dependence ( $\lambda = 0.36$  eV) resulting in an increase in the charge recombination rate to  $^3\text{ANI}$ .

#### 4.4.3 Photophysical Processes at Low Temperature

TA data for **4.1a** in PrCN at 105 K show that electron transfer occurs following photoexcitation. However, the charge separation kinetics are non-exponential and much slower than in any solvent studied at room temperature. Charge separation appears to be competitive with fluorescence and intersystem crossing from  $^1\text{ANI}$ , resulting in a low yield of the charge separated state. The charge separation can be fit to a highly stretched exponential, indicating an

inhomogeneous sample with a wide range of excited state populations. This may reflect local differences in the solvent environment, conformations, and/or aggregation. This model is simplified to fit the nsTA data by dividing the distribution of excited state populations into two groups: those at the “fast” end charge separate quickly (within the IRF of the nsTA experiment), while those at the “slow” end intersystem cross and fluoresce.

In **4.1b**, evidence of the charge separated state is never observed, similar to **4.1b** in benzene at room temperature. In the latter case, direct intersystem crossing could be ruled out by careful comparison to **4.1a**, which showed loss of  $^1\text{ANI}^*$  at the same rate as **4.1b**. In PrCN at 105 K however, the excited state is lost much more quickly in **4.1b** than in **4.1a**, meaning that either direct intersystem crossing or charge separation followed by rapid recombination to  $^3\text{ANI}^*$  could explain this data. Thus the low temperature TA data do not provide a firm assignment of the excited state deactivation process in **4.1b**. However, the TA data for **4.1b** at low temperature clearly show the presence of  $^3\text{ANI}^*$ , which will prove useful in analyzing the EPR data (see below).

In all solvents studied, the population of  $^3\text{ANI}^*$  formed in **4.1b** decays more quickly than in **4.1a**. This effect has been reported previously in many covalent radical-chromophore systems and is likely due to EISC.<sup>162</sup> At 105 K in PrCN, quenching of  $^3\text{ANI}^*$  by bimolecular collisions is eliminated, and the lifetime of this species in **4.1a** exceeds the time window of the nsTA experiment. In contrast, the decay of  $^3\text{ANI}^*$  is again accelerated for **4.1b** compared to **4.1a**.

#### 4.4.4 Magnetic Coupling Between BDPA and <sup>3\*</sup>ANI

EPR data for **4.1b** in PrCN at 105 K and at 10 K show two new species not observed at room temperature. While no ESE can be detected for the broader of these two signals, transient nutation results for the narrower signal show a nutation frequency identical to or slightly lower than that of the unperturbed BDPA signal. Equation 4.1 describes the dependence of the nutation frequency on the spin multiplicity of the paramagnetic species,

$$\omega_{nut}(m_s, m_s + 1) = \frac{g_l \beta_e B_l}{\hbar} \sqrt{S(S + 1) - m_s(m_s + 1)} \quad (4.1)$$

where  $\omega_{nut}$  is the nutation frequency for a given EPR transition between sublevels  $m_s$  and  $m_s + 1$ , for a species with spin quantum number  $S$ ,  $B_l$  is the microwave excitation field,  $g_l$  is the  $g$ -factor at the orientation being excited,  $\beta_e$  is the Bohr magneton, and  $\hbar$  is the reduced Planck constant.<sup>168-170</sup> From eq 1, the EPR transitions in a quartet state should show nutation frequencies equal to  $\sqrt{3}$  and 2 times the frequency for a doublet state, and those for a triplet state should show a frequency of  $\sqrt{2}$  times the doublet state nutation frequency (assuming no significant differences in  $g$ -factor between these species). The observation of similar nutation frequencies for the new feature and unperturbed BDPA indicate that this new feature must arise from a doublet state. This signal is substantially broader than the unperturbed BDPA signal from unexcited molecules of **4.1b**, so it cannot be attributed simply to polarized BDPA. This signal instead arises from an interaction between BDPA and <sup>3\*</sup>ANI formed by charge recombination or EISC.

Such an interaction can be divided into two regimes depending on the strength of the exchange coupling between BDPA and <sup>3\*</sup>ANI.<sup>162, 171-172</sup> In the weak coupling regime, EPR signals will be split by interaction with the other paramagnetic species, but the system is best described as separate doublet and triplet species. In the strong coupling regime, these states mix

to populate quartet and excited doublet states. Either a quartet or triplet species could give rise to the broad, transient signal, while transitions in the quartet and/or doublet manifolds could explain the narrower transient signal.

We first consider the possibility that the system is in the strong coupling regime. In this case, the lack of a detectable ESE from the broader signal and the transient nutation data indicate that the quartet state cannot be detected and only the excited doublet state produces a detectable echo. However, this state should give rise to a single transition, split only by a smaller hyperfine coupling than the parent radical.<sup>162, 173</sup> Instead, two lines are observed, with a width much broader than that expected from the excited doublet state. The observed EPR spectrum therefore cannot arise from a system with strong exchange coupling between BDPA and  $^3\text{ANI}$ .

The observed spectrum could arise from a system with weak exchange coupling between BDPA and  $^3\text{ANI}$ , in which the dipolar coupling between these species splits the EPR signals. EasySpin simulations<sup>174</sup> of the spectra resulting from this model can reproduce the observed line positions using zero-field splitting parameters from isolated  $^3\text{ANI}$  and a dipolar coupling  $D = 50$  MHz between BDPA and  $^3\text{ANI}$  (Figure B.22). Using the point dipole approximation,  $D = 2785 \text{ mT} \cdot \text{\AA}^3 / r^3$ , where  $r$  is the distance between BDPA and  $^3\text{ANI}$ . When  $D = 50$  MHz,  $r = 11.6 \text{ \AA}$ , which agrees well with the  $11.9 \text{ \AA}$  center-to-center distance of BDPA and  $^3\text{ANI}$  determined by MM+ molecular mechanics energy minimization of **4.1b**. The observed polarization pattern of the EPR spectrum is difficult to simulate, but is similar to that reported previously for a weakly coupled triplet-radical system following EISC.<sup>171</sup> The observed low temperature EPR data show that the exchange coupling between BDPA and  $^3\text{ANI}$  is small, and it is therefore appropriate to discuss the system following charge recombination in terms of separate doublet and triplet states.

This finding is not surprising in light of the saturated piperazine linker separating BDPA and  $^3\text{ANI}$  as well as the long distance between them,<sup>171-172</sup> as compared to systems showing strong radical-triplet coupling.<sup>40, 48-49, 148, 162, 167</sup>

#### 4.4.5 Spin Polarization of BDPA

In all three solvents studied, the EPR signal of BDPA in **4.1b** is emissively polarized at room temperature. The observation that the echo amplitude becomes more emissive upon photoexcitation following an initial  $\pi$  microwave inversion pulse excludes the possibility that the observed amplitude changes are due to other effects such as enhanced spin relaxation rates or oxidation/reduction of BDPA to form a diamagnetic species. Additionally, loss of BDPA due to oxidation is unlikely because its oxidation potential is 0.12 V more positive than mPD (Table 4.1).

Several mechanisms have been described in the literature by which nonequilibrium spin polarization resulting from photoexcitation can be transferred to a stable radical. In the RP mechanism, the radical is polarized as a result of spin-selective recombination of the RP,<sup>46, 175-178</sup> and localized triplet states resulting from charge recombination do not play a role.<sup>130, 150</sup> In the radical-triplet pair mechanism (RTPM), electron spin polarization transfer (ESPT) mechanism, and the reversed quartet mechanism (RQM), strong interactions between the radical and a localized triplet state (which may arise from RP charge recombination or spin orbit induced intersystem crossing) lead to polarization.<sup>173, 179-180</sup> Finally, EISC in systems with weak coupling between the radical and triplet species has been proposed to directly polarize the radical.<sup>171</sup> Both charge recombination and  $^3\text{ANI}$  decay in **4.1b** at room temperature proceed more quickly than

the instrument response time of the EPR experiment, meaning it is not possible to correlate the growth of polarization with kinetics obtained from optical spectroscopy. The low temperature EPR results provide more information by allowing measurement of the magnetic coupling between  $^3\text{*ANI}$  and BDPA. These measurements show that  $^3\text{*ANI}$  and BDPA do not form a quartet state, ruling out the RQM as a source of polarization transfer. The RPTM and ESPT mechanisms also depend on strong exchange coupling between the radical and triplet,<sup>180</sup> and can therefore be excluded as well.

A contribution to the polarization from diffusional encounters of  $^3\text{*ANI}$  with BDPA on nearby ground state molecules can also be ruled out by estimating the rate of this process. The good agreement between a first-order model and the observed loss of  $^3\text{*ANI}$  in **4.1b** at room temperature indicates that the bimolecular kinetics of this diffusion controlled encounter can be approximated by a pseudo-first order rate equation, i.e., the concentration of ground state molecules is much larger than that of excited molecules containing  $^3\text{*ANI}$ , and this concentration remains approximately constant over time. The effective unimolecular rate constant  $k_{\text{eff}}$  for this reaction is then equal to the product of the concentration of the ground state and the diffusion limited rate constant  $k_{\text{D}}$  derived from the Stokes-Einstein equation.<sup>181</sup> The concentration of **4.1b** in the ground state is  $2 \times 10^{-4}$  M based on the published extinction coefficient of ANI.<sup>161</sup> Using the spherical molecule approximation,  $k_{\text{eff}}$  is estimated to be  $2.2 \times 10^6 \text{ s}^{-1}$  in benzene ( $\eta = 0.605$  cP),  $2.9 \times 10^6 \text{ s}^{-1}$  in THF ( $\eta = 0.456$  cP), and  $2.4 \times 10^6 \text{ s}^{-1}$  in PrCN ( $\eta = 0.553$  cP).<sup>151</sup> Because these rate constants are significantly smaller than those for both the loss of  $^3\text{*ANI}$  observed by TA and the development of spin polarization observed by EPR, intermolecular polarization transfer through the ESPT mechanism should not be significant.

This leaves two possible mechanisms to explain the observed polarization of BDPA at room temperature: EISC, and polarization transfer from the RP. Given the lack of evidence for the charge-separated state in **4.1b** at low temperature and the similarity of the polarization pattern to that reported from the EISC mechanism,<sup>171</sup> it is likely that EISC accounts for the spin polarization at low temperature. At room temperature however, EISC is definitely not observed in THF and PrCN, and is probably not a major pathway in benzene. This leaves the RP mechanism as the most likely source of the spin polarization at room temperature. Preparation and study of polarization transfer in a similar molecule in which the RP state is energetically inaccessible could help resolve this question more definitively, assuming EISC produces a measurable yield of <sup>3\*</sup>ANI, but the design of a directly-comparable molecule is challenging.

## 4.5 Conclusions

We have prepared a molecular donor-acceptor system in which photoinduced charge separation produces a strongly coupled RP, where the exchange coupling between the radicals is much larger than the hyperfine couplings within the radicals. Upon introduction of a third spin in the form of a covalently-attached stable radical, charge separation remains the dominant pathway, but interconversion of singlet and triplet RP states is accelerated by at least three orders of magnitude. The presence of an energetically-accessible triplet recombination product in the system results in solvent-dependent effects of this interconversion on RP lifetime and provides an optical observable for these spin dynamics. Previously studied radical-RP systems containing weakly coupled RPs have shown similar radical pair intersystem crossing on a timescale of 10s

to 100s of ns. Here, we present the first evidence of RP spin dynamics occurring on the picosecond timescale, demonstrating that the exchange coupling within the RP has a large effect on these dynamics. Spin evolution in organic molecules is often assumed to be slow (ns to  $\mu\text{s}$ )<sup>145, 150, 182</sup> due to weak spin-orbit coupling, but these results highlight that magnetic coupling between spins – interactions that are negligible on the electronic energy scale – can control reaction rates on an ultrafast timescale.

Time-resolved EPR spectroscopy shows that this rapid intersystem crossing process is associated with substantial polarization of the stable radical. The ability to prepare a polarized electron spin at room temperature by photoexcitation suggests that similar radical-RP systems may be useful as a starting point for DNP and molecular spintronics. The exchange coupling between BDPA and  $^3\text{ANI}$  is found to be weak, ruling out polarization transfer mechanisms that depend on the populating the quartet state in this system. These results therefore likely represent the first observation of electron spin polarization transfer from a strongly coupled RP in which one radical comprising the RP is coupled to a stable radical. Future work to measure or estimate the coupling constants in the intermediate triradical state should allow theories of RP polarization transfer to be tested for the first time for the strong coupling regime within the RP.

## CHAPTER 5

# Spin Polarization Transfer from a Photogenerated Radical Ion Pair to a Stable Radical Controlled by Charge Recombination

Adapted from Horwitz, N. E.; Phelan, B. T.; Nelson, J. N.; Mauck, C. M.; Krzyaniak, M. D.; Wasielewski, M. R. "Spin Polarization Transfer from a Photogenerated Radical Ion Pair to a Stable Radical Controlled by Charge Recombination." *The Journal of Physical Chemistry A*, **121**, 4455-4463 (2017).

## 5.1 Introduction

Molecular-scale devices that use electron spins to carry information are a promising area for the development of future information processing technologies, including quantum computation.<sup>120-121</sup> An essential prerequisite for such spintronic devices is the ability to initialize the system in a well-defined quantum state.<sup>4</sup> Highly spin-polarized states occur in many photoexcited molecular systems, including triplet states formed by spin-orbit-induced intersystem crossing<sup>183</sup> and radical ion pair (RP) states resulting from photoinduced electron transfer.<sup>141, 143</sup> These RP states provide an important means to generate high initial spin polarization, but they are typically short-lived, so that transferring this polarization to a stable unpaired spin<sup>40, 162, 167, 171, 184-185</sup> can serve to extend the polarization lifetime.

Here we focus on electron donor-acceptor systems covalently attached to a stable radical in which photoinduced electron transfer from the donor to the acceptor produces a highly spin-polarized RP that interacts with a stable radical to produce an overall triradical state. Electron spin polarization transfer from a RP to a stable radical has been demonstrated in several systems,<sup>46, 48-49, 130, 150</sup> with the stable radical remaining spin polarized long after RP recombination. This recombination process is spin selective, with the singlet and triplet RP states recombining at different rates to produce the singlet ground state and the neutral triplet excited state of the donor-acceptor molecule, respectively. Using donor-acceptor systems for solar energy conversion also requires long-lived charge separated states,<sup>55, 63, 118-119</sup> and several studies have taken advantage of spin selectivity to control RP lifetimes.<sup>45, 122-124, 126-129, 136, 186</sup> Spin

control of charge recombination thus provides an additional motivation for studying the spin dynamics of multi-spin systems.

Theoretical studies of spin polarization transfer from a photogenerated RP to a stable radical have highlighted several parameters that affect the rate, sign, and magnitude of polarization transfer, including the pairwise spin-spin exchange couplings between the three radicals and the charge recombination rates of the singlet and triplet RPs.<sup>175-176, 178</sup> The dependence of the polarization transfer magnitude on the spin-spin exchange coupling ( $2J$ ) within the RP has been measured and found to be consistent with these predictions;<sup>150</sup> yet, there have been no experimental studies of its dependence on the charge recombination rate constants of the singlet and triplet RPs,  $k_{CRS}$  and  $k_{CRT}$ , respectively.

Here, we report the preparation of a molecule designed to investigate how  $k_{CRS}$  and  $k_{CRT}$  affect spin polarization transfer. Because singlet and triplet RPs recombine to different products, the free energy change for these reactions can be tuned separately.<sup>139, 157</sup> Molecules **5.1a** and **5.1b** (Figure 5.1) take advantage of 4-aminonaphthalene-1,8-dicarboximide (ANI) as the chromophore and naphthalene-1,4:5,8-bis(dicarboximide) (NDI) as the acceptor, which have been shown to form RPs in high yield following photoexcitation,<sup>161</sup> and a *m*-phenylenediamine (mPD) is used as a secondary electron donor because of its favorable oxidation potential and ease of attachment to a stable radical.<sup>45</sup> In **5.1b**, a stable  $\alpha,\gamma$ -bisdiphenylene- $\beta$ -phenylallyl (BDPA $\cdot$ ) radical is attached to the mPD donor to enable spin polarization transfer in the photogenerated three-spin system, while **5.1a** serves as a reference molecule with BDPA $\cdot$  replaced by its diamagnetic precursor, BDPAH. Such donor-chromophore-acceptor triads can form the final mPD $^{+\cdot}$ -ANI-NDI $\cdot$  RP through one of two intermediates: mPD $^{+\cdot}$ -ANI $\cdot$ -NDI or

mPD-ANI<sup>+</sup>-NDI<sup>-</sup>, depending on which initial electron transfer reaction is faster. As mPD<sup>+</sup>-ANI<sup>-</sup>-NDI has been shown to undergo intersystem crossing and charge recombination on the picosecond timescale when BDPA<sup>•</sup> is present,<sup>45</sup> ANI and NDI were linked directly without a spacer group to favor high yield initial formation of mPD-ANI<sup>+</sup>-NDI<sup>-</sup>.<sup>75-76</sup> Transient optical absorption spectroscopy is used to follow the photoinduced electron transfer reactions in **5.1a** and **5.1b**, and time-resolved electron paramagnetic resonance (TREPR) spectroscopy is used to measure the spin polarization of BDPA<sup>•</sup>.

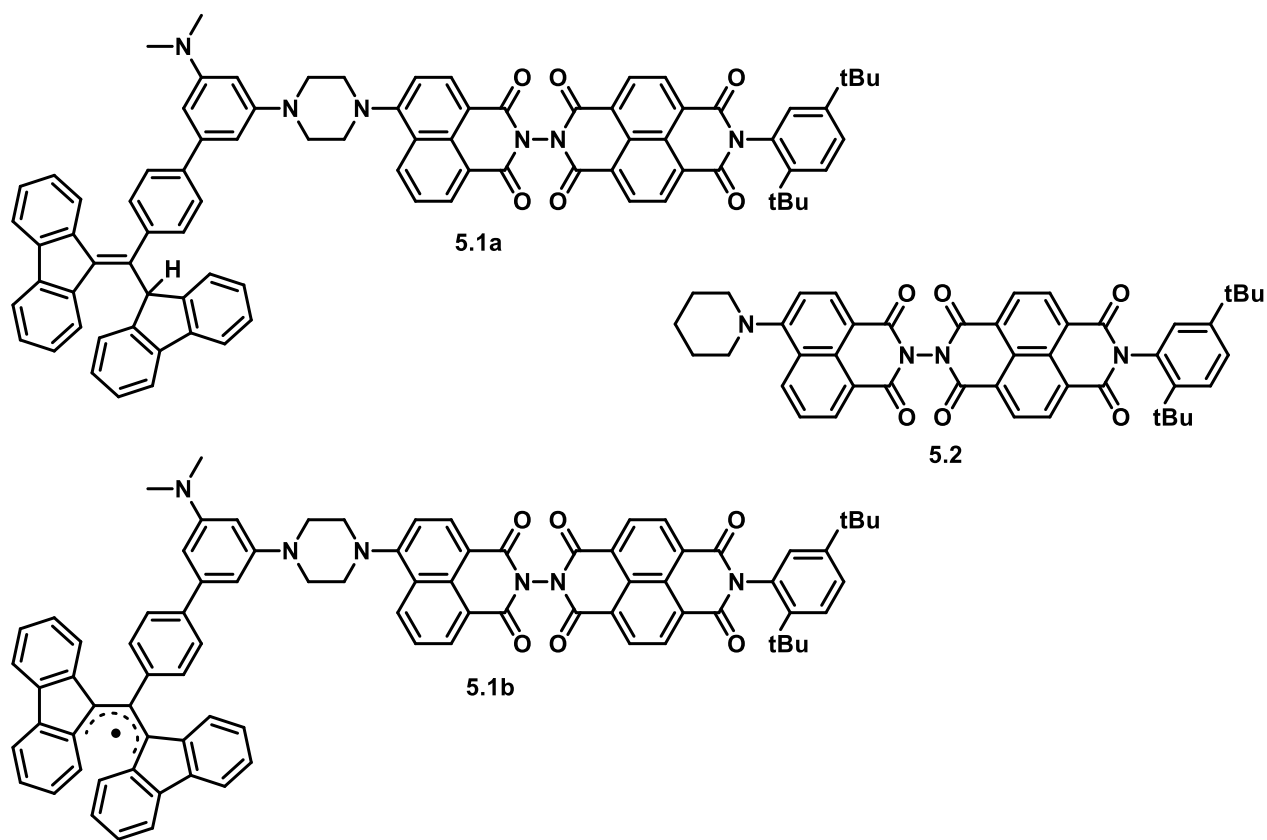


**Figure 5.1.** Structures of the molecules used in this study.

## 5.2 Experimental

### 5.2.1 Synthesis

The synthesis and characterization of compounds **5.1-5.6** is described in detail in Appendix B. Benzene was distilled before use from CaH<sub>2</sub> and stored in an N<sub>2</sub>-filled glovebox. Fluorobenzene was treated with P<sub>2</sub>O<sub>5</sub> and distilled as described by Armarego and Chai.<sup>66</sup> Dry, inhibitor-free THF and dry toluene were used in all other spectroscopic measurements. Compounds **5.1a** and **5.2** were purified by preparative thin layer chromatography on SiO<sub>2</sub> prior to optical and EPR spectroscopy, while **5.1b** was prepared from **5.1a** purified in this fashion, then eluted through a SiO<sub>2</sub> plug. Purified **5.1a** and **5.1b** were stored in the dark in a -20 °C freezer.

### 5.2.2 Optical Spectroscopy

Ground-state absorption measurements were made on a Shimadzu UV-1800 spectrophotometer. Femtosecond visible transient absorption spectroscopy (fsTA) experiments were conducted using a commercial regeneratively amplified Ti:sapphire laser system (Tsunami oscillator/Spitfire amplifier, Spectra-Physics) described previously.<sup>187</sup> Before interaction with the sample, the probe was split using a neutral density filter so that one portion interacted with the sample and one portion provided a reference spectrum. The pump was sent through a commercial depolarizer (DPU-25-A, Thorlabs, Inc.) to suppress the effects of rotational dynamics and chopped at 500 Hz. The pump was focused to ~0.2-1.0 mm diameter and the probe to ~0.1 mm diameter at the sample. The reference probe and the transmitted probe were

coupled into optical fibers and detected using a customized Helios spectrometer and Helios software (Ultrafast Systems, LLC). Nanosecond visible transient absorption spectroscopy (nsTA) experiments were performed using the pump pulse described for the fsTA experiments paired with a photonic crystal fiber ultra-broadband probe generated by a customized EOS spectrometer (Ultrafast Systems, LLC). The samples were irradiated with 1  $\mu$ J pulses centered at 414 nm or 500 nm and the temporal resolution was  $\sim$ 120 fs to  $\sim$ 280 fs in the fsTA experiments and  $\sim$ 600 ps in the nsTA experiments. Visible fsTA spectra were collected for 3-5 s at each pump-probe time delay; nsTA spectra were collected using similar durations. All datasets were background-subtracted to remove scattered pump light and spontaneous emission and corrected for group delay dispersion and time zero using Surface Explorer (Ultrafast Systems, LLC).

Nanosecond transient absorption spectroscopy and corresponding magnetic field effects were measured using the 355 nm output of a pulsed frequency-tripled Continuum 8000 Nd:YAG laser to pump a Continuum Panther OPO. The 7 ns, 416 nm pump output was filtered through two dichroic mirrors, focused to a 1.5 mJ, 5 mm diameter spot at the sample, and matched to that of the probe pulse generated using a xenon flashlamp (EG&G Electro-Optics FX-200). The signal was collected at single wavelengths with a monochromator (HORIBA Triax 180) and detected using a photomultiplier tube (Hamamatsu R928).

Samples for fsTA and nsTA were prepared with an optical density between 0.4 and 0.7 at 414 nm in 2 mm quartz cuvettes fused to a quartz bulb for degassing. Samples were subjected to four freeze-pump-thaw degassing cycles on a vacuum line ( $10^{-4}$  Torr) and sealed under vacuum.

Samples for magnetic field effect experiments prepared with an optical density between 0.4 and 0.7 at 416 nm were placed in a 10 mm quartz cuvette and degassed with up to five

freeze-pump-thaw cycles on a vacuum line ( $10^{-4}$  Torr). The cuvette was placed between the poles of an electromagnet (Walker Scientific HV-4W) with a water-cooled power supply (Walker Magnion HS-735). The field strength was measured by a Hall effect probe interfaced with a gaussmeter (Lakeshore 450). The magnetic field effect experiment was performed as described previously.<sup>157</sup> To account for any sample degradation over the several hours of measurements required for each experiment, kinetics at  $B = 0$  mT were measured at regular intervals and fit to a linear baseline.

### 5.2.3 Analysis of Transient Absorption Data

The kinetic analyses of the fsTA data and some nsTA data were performed using lab-written programs in MATLAB<sup>154</sup> and were based on a global fit of kinetic vectors following singular value decomposition with the solution to a first order kinetic model. The remainder of the nsTA data was fit to a sum of exponentials at single wavelengths, or decomposed into basis spectra. Full details of these procedures are reported in Appendix D.

### 5.2.4 EPR Spectroscopy

EPR measurements were made at X-band ( $\sim 9.5$  GHz) using a Bruker Elexsys E680-X/W EPR spectrometer outfitted with a split ring resonator (ER4118X-MS5). Measurements were performed at room temperature. Sample solutions (optical density between 0.4 and 0.7 in 2 mm cuvette at 416 nm,  $\sim 10^{-4}$  M) were loaded into quartz tubes (1.80 mm o.d.  $\times$  1.50 mm i.d.), subjected to four freeze-pump-thaw degassing cycles on a vacuum line ( $10^{-4}$  Torr), and sealed under vacuum using an oxy-hydrogen torch.

Continuous wave (CW) EPR spectra were measured using 0.6 mW microwave power and 0.01 mT field modulation at 100 kHz. Time-resolved EPR measurements were performed following photoexcitation with 7 ns, 1.8 mJ, 416 nm pulses using the output of an optical parametric oscillator (Spectra-Physics Basi-scan), pumped with the 355 nm output of a frequency-tripled Nd:YAG laser (Spectra-Physics Quanta-Ray Pro 350). Time-resolved EPR measurements were collected using electron spin echo (ESE) detection. A 1 kW TWT amplifier (Applied Systems Engineering 117X) was employed to generate high-power microwave pulses. The resonator was partially overcoupled to maximize echo intensity and minimize ringing following microwave pulses. ESE data was obtained with a  $\pi/2$ - $\tau$ - $\pi$  pulse sequence with  $\pi/2 = 16$  ns,  $\pi = 32$  ns, and  $\tau = 120$  ns. The integrated echo intensity was recorded as a function of the magnetic field to yield the spectrum. If the sample is photoexcited at some time  $t$  prior to the  $\pi/2$ - $\tau$ - $\pi$  pulse sequence, spectra can be collected of the transient species as a function of  $t$ .

## 5.3 Results and Discussion

### 5.3.1 Optical Spectroscopy

The UV-visible absorption spectrum of **5.1a** in benzene (Figure 5.2) shows peaks at 384, 366, and 341 nm from NDI, a shoulder near 400 nm from ANI, and a peak at 324 nm due to BDPAH. In **5.1b**, the 324 nm band is replaced by new features near 874, 504, and 340 nm from BDPA<sup>\*</sup>. The excitation wavelength of 414-416 nm used for transient optical absorption and transient EPR spectroscopies was selected to maximize excitation of ANI over BDPA<sup>\*</sup> and NDI.

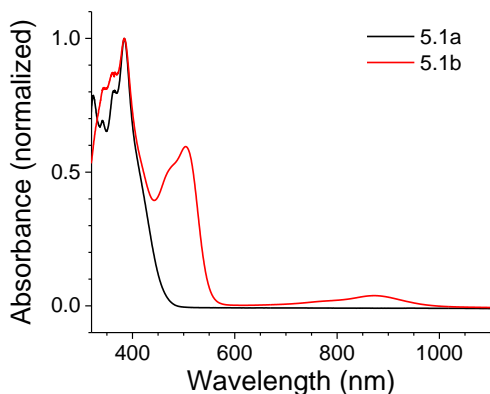


**Figure 5.2.** UV-visible absorption spectra of **5.1a** and **5.1b** in benzene.

### 5.3.2 Energetics of Electron Transfer Reactions

The free energy changes for photoinduced electron transfer reactions in **5.1a** and **5.1b** were estimated using previously published values for the redox potentials of the mPD electron donor, the ANI chromophore, and the NDI electron acceptor, along with the emission energies of the lowest singlet and triplet excited states,  $^1\text{*ANI}$  and  $^3\text{*NDI}$ .<sup>45, 161</sup> These values were used to estimate RP energies as described earlier.<sup>161</sup> Details of these calculations are presented in Appendix D and summarized in Table 5.1.

Compound	$\Delta G_{\text{CS1}}$	$\Delta G_{\text{CS2}}$	$\Delta G_{\text{CRS}}$	$\Delta G_{\text{CRT}}$	$\lambda_{\text{CRS}}$	$\lambda_{\text{CRT}}$
<b>5.1a</b> , benzene	-0.52	-0.31	-1.98	0.05	0.31	0.26
<b>5.1a</b> , 5:95 fluorobenzene:benzene	-0.54	-0.31	-1.95	0.08	0.39	0.34
<b>5.1a</b> , 10:90 fluorobenzene:benzene	-0.56	-0.32	-1.92	0.11	0.45	0.40
<b>5.1b</b> , benzene	-0.52	-0.34	-1.95	0.08	0.31	0.26
<b>5.1b</b> , 5:95 fluorobenzene:benzene	-0.54	-0.34	-1.92	0.11	0.39	0.34
<b>5.1b</b> , 10:90 fluorobenzene:benzene	-0.56	-0.35	-1.89	0.14	0.45	0.40

**Table 5.1.** Estimated free energy changes ( $\Delta G$ ) and reorganization energies ( $\lambda$ ) in eV for charge separation (“CS1”), charge shift (“CS2”), and singlet (“CRS”) and triplet (“CRT”) charge recombination reactions in **5.1a** and **5.1b**.

The estimates in Table 5.1 indicate that both electron transfer steps to form the  $\text{mPD}^{+\bullet}$ -ANI-NDI $^{\bullet-}$  RP should be energetically favorable for both **5.1a** and **5.1b** in all three solvents tested. Charge recombination of  $^1(\text{mPD}^{+\bullet}$ -ANI-NDI $^{\bullet-})$  to the ground state is expected to be in the Marcus inverted region ( $-\Delta G_{\text{CRS}} > \lambda_{\text{CRS}}$ ), while that of  $^3(\text{mPD}^{+\bullet}$ -ANI-NDI $^{\bullet-})$  is slightly endergonic for **5.1a** and **5.1b**, and are essentially the same within the error of calculating the RP energy. This raises the possibility that  $^3(\text{mPD}^{+\bullet}$ -ANI-NDI $^{\bullet-})$  and its charge recombination product  $^3\text{NDI}$  could exist in equilibrium during the charge recombination process, which has been observed previously in similar molecules.<sup>161</sup>

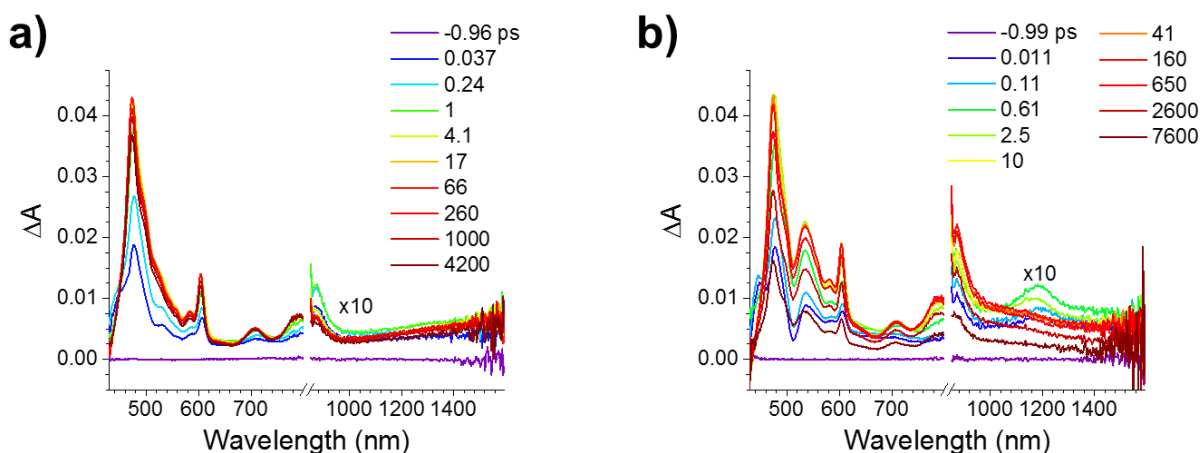


**Figure 5.3.** fsTA spectra in benzene following excitation with 414 nm laser pulse: (a) **5.1a**; (b) **5.1b**.

### 5.3.3 Transient Absorption Spectroscopy

To investigate charge separation and recombination reactions following photoexcitation, transient absorption spectroscopy was performed on **5.1a** and **5.1b** in de-aerated benzene. Selected fsTA spectra of **5.1a** and **5.1b** at 295 K are shown in Figures 5.3a and 5.3b,

respectively. In **5.1a**, absorption bands characteristic of  $\text{NDI}^{\bullet}$  rise at 475, 605, 710, and 790 nm within the instrument response function of  $\sim 0.3$  ps, indicating ultrafast formation of  $\text{mPD-ANI}^{++}\text{-NDI}^{\bullet}$ . A slight shift of these bands is observed at later times that can be fit to a species-associated  $\text{A} \rightarrow \text{B}$  kinetic model (Figure D.3) with  $\tau = 7.9$  ps, which most likely results from torsional motion of the piperazine about C-N bond linking it to the naphthalene-1,8-dicarboximide. The transient spectrum does not change significantly over the remaining 7 ns pump-probe time window of the fsTA apparatus, and this decay is not included in fitting. FsTA data in the near-infrared (NIR) region shows subpicosecond formation of a weak feature near 1600 nm in **5.1a** due to formation of  $\text{mPD}^{++}$  (Figure D.6) showing that the secondary electron transfer  $\text{mPD-ANI}^{++}\text{-NDI}^{\bullet} \rightarrow \text{mPD}^{++}\text{-ANI-NDI}^{\bullet}$  also occurs on a subpicosecond timescale. This further supports the conclusion that the  $\tau = 7.9$  ps process is due to a structural relaxation rather than electron transfer from mPD to  $\text{ANI}^{++}$ .

In **5.1b**, similar features and dynamics are observed in the fsTA spectra, but a new band is present near 530 nm. This feature is attributed to a Stark shift of the  $\text{BDPA}^{\bullet}$  ground state absorption as a result of the electric field generated by the nearby  $\text{mPD}^{++}\text{-ANI-NDI}^{\bullet}$  RP.<sup>188-190</sup> In the NIR region, the small feature near 1200 nm at early times is due to parallel excitation of  $\text{BDPA}^{\bullet}$  by the 414 nm pump pulse. Previous work has shown that excited  $^2\text{BDPA}^{\bullet}$  decays to its ground state rapidly and does not lead to long-lived electron transfer or spin polarization of  $\text{BDPA}^{\bullet}$  in a similar molecule.<sup>45</sup> The NIR band from  $\text{mPD}^{++}$  is red-shifted in molecules containing  $\text{mPD}^{++}$  and  $\text{BDPA}^{\bullet}$ , but can be observed in the shortwave infrared transient absorption spectrum of **5.1b** at  $\sim 2000$  nm (Figure D.7), indicating that the terminal RP,  $\text{BDPA}^{\bullet}\text{-mPD}^{++}\text{-ANI-NDI}^{\bullet}$ , still forms in this compound. Fitting to a species-associated  $\text{A} \rightarrow \text{B} \rightarrow \text{ground state}$  kinetic

model (Figure D.4) once again shows that small spectral shifts occur in  $\tau = 6.5$  ps, which are attributable to the same small structural changes as noted above.

### 5.3.4 Equilibrium Between the Triplet RP and $^3\text{NDI}$

Transient absorption spectroscopy on the nanosecond to microsecond timescale (nsTA) was used to follow charge recombination in **5.1a** and **5.1b**. In contrast to most other molecular donor-chromophore-acceptor systems, these compounds show non-exponential charge recombination, suggesting the presence of multiple populations of RPs that interconvert slowly relative to the recombination reaction. Additionally, the nsTA spectra change shape with time, e.g. the band near 450 nm increases relative to the features from  $\text{NDI}^{\bullet-}$  (Figure 5.4). In molecules containing ANI directly connected to NDI,  $^3\text{NDI}$  is known to absorb at this wavelength (Figure D.8). However, kinetic models that include recombination of a single RP species to the singlet ground state and  $^3\text{NDI}$  charge recombination products do not fit this data very well (Figures D.9 and D.12).

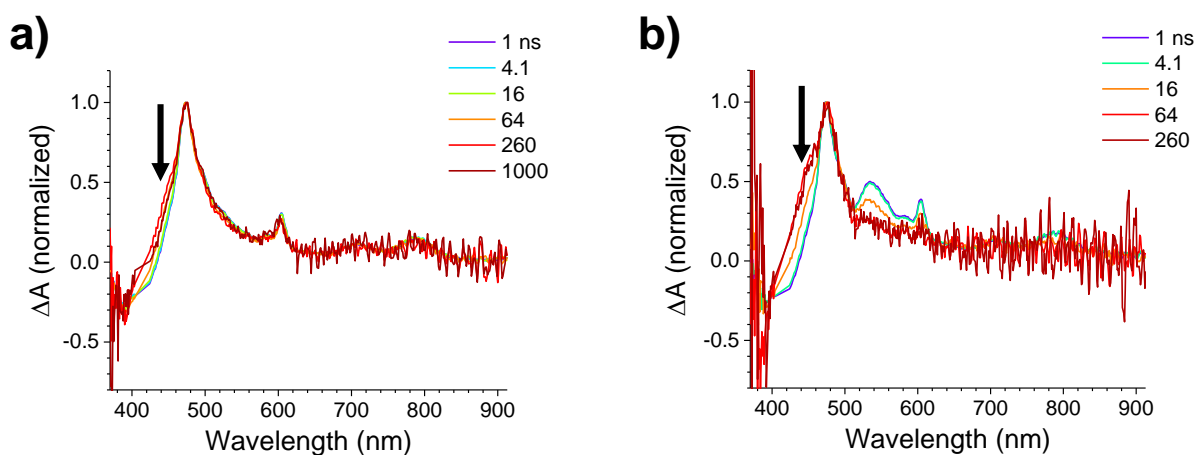


**Figure 5.4.** Nanosecond transient absorption spectra normalized at different times following photoexcitation in benzene: (a) **5.1a**; (b) **5.1b**. Raw data is presented in Appendix D.

To test the hypothesis that both  $\text{mPD}^{++}\text{-ANI-NDI}^{\bullet}$  and  ${}^3\text{*NDI}$  contribute to the late-time nsTA spectra, the nsTA spectra were fitted as a linear combination of two reference spectra at each time point (details of these fits are presented in the Appendix D). The reference spectra for  $\text{BDPAH-mPD}^{++}\text{-ANI-NDI}^{\bullet}$  and  $\text{BDPA}^{\bullet}\text{-mPD}^{++}\text{-ANI-NDI}^{\bullet}$  in **5.1a** and **5.1b**, respectively, were obtained  $\sim 1$  ns after the pump pulse, while that for  ${}^3\text{*NDI}$  was obtained from a species-associated fit to nsTA data from **5.2**. This model fits the data well, but due to uncertainties with regard to the extinction coefficient of  ${}^3\text{*NDI}$  in **5.1a**, **5.1b**, and **5.2**, only changes in the contributions of the RP relative to  ${}^3\text{*NDI}$  over time are considered. Examining the kinetics for **5.1a** in benzene (Figure 5.5a) shows that following the  $\sim 0.7$  ns instrument response time, the contribution from the RP decays. A residual population of RP remains, decaying on the microsecond timescale. The  ${}^3\text{*NDI}$  contribution rises during the rapid decay of the RP, then decays with a similar rate to the residual RP. A similar trend is seen for **5.1b** in benzene (Figure 5.5c). These results clearly show the existence of two populations of the RP in both molecules. The fact that  ${}^3\text{*NDI}$  decays at a rate similar to the slowly-decaying RP population suggests that these species are in equilibrium, a hypothesis supported by the small energy gap between these states. The existence of two slowly-interconverting RP populations can then be explained by spin restrictions: the triplet RP can equilibrate with  ${}^3\text{*NDI}$ , while the singlet RP cannot.

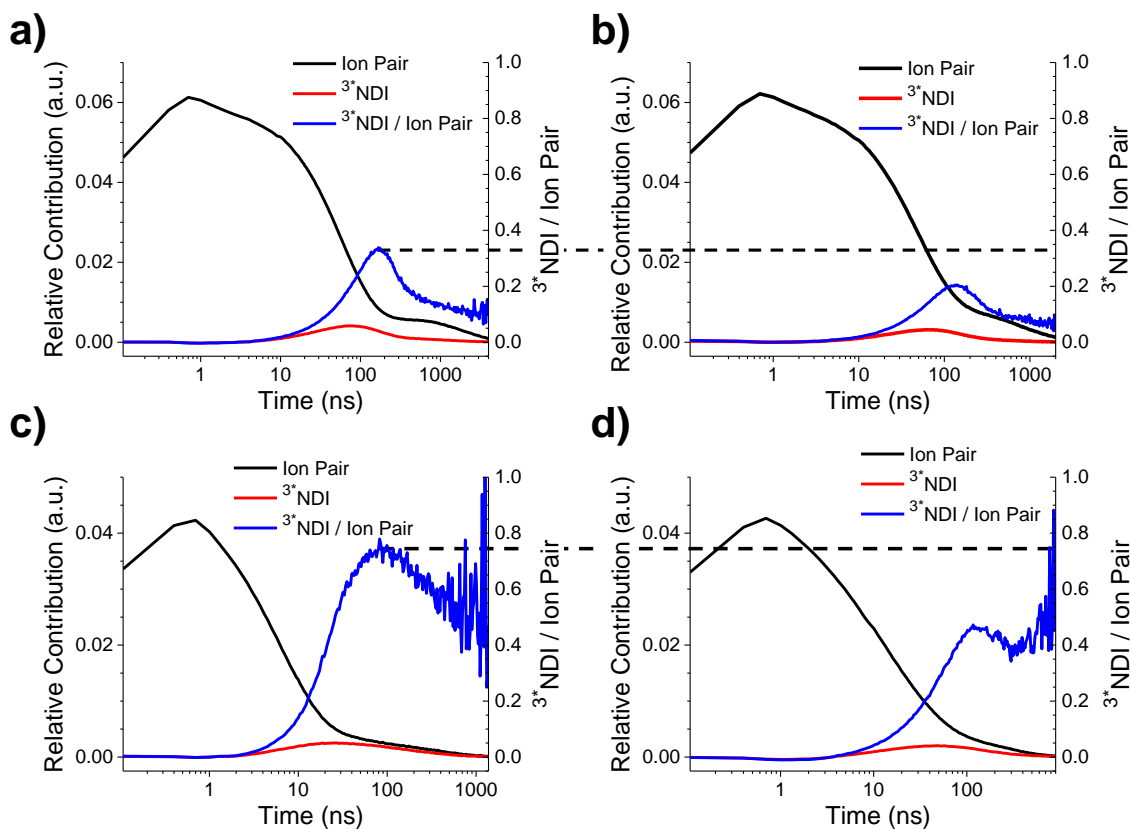


**Figure 5.5.** Contributions from RP and  $^3\text{NDI}$  states as a function of time for (a) **5.1a** in benzene; (b) **5.1a** in 10% fluorobenzene/benzene; (c) **5.1b** in benzene; (d) **5.1b** in 10% fluorobenzene/benzene. Raw data, reference spectra, and fitting details are presented in Appendix D.

The hypothesis of an equilibrium between the triplet RP and  $^3\text{NDI}$  can be tested by increasing the dielectric constant of the solvent. Compared to nonpolar benzene, more polar solvents will stabilize the RP, but not have a large effect on the energy of  $^3\text{NDI}$ . This should lead to the equilibrium shifting towards the RP state as solvent polarity increases. The nsTA data was acquired in a mixed solvent containing 10% (v/v) fluorobenzene in benzene and the data decomposed into RP and  $^3\text{NDI}$  contributions as described above (Figures 5.5b and 5.5d). Compared to the data in benzene, the ratio of  $^3\text{NDI}$  to RP is lowered by about half in this

solvent, for both **5.1a** and **5.1b**. This is strong evidence for the existence of an equilibrium between the RP state and  $^3\text{NDI}$ .

### 5.3.5 Magnetic Field Effects on Charge Recombination

To show that the RP species involved in the equilibrium is specifically the triplet RP, and not the optically indistinguishable singlet RP, nsTA experiments were performed in an applied static magnetic field. Mixing between the singlet and triplet RP states (S-T mixing) depends on the spin-spin exchange coupling between the radicals,  $2J$ . The energy of the singlet RP is unaffected by an applied static magnetic field, but the three triplet states will be split by the Zeeman interaction, so that when the field  $B = 2J$ , one of the triplet sublevels will be degenerate with the singlet state (Figure 5.6a), so that increased S-T mixing results in an increase in triplet RP yield. For example, if  $k_{CRT} > k_{CRS}$ , charge recombination then results in a corresponding increase in  $^3\text{NDI}$  yield and decrease in RP yield.<sup>75</sup>

Magnetic field effect experiments performed on **5.1a** in toluene show that the yield of the slowly decaying species reaches a maximum at  $B = 2J = 19.2 \pm 0.3$  mT (Figure 5.6c). This measurement was also attempted on **5.1b**, but due to the high rate of S-T mixing at zero-field induced by  $\text{BDPA}^{\bullet}$ , no maximum in the yield of slowly decaying species was observed.<sup>131</sup> Full nsTA spectra of **5.1a** were then collected at  $B = 0$  mT and at  $B = 19$  mT, and decomposed into RP and  $^3\text{NDI}$  contributions as described above (Figure 5.6d). When  $B = 19$  mT, the amount of both triplet RP and  $^3\text{NDI}$  increase relative to  $B = 0$  mT, which is consistent with an equilibrium between the RP and  $^3\text{NDI}$ .

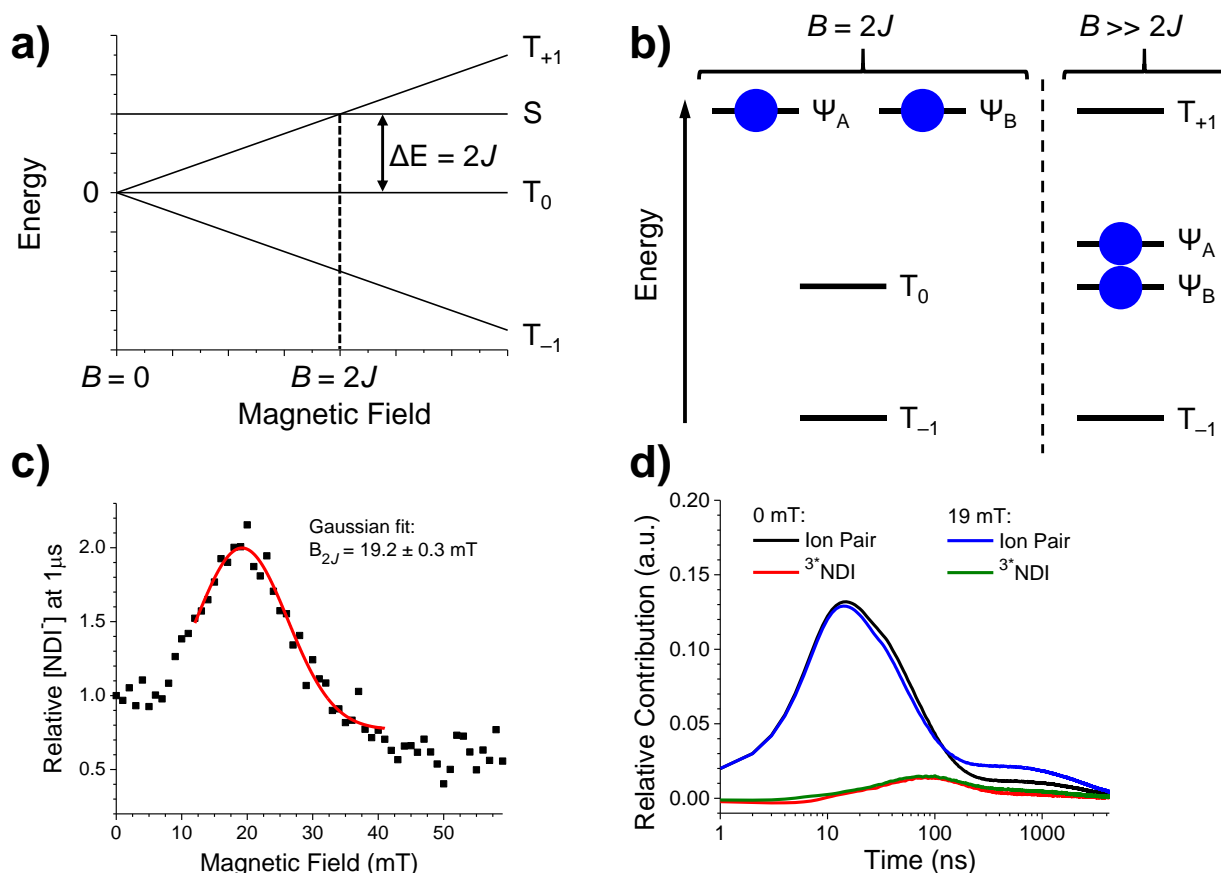


**Figure 5.6.** (a) Schematic showing dependence of the RP state energies on external magnetic field, with  $2J < 0$ . (b) Population of these states following S- $T_{+1}$  mixing at  $B = 2J$  and S- $T_0$  mixing at  $B \gg 2J$ , denoted by size of filled circles.  $\Psi_A$  and  $\Psi_B$  are the new eigenstates resulting from S-T mixing. (c) Long-lived ( $1 \mu\text{s}$ ) nsTA signal at 473 nm as a function of magnetic field for **5.1a** in de-aerated toluene at 295 K. The peak is fit to a Gaussian centered at 19.2 mT. (d) Relative contributions from RP and  $^3\text{NDI}$  states as a function of time at 473 nm for **5.1a** in benzene at  $B = 0 \text{ mT}$  and 19 mT. The raw data are presented in Figure D.16.

Under all conditions studied for **5.1a** and **5.1b**, the  $^3\text{NDI}/\text{RP}$  ratio decreases with time after the initial rise of the  $^3\text{NDI}$  contribution. This indicates a shift in the equilibrium constant to favor the RP state. Conformational dynamics are likely responsible for stabilizing the RP state and shifting the equilibrium toward the RP. Multiple conformers have been identified in a similar compound, with interconversion occurring on the timescale of charge recombination.<sup>191</sup> The

conformational change may involve a “harpooning” motion that reduces the distance between the ions and stabilizes the RP by decreasing the Coulombic contribution to the RP energy.<sup>192</sup>

### 5.3.6 TREPR Spectroscopy

TREPR measurements on **5.1a** show only a very weak spin-correlated RP signal, consistent with the relatively large  $2J$  in this molecule.<sup>141, 143</sup> The remaining TREPR experiments were performed only on **5.1b**, where signals from the polarized BDPA<sup>•</sup> radical overwhelm the weak RP signal (Figure D.18). Electron spin echo (ESE) detected TREPR can be carried out on **5.1b** at 295 K in solution because the transverse relaxation time ( $T_2$ ) of BDPA<sup>•</sup> is long.<sup>45, 166</sup> The ESE experiments in benzene show polarization transfer from the RP to the stable BDPA<sup>•</sup> radical as expected (Figure 5.7b). However, this polarization transfer occurs with multiple rates, in contrast to previous examples. In benzene, an initial positive polarization of BDPA<sup>•</sup> is observed, occurring within the instrument response of the EPR experiment. This positive polarization then shows a biexponential decay with time constants of  $\tau_1 = 160$  ns (45%) and  $\tau_2 = 590$  ns (55%), becoming slightly negative. These rates are much faster than the spin-lattice relaxation time,  $T_1 = 93$   $\mu$ s of BDPA<sup>•</sup> in **5.1b** (Figure D.19), indicating that this process is not decay of the initial positive polarization, but additional, negative polarization transferred from the RP or <sup>3</sup>\*NDI. The TREPR measurements were repeated on **5.1b** in mixed solvents comprising 5% and 10% (v/v) fluorobenzene in benzene. As the solvent polarity increases, the negative polarization transfer process becomes faster and larger in magnitude (Figure 5.7b). In tetrahydrofuran, a much more polar solvent, no polarization of BDPA<sup>•</sup> is observed, likely due to subnanosecond charge recombination that is much faster than these spin dynamics (Figure D.5).

The kinetics in all three benzene-containing solvents require two exponential decay components for an adequate fit (Figures D.22-D.24). Fitted time constants are presented in Table 5.2. The slight fluctuations visible in the kinetic traces in Figure 5.7b are the result of instrumental drift and are not reproducible. Beyond introducing additional uncertainty into the kinetic fits, we do not expect these fluctuations to impact the conclusions of this study.

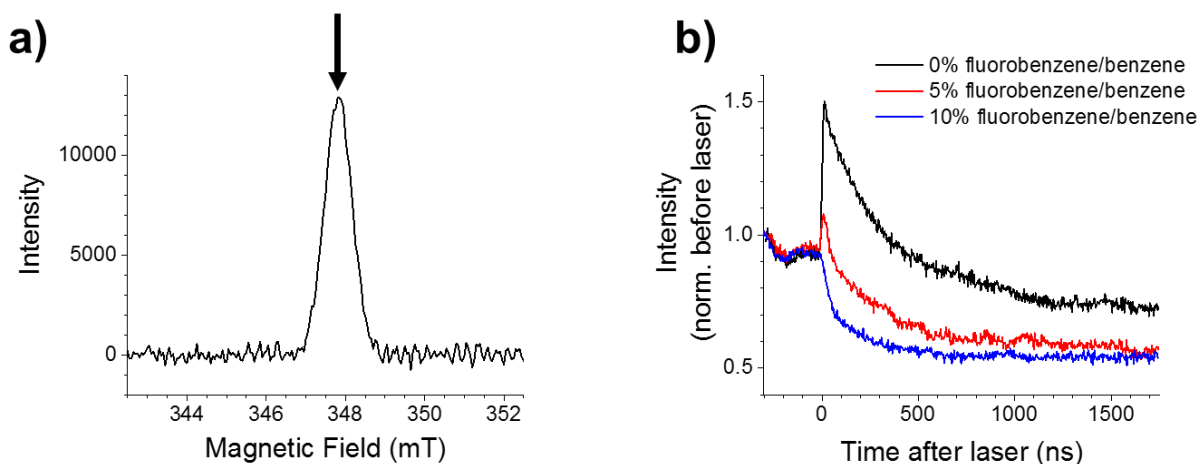


**Figure 5.7.** Time-resolved EPR on **5.1b**: (a) steady-state spectrum in benzene in the absence of photoexcitation; (b) kinetic traces at the maximum field position for samples in benzene and mixed solvents.

Solvent	$\tau_1$ , ns (rel. amp.)	$\tau_2$ , ns (rel. amp.)
0% fluorobenzene/benzene	$160 \pm 20$ (45%)	$590 \pm 70$ (55%)
5% fluorobenzene/benzene	$24 \pm 4$ (38%)	$316 \pm 9$ (62%)
10% fluorobenzene/benzene	$30 \pm 5$ (50%)	$220 \pm 10$ (50%)

**Table 5.2.** Polarization transfer time constants and relative amplitudes for **5.1b**.

While both RPs and  $^3\text{NDI}$  are present on the timescale of the negative polarization, the increase of this negative contribution in more polar solvents, where less  $^3\text{NDI}$  is observed, suggests that the RP is responsible for the additional polarization. Previous studies have shown that the polarization magnitude depends on  $2J$ , which in turn depends on the free energy change

for charge recombination,<sup>111</sup> which is one possible source of the observed solvent dependence. However, neither the singlet nor the triplet charge recombination reactions in **5.1b** are expected to transition from the Marcus inverted region to the normal region as a result of the change in solvent; therefore,  $2J$  is not expected to change significantly in the solvents studied.

This leaves the selective charge recombination of the singlet and triplet RPs as the most likely source of the observed solvent dependence of BDPA<sup>\*</sup> polarization in **5.1b**. The RP is generated in the singlet (S) state, which then decays through recombination to the singlet ground state and intersystem crossing to the three triplet RP states ( $T_{-1}$ ,  $T_0$ ,  $T_{+1}$ ) in the high magnetic field limit. In the TREPR experiments,  $B \gg 2J$ , such that spin mixing primarily involves the S and  $T_0$  states.<sup>73, 143</sup> As shown in Figure 5.6b, this results in population of the two states  $\Psi_A$  and  $\Psi_B$  that result from S- $T_0$  mixing in the RP. Spin relaxation in the RP or in the equilibrated <sup>3\*</sup>NDI can lead to population of the  $T_{\pm 1}$  levels.<sup>139, 193</sup> Because the two mixed states  $\Psi_A$  and  $\Psi_B$  have some singlet character, these populations recombine quickly to the singlet ground state. In contrast, any RPs in the  $T_{-1}$  and  $T_{+1}$  states must undergo slow spin relaxation before recombination.<sup>134</sup> At late times, the spin polarization of the RP inverts, with the initially populated  $\Psi_A$  and  $\Psi_B$  having a lower population than  $T_{-1}$  and  $T_{+1}$ , as outlined in Figure 5.8. This inversion should also lead to the inversion of the polarization transferred to the radical BDPA<sup>\*</sup>, as observed in the TREPR data. Such an inversion of the RP spin polarization, monitored by the TREPR signal of a more weakly-coupled RP, has been observed previously in a system where the triplet recombination product is in equilibrium with the triplet RP.<sup>194</sup> Consistent with this explanation, absorptive polarization of BDPA<sup>\*</sup> is observed within the EPR instrument response,

while  $\Psi_A$  and  $\Psi_B$  are still populated. Likewise, emissive polarization of  $\text{BDPA}^{\bullet}$  is seen to accumulate after the fast singlet recombination has depleted  $\Psi_A$  and  $\Psi_B$ .

This model can explain the observed solvent dependence of the polarization transfer rates. As solvent polarity is increased, the equilibrium shifts to increase the population of triplet RP states and decrease the population of the  $^3\text{NDI}$  state.  $^3\text{NDI}$  is distant from  $\text{BDPA}^{\bullet}$ , and the weak coupling between these species means that  $^3\text{NDI}$  is unlikely to contribute to the polarization of  $\text{BDPA}^{\bullet}$ . Increasing solvent polarity increases the population of the triplet RP states responsible for the emissive spin polarization, resulting in a faster apparent rate of emissive polarization transfer to  $\text{BDPA}^{\bullet}$ . Direct decay of  $^3\text{NDI}$  to the ground state, observed in the model compound **5.2**, depletes the total population of the equilibrated triplet RP/ $^3\text{NDI}$  state. This likely results in the observed increase of the final emissive polarization in more polar solvents, as less time spent in the  $^3\text{NDI}$  state would reduce this loss.

The observed biexponential nature of the negative polarization likely results from the presence of at least two conformers of **5.1b** as suggested by the shift in the equilibrium constant noted previously. Conformational changes are likely to result in changes in the value of  $2J$  within the RP, which has been shown to affect the magnitude of polarization transfer to the stable radical.<sup>47</sup> However, it is not expected that this process alone can account for the observed inversion of the polarization direction with time. Theoretical studies have indicated that the sign of polarization transfer is determined in part by the sign of  $2J$  within the radical pair.<sup>176, 195</sup> As noted above, the singlet charge recombination is far in the inverted regime, and the small shift in radical ion pair energy resulting from the conformational change is therefore not expected to result in a change in the sign of  $2J$ , just in its magnitude.

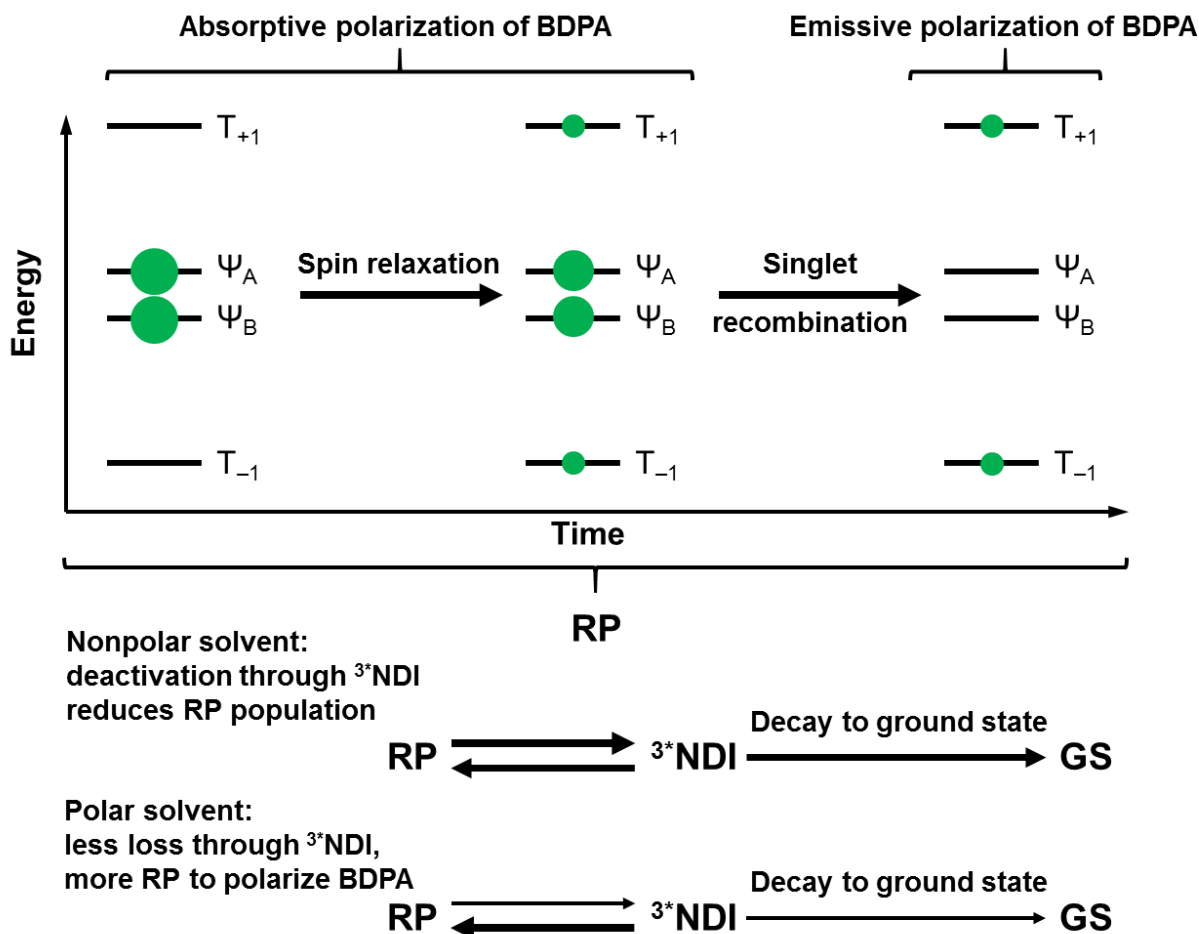


**Figure 5.8.** Schematic diagram (not to scale) showing changes in the RP spin state populations over time, and the influence of solvent polarity on the total RP population. This model is proposed to account for the observed inversion of the BDPA<sup>\*</sup> polarization with time, and the solvent dependence of the polarization rates.

## 5.4 Conclusions

We have prepared a stable radical/donor/chromophore/acceptor molecule in which photoinduced electron transfer produces a RP coupled to a stable radical. Recombination of the RP is spin selective, with the triplet RP states equilibrating with the neutral triplet state of the

acceptor. Charge recombination alters the populations of the RP spin states, resulting in two opposing polarization transfer processes. Small changes in solvent polarity shift the equilibrium between the triplet RP and the neutral triplet state of the acceptor resulting in different polarization transfer rates from the RP to the stable radical. These results highlight the mutual dependence of electron transfer rates and spin dynamics in donor-acceptor systems, and provide experimental evidence for predictions that radical ion pair recombination rates affect polarization transfer.

## CHAPTER 6

# Synthesis and Characterization of a Biradical-Donor-Acceptor System for Investigation of Spin Coherence Transfer

## 6.1 Introduction

The development of molecular spintronics requires both a detailed understanding of the dynamics of complex multi-spin systems and the ability to control the flow of spin information between sites.<sup>7</sup> As such, spin-spin interactions that allow transfer of spin polarization and coherence are of particular interest. As discussed in previous chapters, electron spin polarization transfer from highly polarized photogenerated states has been well documented in molecules containing a photogenerated radical pair or triplet state coupled to a stable radical.<sup>44-45, 47, 196-199</sup> Less well-studied is the possibility of transferring electron spin coherence between sites, a prerequisite for creating spin-based devices for quantum computers.<sup>200-202</sup> Quantum teleportation is one such process that allows for exact reconstruction of a coherent spin state at a new site,<sup>203</sup> and an implementation of this process using electron transfer in organic molecules has been proposed.<sup>204-205</sup> Other studies have suggested that spin coherence transfer can also be mediated by exchange coupling between spins.<sup>50</sup> Transfer of nuclear coherences between exchange-coupled nuclei has been observed by nuclear magnetic resonance (NMR) spectroscopy<sup>206-207</sup> and is better studied than the analogous process for electron spins.

To investigate the feasibility of these processes, we have designed and synthesized a photogenerated four-spin system in which a photogenerated radical pair bridges two stable radicals. Such a system is expected to show polarization transfer from the photogenerated radical pair to one or both stable radicals, and may allow coherence transfer between the stable radicals by creating a chain of exchange-coupled spins.

For these studies it is necessary to design a molecule that can form the desired photogenerated radical pair in good yield upon photoexcitation. Several processes have been documented that can compete with the formation of this state. Rapid intersystem crossing (to form an unreactive high spin state) and rapid internal conversion have been reported for excited chromophores bound to stable radicals.<sup>40, 43, 208-210</sup> For this reason, **6.1** was based on a family of donor-chromophore-acceptor molecules in which the 4-amino-1,8-naphthalimide (ANI) chromophore is in the middle of the molecule,<sup>78</sup> distal from the radical attachment points. It is necessary to use two different stable radicals so that the radicals can be distinguished in the EPR experiments. Additionally, to form the desired four-spin system, electron transfer reactions involving the stable radicals must be avoided.  $\alpha,\gamma$ -Bisdiphenylene- $\beta$ -phenylallyl (BDPA $\cdot$ ) and (2,2,6,6-tetramethylpiperidin-1-yl)oxyl (TEMPO $\cdot$ ) were selected as the stable radicals to satisfy these criteria. While the g-factors of BDPA $\cdot$  and TEMPO $\cdot$  are similar, the broad spectrum of TEMPO $\cdot$  allows partially selective manipulation of the spin states of the radicals. Additionally, a BDPA $\cdot$ -TEMPO $\cdot$  biradical has been reported,<sup>211</sup> suggesting that synthesis of this molecule should be tractable. A *meta*-phenylenediamine (mPD) electron donor was selected for its favorable oxidation potential and ease of attachment of BDPA $\cdot$ .<sup>45</sup> The electron transfer reactions to form the radical pair must be faster than the excited state lifetime of the chromophore, and back electron transfer reactions must be slow enough (10s of ns) to allow observation by EPR spectroscopy. In the first attempt to prepare a molecule for this project, a dimethylphenyl bridge was used between ANI and the naphthalenediimide (NDI) electron acceptor to slow recombination (resulting in the donor-acceptor system in **7.1**). However, the intermediate BDPA $\cdot$ -mPD $^{+\cdot}$ -ANI $\cdot$ -NDI state was found to recombine on the picosecond timescale in the

presence of  $\text{BDPA}^\bullet$ ,<sup>45</sup> resulting in a very low yield of  $\text{BDPA}^\bullet\text{-mPD}^{+\bullet}\text{-ANI-NDI}^\bullet$ . To avoid this issue, **6.1** was designed with a direct (hydrazine-bridged) connection between ANI and NDI, which leads to formation of  $\text{mPD-ANI}^{+\bullet}\text{-NDI}^\bullet$  after the first electron transfer step.<sup>75-76</sup>

To understand the effects of the stable radicals and provide negative controls for the coherence transfer experiments, it is also necessary to prepare control molecules containing one or zero stable radicals. The diamagnetic precursor to  $\text{BDPA}^\bullet$ , termed  $\text{BDPAH}$ , was used to construct **5.1a** as the zero-radical control. **5.1b** serves as the  $\text{BDPA}^\bullet$ -only control. Due to synthetic difficulties detailed below, **6.2** utilizes a phenyl group in place of  $\text{BDPAH}$  to provide the  $\text{TEMPO}^\bullet$ -only control.

## 6.2 Experimental

### 6.2.1 Synthesis

The synthesis and characterization of compounds **6.1-6.7** is described in detail in Appendix D. Benzene was distilled before use from  $\text{CaH}_2$  and stored in an  $\text{N}_2$ -filled glovebox. Dry, inhibitor-free THF and dry toluene were used in all other spectroscopic measurements. Compounds **6.2** and **6.4** were purified by preparative thin layer chromatography on  $\text{SiO}_2$  prior to EPR and optical spectroscopy, while **6.1** was prepared from **6.4** purified in this fashion, then eluted through a  $\text{SiO}_2$  plug. Purified **6.2** and **6.4** were stored in the dark in a  $-20^\circ\text{C}$  freezer.

### 6.2.2 Optical Spectroscopy

Ground-state absorption measurements were made on a Shimadzu UV-1800 spectrophotometer. Femtosecond visible transient absorption spectroscopy (fsTA) experiments were conducted using a commercial regeneratively amplified Ti:sapphire laser system (Tsunami oscillator/Spitfire amplifier, Spectra-Physics) described previously.<sup>152</sup> Before interaction with the sample, the probe was split using a neutral density filter so that one portion interacted with the sample and one portion provided a reference spectrum. The pump was sent through a commercial depolarizer (DPU-25-A, Thorlabs, Inc.) to suppress the effects of rotational dynamics and chopped at 500 Hz. The pump was focused to ~0.2-1.0 mm diameter and the probe to ~0.1 mm diameter at the sample. The reference probe and the transmitted probe were coupled into optical fibers and detected using a customized Helios spectrometer and Helios software (Ultrafast Systems, LLC). Nanosecond visible transient absorption spectroscopy (nsTA) experiments were performed using the pump pulse described for the fsTA experiments paired with a photonic crystal fiber ultra-broadband probe generated by a customized EOS spectrometer (Ultrafast Systems, LLC). The samples were irradiated with 1  $\mu$ J pulses centered at 414 nm or 500 nm and the temporal resolution was ~120 fs to ~280 fs in the fsTA experiments and ~600 ps in the nsTA experiments. Visible fsTA spectra were collected for 3-5 s at each pump-probe time delay; nsTA spectra were collected using similar durations. All datasets were background-subtracted to remove scattered pump light and spontaneous emission and corrected for group delay dispersion and time zero using Surface Explorer (Ultrafast Systems, LLC).

### 6.2.3 Analysis of Transient Absorption Data

The kinetic analyses of the fsTA data were performed using home written programs in MATLAB<sup>154</sup> and were based on a global fit of kinetic vectors following singular value decomposition with the solution to a first order kinetic model. The nsTA data was decomposed into basis spectra as described in Chapter 5. Full details of these procedures are reported in Appendix D.

### 6.2.4 EPR Spectroscopy

EPR measurements were made at X-band (~9.5 GHz) using a Bruker Elexsys E680-X/W EPR spectrometer outfitted with a split ring resonator (ER4118X-MS5). Measurements were performed at room temperature or at 85 K using an Oxford Instruments CF935 continuous flow cryostat with liquid N<sub>2</sub>. Sample solutions (optical density between 0.4 and 0.7 in 2 mm cuvette at 416 nm, ~10<sup>-4</sup> M) were loaded into quartz tubes (1.80 mm o.d. × 1.50 mm i.d.), subjected to four freeze–pump–thaw degassing cycles on a vacuum line (10<sup>-4</sup> Torr), and sealed under vacuum using an oxy-hydrogen torch.

Continuous wave (CW) EPR spectra were measured using 0.6 mW microwave power and 0.01 mT field modulation at 100 kHz. Time-resolved EPR measurements were performed following photoexcitation with 7 ns, 1.8 mJ, 416 nm pulses using the output of an optical parametric oscillator (Spectra-Physics Basi-scan), pumped with the output of a frequency-tripled Nd:YAG laser (Spectra-Physics Quanta-Ray Pro 350). Time-resolved EPR measurements were collected using electron spin echo (ESE) detection or transient continuous wave (TCW) detection. For TCW-EPR the transient magnetization following photoexcitation was detected in

quadrature under CW microwave irradiation (2–20 mW), without field modulation. Sweeping the magnetic field gave 2D spectra versus both time and magnetic field. For each kinetic trace, the signal acquired prior to the laser pulse was subtracted from the data. Kinetic traces recorded at magnetic field values off-resonance were considered background signals, whose average was subtracted from all kinetic traces. For ESE detection, a 1 kW TWT amplifier (Applied Systems Engineering 117X) was employed to generate high-power microwave pulses. The resonator was partially overcoupled to maximize echo intensity and minimize ringing following microwave pulses. ESE data was obtained with a  $\pi/2$ - $\tau$ - $\pi$  pulse sequence with  $\pi/2 = 16$  ns,  $\pi = 32$  ns, and  $\tau = 120$  ns. The integrated echo intensity was recorded as a function of the magnetic field to yield the spectrum. If the sample is photoexcited at some time  $t$  prior to the  $\pi/2$ - $\tau$ - $\pi$  pulse sequence, spectra can be collected of the transient species as a function of  $t$ . Double electron-electron resonance (DEER) data was analyzed using DeerAnalysis 2016.<sup>212</sup>

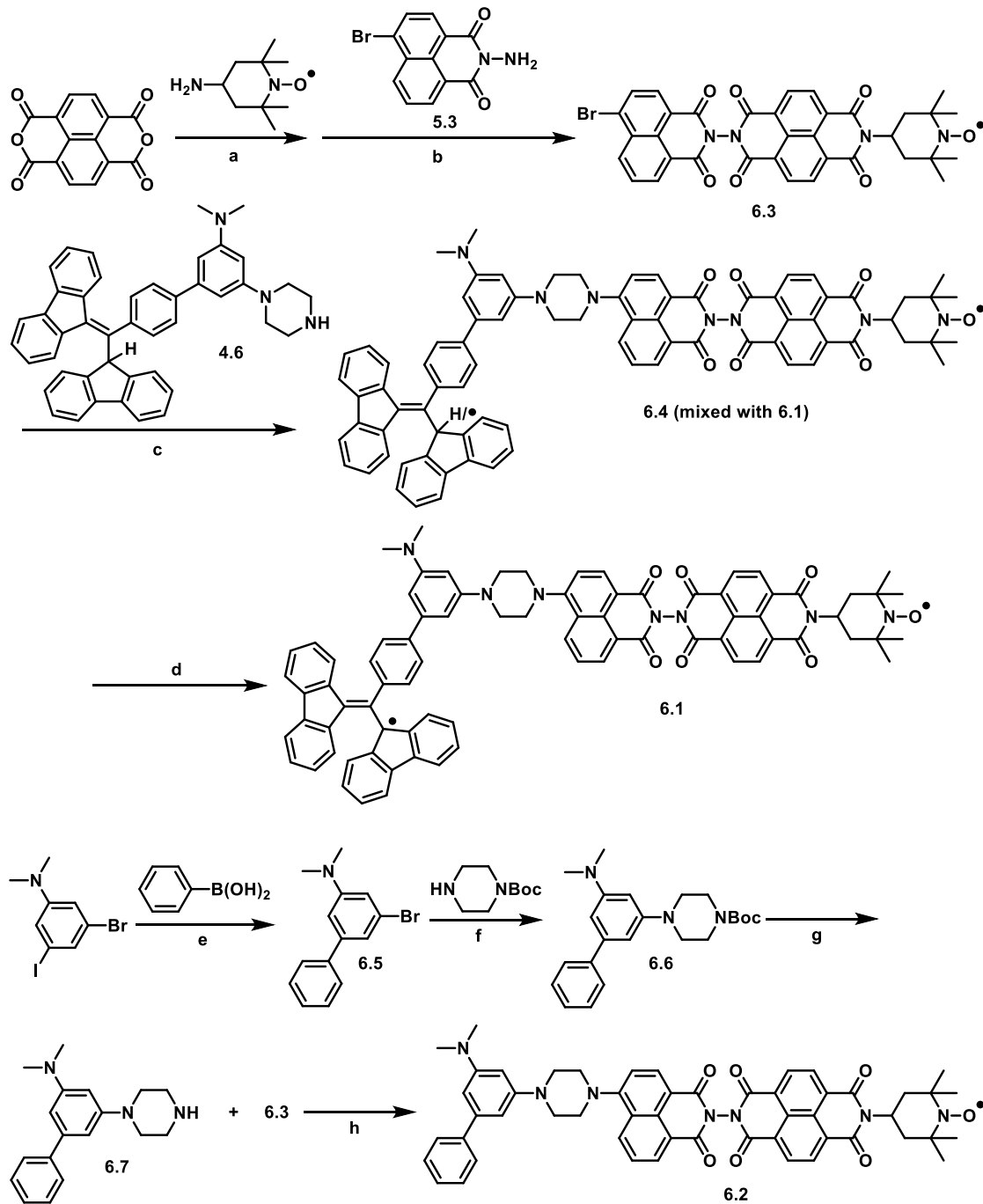


**Figure 6.1.** Synthetic scheme for synthesis of **6.1** and **6.2**. a) DMF, reflux, 19 h, not isolated. b) 2-methoxyethanol, reflux, 18 h, 21%. c) 2-methoxyethanol, reflux, 2 d, ~2%. d) DBU, MnO<sub>2</sub>, THF, 15 min, quant. e) Pd(PPh<sub>3</sub>)<sub>4</sub>, K<sub>2</sub>CO<sub>3</sub>, toluene/EtOH/H<sub>2</sub>O, reflux, 20 h, 67%. f) Pd<sub>2</sub>(dba)<sub>3</sub>, P(tBu)<sub>3</sub>, NaOtBu, toluene, 100 °C, 15 h, 36%. g) 12 M HCl, EtOH, reflux, 100 min, quant. h) 2-methoxyethanol, reflux, 16 h.

## 6.3 Results and Discussion

### 6.3.1 Synthesis

The synthesis of **6.1** and **6.2** is outlined in Figure 6.1. **6.1** and **6.2** were prepared by forming the ANI chromophore as the last step, in a nucleophilic aromatic substitution reaction. This reaction was found to proceed in low yield in molecules containing BDPAH, so this reaction was performed as the final step before BDPA<sup>•</sup> radical generation. The intermediate **6.3** was synthesized via two condensation reactions involving 1,8,4,5-naphthalenetetracarboxylic dianhydride, 4-amino-TEMPO<sup>•</sup>, and **5.3**. Due to the difficulty in characterizing and purifying the TEMPO<sup>•</sup>-naphthalenemonoimide intermediate, this compound was not isolated. Synthesis of **6.4** produced a product that also contained some BDPA<sup>•</sup>. While this contaminant is the final product **6.1**, pure **6.4** is also needed as a control compound. Reduction of this product with sodium dithionite was found to also cause reduction of NDI and TEMPO<sup>•</sup>, including to the parent piperidine. Attempts to selectively photodegrade BDPA<sup>•</sup> using blue light also resulted in substantial degradation when tested on **5.1a** contaminated with **5.1b**. For this reason, **6.2** – containing an inert phenyl group in place of BDPAH – was prepared as the TEMPO<sup>•</sup>-only control compound. **6.7** was prepared analogously to **4.6** and reacted with **6.3** to afford **6.2**.

### 6.3.2 Steady-state characterization

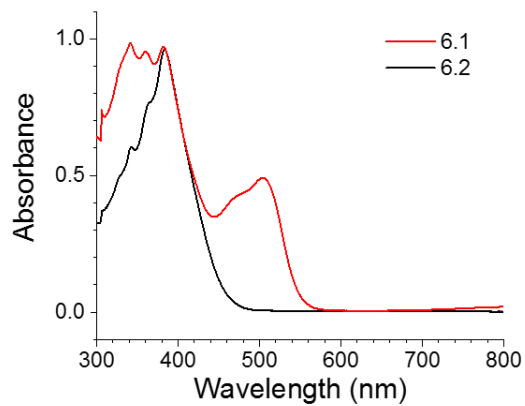


**Figure 6.2.** UV-visible absorption spectra of **6.1** and **6.2** in toluene solution at room temperature.

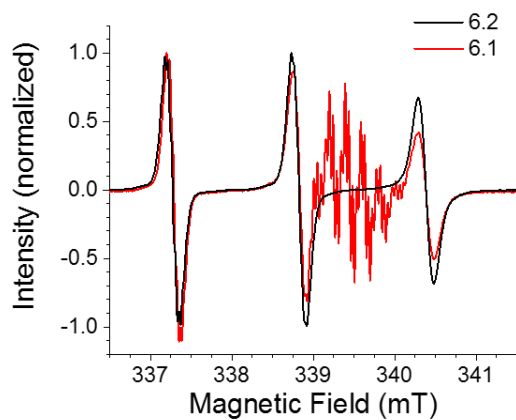


**Figure 6.3.** CW-EPR spectra of **6.2** in benzene and **6.1** in toluene at room temperature.

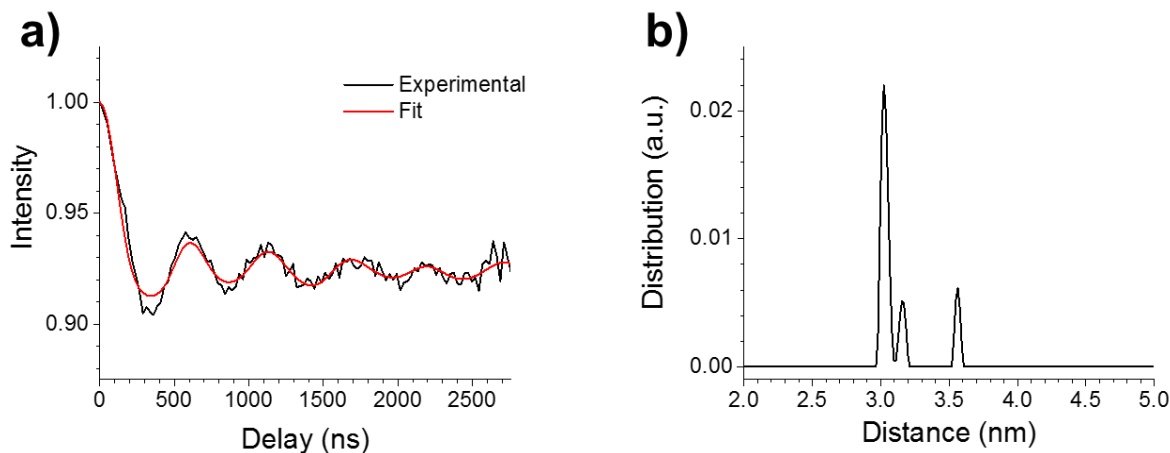


**Figure 6.4.** DEER modulations (a) and fitted distance distribution (b) for **6.1** in toluene at 85 K.

Following synthesis and purification, basic steady-state characterization of these compounds was performed using optical, EPR, and NMR spectroscopies.  $^1\text{H-NMR}$  spectroscopy confirms the presence and purity of  $\text{TEMPO}^\bullet$  in **6.1** and **6.2** through broadening of the NDI proton peaks. The UV-visible-NIR absorption spectrum of **6.2** (Figure 6.2) shows a series of peaks near 380 nm due to NDI, and a shoulder near 400 nm due to ANI. In **6.1**, the same features are present, but there is additional absorption near 350, 500, and 800 nm (not all of this band is visible in Figure 6.2; in other BDPA $^\bullet$  compounds this band peaks near 875 nm) due to BDPA $^\bullet$ . The continuous wave (CW) EPR spectrum of **6.2** shows a signal with three lines, characteristic of  $\text{TEMPO}^\bullet$ . The spectrum of **5.1b** (see Chapter 5) shows a spectrum with more closely spaced lines due to BDPA $^\bullet$ . **6.1** shows both signals, indicating that both BDPA $^\bullet$  and  $\text{TEMPO}^\bullet$  are present (Figure 6.3). Finally, double electron-electron resonance (DEER) EPR was used to confirm the presence of both BDPA $^\bullet$  and  $\text{TEMPO}^\bullet$  on the same molecule in samples of **6.1**. DEER is a pulsed EPR experiment that measures the strength of the dipolar coupling between two stable radicals, providing information on the distance separating them. The DEER

modulations and fitted distance distribution for **6.1** are shown in Figure 6.4. The peak distance of 3.0 nm from DEER is very close to the estimate of 3.2 nm between BDPA and TEMPO from a molecular mechanics simulation of **6.1**. This experiment proves that BDPA and TEMPO are present on the same molecule. While rotation around the bonds between piperazine, mPD, and BDPA can result in an interradsical distance as short as 1.4 nm, the lack of peaks with shorter distances suggests that such conformers are not significant (a small peak with a longer distance of 3.6 nm is not reasonable from the structure and is likely a fitting artifact).

## 6.3.3 Transient absorption spectroscopy

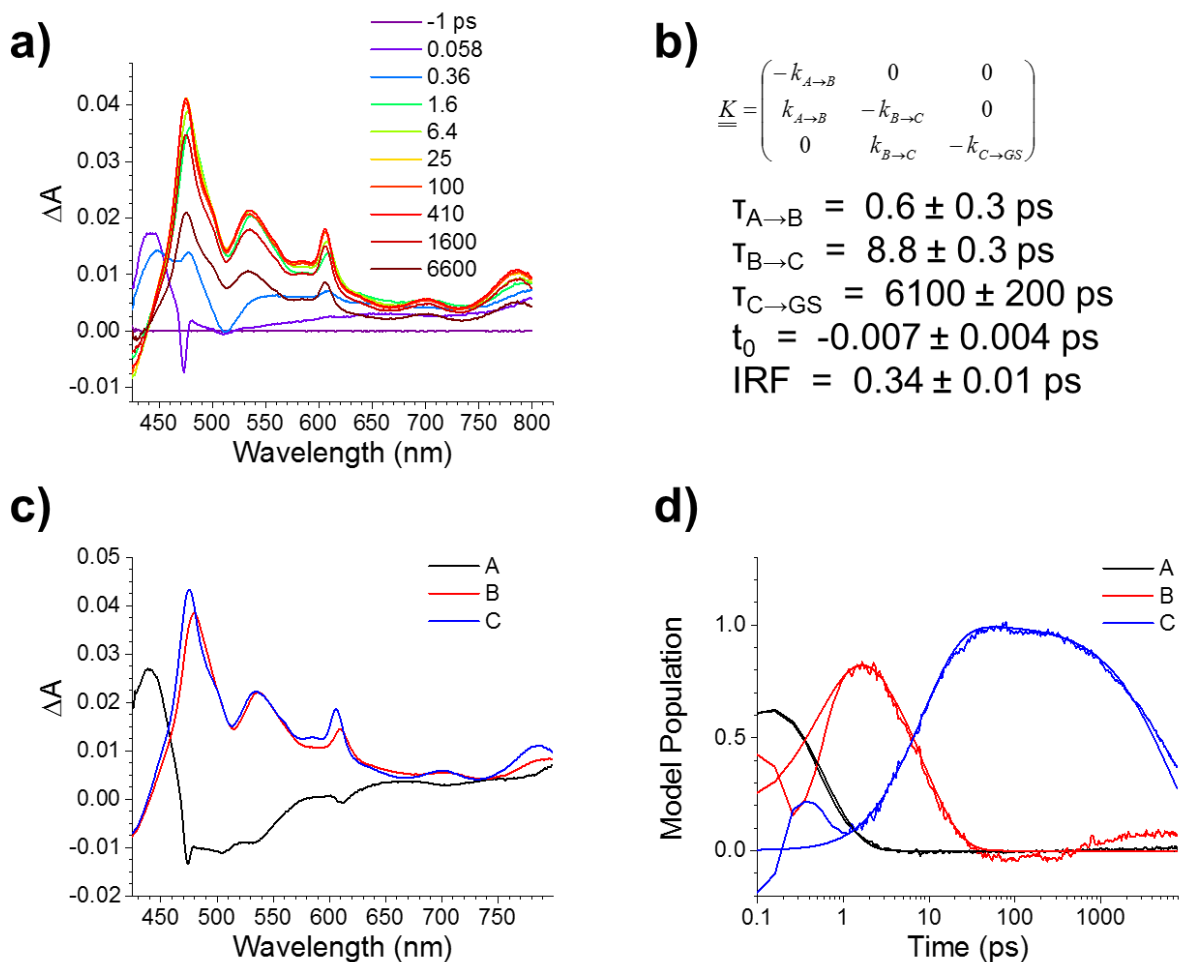


**Figure 6.5.** Femtosecond transient absorption spectra (a) of **6.1** in air-free toluene following excitation at 414 nm. Spectra were fitted to a species-associated kinetic model (b). Species spectra (c) and populations over time (d) are shown.

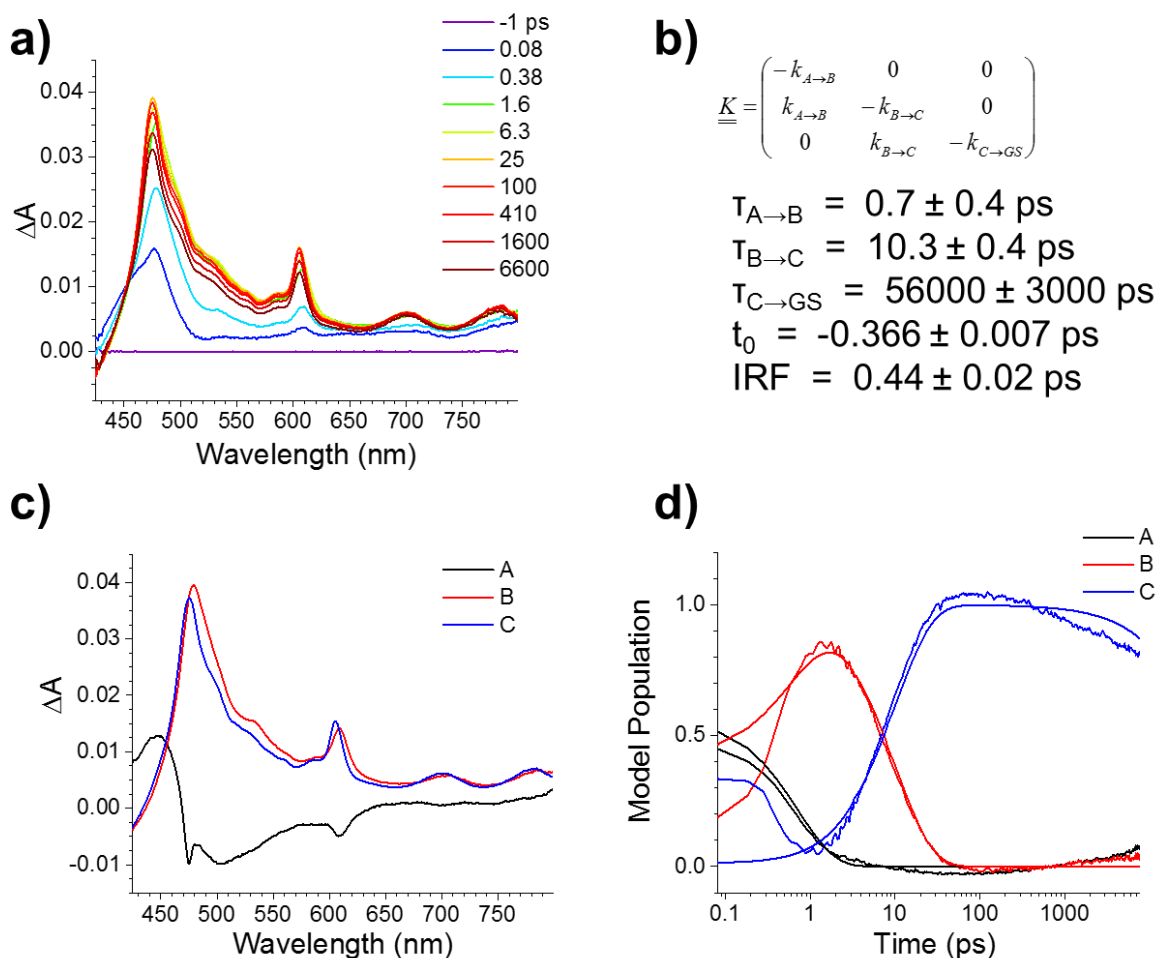


**Figure 6.6.** Femtosecond transient absorption spectra (a) of **6.2** in air-free toluene following excitation at 414 nm. Spectra were fitted to a species-associated kinetic model (b). Species spectra (c) and populations over time (d) are shown.

Transient absorption spectroscopy was used to follow charge separation and recombination electron transfer reactions. The femtosecond transient absorption (fsTA) spectra of **5.1a** and **5.1b** have been previously reported in Chapter 5. The fsTA spectra of **6.1** and **6.2** in toluene at room temperature are presented in Figures 6.5 and 6.6. Similarly to **5.1a** and **5.1b**, **6.1** and **6.2** show subpicosecond formation of new absorption bands near 475, 605, 710, and 790 nm, characteristic for  $\text{NDI}^{\cdot-}$ . In **6.1**, an additional feature grows in at the same rate near 530 nm,

which is assigned to a Stark shift of the BDPA<sup>\*</sup> absorption by analogy to **5.1b**. As with **5.1a**, **5.1b**, and **5.2**, an additional process associated with a slight shift of these absorption features can be fit with a time constant near 10 ps. This process is assigned to structural relaxation in the ANI-NDI unit, probably a rotation around the C-N bond linking the piperazine and naphthalene in ANI. By the end of the 7 ns time window of the fsTA experiment, both **6.1** and **6.2** show some decay of these features, with the decay being faster in **6.1**. Nanosecond transient absorption (nsTA) is used to further investigate this charge recombination process (Figures 6.7a and 6.7b). **6.1** and **6.2** in room temperature toluene behave similarly to **5.1a** and **5.1b**, showing decays that cannot be fit to single exponential functions at single wavelengths, and do not fit well to species-associated kinetic models with one or two intermediates decaying to the ground state. As in **5.1a** and **5.1b** this is likely due to the presence of an equilibrium between the triplet radical ion pair state and a localized triplet state on NDI.

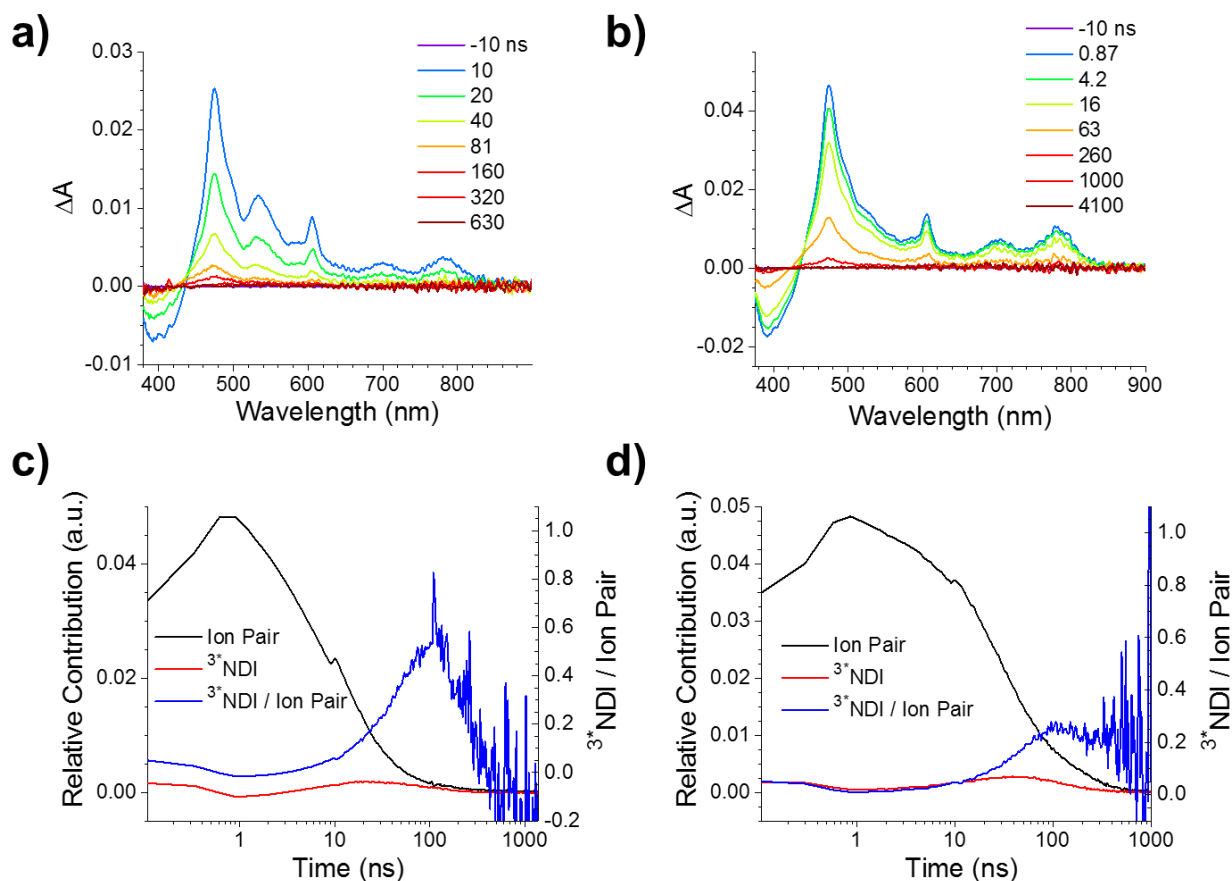


**Figure 6.7.** Nanosecond transient absorption spectra of (a) **6.1** and (b) **6.2** in toluene at room temperature following excitation at 414 nm. Contributions of the ion pair and  $^3\text{NDI}$  in these spectra over time, as derived from basis spectrum fitting, are shown for (c) **6.1** and (d) **6.2**.

To test this explanation, nsTA spectra from **6.1** and **6.2** were fit at each time point to a linear combination of two basis spectra: a reference spectrum of  $^3\text{NDI}$  in **5.2**, and a spectrum of **5.1b** or **5.1a** respectively at 1 ns after the laser pulse, assumed to be the pure radical ion pair spectrum. As with **5.1a** and **5.1b**, these fits reproduce the nsTA data well, and yield contributions of the ion pair and  $^3\text{NDI}$  species as a function of time (Figures 6.7c and 6.7d). Neglecting some fitting artifacts at  $<1$  ns, the  $^3\text{NDI}$  contribution increases as the ion pair contribution decays. In **6.2**, the ratio of these species reaches a relatively constant value as the

remaining transient signal decays. In **6.1**, the ratio decreases during this period, suggesting a stabilization of the ion pair under the equilibrium model. It is not clear why the  $^3\text{NDI}$  contribution decreases more quickly for **6.1** than for **6.2**, but the results for **6.2** at least are consistent with the equilibrium model introduced in Chapter 5.

Because spin relaxation typically becomes faster with higher temperature, the transient absorption experiments were also performed in butyronitrile (PrCN) at 105 K. At this temperature, PrCN is a very viscous liquid that can be treated as a solid on the timescales relevant to nsTA and EPR spectroscopy.<sup>213</sup> In frozen solids, solvent molecules are not able to reorient to stabilize ions, and there are often conformational changes in solute molecules; thus, electron transfer dynamics often differ from those at room temperature. The fsTA and nsTA spectra of **6.1** in PrCN at 105 K are presented in Figure 6.8. Overall, the fsTA and nsTA data are similar to the data at room temperature, but additional features are present. Most notably, there is additional absorption near 600-650 nm that does not correspond to any species observed at room temperature. This absorption persists into the microsecond regime in the nsTA data, and following TA experiments, a permanent blue spot is observed on the sample. The most likely species that accounts for this absorption is the  $\text{BPDA}^-$  anion, which can form by one-electron reduction of  $\text{BDPA}^\bullet$  and is known to absorb in this range.<sup>214</sup> The observation of  $\text{BPDA}^-$  in this system is unexpected, as the reducing part of **6.1** (NDI) is distant from  $\text{BDPA}^\bullet$ . It is therefore likely that this observation indicates aggregation of **6.1** upon freezing, with some clusters of molecules exhibiting stacking of  $\text{BDPA}^\bullet$  and NDI or ANI. The observed broadening of the  $\text{NDI}^\bullet$  peak near 480 nm is also consistent with interaction of NDI with another part of the molecule due to aggregation. This aggregation, combined with the apparent involvement of

BDPA<sup>•</sup> in the photoinduced redox reactions, renders **6.1** unsuitable for coherence transfer experiments at low temperature. For this reason, the EPR experiments in this chapter are all conducted at 295 K in liquid solution.

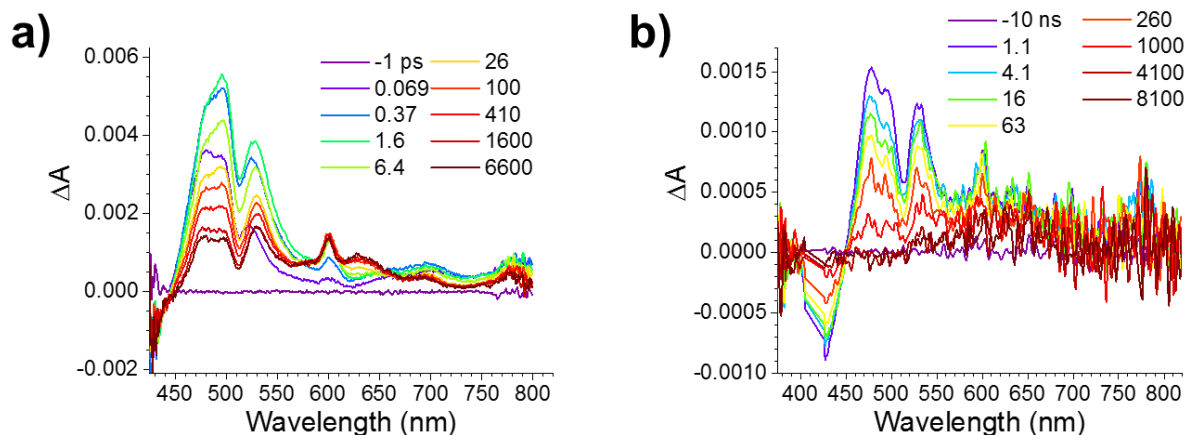


**Figure 6.8.** fsTA (a) and nsTA (b) spectra of **6.1** in PrCN at 105 K, following excitation at 414 nm. A Savitsky-Golay filter with a 5 nm window has been applied to the nsTA data in the wavelength domain.

### 6.3.4 EPR spectroscopy: polarization transfer and spin relaxation

Time-resolved EPR spectroscopy was performed on **6.1** and **6.2** in room temperature toluene. **6.2** shows very strong negative polarization of TEMPO<sup>•</sup> following photoexcitation, similar to a close analogue reported previously.<sup>130-131</sup> **6.1** shows negative polarization of both TEMPO<sup>•</sup> and BDPA<sup>•</sup>, in contrast to **5.1b** in toluene, where positive polarization of BDPA<sup>•</sup> is initially observed (Figure 6.9). This suggests that the presence of TEMPO<sup>•</sup> is somehow altering the spin dynamics of **6.1** as compared to **5.1b**.

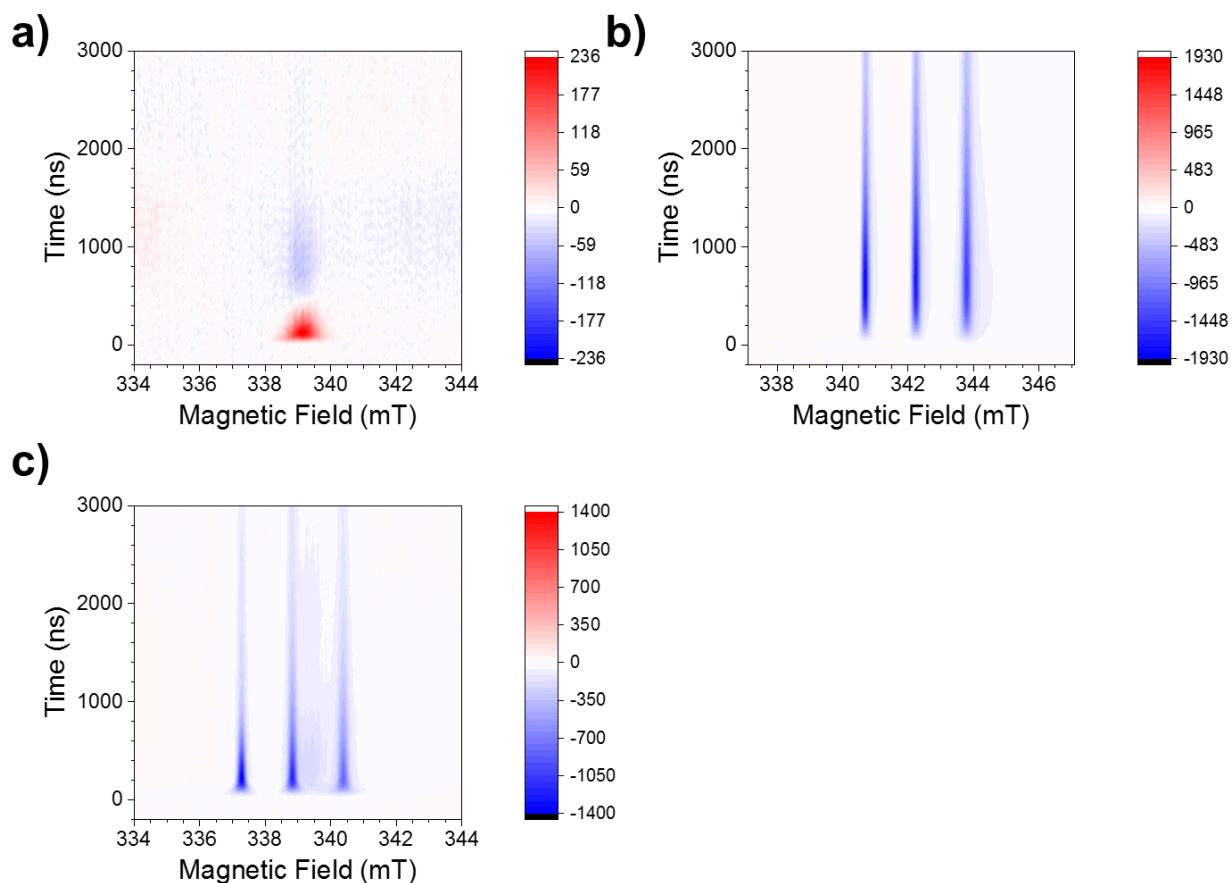


**Figure 6.9.** Contour plots showing time-resolved EPR signals from (a) **5.1b** in toluene, (b) **6.2** in benzene, and (c) **6.1** in toluene, all at room temperature following 416 nm excitation.

There are several mechanisms by which TEMPO<sup>•</sup> could be affecting the spin state of BDPA<sup>•</sup> following photoexcitation. Firstly, the polarization of BDPA<sup>•</sup> in **5.1b** was observed to change from positive to negative when the solvent was made slightly more polar, an effect attributed to a lowering of the radical ion pair energy. In addition to containing an unpaired spin, TEMPO<sup>•</sup> also has a strong dipole moment associated with the N-O bond.<sup>215</sup> One possibility is that TEMPO<sup>•</sup> is slightly lowering the ion pair energy, mimicking the effect of a more polar solvent. This mechanism is supported by the nsTA data. In **5.1a**, as the solvent polarity was increased, the contribution of <sup>3</sup>\*NDI to the spectrum decreased. In **6.2** in toluene, this

contribution was more similar in magnitude to that of **5.1a** in 10% fluorobenzene/benzene as compared to pure benzene. Likewise, the maximum value of the  $^{3*}\text{NDI}/\text{ion}$  pair ratio in **6.1** in toluene was similar to that of **5.1b** in 10% fluorobenzene/benzene. While some of this difference likely results from the slightly higher dielectric constant of toluene ( $\epsilon = 2.38$ ) versus benzene ( $\epsilon = 2.27$ ), the presence of TEMPO $\cdot$  likely decreases the ion pair energy by a small amount in **6.1** and **6.2**.

An additional possibility is that the strong, negative polarization of TEMPO $\cdot$  is inducing negative polarization of BDPA $\cdot$  through a cross-relaxation mechanism. Cross-relaxation involves mutual spin flips of coupled (electron or nuclear) spins and leads to equilibration of polarization between the spins.<sup>216-218</sup> The cross-relaxation mechanism can be probed in **6.1** in the absence of photoexcitation by using a  $\pi$  microwave pulse to selectively induce negative polarization in TEMPO $\cdot$ . In this experiment, a  $\pi$ -pulse is applied to the sample, and after some delay, a Hahn echo sequence is applied to read out the BDPA $\cdot$  polarization. The frequency of the microwave pulses in the Hahn echo sequence is fixed to the resonant frequency of BDPA $\cdot$  at a fixed magnetic field position, while the initial  $\pi$ -pulse is applied at a variable frequency. When the initial  $\pi$ -pulse is also resonant with BDPA $\cdot$ , a negative polarization is observed that decays as the delay is increased, as expected. When the  $\pi$ -pulse is resonant with TEMPO $\cdot$  instead, the BDPA $\cdot$  signal does not become negative, but does show a loss over about 2  $\mu\text{s}$  followed by a slow recovery (Figure 6.10; a weak background signal with the  $\pi$ -pulse not resonant with either radical was subtracted from this data). This is consistent with cross-relaxation between the two radicals on the microsecond timescale, but some caution is warranted due to the overlap of the BDPA $\cdot$  signal with two of the TEMPO $\cdot$  lines. If the  $^{14}\text{N}$  nuclear  $T_1$  relaxation is fast enough,

these lines will also show a loss of signal following inversion of the other TEMPO<sup>•</sup> line. Indeed, Enkin et al. show that this relaxation occurs on the microsecond timescale in several nitroxides and produces similar kinetics to those in Figure 6.10 when one nitroxide line is inverted.<sup>219</sup> Therefore, additional experiments are necessary to prove electron-electron cross-relaxation in **6.1**.

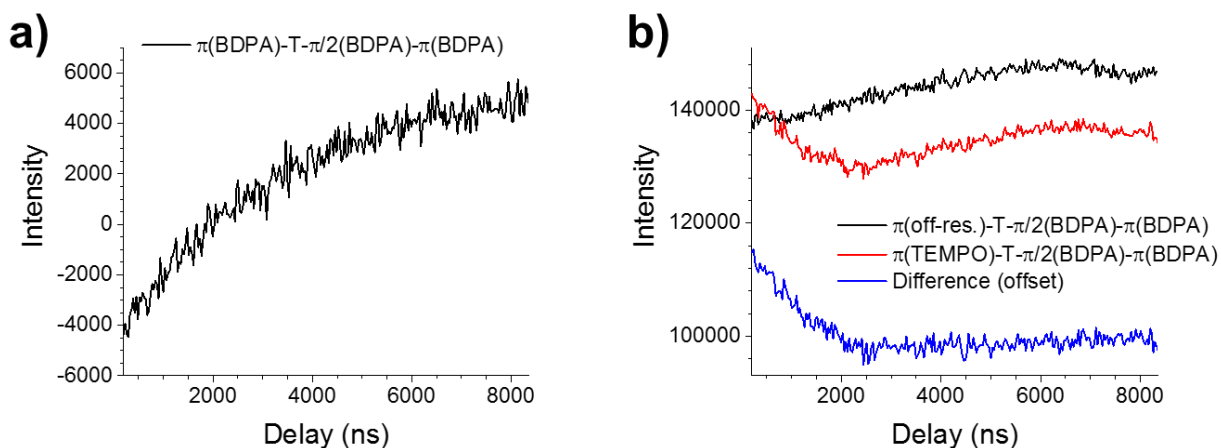


**Figure 6.10.** Changes in the spin echo EPR signal from BDPA<sup>•</sup> following inversion of (a) BDPA<sup>•</sup> or (b) one hyperfine line of TEMPO<sup>•</sup>.

Further support for the presence of cross-relaxation in **6.1** comes from measurements of the  $T_1$  (spin-lattice) relaxation times of **6.1**, **6.2**, and **5.1b**, performed by a saturation recovery EPR experiment (Table 6.1). In **5.1b**, the BDPA<sup>•</sup>  $T_1$  relaxation time is 76  $\mu\text{s}$  as measured in toluene at room temperature. In contrast, in **6.1**, this time shortens to only 5.2  $\mu\text{s}$  under the same conditions. The  $T_1$  values for TEMPO<sup>•</sup> also shorten from 1120 ns in **6.2** to 910 ns in **6.1**. Under the assumption that cross-relaxation is the only source of additional relaxation in **6.1** compared to **6.2** and **5.1b**, the time constant of the cross-relaxation process can be estimated from these values: the relaxation rate in **6.1** should be the sum of the cross-relaxation rate and the intrinsic

relaxation rate obtained from **6.2** or **5.1b**. As expected, the cross-relaxation time constant obtained using the BDPA<sup>•</sup> T<sub>1</sub> is equal to that obtained using TEMPO<sup>•</sup>, within the error of the measurement.

Compound	Radical	Time constant (μs)
<b>5.1b</b>	BDPA <sup>•</sup>	76 ± 1
<b>6.2</b>	TEMPO <sup>•</sup>	1.12 ± 0.06
<b>6.1</b>	BDPA <sup>•</sup>	5.2 ± 0.2
<b>6.1</b>	TEMPO <sup>•</sup>	0.91 ± 0.07
Cross-relaxation time constant from BDPA <sup>•</sup> data		5.6 ± 0.2
Cross-relaxation time constant from TEMPO <sup>•</sup> data		5 ± 2

**Table 6.1.** T<sub>1</sub> relaxation time constants and extrapolated cross-relaxation time constants for ~10<sup>-4</sup> M solutions of **5.1b**, **6.2**, and **6.1** in toluene at room temperature.

While the above results show cross-relaxation is contributing to the polarization of BDPA<sup>•</sup> in **6.1** at late times, it is also possible that TEMPO<sup>•</sup> may be perturbing the spin state of the radical ion pair and directly affecting polarization transfer to BDPA<sup>•</sup> from the radical ion pair. Any such effects are more difficult to discuss, as there is little theory on such four-spin systems. The difficulty of measuring the exchange coupling between mPD<sup>•</sup> and BDPA<sup>•</sup> also prevents a quantitative simulation of this system.

### 6.3.5 EPR spectroscopy: coherence transfer experiments

Despite the complexity of these molecules, some simple coherence transfer experiments were performed with the aim of transferring a spin coherence from BDPA<sup>•</sup> to TEMPO<sup>•</sup> or vice versa. In this experiment, a π/2-pulse is applied at a fixed frequency resonant with one of the radicals, which produces a spin coherence. The sample is then photoexcited immediately after this pulse, and after some delay τ, a π-pulse is applied. The frequency of the π-pulse is swept across the spectrum. In the absence of coherence transfer, a spin echo is only expected when the

two pulses excite the same population of the same radicals. For samples in liquid solution, different hyperfine lines are due to populations with different nuclear spin states, which interconvert slowly relative to  $\tau$ . Therefore, when a selective  $\pi/2$ -pulse is applied to one line of TEMPO $\cdot$ , only a single, narrow line is expected instead of the three-line EPR spectrum of TEMPO $\cdot$ . If instead, coherence is transferred to the radical excited by the  $\pi$ -pulse after photoexcitation of the molecule, a spin echo will be observed. These experiments were performed on **6.1** in room temperature toluene with the initial  $\pi/2$ -pulse applied to both BDPA $\cdot$  and TEMPO $\cdot$ , both with and without a laser pulse to photoexcite the sample (Figure 6.11). While the expected spin echo signal is seen when the frequencies of the  $\pi/2$ - and  $\pi$ -pulses are coincident, in all cases no other features are observed. When exciting a coherence on TEMPO $\cdot$ , a signal from BDPA $\cdot$  is expected at 9676 MHz from the field-swept spin echo spectrum (Figure 6.11), but no feature is observed at this frequency. Likewise when exciting a coherence on BDPA $\cdot$ , signals from TEMPO $\cdot$  would be expected at 9800, 9757, and 9713 MHz, and again, no such features are observed. The only difference seen with photoexcitation of the sample is a loss of the signal when exciting TEMPO $\cdot$ , consistent with the negative polarization transfer described previously.

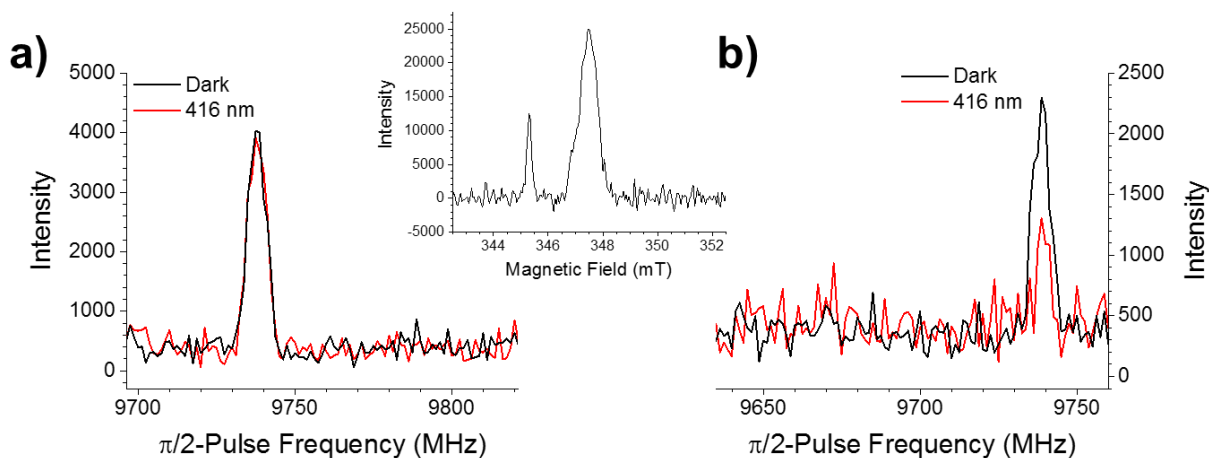


**Figure 6.11.** Results of coherence transfer experiment performed with (a)  $\pi/2$ -pulse resonant with BDPA $\cdot$  or (b)  $\pi/2$ -pulse resonant with TEMPO $\cdot$ . Inset: field-swept spin echo detected spectrum of **6.1** in toluene, collected with the selective microwave pulses used for the coherence transfer experiment.

## 6.4 Conclusions

We have prepared a molecule in which an electron donor-acceptor system bridges two stable radicals, BDPA $\cdot$  and TEMPO $\cdot$ . Upon photoexcitation, electron transfer reactions in the donor-acceptor system create a pair of additional radicals, yielding a four-spin system. To the best of our knowledge, this is the first example of a photogenerated radical pair coupled to two additional stable radicals. EPR spectroscopy reveals polarization transfer from the photogenerated radical ion pair to both of the coupled radicals, with the direction of polarization to BDPA $\cdot$  differing from a control containing only BDPA $\cdot$  and the donor-acceptor system. Additional EPR experiments provide evidence for cross-relaxation between BDPA $\cdot$  and TEMPO $\cdot$ , providing a mechanism for the strong, negative polarization of TEMPO $\cdot$  to be transferred to BDPA $\cdot$  after recombination of the radical ion pair. This cross-relaxation process is

both a process that can be exploited and a potential limitation when developing multi-spin systems for spintronics applications. It is unclear if the polarization transfer can be understood by considering the influence of each stable radical separately, or if the dynamics of the overall four-spin system are important, and this highlights the need for additional theoretical studies to understand these four-spin systems. EPR experiments were also performed to look for spin coherence transfer between BDPA<sup>•</sup> and TEMPO<sup>•</sup>, which was not observed. The use of more complex pulse sequences for coherence transfer, as described in the NMR literature,<sup>207</sup> may offer some advantages over the simple experiment performed here, but these experiments are limited by the short lifetime of the photogenerated radical pair in **6.1**. Again, more theoretical investigations of these systems can help clarify what interactions between radicals can enable coherence transfer, and what EPR experiments are best to detect this transfer. For such simulations, it is necessary to know the value of the magnetic coupling constants between all four of the radicals. In the present system, the instability of the electron donor radical cation prevents measurement of the interaction between mPD<sup>•+</sup> and BDPA<sup>•</sup>. To simplify comparisons to theoretical models, future studies should focus on molecules in which all of the relevant exchange and dipolar interactions between electron spins can be measured.

## CHAPTER 7

# Fast Measurement of Radical Pair Spin States by Stimulated Back Electron Transfer

## 7.1 Introduction

### 7.1.1 Motivation and Background

Photoinduced electron transfer reactions generate pairs of radicals in unique, coherent spin states. These coherent spin states have attracted interest for their potential applications in quantum information processing,<sup>204-205, 220</sup> as well as their importance in natural photosynthesis<sup>14</sup> and sensing of magnetic fields by living organisms.<sup>11</sup> In radical pairs (RPs) with weak coupling between the two radicals, this initial state contains a coherent superposition between the singlet state and one of the triplet states. This zero quantum coherence (ZQC) may be useful as a qubit for quantum information processing, and its frequency contains information about the magnetic environment of the radicals. Before ZQCs can be exploited for these applications, more work is needed to understand and optimize the factors that influence their lifetimes. For these studies, it is necessary to be able to detect the ZQC formed after photoexcitation of a system.

The ZQC manifests as an oscillation in the singlet and triplet character of the RP with time. Detection of RP spin states is difficult, as the singlet and triplet radical pairs are indistinguishable optically and the ZQCs do not give rise to electron paramagnetic resonance (EPR) signals. Detection techniques therefore rely on transferring these states to a detectable product. For EPR detection, microwave irradiation is used to transfer the ZQC to a single quantum coherence detectable by EPR. This technique has been applied successfully to detect ZQCs in several systems, using both continuous (CW) and pulsed microwave radiation.<sup>71, 221</sup> However, EPR detection has a number of limitations. The time resolution is limited by the resonator time constant in CW techniques or the length of the pulse sequence when using pulsed

microwave radiation, both on the order of tens of ns in a typical EPR spectrometer.

Additionally, the microwave radiation can excite single quantum coherences even after the ZQC has dephased, and CW microwaves induce Torrey oscillations,<sup>222</sup> leading to background signals that complicate detection of the ZQC.

Optical RP spin measurement techniques involve detection of singlet or triplet products following recombination of the RP, making them a form of reaction-yield detected magnetic resonance (RYDMR). Studies of optical detection of RP spin states have mostly examined systems in which the RP recombines to a singlet excited state, which can be detected via fluorescence. The requirement that the RP energy lies above the lowest singlet excited state excludes almost all fixed-geometry photogenerated RPs, systems that allow precise synthetic tuning of magnetic coupling constants between the radicals.<sup>47, 75</sup> Such tuning is important for studying the effect of these parameters on ZQC frequency and lifetime. As a result, optical techniques have mostly been applied to RPs in which the electron donor and acceptor diffuse freely in solution (where an increase in entropy drives formation of enthalpically-unfavorable RPs), or those generated using ionizing radiation. Despite this limitation, optical techniques provide low-background detection with high time resolution, which is limited by the fluorescence lifetime (typically several ns). Murai and coworkers have been able to detect Torrey oscillations induced by continuous microwave irradiation by monitoring the optical absorption or the fluorescence of a RP recombination product.<sup>223-225</sup> Batchelor et al. have reported oscillations in the fluorescence signal resulting from RP recombination, attributed to the ZQC.<sup>226</sup> Molin et al. have performed similar experiments on RPs generated by pulsed radiolysis, and characterized the effect of hyperfine coupling and g-factor difference on the observed ZQC

frequencies.<sup>227-228</sup> In a separate publication, Molin and Salikhov suggest that the exchange coupling between the radicals should also affect the ZQC, but they note that measurement of these effects are not possible in RPs without a fixed distance and fixed exchange coupling.<sup>229</sup> As described above, this requirement precludes the use of optical spin measurement techniques for these studies, necessitating the use of EPR or alternative optical detection schemes.

### 7.1.2 Proposed Spin Measurement Scheme

In this study, we propose a new RYDMR-based technique in which a second laser pulse is used to stimulate formation of singlet and triplet products from the radical pair through photoinduced electron transfer reactions. The formation of products is thereby gated by the timing of the second laser pulse, allowing the time for radical pair spin evolution to be separated from the timescale of detection. Instead of being limited by the timescale of the detection method – such as a fluorescence lifetime or the time resolution of an EPR spectrometer – the time resolution of the spin measurement is now limited by the laser pulse length and the rates of the photoinduced electron transfer reactions, which can easily reach the picosecond timescale.

Photoinduced electron transfer reactions following a second laser pulse have been applied previously to the detection of ZQC in an RP. In the “J-jump” experiment, a first laser pulse produces an RP with strong exchange coupling that is EPR silent. A second laser pulse excites the radical anion in this RP, triggering electron transfer to a more distant acceptor and forming a weakly coupled RP that is EPR active. The intensity of the EPR signal following the second laser pulse was found to decay quickly with the delay between the laser pulses, an effect attributed to the decay of the ZQC.<sup>145, 230</sup> These experiments highlight the ability of

photoinduced electron transfer reactions to probe spin states without significant perturbation, however, this scheme can only probe the ZQC in the strongly coupled RP formed after the first laser pulse. Many of the RPs of interest for photosynthesis and biological compasses are much more weakly coupled, and show more pronounced oscillations due to the ZQC.

Here we focus specifically on detecting a triplet recombination product arising from weakly coupled RPs in the triplet state. If the RP energy is kept below that of the lowest energy triplet state, then spontaneous recombination to the triplet product can be prevented, allowing this process to be gated by the second laser pulse through formation of a higher energy intermediate. Because direct recombination through the triplet channel of weakly coupled radical pairs is typically on the nanosecond timescale when energetically accessible,<sup>231</sup> it cannot compete with the short excited state lifetimes typical of radical ions.<sup>58</sup> In the proposed scheme, following spin evolution in the weakly coupled RP, the second laser pulse instead triggers a back electron transfer to form a more strongly coupled RP in which recombination to the triplet product is rapid. Since the second laser pulse should not affect the spin state of the transferred electron, and since spin evolution is slow in the strongly coupled intermediate RP, the spin state of the weakly coupled RP at the time of the second pulse should be preserved in the strongly coupled RP. The yield of triplet product following the second pulse should therefore correlate to the population of the triplet states in the weakly coupled RP.

While this scheme can potentially provide much greater time resolution than other RP spin measurement techniques, it is initially proposed only for systems meeting a narrow set of criteria. A triad of electron donor/acceptors capable of undergoing two-step photoinduced electron transfer is required. The energy of the initially formed RP must be above that of the

lowest triplet excited state in the molecule, and that of the final RP must be below this energy. At least one of the radicals in the final RP must have a strong absorption distinct from the ground state molecule. Following excitation of this radical, electron or hole transfer must proceed quickly relative to the spin evolution to form the initial RP. Finally, the initial RP in its triplet state must recombine quickly to a local triplet excited state.

### 7.1.3 Molecules Used in this Study

To test this concept, we have prepared three donor-chromophore-acceptor triads (Figure 7.1) that are predicted to meet the energetic and kinetic requirements outlined above. 1,4,5,8-Naphthalenediimide (NDI) is selected as the terminal electron acceptor on the basis of the strong absorption and relatively long excited state lifetime of its radical anion,<sup>58</sup> allowing electron transfer from this state to be competitive with excited state decay. A well-characterized donor-chromophore-acceptor triad utilizing NDI along with an 4-amino-1,8-naphthalimide (ANI) chromophore and an *N*-alkylated 4-methoxyaniline electron donor almost meets the energetic requirements detailed previously. Electron paramagnetic resonance (EPR) and transient optical absorption (TA) measurements indicate that in liquid toluene, the final RP is in equilibrium with the lowest excited triplet state in the molecule, localized to NDI.<sup>78</sup> Lowering the energy of this radical ion pair state by switching to a more polar solvent or substituting the electron donor with a more easily oxidized moiety should lower the final ion pair energy sufficiently to prevent recombination of this state to  $^3\text{*NDI}$  or  $^3\text{*ANI}$ .

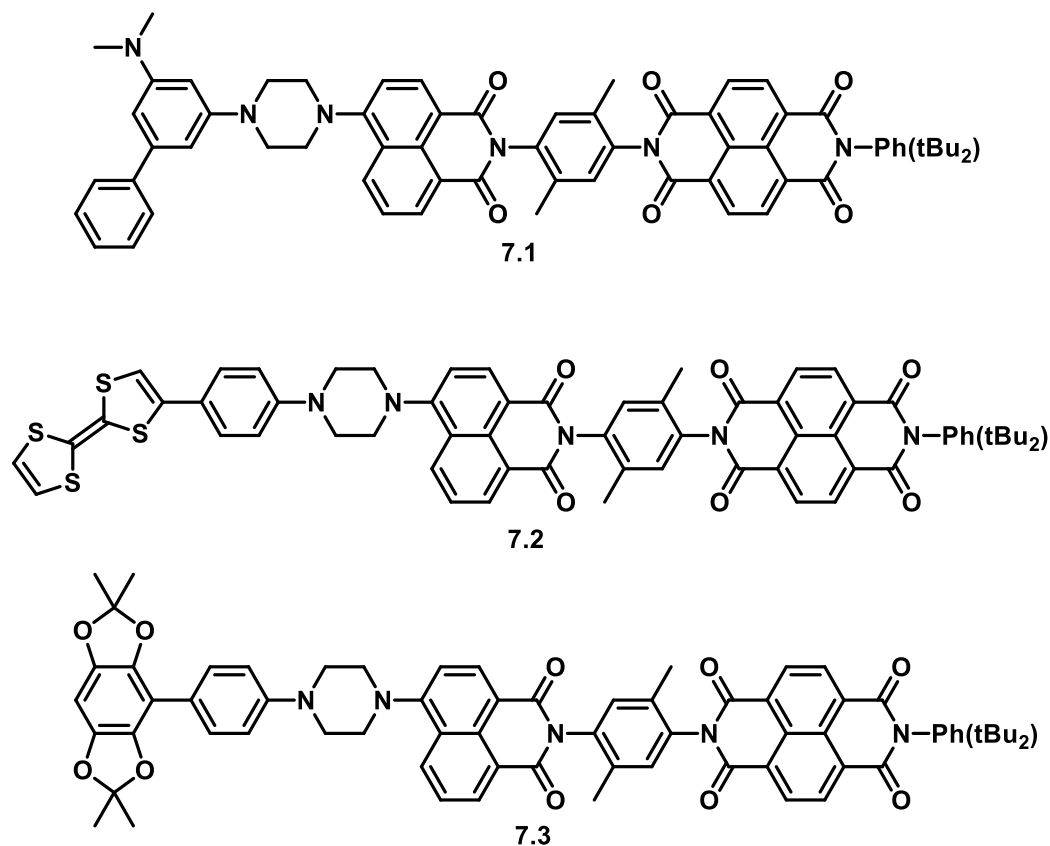


**Figure 7.1.** Molecules 7.1, 7.2, and 7.3 used in this study.

EPR and phosphorescence detection of triplet states are facilitated by working in a solid matrix, where polar solvents cannot reorient to solvate ion pair states. For this reason, we have chosen to focus on introducing stronger electron donors instead of solely changing the solvent used for these experiments. Three electron donors (D) were selected for this study: an alkylated *meta*-phenylenediamine (mPD) derivative,<sup>45</sup> tetrathiafulvalene (TTF), and 2,2,6,6-tetramethylbenzo[1,2-d:4,5-d']bis([1,3]dioxole) (BDX), with TTF and BDX connected through an aniline linker.<sup>70</sup> The radical cations of these donors have different magnetic properties, with  $\text{TTF}^{\cdot+}$  having a large isotropic g-factor of 2.0072 and a highly anisotropic g-factor in solid samples,<sup>232</sup> unusual for an organic radical. While the radical cation of mPD is unstable, it is

expected to be similar to that of N,N,N',N'-tetramethyl-*para*-phenylenediamine, which has an isotropic g-factor of 2.0034.<sup>233</sup> BDX<sup>+</sup> has an isotropic g-factor of 2.0040, and has limited hyperfine interactions, expected to result in a smaller range of ZQC frequencies.<sup>160</sup> In this study, we first characterize the formation of RPs in **7.1-7.3** following excitation of ANI by a single laser pulse, using transient absorption (TA) spectroscopy and time-resolved electron paramagnetic resonance (EPR) spectroscopy. We then model and investigate the formation of a triplet recombination product following excitation of NDI<sup>-</sup> by a second laser pulse. Finally, we examine the yield of this triplet state versus the separation in time between the two laser pulses to attempt to measure the ZQC in **7.1-7.3**. Time-resolved EPR and phosphorescence spectroscopies are used to detect the triplet recombination product.

## 7.2 Experimental

### 7.2.1 Synthesis

Detailed synthetic procedures for preparation of **7.1** are given in Appendix B. The synthesis of **7.2** and **7.3** has been reported previously.<sup>47, 71</sup> Dry toluene and dichloromethane (DCM) for optical and EPR experiments were obtained from a Glass Contour solvent dispensing system. Butyronitrile (PrCN) was treated with HCl, distilled from K<sub>2</sub>CO<sub>3</sub>, and dried over Al<sub>2</sub>O<sub>3</sub> as described by Armarego and Chai.<sup>66</sup> Fluorobenzene was treated with P<sub>2</sub>O<sub>5</sub> and distilled as described by Armarego and Chai.<sup>66</sup>

### 7.2.2 Optical Absorption Spectroscopy

Ground-state absorption measurements were made on a Shimadzu UV-1601 spectrophotometer. Femtosecond visible transient absorption spectroscopy (fsTA) experiments were conducted using a commercial regeneratively amplified Ti:sapphire laser system (Tsunami oscillator/Spitfire amplifier, Spectra-Physics) described previously.<sup>234</sup> Before interaction with the sample, the probe was split using a neutral density filter so that one portion interacted with the sample and one portion provided a reference spectrum. The pump was sent through a commercial depolarizer (DPU-25-A, Thorlabs, Inc.) to suppress the effects of rotational dynamics and chopped at 500 Hz. The pump was focused to ~0.2-1.0 mm diameter and the probe to ~0.1 mm diameter at the sample. The reference probe and the transmitted probe were coupled into optical fibers and detected using a customized Helios spectrometer and Helios software (Ultrafast Systems, LLC). Nanosecond visible transient absorption spectroscopy (nsTA) experiments were performed using the pump pulse described for the fsTA experiments paired with a photonic crystal fiber ultra-broadband probe generated by a customized EOS spectrometer (Ultrafast Systems, LLC).

Samples for fsTA and nsTA at room temperature were prepared with an optical density between 0.4 and 0.7 at 414 nm in 2 mm quartz cuvettes fused to a quartz bulb for degassing. Samples were subjected to four freeze–pump–thaw degassing cycles on a vacuum line ( $10^{-4}$  Torr) and sealed under vacuum. Samples for low temperature fsTA and nsTA were prepared as dichloromethane solutions with an optical density between 0.4 and 0.7 at 414 nm in 2 mm quartz cuvettes. The dichloromethane was evaporated and the samples reconstituted with an equal volume of PrCN in an N<sub>2</sub>-filled glovebox. The resulting solutions were loaded into an optical

sample cell consisting of two quartz windows separated by a 2 mm PTFE spacer, and the cell was sealed under N<sub>2</sub>. Low temperature transient absorption measurements were performed using a Janis VNF-100 cryostat and a Cryo-Con 32B temperature controller. Low temperature samples in PrCN were cooled rapidly to 77 K by flooding the cryostat with liquid N<sub>2</sub> to produce a cracked glass. Samples were then annealed at 120 K to remove cracks and cooled to 105 K (further cooling past the glass transition temperature of 95 K caused the solvent to crack again, precluding optical measurements). At 105 K, PrCN is a very viscous supercooled liquid with a dielectric relaxation time of approximately 10 ms.<sup>213</sup> Since the timescale of solvent motion at this temperature is much longer than that of the photoinduced processes observed here, PrCN at 105 K can be treated as a solid for the purposes of this study.

The samples were irradiated with 1  $\mu$ J pulses centered at 414 nm or 500 nm and the temporal resolution was  $\sim$ 120 fs to  $\sim$ 280 fs in the fsTA experiments and  $\sim$ 600 ps in the nsTA experiments. Visible fsTA spectra were collected for 3-5 s at each pump-probe time delay; nsTA spectra were collected using similar durations. All datasets were background-subtracted to remove scattered pump light and spontaneous emission and corrected for group delay dispersion and time zero using Surface Explorer (Ultrafast Systems, LLC).

Singular Value Decomposition(SVD) analysis of transient absorption spectra was performed in Matlab<sup>154</sup> using home written programs. The 2-dimensional spectra were deconvoluted by SVD to produce an orthonormal set of basis spectra which describe the wavelength dependence of the species and a corresponding set of orthogonal vectors which describes the time dependent amplitude of the basis spectra.<sup>155</sup> A species associated first order kinetic model<sup>156</sup> was fit to a linear combination of the time dependent amplitude vectors and the

same linear combination of basis spectra was used to construct the spectra for the chemical species.

### 7.2.3 EPR Spectroscopy

EPR measurements were made at X-band (~9.5 GHz) using a Bruker Elexsys E680-X/W EPR spectrometer outfitted with a split ring resonator (ER4118X-MS5). Measurements were performed using an Oxford Instruments CF935 continuous flow cryostat with liquid N<sub>2</sub>. Sample solutions (optical density between 0.4 and 0.7 in 2 mm cuvette at 416 nm, ~10<sup>-4</sup> M) were loaded into quartz tubes (4.0 mm o.d. × 3.0 mm i.d.), subjected to four freeze–pump–thaw degassing cycles on a vacuum line (10<sup>-4</sup> Torr), and sealed under vacuum using an oxy-hydrogen torch.

Time-resolved EPR measurements were collected at 85 K using ESE detection or transient continuous wave (TCW) detection. For ESE-detected experiments, a 1 kW TWT amplifier (Applied Systems Engineering 117X) was employed to generate high-power microwave pulses. The resonator was partially overcoupled to maximize echo intensity and minimize ringing following microwave pulses. ESE data was obtained with a  $\pi/2$ - $\tau$ - $\pi$  pulse sequence with  $\pi/2 = 16$  ns,  $\pi = 32$  ns, and  $\tau = 120$  ns. The integrated echo intensity is recorded as a function of the magnetic field to yield the spectrum. If the sample is photoexcited at some time  $t$  prior to the  $\pi/2$ - $\tau$ - $\pi$  pulse sequence, spectra can be collected of the transient species as a function of  $t$ .

For TCW-EPR the transient magnetization following photoexcitation was detected in quadrature under CW microwave irradiation (2–20 mW), without field modulation. Sweeping the magnetic field gave 2D spectra versus both time and magnetic field. For each kinetic trace,

the signal acquired prior to the laser pulse was subtracted from the data. Kinetic traces recorded at magnetic field values off-resonance were considered background signals, whose average was subtracted from all kinetic traces.

Time-resolved EPR measurements were performed following photoexcitation with 7 ns, 1.8 mJ, 416 nm pulses using the output of an optical parametric oscillator (OPO; Spectra-Physics Basi-scan), pumped with the output of a frequency-tripled Nd:YAG laser (Spectra-Physics Quanta-Ray Pro 350). EPR experiments utilizing two pump laser pulses were performed using two frequency tripled Q-switched Nd:YAG lasers (Spectra-Physics Quanta-Ray Lab 150 and Pro 350) pumping separate OPOs (Spectra-Physics Basi-scan). The laser pulses were intersected at a 90° angle and combined with the aid of a sapphire disc oriented at 45° to the beams. The light was then focused into an optical fiber for delivery to the EPR instrument. One laser was used as the master clock for the experiment. The two lasers were linked so that the flashlamp firing was synchronized. The “advanced sync” output from the master laser (occurring approximately 500 ns before the Q-switch fires) was directed into a Stanford Research Systems DG535 delay generator. The DG535 was used to generate delayed outputs to trigger the Q-switch of the slave laser and data collection by the EPR spectrometer digitizer (Bruker SpecJet II). A custom-written Python script was used with a Prologix USB-GPIB controller to set the delays on the DG535 and in conjunction with the Xepr API to trigger data collection by the Bruker Xepr software controlling the EPR spectrometer.

#### 7.2.4 Simulations

Kinetic simulations of the spin measurement scheme were performed with a modified version of the programs used to fit transient optical spectra. A species associated first order kinetic model, detailed in the text, was constructed to account for each electron transfer step after the second pump laser pulse. Singlet and triplet radical pairs were treated as separate species. ZQC frequencies were simulated using the method of Nelson et al.<sup>71</sup>

#### 7.2.5 Phosphorescence Spectroscopy

Samples for time-resolved phosphorescence spectroscopy were excited using the same laser setup as for time-resolved EPR experiments. Phosphorescence signals were detected using a Burle 8852 photomultiplier tube contained in a Products for Research PR1400 enclosure. The photomultiplier tube was driven by a Hewlett Packard 6516A power supply. Signals were detected across a 100 k $\Omega$  load using a LeCroy WaveSurfer 42Xs oscilloscope. A chopper wheel (Thorlabs MC2000 with MC1F2 wheel) was used to prevent detection of scattered pump light and prompt fluorescence by blocking the beam path for the first several ms after excitation. The chopper wheel was kept in phase with the excitation laser(s) using a trigger pulse generated by a DG535 delay generator synced to the laser(s).

For phosphorescence experiments with two pump pulses, the same laser setup was used as for EPR experiments with two pump pulses. A LabVIEW program was used to set the delay on the DG535 delay box and to record data from the oscilloscope used for phosphorescence detection.

All phosphorescence experiments were performed at 77 K using a quartz finger dewar filled with liquid N<sub>2</sub>. Samples were prepared identically to those for EPR spectroscopy. Experiments with an applied magnetic field were performed using a Walker Scientific HV4W electromagnet, Walker Scientific HS735 power supply, and Lakeshore 450 Gaussmeter with Hall probe.

## **7.3 Results and Discussion**

### **7.3.1 Steady-state Optical Spectroscopy**

The UV-visible absorption spectrum of **7.1** (Figure 7.2) shows a shoulder near 420 nm and peaks near 380 and 360 nm. The shoulder is attributed to absorption of the ANI chromophore, while the sharper peaks are due to NDI. **7.2** and **7.3** show similar features. In **7.2**, excess absorption red of 400 nm (as compared to the NDI features) is due to absorption by the TTF electron donor. Excess absorption near 360 nm in **7.3** is attributed to absorption by the BDX electron donor in that compound.

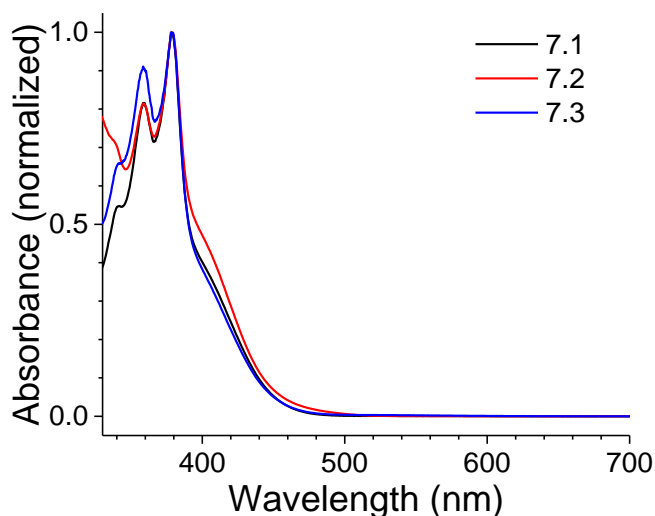


**Figure 7.2.** UV-visible absorption spectra of **7.1**, **7.2**, and **7.3** in THF at room temperature.

### 7.3.2 Energetics of Electron Transfer Reactions

The proposed spin measurement scheme relies on alignment of the energy levels of the radical ion pair and localized triplet states. To guide the selection of molecules and solvents for these experiments, the radical ion pair energy levels were estimated using the Weller equation as described previously.<sup>78</sup> These estimates were compared to the reported energies of singlet and triplet excited states to obtain the free energy change associated with singlet and triplet charge recombination reactions (Table 7.1). From these calculations, it is also predicted that both the initial charge separation reaction to form  $D^{+}\text{-ANI}^{\bullet-}\text{-NDI}$  and the subsequent charge shift reaction to form  $D^{+}\text{-ANI-NDI}^{\bullet}$  will be favorable in polar (THF) and nonpolar (toluene) solvents (free energy changes not shown). For the spin measurement experiment to be successful, recombination to  ${}^3\text{*NDI}$  of the terminal  $D^{+}\text{-ANI-NDI}^{\bullet}$  radical ion pair should be unfavorable, while that from the  $D^{+}\text{-ANI}^{\bullet-}\text{-NDI}$  radical ion pair (formed by photoinduced back electron

transfer) should be favorable. From the estimates in Table 7.1, **7.3** is expected to fulfill these criteria only in more polar solvents such as THF. For **7.1**, the recombination of the terminal radical ion pair to  $^3\text{NDI}$  is predicted to be isoergic in nonpolar solvents but endoergic in polar solvents; therefore, **7.1** should meet the energetic criteria in polar solvents, and possibly in nonpolar solvents depending on the accuracy of these estimates. **7.2** is predicted to meet these criteria in both polar and nonpolar solvents, though in polar solvents, the energy of the  $\text{TTF}^{+\cdot}-\text{ANI}^{\cdot-}-\text{NDI}$  radical ion pair is close enough to  $^3\text{NDI}$  that recombination to this state may be slow.

State (Compound)	Solvent	$\Delta G_{\text{CRS}}$ (eV)	$\Delta G_{\text{CRT}}$ (eV)
$\text{mPD}^{+\cdot}-\text{ANI}^{\cdot-}-\text{NDI}$ ( <b>7.1</b> )	Toluene ( $\epsilon_{\text{S}} = 2.38$ )	-2.55	-0.52
$\text{mPD}^{+\cdot}-\text{ANI}-\text{NDI}^{\cdot}$ ( <b>7.1</b> )	Toluene	-2.03	0.00
$\text{mPD}^{+\cdot}-\text{ANI}^{\cdot-}-\text{NDI}$ ( <b>7.1</b> )	THF ( $\epsilon_{\text{S}} = 7.52$ )	-2.39	-0.36
$\text{mPD}^{+\cdot}-\text{ANI}-\text{NDI}^{\cdot}$ ( <b>7.1</b> )	THF	-1.63	+0.40
$\text{TTF}^{+\cdot}-\text{ANI}^{\cdot-}-\text{NDI}$ ( <b>7.2</b> )	Toluene	-2.47	-0.44
$\text{TTF}^{+\cdot}-\text{ANI}-\text{NDI}^{\cdot}$ ( <b>7.2</b> )	Toluene	-1.77	+0.26
$\text{TTF}^{+\cdot}-\text{ANI}^{\cdot-}-\text{NDI}$ ( <b>7.2</b> )	THF	-2.14	-0.11
$\text{TTF}^{+\cdot}-\text{ANI}-\text{NDI}^{\cdot}$ ( <b>7.2</b> )	THF	-1.31	+0.72
$\text{BDX}^{+\cdot}-\text{ANI}^{\cdot-}-\text{NDI}$ ( <b>7.3</b> )	Toluene	-2.84	-0.81
$\text{BDX}^{+\cdot}-\text{ANI}-\text{NDI}^{\cdot}$ ( <b>7.3</b> )	Toluene	-2.18	-0.15
$\text{BDX}^{+\cdot}-\text{ANI}^{\cdot-}-\text{NDI}$ ( <b>7.3</b> )	THF	-2.54	-0.51
$\text{BDX}^{+\cdot}-\text{ANI}-\text{NDI}^{\cdot}$ ( <b>7.3</b> )	THF	-1.73	+0.30

**Table 7.1.** Free energy changes for recombination of the specified radical ion pairs to the singlet ground state or to the lowest energy triplet state,  $^3\text{NDI}$  at 2.03 eV.

### 7.3.3 Transient Optical Absorption Spectroscopy Following a Single Pump Pulse

Previously reported transient absorption measurements on **7.2** and **7.3** in toluene solutions at room temperature confirm that these molecules undergo two-step electron transfer following excitation at 414 nm, forming radical ion pairs.<sup>71</sup> Transient absorption measurements were conducted on **7.1** under the same conditions to verify high yield formation of the desired radical ion pair state. The femtosecond transient absorption (fsTA) spectra of **7.1** initially shows

absorptive features near 440 nm and a negative feature near 500 nm assigned to  $^1\text{ANI}$  excited state absorption and stimulated emission respectively (Figure 7.3). These features give way to absorptive bands at 430 nm and near 500 nm around 100 ps, and at later times, the spectrum becomes dominated by strong absorptive features at 480, 605, 700, and 750 nm. The earlier features are characteristic for  $\text{ANI}^{\cdot-}$  and likely contain some contribution from  $\text{mPD}^{+\cdot}$ , while the later features are distinctive for  $\text{NDI}^{\cdot-}$ . These data suggest that charge separation occurs in two steps, first forming the radical ion pair  $\text{mPD}^{+\cdot}\text{-ANI}^{\cdot-}\text{-NDI}$ , then the desired radical ion pair  $\text{mPD}^{+\cdot}\text{-ANI-NDI}^{\cdot-}$ . Fitting the fsTA data to a species-associated model with  $^1\text{ANI}$  as species A,  $\text{mPD}^{+\cdot}\text{-ANI}^{\cdot-}\text{-NDI}$  as species B, and  $\text{mPD}^{+\cdot}\text{-ANI-NDI}^{\cdot-}$  as species C yields time constants of 17 ps and 640 ps for  $\text{A} \rightarrow \text{B}$  and  $\text{B} \rightarrow \text{C}$  respectively. Nanosecond transient absorption (nsTA) was performed to observe the charge recombination reaction, yielding a time constant of 160 ns for the process  $\text{C} \rightarrow \text{ground state}$  (Figure 7.4). The time constants of charge separation and recombination for **7.1-7.3** are summarized in Table 7.2. While this data is presented for compounds in toluene solution due to data availability, the energetic estimates presented previously suggest that the spin measurement experiment will likely need to be performed in more polar solvent to prevent recombination of the final radical ion pair to  $^3\text{NDI}$ . Nonetheless, these time constants allow some comparison of molecules **7.1-7.3**. Additionally, time constants for these reactions in THF are presented for **7.1** to show the effect of using a more polar solvent.

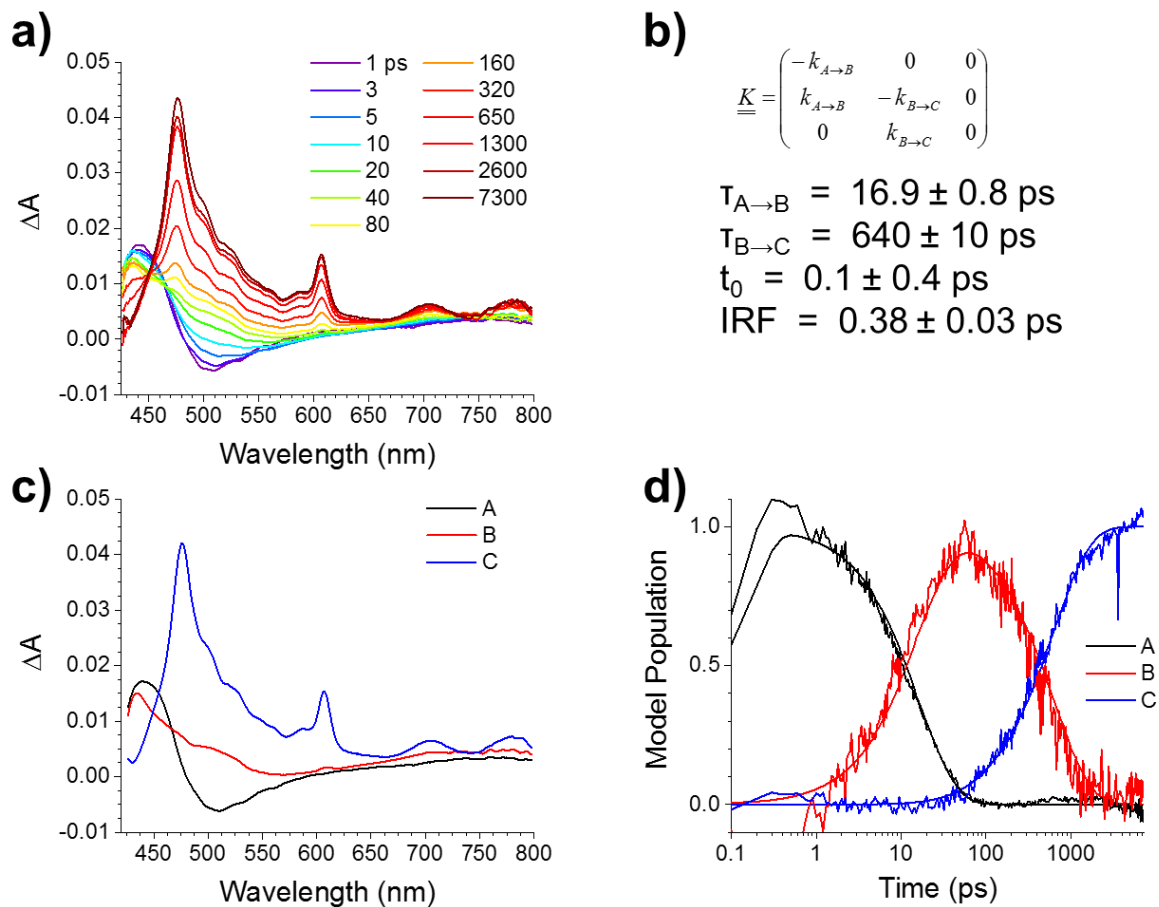


**Figure 7.3.** fsTA spectra (a) of **7.1** in toluene at room temperature following excitation at 414 nm. Spectra were fitted to a species-associated kinetic model (b). Species spectra (c) and populations over time (d) are shown.

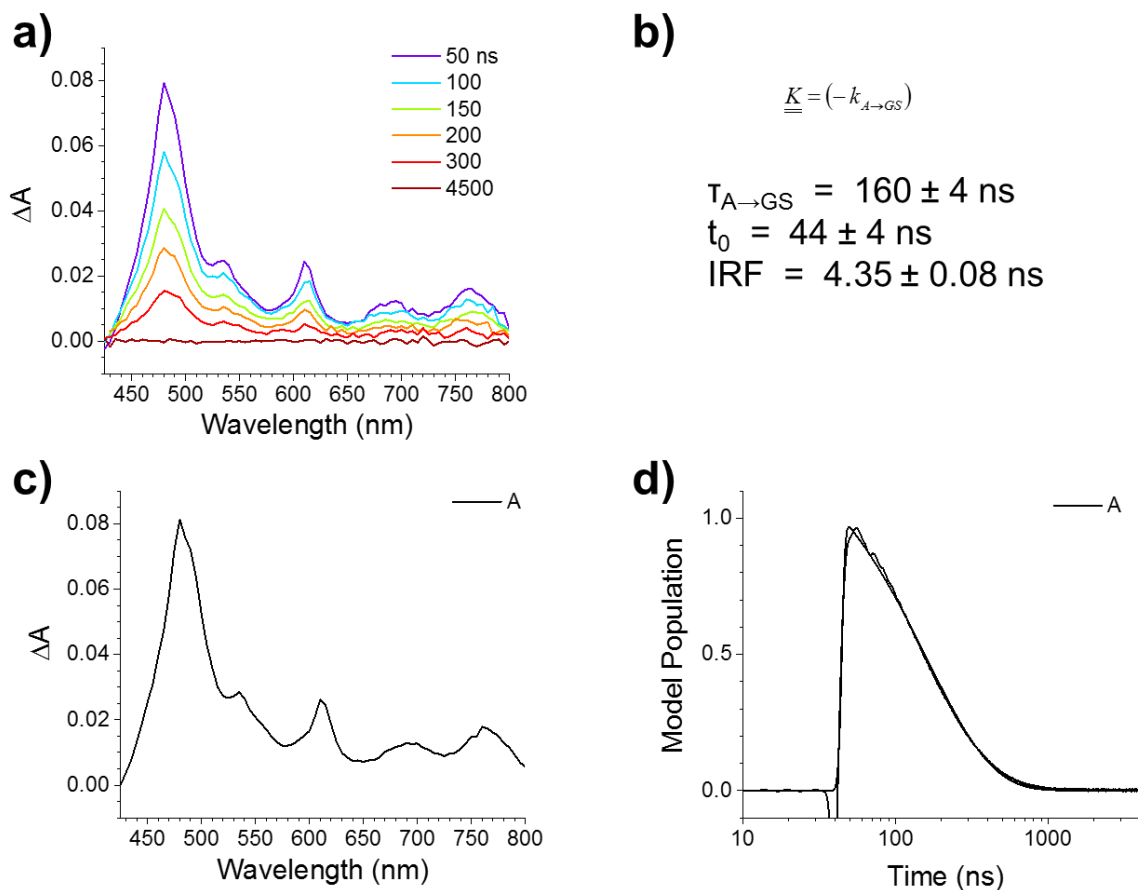


**Figure 7.4.** nsTA spectra of **7.1** in toluene at room temperature following excitation at 416 nm. Spectra were fitted to a species-associated kinetic model (b). Species spectra (c) and populations over time (d) are shown.

To assess the feasibility of the proposed spin measurement scheme, it is also helpful to understand the rates of singlet and triplet charge recombination from the primary radical ion pair,  $D^{\bullet+}$ -ANI $^{\bullet-}$ -NDI. Because minimal population of the triplet sublevels occurs following formation of this strongly-coupled radical pair without an applied magnetic field, the rate of singlet charge recombination is assumed to be equal to the rate of charge recombination measured by transient absorption on the corresponding D-ANI model compound. Charge recombination rates for the triplet radical ion pairs are more difficult to obtain, but an upper bound on this time constant is

the recombination rate for D-ANI compounds containing a stable radical, in which intersystem crossing to the triplet radical pair is rapid. These data are only available for the D-ANI fragment of **7.1** coupled to BDPA<sup>\*</sup>, **4.1b**, and are included in Table 7.2.

Compound	Solvent	$\tau_{CS1}$	$\tau_{CS2}$	$\tau_{CRS}$	$\tau_{CRT}$
<b>7.1</b>	THF	$3.1 \pm 0.3$ ps	$137 \pm 2$ ps	$248 \pm 2$ ns	not observed
<b>7.1</b>	Toluene	$16.9 \pm 0.8$ ps	$640 \pm 10$ ps	$160 \pm 4$ ns	not observed
<b>4.1</b>	THF	$3.3 \pm 0.3$ ps (from <b>4.1a</b> )	not applicable	$274 \pm 5$ ps (from <b>4.1a</b> )	$25.1 \pm 0.5$ ps (from <b>4.1b</b> )
<b>7.2</b> <sup>71</sup>	Toluene	$5.1 \pm 0.3$ ps	$228 \pm 4$ ps	$154 \pm 2$ ns	not observed
<b>7.3</b> <sup>47</sup>	Toluene	$13 \pm 3$ ps	$300 \pm 20$ ps	$200 \pm 60$ ns	not determined

**Table 7.2.** Time constants for charge separation ( $\tau_{CS1}$ ), charge shift ( $\tau_{CS2}$ ), and singlet ( $\tau_{CRS}$ ) and triplet ( $\tau_{CRT}$ ) charge recombination for **7.1-7.3** at room temperature, obtained from species-associated fits to transient absorption measurements on **7.1-7.3** or their D-ANI model compounds. Due to the model used for fitting,  $\tau_{CS2}$  also contains a contribution from recombination of the primary radical pair, which is significant for data in THF.

At low temperatures in frozen solvents, polar solvent molecules are unable to reorient to stabilize charged products of electron transfer reactions. Additionally, conformational changes in solute molecules can reduce the magnitude of the electronic coupling for charge separation and recombination. To gain a better understanding of the rates of these electron transfer reactions in the frozen solvents used for EPR experiments, transient absorption measurements were performed on **7.1** in PrCN at 105 K (Figures 7.5 and 7.6). The same features corresponding to the initial and final radical ion pairs are observed in this data. Species associated fitting to the fs- and nsTA data yields time constants of 5.1 ps for the initial charge separation, 279 ps for the charge shift, and 34  $\mu$ s for the charge recombination.

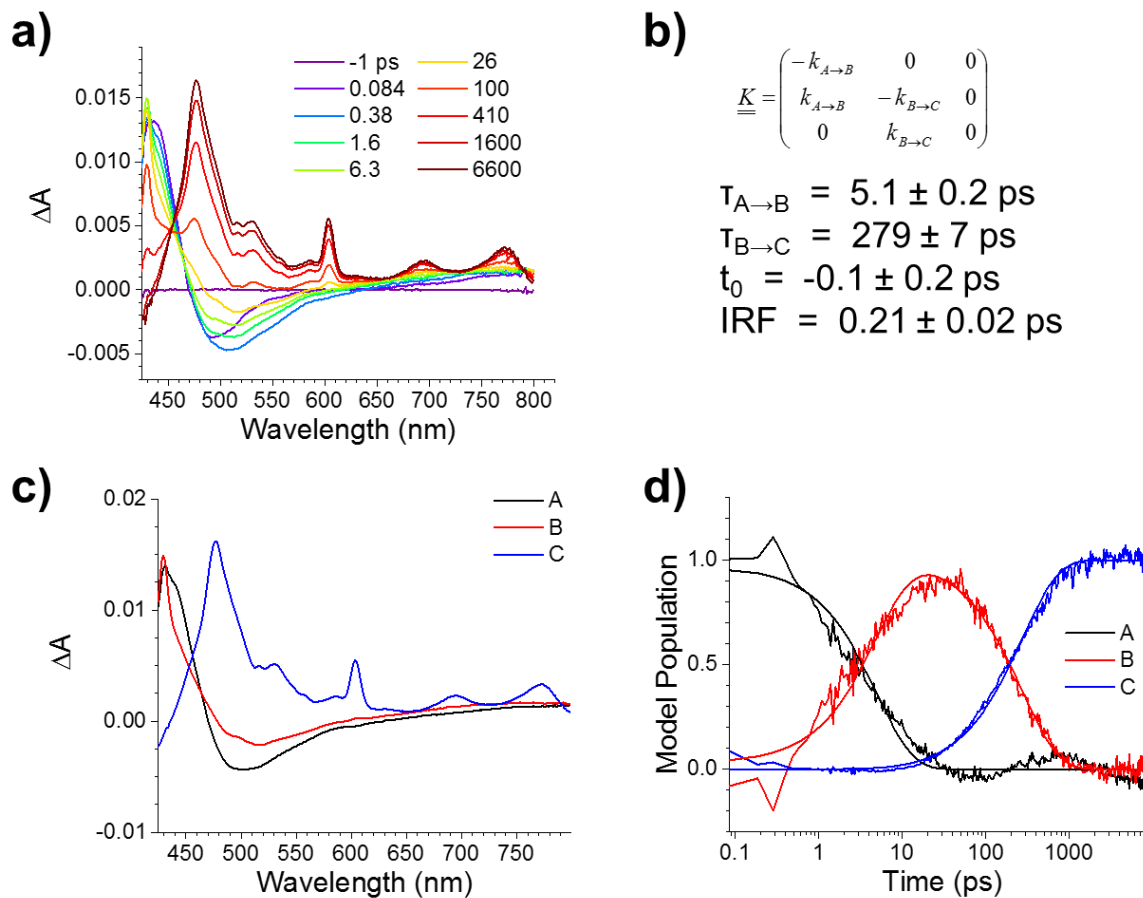


**Figure 7.5.** fsTA spectra (a) of **7.1** in PrCN at 105 K following excitation at 414 nm. Spectra were fitted to a species-associated kinetic model (b). Species spectra (c) and populations over time (d) are shown.

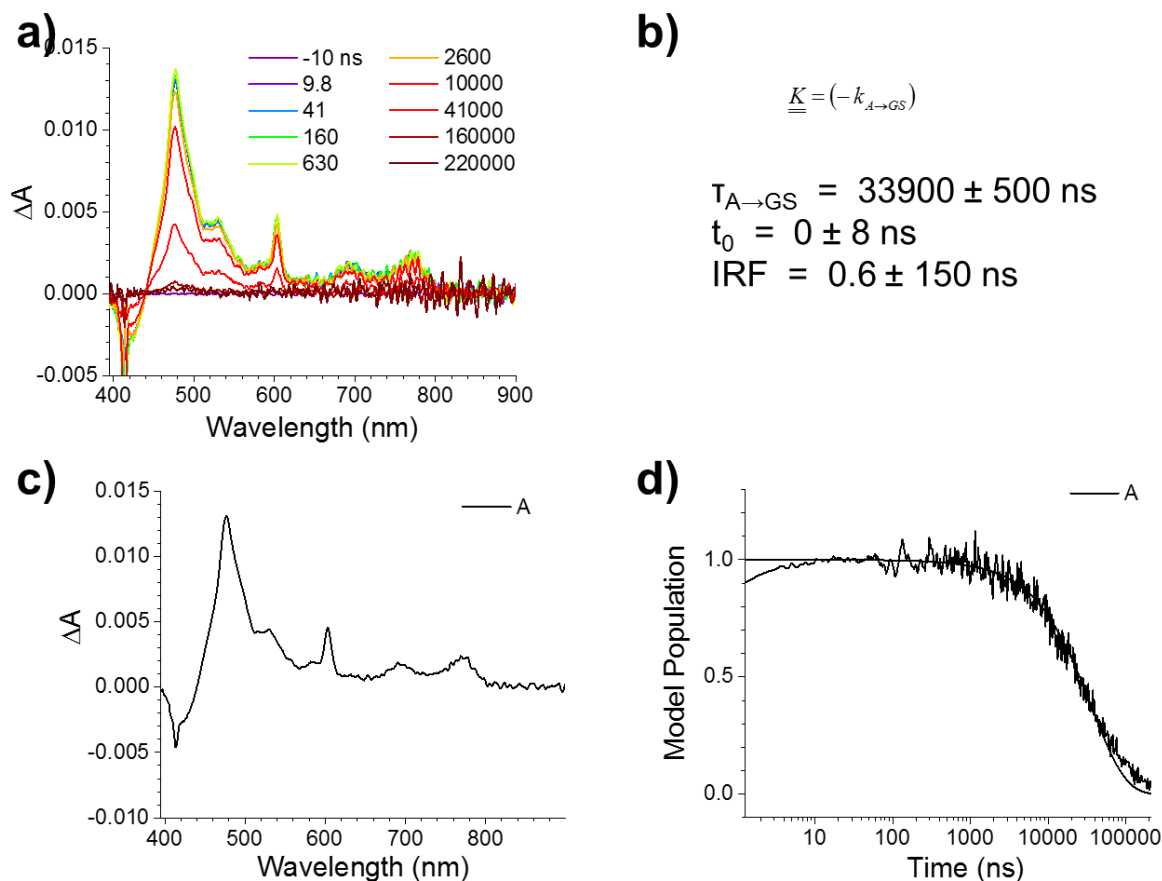


**Figure 7.6.** nsTA spectra (a) of **7.1** in PrCN at 105 K following excitation at 414 nm. Spectra were fitted to a species-associated kinetic model (b). Species spectra (c) and populations over time (d) are shown.

### 7.3.4 EPR Spectroscopy Following a Single Pump Pulse

Time-resolved EPR (TR-EPR) spectroscopy was performed on **7.1-7.3** following a single pump laser pulse as an additional confirmation of RP formation, and to investigate the energetics of recombination to  $^3\text{N}^{\bullet}\text{DI}$  (Figure 7.7). To detect EPR signals from  $^3\text{N}^{\bullet}\text{DI}$ , it is necessary to work in a solid matrix such as a frozen solvent. As such, TR-EPR experiments were conducted at 85 K in frozen toluene and PrCN. The TR-EPR spectra of all three molecules in both solvents show narrow signals due to the spin-correlated radical pairs. In **7.1** and **7.3**, the four radical pair

EPR transitions partially overlap, resulting in observation of an emissive-absorptive (*e-a*) polarization pattern. In **7.2**, due to the larger *g*-factor difference between  $\text{TTF}^{+\bullet}$  and  $\text{NDI}^{\bullet-}$ , all four transitions are observed to yield a *e-a-e-a* polarization pattern. A small emissive shoulder at high field in this sample is due to the *g*-anisotropy of  $\text{TTF}^{+\bullet}$ . The TR-EPR results therefore confirm that the charge separation reactions observed in the room temperature transient absorption also occur in frozen toluene and PrCN, as expected from the low temperature transient absorption measurements on **7.1**.

More interestingly, a strong  $^3\text{NDI}$  spectrum is observed from **7.1** in toluene at 85 K, but not in PrCN at 85 K. The spectrum in toluene has a *a-e-e-a-a-e* polarization pattern, confirming that the observed  $^3\text{NDI}$  arises from radical pair recombination.<sup>235</sup> The absence of this signal in PrCN suggests that the radical ion pair energy in this solvent is lowered enough to make  $^3\text{NDI}$  energetically inaccessible. Because the frozen PrCN molecules are unable to reorient to solvate the radical ion pair, this may be a result of preorganization of the solvent molecules around the solute. Likewise in **7.3**, no triplet signal is observed in PrCN. For **7.2**, the ion pair energy is lowered enough by the electron rich TTF donor that  $^3\text{NDI}$  should be inaccessible in both toluene and PrCN. However, a very weak triplet signal is observed from **7.2** in toluene. This signal introduces an undesired background into the spin measurement experiments, and may arise from recombination of the primary  $\text{TTF}^{+\bullet}$ - $\text{ANI}^{\bullet-}$ - $\text{NDI}$  radical pair in competition with charge shift to form  $\text{TTF}^{+\bullet}$ - $\text{ANI}$ - $\text{NDI}^{\bullet-}$ .

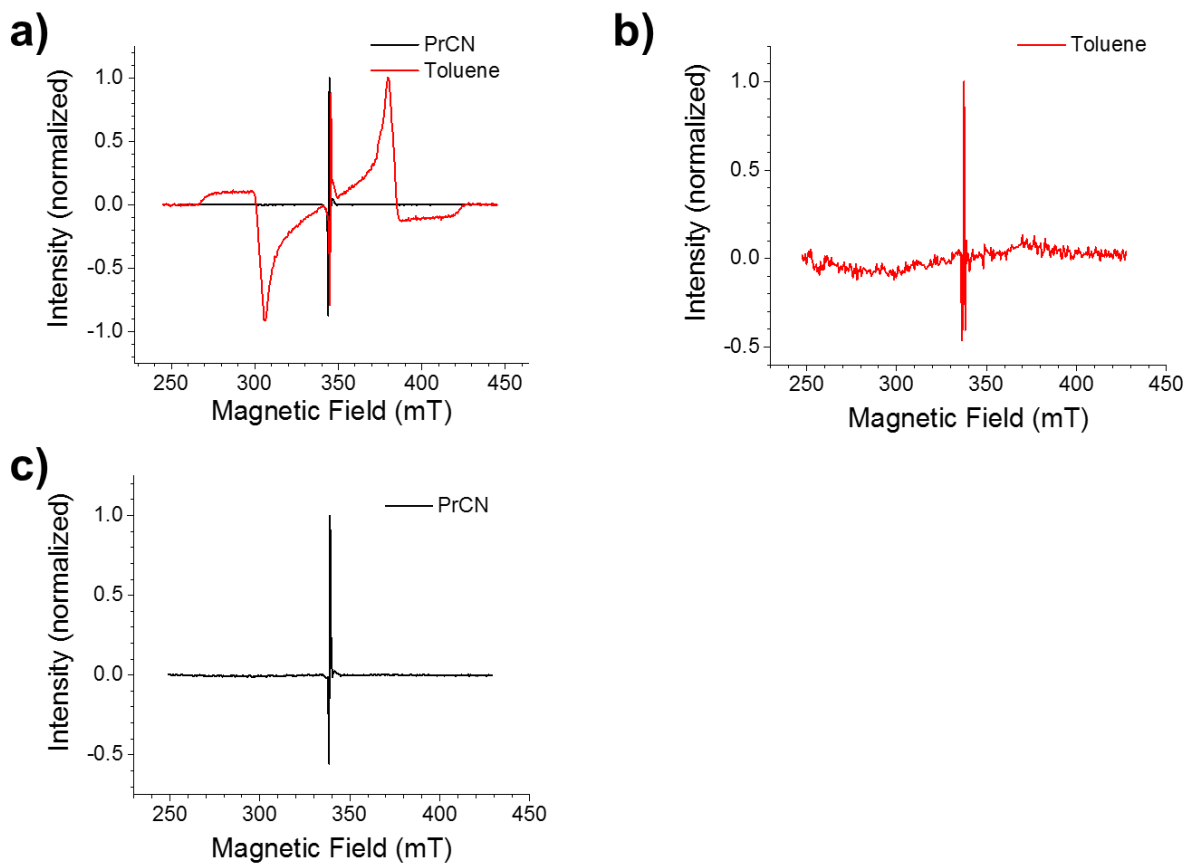


**Figure 7.7.** TR-EPR spectra of (a) **7.1**, (b) **7.2**, and (c) **7.3** in toluene and/or PrCN at 85 K following excitation at 416 nm. Spectra are shown at a fixed time after excitation corresponding to the maximum radical pair signal (if no triplet signal is present) or when both radical pair and triplet signals are strong.

## 7.3.5 Simulations of the ZQC Frequencies and Detection Scheme

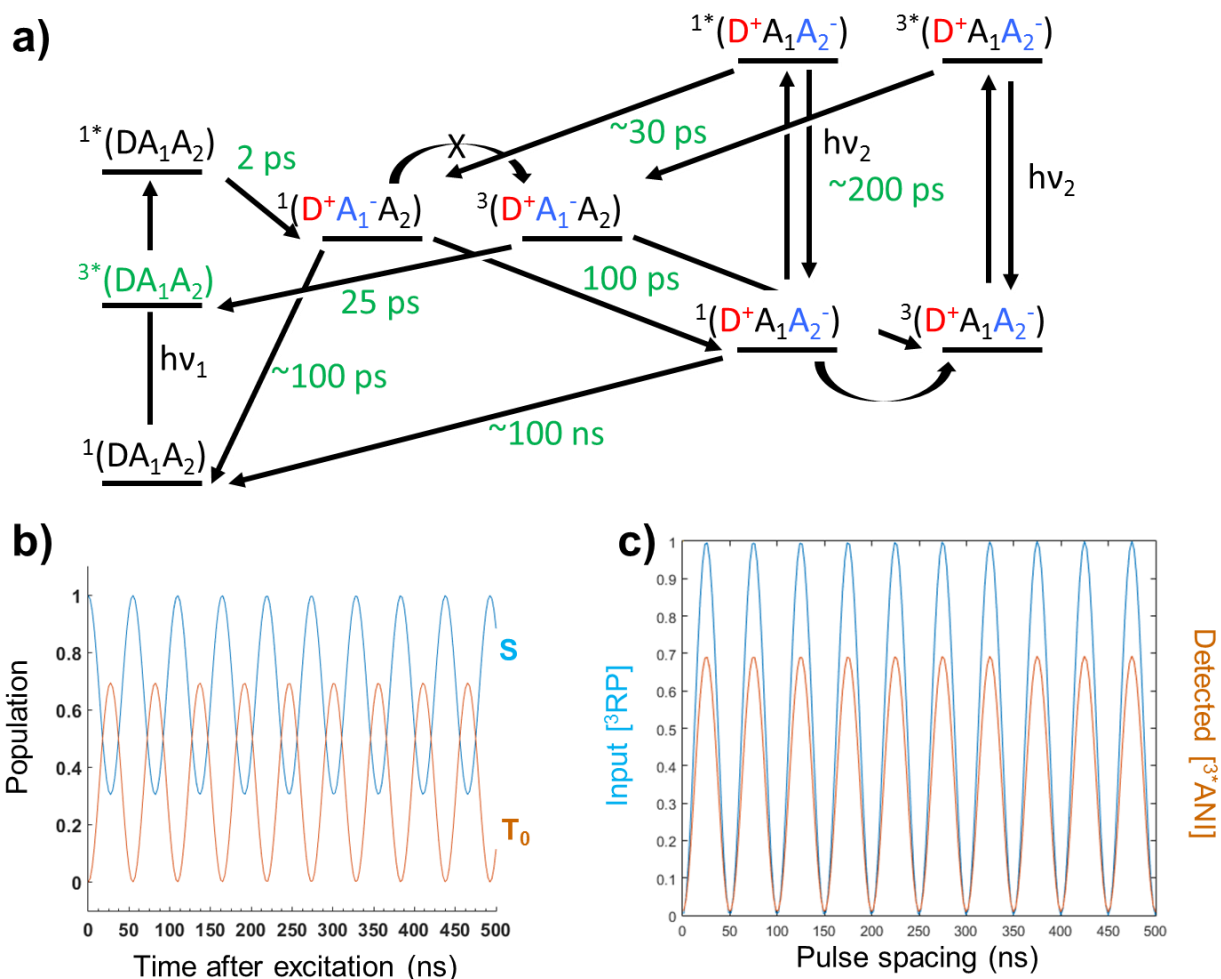


**Figure 7.8.** (a) Electron transfer pathways for the proposed spin measurement scheme, where D is mPD, A<sub>1</sub> is ANI, and A<sub>2</sub> is NDI. Estimated time constants for each step are included for **7.1** in THF at room temperature.  $3^*(DA_1A_2)$ , highlighted in green, is the final product used to read out the spin state of the  $D^+A_1A_2^-$  radical pair. (b) Simulated time evolution of the singlet and triplet radical pair populations in **7.2** in liquid solution due to the ZQC, neglecting dephasing and hyperfine coupling. (c) Kinetic simulation of  $3^*$ ANI yield following the second laser pulse, using the model in (a). An oscillating triplet radical pair population, also shown, is used as the input signal.

Using the electron transfer time constants determined in Section 7.3.3 and in previous work, we can estimate the overall yield of the proposed spin measurement scheme. The

procedure used for fitting the transient absorption data was used to generate a kinetic simulation following the species-associated model shown in Figure 7.8a. Due to better availability of the relevant time constants, the simulation was performed on **7.1**, even though no significant ZQC oscillations are expected in this molecule. It is assumed that recombination of the back electron transfer product initially produces  $^3\text{ANI}$ , which may then undergo energy transfer to form the lower energy  $^3\text{NDI}$ . From this simulation, the expected conversion of triplet radical pair to  $^3\text{ANI}$  following the second laser pulse is close to 70%. Additionally, this kinetic scheme is able to preserve the expected ZQC oscillations. When the initial triplet radical pair population is approximated as a cosine wave with a period of 50 ns (similar to the expected ZQC period for **7.2**<sup>71</sup>), corresponding oscillations are observed in the  $^3\text{ANI}$  population (Figure 7.8c). These results indicate that the proposed spin measurement scheme should allow observation of ZQCs from **7.2** and **7.3**, assuming the electron transfer rate constants do not differ too much from those in **7.1**.

### 7.3.6 Transient Optical Absorption Spectroscopy with Two Pump Pulses

Previous results from Chapter 2 suggest that following excitation of  $\text{NDI}^{\bullet-}$  in a radical ion pair in **7.1**, **7.2**, or **7.3**, back electron transfer from  $\text{NDI}^{\bullet-}$  to ANI should occur. To test this hypothesis, fsTA experiments were performed with two pump pulses (at 414 nm to excite ANI and at 605 nm to excite  $\text{NDI}^{\bullet-}$ ) and one probe pulse. A fixed 3.7 ns delay was used between the two pump pulses to allow formation of the  $\text{D}^{\bullet+}$ -ANI- $\text{NDI}^{\bullet-}$  radical ion pair following the first pump. Due to the fixed delay time and lack of an applied magnetic field, we do not expect to observe evidence of a ZQC in these experiments, but should be able to verify the kinetic model

shown in Figure 7.8. The pump-pump-probe fsTA spectra and fits for **7.1** in THF at room temperature are shown in Figure 7.9. These spectra are referenced to the transient spectrum following the first pump pulse instead of to the ground state; thus, in the absence of the second pump pulse, we still expect to see a small negative signal at late times as the  $D^{+}\text{-ANI-NDI}^{\bullet}$  radical ion pair decays. fsTA data were fit to a species-associated  $A \rightarrow B \rightarrow C$  model, with an additional species added to account for a coherence artifact (not shown). The spectra initially show the ground state bleach of  $NDI^{\bullet}$  near 480 nm. Near 10 ps, this bleach remains, but an additional absorptive feature near 430 nm has grown in. This feature is characteristic for  $ANI^{\bullet}$ , suggesting that the initial  ${}^2NDI^{\bullet}$  undergoes back electron transfer to ANI with a time constant of 7.7 ps (per the species-associated fit). This feature decays with a time constant of 175 ps, leaving a persistent  $NDI^{\bullet}$  bleach. The 175 ps decay of the  $mPD^{+}\text{-ANI}^{\bullet}\text{-NDI}$  state reflects a combination of decay to the true ground state and charge shift from  $ANI^{\bullet}$  to NDI. The persistent bleach reflects a loss of  $mPD^{+}\text{-ANI-NDI}^{\bullet}$  to this first process and to the natural decay of unexcited  $mPD^{+}\text{-ANI-NDI}^{\bullet}$  during the experiment. The lack of absorptive features near 450 nm at late times suggests that formation of  ${}^3ANI$  as a recombination product is minor, however the overlap of this feature with the  $NDI^{\bullet}$  bleach means that a small yield of triplet cannot be ruled out. Additionally, if energy transfer from  ${}^3ANI$  to NDI is rapid, the resulting  ${}^3NDI$  will be difficult to observe due to the overlap with the  $NDI^{\bullet}$  bleach.

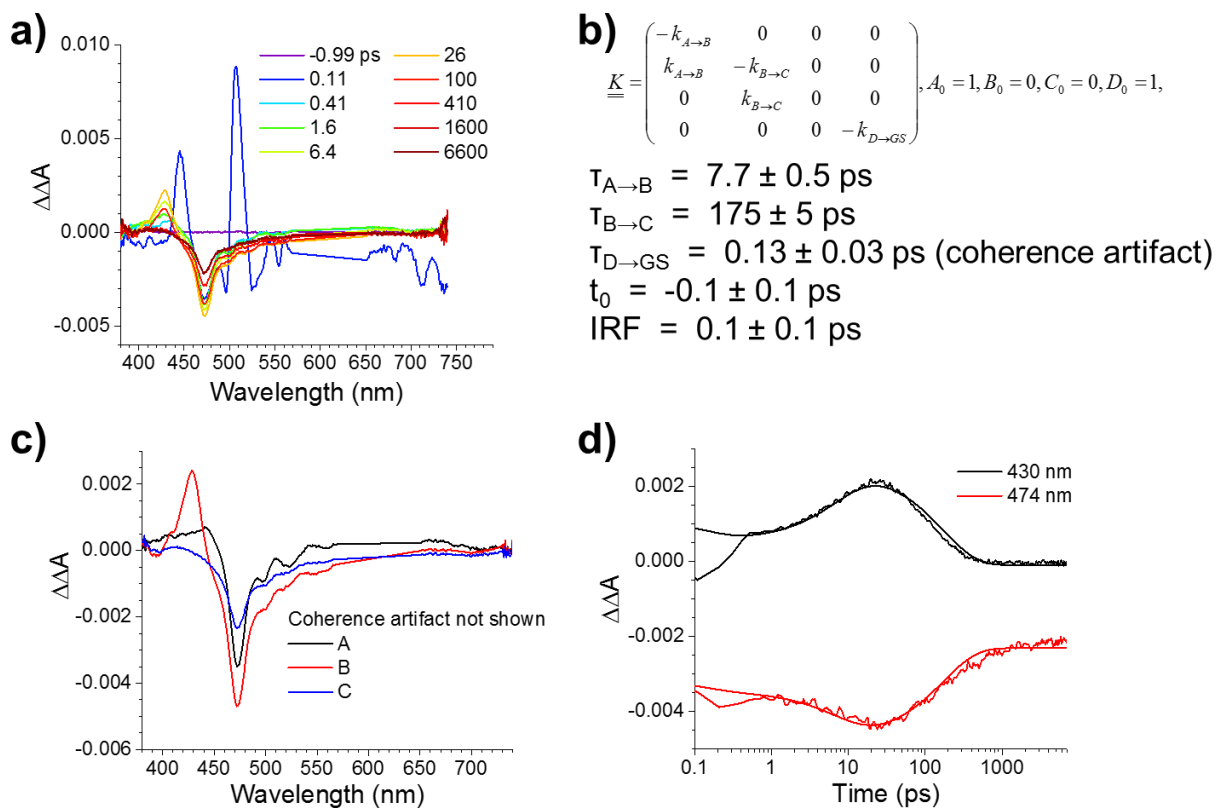


**Figure 7.9.** fsTA spectra (a) of **7.1** in THF at room temperature following excitation by two pump pulses, first at 414 nm and then at 605 nm following a 3.7 ns delay. Kinetic data at two relevant wavelengths were fitted to a species-associated kinetic model (b). Species spectra (c) and populations over time (d) are shown.

The pump-pump-probe fsTA spectra for **7.2** in toluene show similar features to those of **7.1** (Figure 7.10). Fitting to a species-associated  $A \rightarrow B \rightarrow C$  model yields time constants of 7.8 ps for back electron transfer and 174 ps for decay of the resulting  $\text{TTF}^{+\bullet}\text{-ANI}^{\bullet\text{-}}\text{-NDI}$  state (again using an additional species to account for a coherence artifact). The persistent bleach at late times is smaller than for **7.1** in THF, presumably because the balance of rates favors charge shift from  $\text{ANI}^{\bullet\text{-}}$  to NDI over recombination of  $\text{TTF}^{+\bullet}\text{-ANI}^{\bullet\text{-}}\text{-NDI}$  to the ground state. These results show that the proposed back electron transfer following the second pump pulse is likely to occur in these compounds.

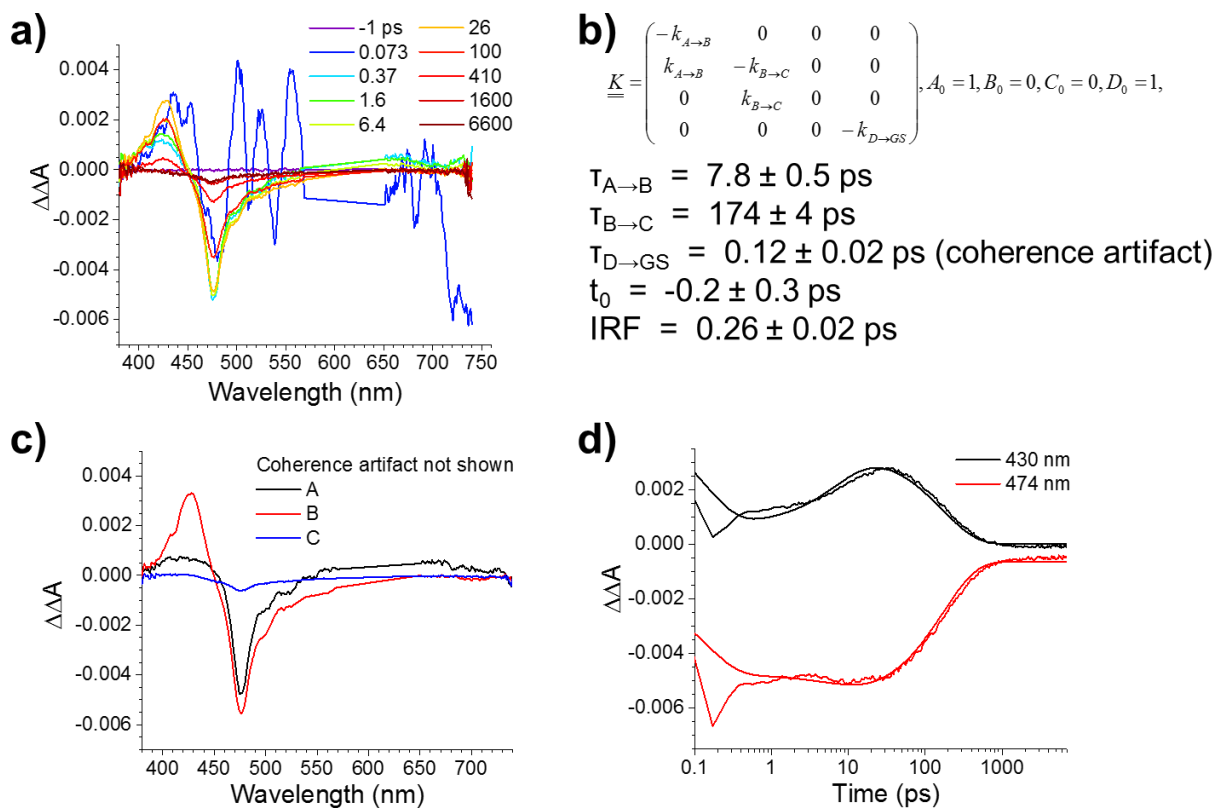


**Figure 7.10.** fsTA spectra (a) of **7.2** in toluene at room temperature following excitation by two pump pulses, first at 414 nm and then at 605 nm following a 3.7 ns delay. Kinetic data at two relevant wavelengths were fitted to a species-associated kinetic model (b). Species spectra (c) and populations over time (d) are shown.

### 7.3.7 EPR Spectroscopy with Two Pump Pulses

Due to instrumental limitations in changing the delay between the two pump pulses and the difficulty in detecting small yields of  $^3\text{*ANI}$  and  $^3\text{*NDI}$ , fsTA is not likely to be useful for the spin measurement scheme. Because triplet and radical pair species are readily distinguishable by time-resolved EPR experiments in solid samples, EPR spectroscopy was used to look for evidence of triplet recombination products following the second pump pulse.

Time-resolved EPR spectra of **7.1** following one (at 416 nm) or two (at 416 nm and 480 nm, separated by a 80 ns delay) pump pulses at 105 K in PrCN are shown in Figure 7.11a. As

shown previously, with excitation at 416 nm, only a radical pair signal from  $mPD^{+\bullet}$ -ANI-NDI $^{\bullet-}$  is observed. When the second pump pulse is introduced, a weak but much broader signal is observed. The intensity of the radical pair signal is reduced, suggesting conversion of the radical pair into another species. The width of the broader signal is consistent with  $^3ANi$  or  $^3NDI$ . More interestingly, the polarization pattern of this signal is consistent with formation of  $^3ANi$  or  $^3NDI$  through recombination of a weakly-coupled radical pair in which S- $T_0$  spin mixing populates the radical pair states (Figure 7.11b). In **4.1a**, which forms only the strongly-coupled  $mPD^{+\bullet}$ -ANI $^{\bullet-}$  radical pair upon excitation,  $^3ANi$  is observed with a different polarization pattern consistent with a spin-orbit charge transfer intersystem crossing mechanism.<sup>30</sup> This strongly suggests that the spin state of the  $mPD^{+\bullet}$ -ANI-NDI $^{\bullet-}$  radical pair is carried over into  $mPD^{+\bullet}$ -ANI $^{\bullet-}$ -NDI and then to  $^3ANi$  following the second pump pulse. This process is essential for the proposed spin measurement scheme and its observation suggests that the scheme should be successful.

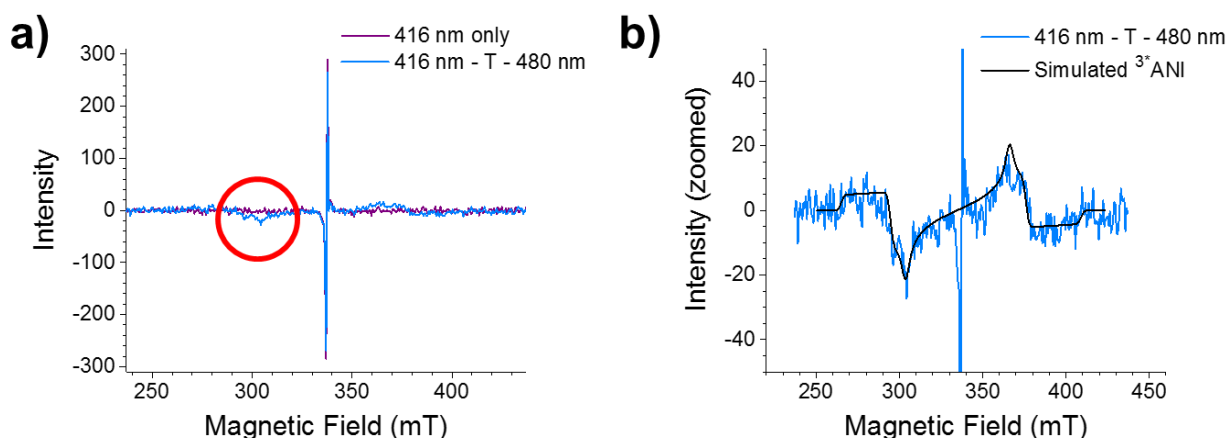


**Figure 7.11.** (a) TR-EPR spectra of **7.1** in PrCN at 105 K, following a single 416 nm laser pulse, or 416 nm and 480 nm pulses separated by  $T = 80$  ns. (b) Zoomed view of the signal following two pump laser pulses, with radical pair triplet simulation.

Because the potential advantage of this technique over other methods to measure ZQCs is the possibility of very high time resolution, it is also important to measure the rate at which triplet recombination product is formed after the second pump pulse. Spin echo-detected EPR experiments were performed at one of the peak magnetic field positions for the triplet, at different times after one or two pump pulses. This data is shown in Figure 7.12a for **7.1** in PrCN at 85 K. In the absence of the second, 480 nm pump, no triplet signal is observed. When this pump is introduced at a fixed delay after the initial 416 nm pump, triplet is formed rapidly, within the time resolution of the EPR experiment. This is consistent with (but not sufficient to prove) the picosecond time resolution expected from transient absorption measurements. This experiment was also performed on **7.3** in PrCN (Figure 7.12b) and **7.2** in toluene, PrCN, and aligned 4-pentyl-4'-cyanobiphenyl (5CB) liquid crystal (Figure 7.13; at 85 K 5CB is an ordinary crystalline solid, but still aligned with the applied magnetic field). **7.3** shows similar behavior to **7.1**, with triplet growing in quickly only after the second pump pulse.

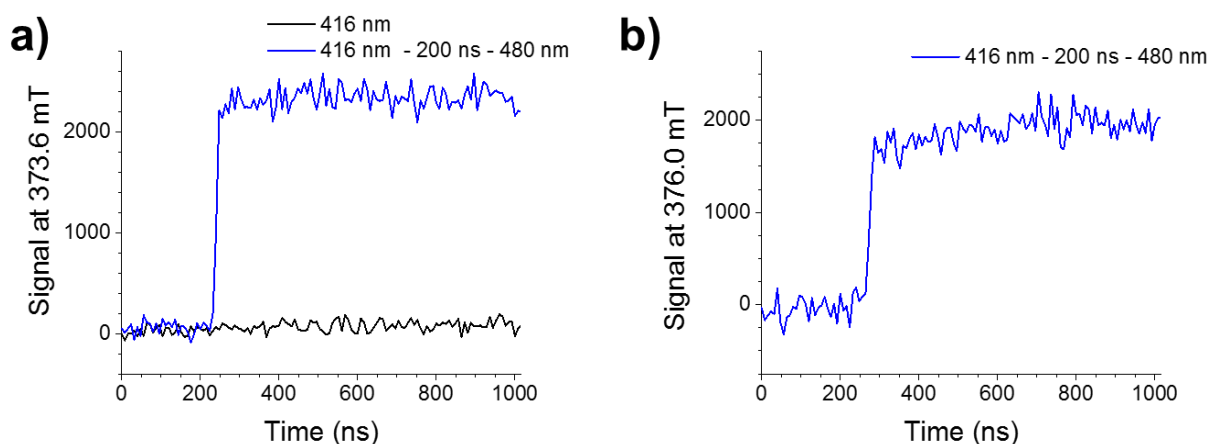


**Figure 7.12.** Echo-detected EPR signals as a function of time after the initial 416 nm pump pulse from (a) **7.1** and (b) **7.3** in PrCN at 85 K. A second pump pulse at 480 nm excites the sample after approximately 200 ns.

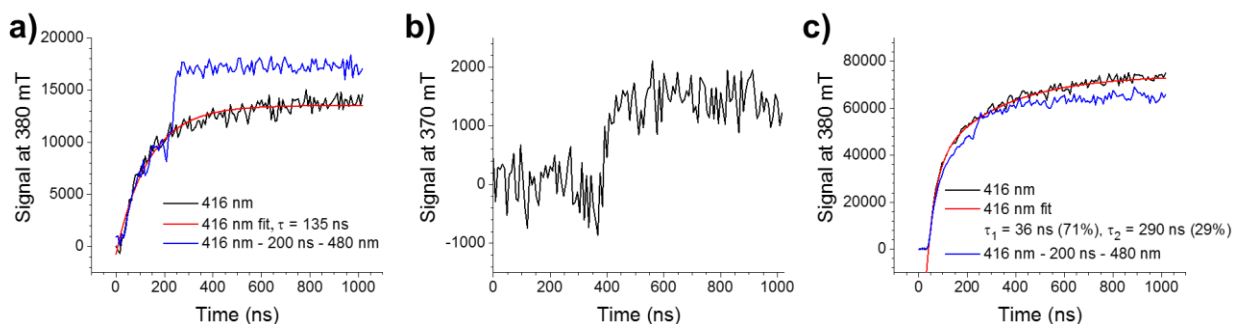


**Figure 7.13.** Echo-detected EPR signals as a function of time after the initial 416 nm pump pulse from 7.2 in (a) toluene, (b) PrCN, and (c) 5CB (aligned parallel to  $B_0$ ) at 85 K. A second pump pulse at 480 nm excites the sample after approximately 200 ns.

In 7.2 however, some triplet signal is observed after only a single pump pulse at 416 nm, in both toluene and 5CB samples. The triplet grows in with a time constant of 135 ns. Upon introduction of the 480 nm pump pulse, some fast triplet formation occurs as expected, but the enhancement in triplet signal versus the single pump experiment is much lower than for 7.1 and 7.3, and is even negative at late times for the 5CB sample. In PrCN, no triplet is observed after the 416 nm pump, but only a small enhancement is seen with the introduction of the 480 nm pump pulse. Additionally, the enhancement in toluene is not very reproducible: a second sample showed even less of a gain in triplet signal with the second pump. These results are unexpected as the radical ion pair in 7.2 should have a lower energy than those in 7.1 and 7.3. Thus, formation of triplet after the first pump pulse is not expected from the relative energies of the radical ion pair state and  $^3\text{*NDI}$  or  $^3\text{*ANI}$  (see Table 7.1). Combined with the lack of reproducibility, this may be a result of degradation of the somewhat unstable TTF electron donor. Molecules lacking the TTF donor could still be excited by the 416 nm pump pulse, forming a  $\text{ANI}^{+\bullet}\text{-NDI}^{\bullet-}$  radical ion pair with enough energy to recombine to  $^3\text{*NDI}$ . Additionally,

in PrCN, the energy of the TTF<sup>+</sup>-ANI<sup>-</sup>-NDI radical ion pair formed by back electron transfer after the second pump pulse may be too low relative to <sup>3</sup>\*ANI, resulting in a poor yield of this triplet recombination product. As such, despite the favorable g-factor difference in **7.2**, expected to result in an easily-detectable ZQC, **7.2** is not likely to be a good candidate for the spin measurement experiment.

The spin measurement experiment was attempted by varying the delay between the two laser pulses, and detecting the resulting triplet signal by EPR. Initially, triplet was detected using TCW-EPR as for the previous experiments. Data for **7.1** in PrCN is presented in Figure 7.14a. No ZQC oscillations are observed, as predicted for **7.1** due to the small g-factor difference within the radical pair. However, an unexpectedly fast decay of the triplet signal with the delay is observed. The decay can be fit by a single exponential function with a time constant of 2.7  $\mu$ s, much faster than the 34  $\mu$ s charge recombination time measured by nsTA under the same conditions. While TCW-EPR offers good signal-to-noise, the constant microwave radiation can induce transitions between different spin states, resulting in Torrey oscillations<sup>222</sup> or an apparent increase in the spin relaxation rate. To investigate if enhanced relaxation due to the CW microwaves was responsible for this fast decay, the experiment was repeated with electron spin echo detection of the triplet state (Figure 7.14b). Again, no oscillations are observed, but the decay of the triplet signal with pulse spacing is much slower. These results suggest that the microwave-induced relaxation is important, and echo detection is therefore a better technique for the spin measurement experiment.

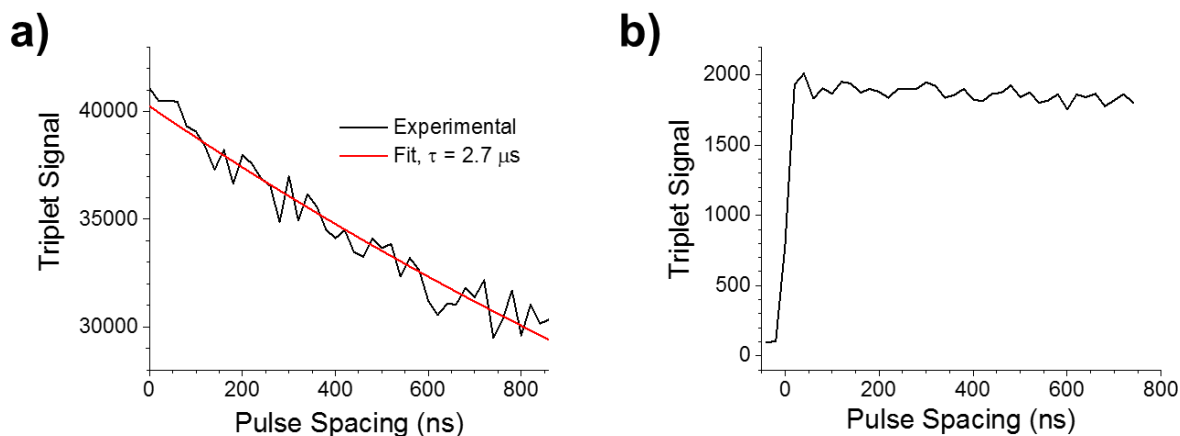


**Figure 7.14.** Triplet EPR signal as a function of the delay between pump pulses, collected for **7.1** in PrCN (a) by TCW-EPR at 105 K and (b) by echo detection at 85 K. The small change in temperature between these measurements is not expected to have a large effect on the data.

Despite the triplet background issue after a single pump pulse, these experiments were also performed on **7.2**. Data was collected on **7.2** in toluene at 85 K using both TCW (Figure 7.15a) and echo (Figure 7.15c) detection. Again, a difference is observed between the two detection methods, with the TCW data showing a slow decay, and the echo-detected data showing only a rise as the two laser pulses cross in time. Due to the small enhancement in triplet signal from **7.2** upon introduction of the second pulse, the signal-to-noise is poor and it is difficult to tell if oscillations are present in the echo-detected data. Past investigations of ZQCs have utilized samples aligned in a liquid crystalline solvent.<sup>86</sup> In randomly-oriented solid samples, g-factor and hyperfine anisotropy leads to a range of ZQC frequencies across the sample. Alignment of the radical pair relative to the applied magnetic field reduces the range of frequencies, making the ZQC easier to detect. Additionally, alignment of the sample improves the EPR signal from the triplet state. The triplet signal from **7.2** in aligned 5CB liquid crystal at 85K is shown in Figures 7.15b and 7.15d. The signal-to-noise ratio is enhanced compared to the

data in toluene. As before, the echo-detected data appears different than the TCW data. The echo-detected data shows a sharp drop in the triplet signal after the second laser pulse, with the signal then recovering. No oscillations are observed. The fact that the triplet signal drops in 5CB after the second pulse is consistent with the kinetics in Figure 7.13, but is not expected from the idealized kinetic scheme and is not promising for detection of the ZQC. 5CB was also investigated as a solvent for **7.1**, but in this solvent, a large amount of triplet formed after a single pulse.

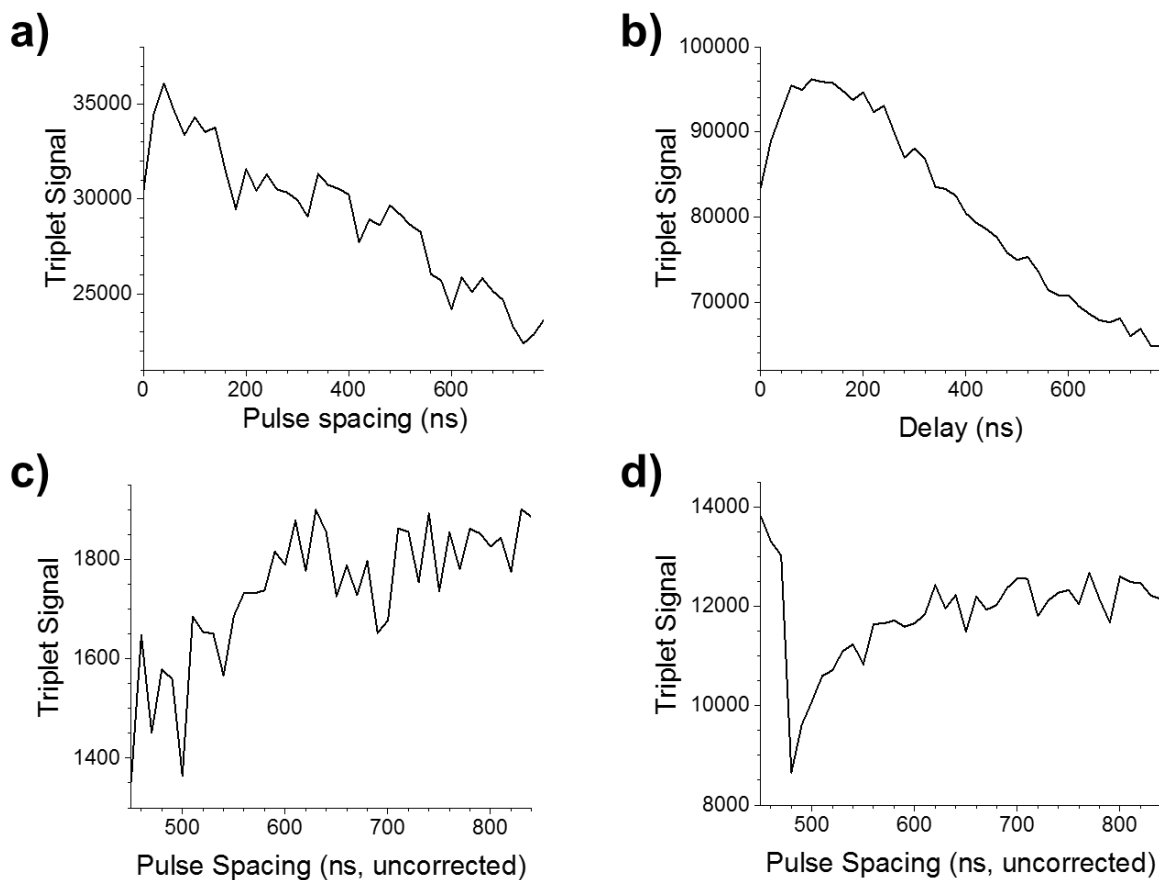


**Figure 7.15.** Triplet EPR signal as a function of the delay between pump pulses, collected for **7.2** (a) in toluene at 85 K by TCW-EPR detection, (b) in aligned 5CB at 85 K by TCW-EPR detection, (c) in toluene at 85 K by echo detection, and (d) in aligned 5CB at 85 K by echo detection.

These experiments were also attempted on **7.3**, which like **7.1** showed formation of triplet only after the second pump pulse in PrCN at 85 K. The spectrum of **7.3** following a 416 nm – 80 ns – 480 nm pulse sequence (80 ns after the second pulse) is shown in Figure 7.16a. As with **7.1**, a triplet signal with an *a-e-e-a-a-e* polarization pattern derived from S-T<sub>0</sub> mixing is present. In contrast to **7.1**, **7.3** is expected to show some detectable ZQC oscillations on account of the larger g-factor difference and weaker exchange coupling in this compound.<sup>71</sup> The spin echo from one line of the RP signal after a single 416 nm laser pulse shows damped oscillations in time after the laser pulse, attributed to the ZQC (Figure 7.16b). The echo from the triplet state was also collected as a function of the spacing between 416 nm and 480 nm pulses. This data shows similar kinetic behavior to the data from the RP signal (Figure 7.16b), but the oscillations appear more heavily damped. The ZQC frequency is proportional to the applied magnetic field, but the difference in magnetic field between these two measurements is relatively small. This difference may arise from the fact that the measurement on the RP signal is partially selective for one or two of the four RP EPR transitions. While the electron transfer reactions required to form the localized triplet state after the second pulse may be slower in frozen solvent compared to the measurements in room temperature liquids, this does not seem to account for the lack of oscillations. These reactions would need to become slower than the oscillation frequency, and this would also affect the rise of the triplet signal. However, the rise of the signal is identical between the two measurements in Figure 7.16b, suggesting the electron transfer reactions are still fast enough in frozen solvents to attain good time resolution.

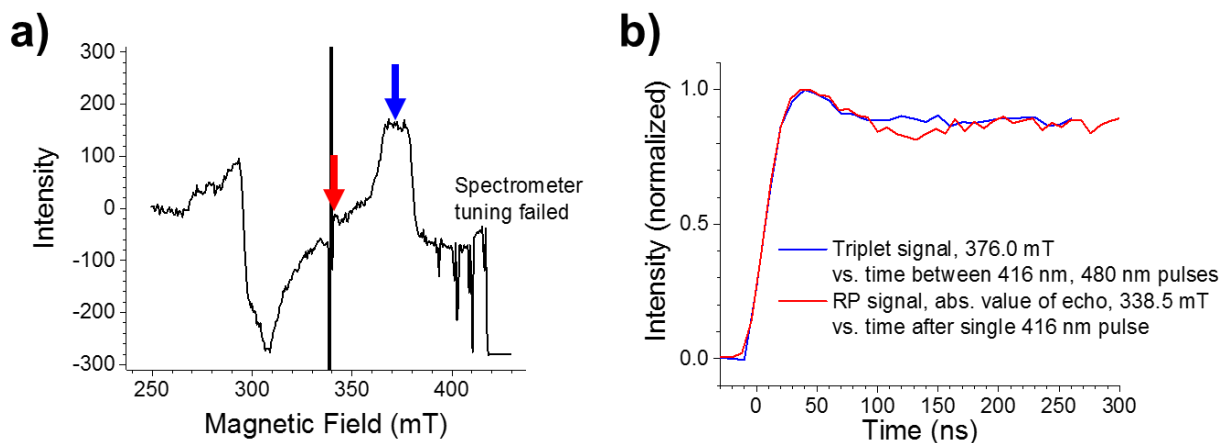


**Figure 7.16.** EPR data from 7.3 in PrCN at 85 K. (a) TCW spectrum 160 ns after 416 nm pulse and 80 ns after 480 nm pulse, showing triplet and radical pair signals. Red and blue arrows denote magnetic field positions for ZQC detection experiments based on the radical pair signal (red) and the triplet signal (blue). Spectrometer artifacts are present on the high-field edge of the spectrum. (b) Comparison of echo-detected kinetics measured from the radical pair signal after a single laser pulse (416 nm), as a function of time after the laser pulse, and those measured from the triplet signal after two laser pulses (416 nm, 480 nm) as a function of the spacing between the two pulses.

### 7.3.8 Phosphorescence Detection of Triplet Recombination Product

Attempts were also made to measure the triplet recombination product by detecting its phosphorescence. Phosphorescence spectroscopy is attractive as it is a zero-background technique: triplet states are the only luminescent species present in these samples that emit at long times ( $\mu\text{s}$  to  $\text{s}$ ) after excitation. Phosphorescence was detected using a photomultiplier tube, gated by a chopper wheel kept slightly out of phase with the pump pulses such that during the pump pulses and for several ms after, light was blocked from reaching the photomultiplier. This procedure prevents detection of scattered excitation light and prompt fluorescence. The triplet state formed in these experiments has a long lifetime of several hundred ms, such that phosphorescence is present throughout the chopper cycle, and some triplet lives until the next

cycle of the laser(s). This is not expected to cause a large problem as the system should quickly reach a steady state during signal averaging.

First, phosphorescence signals from **7.2** and **7.3** were compared between 416 nm – delay – 480 nm and 480 nm – delay – 416 nm pulse sequences. The first sequence should be able to drive the desired back electron transfer to form a triplet recombination product, but in the second, the initial 480 nm pulse should not be absorbed by the sample. While this second pulse sequence is equivalent to using a single 416 nm pulse, the 480 nm pulse alone was found to produce a small phosphorescence signal, possibly from phosphorescent impurities in glass filters used in the detection apparatus, which is accounted for under this procedure. This “on-off” ratio therefore provides a measure of how much triplet is produced through the back electron transfer reaction. These results are presented in Table 7.3. As expected from the EPR results, **7.3** in PrCN at 77 K shows increased formation of triplet with the pulses in the correct time order. In contrast, **7.2** in toluene at 77 K actually shows a drop in triplet yield with the second pump. Because the TTF donor in **7.2** is unstable to acids, 1% pyridine (a weak base) was added to the solvent in an attempt to stabilize the molecule, in case degradation of the TTF donor was responsible for phosphorescence after only a single 416 nm laser pulse. However, the ratio in toluene with 1% pyridine is nearly identical to that in neat toluene. **7.2** in PrCN with 1% pyridine shows a ratio slightly above 1, but not nearly as high as that for **7.3**. These results indicate that the spin measurement experiment is unlikely to be successful on **7.2** in toluene, but may work for **7.3**, and possibly for **7.2** in PrCN.

Molecule	Solvent	Second pump on/off ratio
<b>7.3</b>	PrCN	5.19
<b>7.2</b>	Toluene	0.85
<b>7.2</b>	Toluene + 1% pyridine	0.84
<b>7.2</b>	PrCN + 1% pyridine	1.17

**Table 7.3.** On/off ratios of phosphorescence following excitation by 416 nm and 480 nm pulses, measured as the ratio of integrated kinetics at delays of +50 ns (near the maximum signal) and -10 ns (with the 480 nm pulse coming before the 416 nm pulse). All samples were measured at 77 K,  $B_0 = 0$  mT.

Next, the phosphorescence signal was monitored as a function of the applied magnetic field. The magnetic field dependence of the triplet yield can indicate if the triplet derives from recombination of a RP, and can be used to determine the exchange coupling in the RP.<sup>75</sup> For **7.2** and **7.3**, the terminal  $D^+ \text{-ANI-NDI}^-$  radical pair has very weak exchange coupling. If spin mixing in this radical pair generates the triplet, the magnetic field effect on triplet yield (MFE) is expected to show a maximum at zero applied field and a sharp dropoff as the applied field is increased. In contrast, if spin mixing in the more strongly coupled  $D^+ \text{-ANI}^- \text{-NDI}$  radical pair generates the triplet, the MFE experiment should show a peak at much higher applied field. The spin measurement scheme relies on the triplet formed after the second laser pulse being derived from the more weakly coupled terminal radical pair, so if the MFE experiment does not show the expected result, the spin measurement experiment is not likely to work. Additionally, this data can help understand the source of the unexpected triplet formed in **7.2** after a single 416 nm pulse. The results of these MFE experiments are presented in Figure 7.17. **7.2** was studied in toluene and PrCN (both with 1% pyridine added) after a single 416 nm pulse. **7.3** was studied with both a single 416 nm pulse and after excitation by a 416 nm – 50 ns – 480 nm pulse sequence. The only experiment that shows a significant field effect is the signal from **7.3** after the two-pulse sequence. In this data, the triplet yield is at a maximum near zero applied field,

and quickly falls off, reaching a plateau above  $\sim 5$  mT (not shown). This result proves that the triplet derives from spin mixing within a weakly coupled radical pair, which in **7.3** can only be the terminal radical pair  $\text{BDX}^{+\bullet}-\text{ANI}-\text{NDI}^{\bullet-}$ . The MFE experiment therefore suggests that phosphorescence detection of the ZQC from this radical pair should be feasible using the two-pulse excitation sequence. The lack of a field effect from the **7.2** samples is consistent with recombination of the intermediate  $\text{TTF}^{+\bullet}-\text{ANI}^{\bullet-}-\text{NDI}$  radical pair leading to triplet formation. Recombination of this pair may compete with the charge shift to form  $\text{TTF}^{+\bullet}-\text{ANI}-\text{NDI}^{\bullet-}$  in frozen solvents.

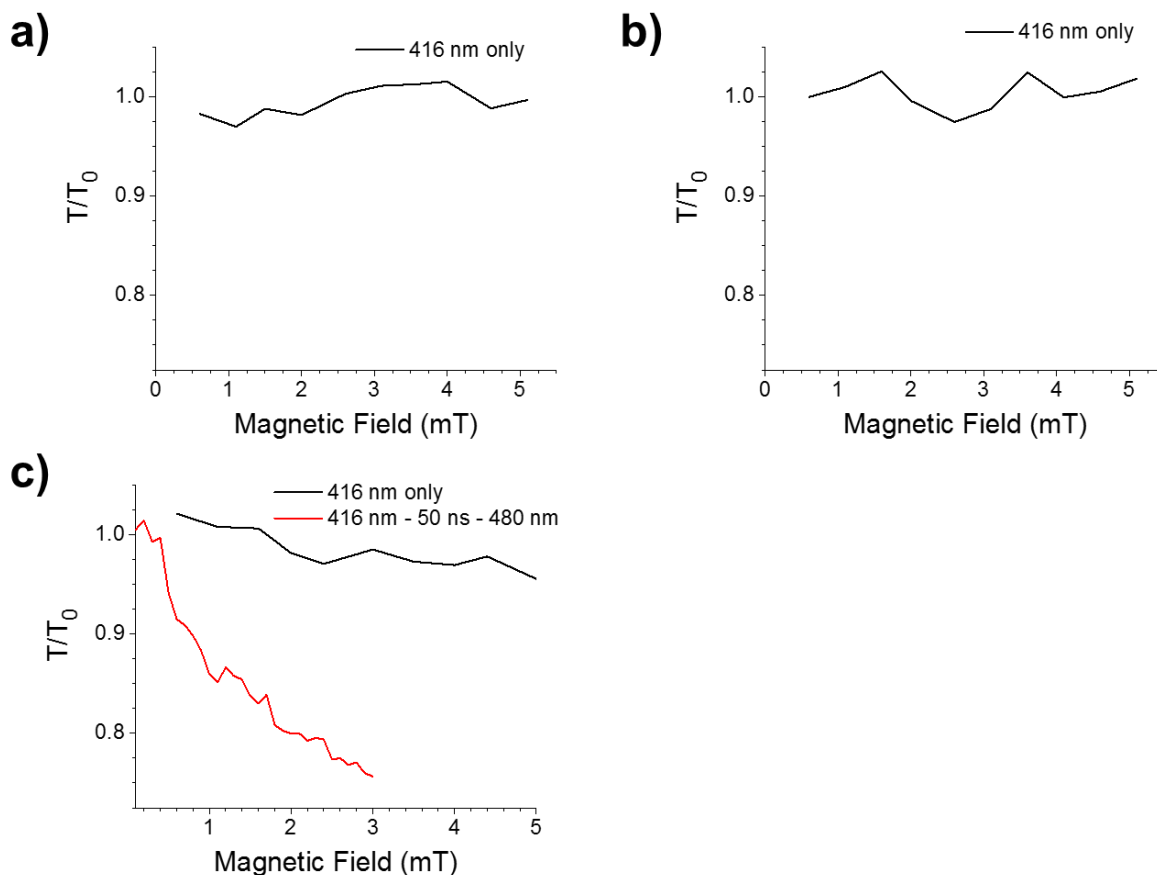


**Figure 7.17.** Magnetic field effects on triplet yields, as measured by phosphorescence, for (a) **7.2** in toluene with 1% pyridine, (b) **7.2** in PrCN with 1% pyridine, and (c) **7.3** in PrCN. Relative triplet yields are reported as  $T/T_0$ , the ratio of the phosphorescence signal at a given magnetic field to that measured with zero applied magnetic field. All samples are measured at 77 K.

The spin measurement experiment was then conducted on several samples by measuring the phosphorescence signal with different delays between the two pump pulses. From the previous results, we don't expect **7.2** to show much dependence of the phosphorescence signal on the delay spacing, but can hopefully observe the ZQC oscillations in **7.3**. These results are shown in Figure 7.18. As expected, samples of **7.2** in toluene and 5CB show only noise as the delay between the two pump pulses is varied. **7.2** in PrCN shows a small increase in yield as the

two pump pulses cross in time, but no oscillations attributable to the ZQC are observed. In contrast, the phosphorescence signal from **7.3** in PrCN shows a strong dependence on pump spacing, with the triplet formation increasing after the pulses cross in time and then decreasing slowly.

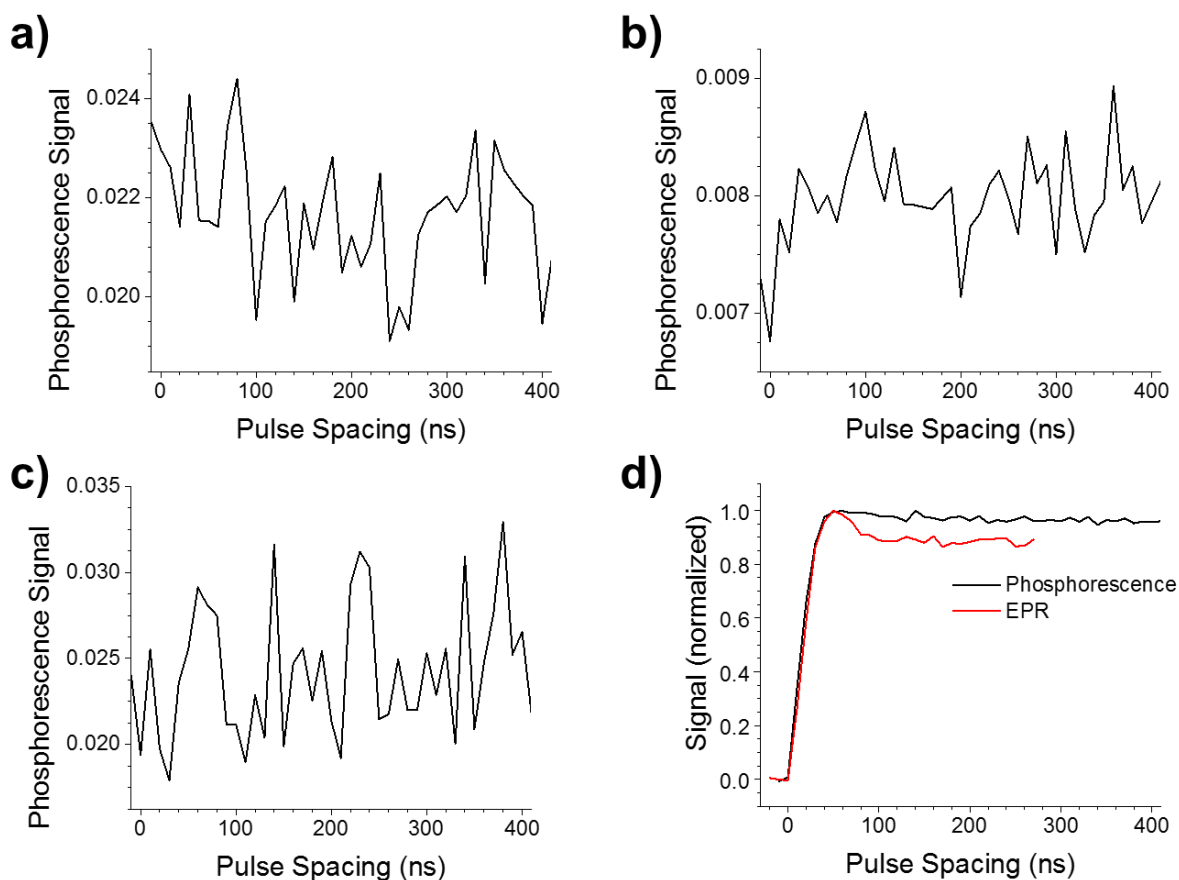


**Figure 7.18.** Phosphorescence signal versus the spacing in time between 416 nm and 480 nm pulses, for (a) **7.2** in toluene, (b) **7.2** in PrCN, (c) **7.2** in 5CB, and (d) **7.3** in PrCN, all measured at 77 K. The data in (d) is compared to EPR-detected data measured on **7.3** in PrCN at 85 K.

We can compare the data for **7.3** directly with the analogous EPR-detected measurement, performed under the same conditions except for a slight temperature difference (85 K for the

EPR experiment vs. 77 K for the phosphorescence experiment). The EPR-detected data contains a slight dip after the initial rise, interpreted as a partial oscillation of the ZQC. In contrast, this feature is not present in the phosphorescence-detected data. This discrepancy likely results from the presence of multiple ZQC frequencies in these samples, as a consequence of g-factor and hyperfine anisotropy. The presence of many dissimilar ZQC frequencies across the ensemble of molecules will lead to washing out of the ZQC oscillations from the bulk sample. While the samples for both experiments are oriented randomly with respect to the applied magnetic field, the EPR experiment involves detection of the triplet signal at a single magnetic field point. The dipolar coupling within the triplet state introduces anisotropy into the triplet EPR spectrum, such that the signal at a specific field position is due to a subpopulation of molecules oriented at a specific angle to the applied magnetic field. The EPR-detected experiment therefore probes only a subset of molecules with a specific orientation, narrowing the range of ZQC frequencies observed. In contrast, the phosphorescence detection imposes no such orientation selection: all triplet states will phosphoresce, regardless of their orientation relative to the magnetic field. Due to this issue, it would be advantageous to conduct the phosphorescence detection experiments in liquid solution, where rotational averaging would reduce the number of ZQC frequencies. However, this experiment was attempted on **5.2** near -78 °C, and no phosphorescence could be detected (in contrast to the same molecule at 77 K in frozen solvent). This suggests that the phosphorescence yield from  $^3\text{N}^{\cdot-}$ NDI is very low in liquid solution. Oriented samples could also circumvent this issue, but **7.1** and **7.3** show high triplet yields after a single 416 nm pulse in frozen 5CB, and **7.2** in 5CB did not show an increase in phosphorescence signal with the second, 480 nm pulse (Figure 7.18c).

## 7.4 Conclusions

We have proposed a scheme to measure the spin state of some radical pairs with an unprecedented time resolution. In this scheme, a laser pulse is used to trigger formation of a triplet recombination product that is otherwise energetically inaccessible. By controlling the time delay between the initial laser pulse used to generate the radical pair and the subsequent measurement laser pulse, the triplet character of the radical pair can be interrogated at different times after its formation.

We have identified and prepared a series of donor-acceptor molecules suitable for this measurement scheme, and have characterized their electron transfer behavior following initial photoexcitation, and following a second measurement laser pulse. We use EPR spectroscopy and phosphorescence to detect the desired triplet product following the measurement pulse. We find that the proposed kinetic scheme is likely correct: excitation of  $\text{NDI}^{\cdot-}$  by a second laser pulse triggers back electron transfer followed by recombination to a singlet or triplet product. The spin state of the triplet recombination product is found to correspond to that of the more weakly coupled radical pair before the second excitation, rather than that of the strongly coupled radical pair formed after back electron transfer. However, we were unable to unambiguously detect the ZQC, in part due to the wide range of ZQC frequencies present in the solid samples required for detection of the triplet recombination product.

While the present results are inferior to previously reported techniques for measuring ZQCs in photogenerated RPs, we have presented a novel method for measuring the spin states of RPs that may be useful in specific situations. Additionally, the broader idea behind this method

of gating the detection with a second laser pulse may allow measurement of spin states with high time resolution in other systems. Any system with a photoinduced, spin-selective process can potentially be a candidate for a similar measurement scheme. For example, fast spin dynamics in singlet fission are thought to be important for the efficiency of this process.<sup>236-239</sup> Identification of an appropriate spin-selective photoprocess in a singlet fission chromophore could enable similar studies.

## REFERENCES

1. Wolf, S. A.; Awschalom, D. D.; Buhrman, R. A.; Daughton, J. M.; von Molnár, S.; Roukes, M. L.; Chtchelkanova, A. Y.; Treger, D. M., Spintronics: A Spin-Based Electronics Vision for the Future. *Science* **2001**, *294* (5546), 1488-1495.
2. Pla, J. J.; Tan, K. Y.; Dehollain, J. P.; Lim, W. H.; Morton, J. J. L.; Jamieson, D. N.; Dzurak, A. S.; Morello, A., A single-atom electron spin qubit in silicon. *Nature* **2012**, *489* (7417), 541-545.
3. Petta, J. R.; Johnson, A. C.; Taylor, J. M.; Laird, E. A.; Yacoby, A.; Lukin, M. D.; Marcus, C. M.; Hanson, M. P.; Gossard, A. C., Coherent Manipulation of Coupled Electron Spins in Semiconductor Quantum Dots. *Science* **2005**, *309* (5744), 2180-2184.
4. DiVincenzo, D. P., The Physical Implementation of Quantum Computation. *Fortschritte der Physik* **2000**, *48* (9-11), 771-783.
5. Childress, L.; Gurudev Dutt, M. V.; Taylor, J. M.; Zibrov, A. S.; Jelezko, F.; Wrachtrup, J.; Hemmer, P. R.; Lukin, M. D., Coherent Dynamics of Coupled Electron and Nuclear Spin Qubits in Diamond. *Science* **2006**, *314* (5797), 281-285.
6. Forrest, S. R.; Thompson, M. E., Introduction: Organic Electronics and Optoelectronics. *Chemical Reviews* **2007**, *107* (4), 923-925.
7. Camarero, J.; Coronado, E., Molecular vs. inorganic spintronics: the role of molecular materials and single molecules. *Journal of Materials Chemistry* **2009**, *19* (12), 1678-1684.
8. Aviram, A.; Ratner, M. A., Molecular rectifiers. *Chemical Physics Letters* **1974**, *29* (2), 277-283.
9. Flood, A. H.; Stoddart, J. F.; Steuerman, D. W.; Heath, J. R., Whence Molecular Electronics? *Science* **2004**, *306* (5704), 2055-2056.
10. Carroll, R. L.; Gorman, C. B., The Genesis of Molecular Electronics. *Angewandte Chemie International Edition* **2002**, *41* (23), 4378-4400.
11. Rodgers, C. T.; Hore, P. J., Chemical magnetoreception in birds: The radical pair mechanism. *Proceedings of the National Academy of Sciences* **2009**, *106* (2), 353-360.
12. Liedvogel, M.; Maeda, K.; Henbest, K.; Schleicher, E.; Simon, T.; Timmel, C. R.; Hore, P. J.; Mouritsen, H., Chemical Magnetoreception: Bird Cryptochrome 1a Is Excited by Blue Light and Forms Long-Lived Radical-Pairs. *PLoS ONE* **2007**, *2* (10), e1106.
13. Hore, P. J.; Hunter, D. A.; McKie, C. D.; Hoff, A. J., Electron paramagnetic resonance of spin-correlated radical pairs in photosynthetic reactions. *Chemical Physics Letters* **1987**, *137* (6), 495-500.
14. Levanon, H.; Möbius, K., Advanced EPR Spectroscopy on Electron Transfer Processes in Photosynthesis and Biomimetic Model Systems. *Annual Review of Biophysics and Biomolecular Structure* **1997**, *26* (1), 495-540.
15. Rao, A.; Chow, P. C. Y.; Gelinas, S.; Schlenker, C. W.; Li, C.-Z.; Yip, H.-L.; Jen, A. K. Y.; Ginger, D. S.; Friend, R. H., The role of spin in the kinetic control of recombination in organic photovoltaics. *Nature* **2013**, *500* (7463), 435-439.
16. Niklas, J.; Poluektov, O. G., Charge Transfer Processes in OPV Materials as Revealed by EPR Spectroscopy. *Advanced Energy Materials* **2017**, 1602226-n/a.
17. Congreve, D. N.; Lee, J.; Thompson, N. J.; Hontz, E.; Yost, S. R.; Reuswig, P. D.; Bahlke, M. E.; Reineke, S.; Van Voorhis, T.; Baldo, M. A., External Quantum Efficiency Above

100% in a Singlet-Exciton-Fission-Based Organic Photovoltaic Cell. *Science* **2013**, *340* (6130), 334-337.

18. Vardeny, Z. V.; Heeger, A. J.; Dodabalapur, A., Fundamental research needs in organic electronic materials. *Synthetic Metals* **2005**, *148* (1), 1-3.

19. Yersin, H.; Rausch, A. F.; Czerwieńiec, R.; Hofbeck, T.; Fischer, T., The triplet state of organo-transition metal compounds. Triplet harvesting and singlet harvesting for efficient OLEDs. *Coordination Chemistry Reviews* **2011**, *255* (21–22), 2622-2652.

20. Ochsner, M., Photophysical and photobiological processes in the photodynamic therapy of tumours. *Journal of Photochemistry and Photobiology B: Biology* **1997**, *39* (1), 1-18.

21. Castano, A. P.; Demidova, T. N.; Hamblin, M. R., Mechanisms in photodynamic therapy: part one—photosensitizers, photochemistry and cellular localization. *Photodiagnosis and Photodynamic Therapy* **2004**, *1* (4), 279-293.

22. Weil, J. A.; Bolton, J. R., *Electron Paramagnetic Resonance: Elementary Theory and Practical Applications*. Wiley: 2007.

23. McConnell, H. M., Indirect Hyperfine Interactions in the Paramagnetic Resonance Spectra of Aromatic Free Radicals. *The Journal of Chemical Physics* **1956**, *24* (4), 764-766.

24. Norris, J. R.; Uphaus, R. A.; Crespi, H. L.; Katz, J. J., Electron Spin Resonance of Chlorophyll and the Origin of Signal I in Photosynthesis. *Proceedings of the National Academy of Sciences of the United States of America* **1971**, *68* (3), 625-628.

25. Saeki, A.; Seki, S.; Tagawa, S., Electrodeless measurement of charge carrier mobility in pentacene by microwave and optical spectroscopy techniques. *Journal of Applied Physics* **2006**, *100* (2), 023703.

26. Warman, J. M.; Gelinck, G. H.; Piet, J. J.; Suykerbuyk, J. W.; de Haas, M. P.; Langeveld-Voss, B. M.; Janssen, R. A.; Hwang, D.-H.; Holmes, A. B.; Remmers, M.; Neher, D.; Muellen, K.; Bauerle, P. In *Time-resolved microwave measurements of the polarizability of photoexcitons on conjugated polymer chains*, 1997; pp 142-149.

27. de Haas, M. P.; Warman, J. M.; Anthopoulos, T. D.; de Leeuw, D. M., The Mobility and Decay Kinetics of Charge Carriers in Pulse-Ionized Microcrystalline PCBM Powder. *Advanced Functional Materials* **2006**, *16* (17), 2274-2280.

28. De Haas, M. P.; Warman, J. M., Photon-induced molecular charge separation studied by nanosecond time-resolved microwave conductivity. *Chemical Physics* **1982**, *73* (1), 35-53.

29. Naaman, R.; Waldeck, D. H., Spintronics and Chirality: Spin Selectivity in Electron Transport Through Chiral Molecules. *Annual Review of Physical Chemistry* **2015**, *66* (1), 263-281.

30. Dance, Z. E. X.; Mickley, S. M.; Wilson, T. M.; Ricks, A. B.; Scott, A. M.; Ratner, M. A.; Wasielewski, M. R., Intersystem Crossing Mediated by Photoinduced Intramolecular Charge Transfer: Julolidine–Anthracene Molecules with Perpendicular  $\pi$  Systems. *The Journal of Physical Chemistry A* **2008**, *112* (18), 4194-4201.

31. Morton, J. J. L.; Tyryshkin, A. M.; Brown, R. M.; Shankar, S.; Lovett, B. W.; Ardavan, A.; Schenkel, T.; Haller, E. E.; Ager, J. W.; Lyon, S. A., Solid-state quantum memory using the  $^{31}\text{P}$  nuclear spin. *Nature* **2008**, *455* (7216), 1085-1088.

32. Closs, G. L.; Forbes, M. D. E.; Norris, J. R., Spin-polarized electron paramagnetic resonance spectra of radical pairs in micelles: observation of electron spin-spin interactions. *The Journal of Physical Chemistry* **1987**, *91* (13), 3592-3599.

33. Prasittichai, C.; Hupp, J. T., Surface Modification of SnO<sub>2</sub> Photoelectrodes in Dye-Sensitized Solar Cells: Significant Improvements in Photovoltage via Al<sub>2</sub>O<sub>3</sub> Atomic Layer Deposition. *The Journal of Physical Chemistry Letters* **2010**, *1* (10), 1611-1615.
34. Proctor, C. M.; Kuik, M.; Nguyen, T.-Q., Charge carrier recombination in organic solar cells. *Progress in Polymer Science* **2013**, *38* (12), 1941-1960.
35. Mohapatra, S. K.; Raja, K. S.; Mahajan, V. K.; Misra, M., Efficient Photoelectrolysis of Water using TiO<sub>2</sub> Nanotube Arrays by Minimizing Recombination Losses with Organic Additives. *The Journal of Physical Chemistry C* **2008**, *112* (29), 11007-11012.
36. Liu, J.; Bai, H.; Wang, Y.; Liu, Z.; Zhang, X.; Sun, D. D., Self-Assembling TiO<sub>2</sub> Nanorods on Large Graphene Oxide Sheets at a Two-Phase Interface and Their Anti-Recombination in Photocatalytic Applications. *Advanced Functional Materials* **2010**, *20* (23), 4175-4181.
37. Ji, Z.; He, M.; Huang, Z.; Ozkan, U.; Wu, Y., Photostable p-Type Dye-Sensitized Photoelectrochemical Cells for Water Reduction. *Journal of the American Chemical Society* **2013**, *135* (32), 11696-11699.
38. Colvin, M. T.; Ricks, A. B.; Scott, A. M.; Smeigh, A. L.; Carmieli, R.; Miura, T.; Wasielewski, M. R., Magnetic Field-Induced Switching of the Radical-Pair Intersystem Crossing Mechanism in a Donor–Bridge–Acceptor Molecule for Artificial Photosynthesis. *Journal of the American Chemical Society* **2010**, *133* (5), 1240-1243.
39. Dance, Z. E. X.; Mi, Q.; McCamant, D. W.; Ahrens, M. J.; Ratner, M. A.; Wasielewski, M. R., Time-Resolved EPR Studies of Photogenerated Radical Ion Pairs Separated by p-Phenylene Oligomers and of Triplet States Resulting from Charge Recombination. *The Journal of Physical Chemistry B* **2006**, *110* (50), 25163-25173.
40. Giacobbe, E. M.; Mi, Q. X.; Colvin, M. T.; Cohen, B.; Ramanan, C.; Scott, A. M.; Yeganeh, S.; Marks, T. J.; Ratner, M. A.; Wasielewski, M. R., Ultrafast Intersystem Crossing and Spin Dynamics of Photoexcited Perylene-3,4:9,10-bis(dicarboximide) Covalently Linked to a Nitroxide Radical at Fixed Distances. *Journal of the American Chemical Society* **2009**, *131* (10), 3700-3712.
41. Wu, Y.; Krzyaniak, M. D.; Stoddart, J. F.; Wasielewski, M. R., Spin Frustration in the Triradical Trianion of a Naphthalenediimide Molecular Triangle. *Journal of the American Chemical Society* **2017**, *139* (8), 2948-2951.
42. Gardner, D. M.; Chen, H.-F.; Krzyaniak, M. D.; Ratner, M. A.; Wasielewski, M. R., Large Dipolar Spin–Spin Interaction in a Photogenerated U-Shaped Triradical. *The Journal of Physical Chemistry A* **2015**, *119* (29), 8040-8048.
43. Colvin, M. T.; Smeigh, A. L.; Giacobbe, E. M.; Conron, S. M. M.; Ricks, A. B.; Wasielewski, M. R., Ultrafast Intersystem Crossing and Spin Dynamics of Zinc meso-Tetraphenylporphyrin Covalently Bound to Stable Radicals. *The Journal of Physical Chemistry A* **2011**, *115* (26), 7538-7549.
44. Rozenshtein, V.; Berg, A.; Stavitski, E.; Levanon, H.; Franco, L.; Corvaja, C., Electron Spin Polarization of Functionalized Fullerenes. Reversed Quartet Mechanism. *The Journal of Physical Chemistry A* **2005**, *109* (49), 11144-11154.
45. Horwitz, N. E.; Phelan, B. T.; Nelson, J. N.; Krzyaniak, M. D.; Wasielewski, M. R., Picosecond Control of Photogenerated Radical Pair Lifetimes Using a Stable Third Radical. *The Journal of Physical Chemistry A* **2016**, *120* (18), 2841-2853.

46. Hoff, A. J.; Hore, P. J., Electron spin polarization in a three-electron spin system. An application to bacterial photosynthesis. *Chemical Physics Letters* **1984**, *108* (1), 104-110.
47. Colvin, M. T.; Carmieli, R.; Miura, T.; Richert, S.; Gardner, D. M.; Smeigh, A. L.; Dyar, S. M.; Conron, S. M.; Ratner, M. A.; Wasielewski, M. R., Electron Spin Polarization Transfer from Photogenerated Spin-Correlated Radical Pairs to a Stable Radical Observer Spin. *The Journal of Physical Chemistry A* **2013**, *117* (25), 5314-5325.
48. Teki, Y.; Tamekuni, H.; Takeuchi, J.; Miura, Y., First evidence for a uniquely spin-polarized quartet photoexcited state of a pi-conjugated spin system generated via the ion-pair state. *Angew Chem Int Edit* **2006**, *45* (28), 4666-4670.
49. Teki, Y.; Tamekuni, H.; Haruta, K.; Takeuchi, J.; Miura, Y., Design, synthesis, and uniquely electron-spin-polarized quartet photo-excited state of a pi-conjugated spin system generated via the ion-pair state. *Journal of Materials Chemistry* **2008**, *18* (4), 381-391.
50. Campos Venuti, L.; Degli Esposti Boschi, C.; Roncaglia, M., Qubit Teleportation and Transfer across Antiferromagnetic Spin Chains. *Physical Review Letters* **2007**, *99* (6), 060401.
51. Martinez, J. F.; La Porte, N. T.; Mauck, C. M.; Wasielewski, M. R., Photo-driven electron transfer from the highly reducing excited state of naphthalene diimide radical anion to a CO<sub>2</sub> reduction catalyst within a molecular triad. *Faraday Discussions* **2017**.
52. La Porte, N. T.; Martinez, J.; Hedstrom, S.; Rudshteyn, B.; Phelan, B. T.; Mauck, C. M.; Young, R. M.; Batista, V. S.; Wasielewski, M. R., Photoinduced Electron Transfer from Rylenediimide Radical Anions and Dianions to Re(bpy)(CO)<sub>3</sub> using Red and Near-infrared Light. *Chemical Science* **2017**.
53. Wu, Y.-L.; Horwitz, N. E.; Chen, K.-S.; Gomez-Gualdron, D. A.; Luu, N. S.; Ma, L.; Wang, T. C.; Hersam, M. C.; Hupp, J. T.; Farha, O. K.; Snurr, R. Q.; Wasielewski, M. R., G-quadruplex organic frameworks. *Nat Chem* **2016**, *advance online publication*.
54. *BP Energy Outlook 2017*; BP p. l. c.: London, UK, 2017.
55. Gust, D.; Moore, T. A.; Moore, A. L., Solar Fuels via Artificial Photosynthesis. *Accounts of Chemical Research* **2009**, *42* (12), 1890-1898.
56. Wasielewski, M. R., Photoinduced electron transfer in supramolecular systems for artificial photosynthesis. *Chemical Reviews* **1992**, *92* (3), 435-461.
57. Benson, E. E.; Kubiak, C. P.; Sathrum, A. J.; Smieja, J. M., Electrocatalytic and homogeneous approaches to conversion of CO<sub>2</sub> to liquid fuels. *Chemical Society Reviews* **2009**, *38* (1), 89-99.
58. Gosztola, D.; Niemczyk, M. P.; Svec, W.; Lukas, A. S.; Wasielewski, M. R., Excited Doublet States of Electrochemically Generated Aromatic Imide and Diimide Radical Anions. *The Journal of Physical Chemistry A* **2000**, *104* (28), 6545-6551.
59. Lu, C.; Fujitsuka, M.; Sugimoto, A.; Majima, T., Dual Character of Excited Radical Anions in Aromatic Diimide Bis(radical anion)s: Donor or Acceptor? *The Journal of Physical Chemistry C* **2017**, *121* (8), 4558-4563.
60. Lu, C.; Fujitsuka, M.; Sugimoto, A.; Majima, T., Unprecedented Intramolecular Electron Transfer from Excited Perylenediimide Radical Anion. *The Journal of Physical Chemistry C* **2016**, *120* (23), 12734-12741.
61. Fujitsuka, M.; Kim, S. S.; Lu, C.; Tojo, S.; Majima, T., Intermolecular and Intramolecular Electron Transfer Processes from Excited Naphthalene Diimide Radical Anions. *The Journal of Physical Chemistry B* **2015**, *119* (24), 7275-7282.

62. Ghosh, I.; Ghosh, T.; Bardagi, J. I.; König, B., Reduction of aryl halides by consecutive visible light-induced electron transfer processes. *Science* **2014**, *346* (6210), 725-728.
63. Wasielewski, M. R., Self-Assembly Strategies for Integrating Light Harvesting and Charge Separation in Artificial Photosynthetic Systems. *Accounts of Chemical Research* **2009**, *42* (12), 1910-1921.
64. Hilczer, M.; Tachiya, M., Unified Theory of Geminate and Bulk Electron–Hole Recombination in Organic Solar Cells. *The Journal of Physical Chemistry C* **2010**, *114* (14), 6808-6813.
65. Weller, A., Photoinduced Electron Transfer in Solution: Exciplex and Radical Ion Pair Formation Free Enthalpies and their Solvent Dependence. In *Zeitschrift für Physikalische Chemie*, 1982; Vol. 133, p 93.
66. Armarego, W. L. F.; Chai, C., *Purification of Laboratory Chemicals*. 7th ed.; Butterworth-Heinemann: Oxford, United Kingdom, 2013.
67. *CRC Handbook of Chemistry and Physics*. 88 ed.; CRC Press: Boca Raton, 2008.
68. Miller, S. E.; Lukas, A. S.; Marsh, E.; Bushard, P.; Wasielewski, M. R., Photoinduced Charge Separation Involving an Unusual Double Electron Transfer Mechanism in a Donor–Bridge–Acceptor Molecule. *Journal of the American Chemical Society* **2000**, *122* (32), 7802-7810.
69. Fujiyama, T.; Sugimoto, K.; Sekiguchi, M. Novel compounds and organic electronic devices. WO2005092901A1, 2005.
70. Carmieli, R.; Mi, Q.; Ricks, A. B.; Giacobbe, E. M.; Mickley, S. M.; Wasielewski, M. R., Direct Measurement of Photoinduced Charge Separation Distances in Donor–Acceptor Systems for Artificial Photosynthesis Using OOP-ESEEM. *Journal of the American Chemical Society* **2009**, *131* (24), 8372-8373.
71. Nelson, J. N.; Krzyaniak, M. D.; Horwitz, N. E.; Rugg, B. K.; Phelan, B. T.; Wasielewski, M. R., Zero Quantum Coherence in a Series of Covalent Spin-Correlated Radical Pairs. *The Journal of Physical Chemistry A* **2017**.
72. Marcus, R. A., The theory of oxidation-reduction reactions involving electron transfer. I. *J. Chem. Phys.* **1956**, *24*, 966-78.
73. Yonemura, H.; Forbes, M. D. E., Electron Spin Exchange in Linked Phenothiazine–Viologen Charge Transfer Complexes Incorporated in “Through-Ring” (Rotaxane)  $\alpha$ -Cyclodextrins. *Photochemistry and Photobiology* **2015**, *91* (3), 672-677.
74. Weiss, E. A.; Tauber, M. J.; Ratner, M. A.; Wasielewski, M. R., Electron Spin Dynamics as a Probe of Molecular Dynamics: Temperature-Dependent Magnetic Field Effects on Charge Recombination within a Covalent Radical Ion Pair. *Journal of the American Chemical Society* **2005**, *127* (16), 6052-6061.
75. Weiss, E. A.; Ratner, M. A.; Wasielewski, M. R., Direct Measurement of Singlet-Triplet Splitting within Rodlike Photogenerated Radical Ion Pairs Using Magnetic Field Effects: Estimation of the Electronic Coupling for Charge Recombination. *J. Phys. Chem. A* **2003**, *107* (19), 3639-3647.
76. Sinks, L. E.; Weiss, E. A.; Giaimo, J. M.; Wasielewski, M. R., Effect of charge delocalization on radical ion pair electronic coupling. *Chemical Physics Letters* **2005**, *404* (4–6), 244-249.

77. Jakobsen, S.; Mikkelsen, K. V.; Pedersen, S. U., Calculations of Intramolecular Reorganization Energies for Electron-Transfer Reactions Involving Organic Systems. *The Journal of Physical Chemistry* **1996**, *100* (18), 7411-7417.
78. Greenfield, S. R.; Svec, W. A.; Gosztola, D.; Wasielewski, M. R., Multistep Photochemical Charge Separation in Rod-like Molecules Based on Aromatic Imides and Diimides. *Journal of the American Chemical Society* **1996**, *118* (28), 6767-6777.
79. Dorinson, A.; Ralston, A. W., Refractive Indices of the Normal Saturated Aliphatic Nitriles. *Journal of the American Chemical Society* **1944**, *66* (3), 361-362.
80. Wohlfarth, C. *Refractive index of pyridine: Datasheet from Landolt-Börnstein - Group III Condensed Matter · Volume 47: "Refractive Indices of Pure Liquids and Binary Liquid Mixtures (Supplement to III/38)" in SpringerMaterials* ([http://dx.doi.org/10.1007/978-3-540-75291-2\\_125](http://dx.doi.org/10.1007/978-3-540-75291-2_125)), Springer-Verlag Berlin Heidelberg.
81. Wohlfarth, C. *Refractive index of N,N-dimethylformamide: Datasheet from Landolt-Börnstein - Group III Condensed Matter · Volume 47: "Refractive Indices of Pure Liquids and Binary Liquid Mixtures (Supplement to III/38)" in SpringerMaterials* ([http://dx.doi.org/10.1007/978-3-540-75291-2\\_67](http://dx.doi.org/10.1007/978-3-540-75291-2_67)), Springer-Verlag Berlin Heidelberg.
82. Hartnig, C.; Koper, M. T. M., Molecular dynamics simulations of solvent reorganization in electron-transfer reactions. *The Journal of Chemical Physics* **2001**, *115* (18), 8540-8546.
83. Small, D. W.; Matyushov, D. V.; Voth, G. A., The Theory of Electron Transfer Reactions: What May Be Missing? *Journal of the American Chemical Society* **2003**, *125* (24), 7470-7478.
84. Savéant, J.-M., Effect of Ion Pairing on the Mechanism and Rate of Electron Transfer. Electrochemical Aspects. *The Journal of Physical Chemistry B* **2001**, *105* (37), 8995-9001.
85. Jones, J. W.; Gibson, H. W., Ion Pairing and Host-Guest Complexation in Low Dielectric Constant Solvents. *Journal of the American Chemical Society* **2003**, *125* (23), 7001-7004.
86. Heinen, U.; Berthold, T.; Kothe, G.; Stavitski, E.; Galili, T.; Levanon, H.; Wiederrecht, G.; Wasielewski, M. R., High Time Resolution Q-Band EPR Study of Sequential Electron Transfer in a Triad Oriented in a Liquid Crystal. *The Journal of Physical Chemistry A* **2002**, *106* (10), 1933-1937.
87. Hirofumi, N.; Masahide, T.; Noboru, H.; Satoshi, N.; Atsuhiko, O., Investigation of Spin-Correlated Ion Pairs in Distance-Fixed Triads by Time-Resolved Electron Paramagnetic Resonance. *Bulletin of the Chemical Society of Japan* **1995**, *68* (8), 2193-2202.
88. Fujitsuka, M.; Ohsaka, T.; Majima, T., Dual electron transfer pathways from the excited C60 radical anion: enhanced reactivities due to the photoexcitation of reaction intermediates. *Physical Chemistry Chemical Physics* **2015**, *17* (46), 31030-31038.
89. Pony Yu, R.; Hesk, D.; Rivera, N.; Pelczer, I.; Chirik, P. J., Iron-catalysed tritiation of pharmaceuticals. *Nature* **2016**, *529* (7585), 195-199.
90. Coropceanu, V.; Cornil, J.; da Silva Filho, D. A.; Olivier, Y.; Silbey, R.; Brédas, J.-L., Charge Transport in Organic Semiconductors. *Chemical Reviews* **2007**, *107* (4), 926-952.
91. Grozema, F. C.; Siebbeles, L. D. A., Mechanism of charge transport in self-organizing organic materials. *International Reviews in Physical Chemistry* **2008**, *27* (1), 87-138.

92. Norris, J. R.; Uphaus, R. A.; Crespi, H. L.; Katz, J. J., Electron Spin Resonance of Chlorophyll and the Origin of Signal I in Photosynthesis. *Proceedings of the National Academy of Sciences* **1971**, *68* (3), 625-628.
93. Quine, R. W.; Mitchell, D. G.; Eaton, G. R., A general purpose Q-measuring circuit using pulse ring-down. *Concepts in Magnetic Resonance Part B: Magnetic Resonance Engineering* **2011**, *39B* (1), 43-46.
94. Tauber, M. J.; Kelley, R. F.; Giaimo, J. M.; Rybtchinski, B.; Wasielewski, M. R., Electron Hopping in  $\pi$ -Stacked Covalent and Self-Assembled Perylene Diimides Observed by ENDOR Spectroscopy. *Journal of the American Chemical Society* **2006**, *128* (6), 1782-1783.
95. Wu, Y.; Nalluri, S. K. M.; Young, R. M.; Krzyaniak, M. D.; Margulies, E. A.; Stoddart, J. F.; Wasielewski, M. R., Charge and Spin Transport in an Organic Molecular Square. *Angewandte Chemie* **2015**, *127* (41), 12139-12145.
96. Wu, Y.; Young, R. M.; Frasconi, M.; Schneebeli, S. T.; Spenst, P.; Gardner, D. M.; Brown, K. E.; Würthner, F.; Stoddart, J. F.; Wasielewski, M. R., Ultrafast Photoinduced Symmetry-Breaking Charge Separation and Electron Sharing in Perylenediimide Molecular Triangles. *Journal of the American Chemical Society* **2015**, *137* (41), 13236-13239.
97. Wilson, T. M.; Zeidan, T. A.; Hariharan, M.; Lewis, F. D.; Wasielewski, M. R., Electron Hopping among Cofacially Stacked Perylenediimides Assembled by Using DNA Hairpins. *Angewandte Chemie International Edition* **2010**, *49* (13), 2385-2388.
98. Roznyatovskiy, V. V.; Gardner, D. M.; Eaton, S. W.; Wasielewski, M. R., Radical Anions of Trifluoromethylated Perylene and Naphthalene Imide and Diimide Electron Acceptors. *Organic Letters* **2014**, *16* (3), 696-699.
99. Watkins, G.; Corbett, J., Defects in irradiated silicon: electron paramagnetic resonance and electron-nuclear double resonance of the Si-E center. *Physical Review* **1964**, *134* (5A), A1359.
100. Nisenoff, M.; Fan, H., Electron Spin Resonance in Neutron-Irradiated Silicon. *Physical Review* **1962**, *128* (4), 1605.
101. Watkins, G., EPR of a trapped vacancy in boron-doped silicon. *Physical Review B* **1976**, *13* (6), 2511.
102. Wiederrecht, G. P.; Svec, W. A.; Wasielewski, M. R.; Galili, T.; Levanon, H., Triplet States with Unusual Spin Polarization Resulting from Radical Ion Pair Recombination at Short Distances. *Journal of the American Chemical Society* **1999**, *121* (33), 7726-7727.
103. Bullock, J. E.; Carmieli, R.; Mickley, S. M.; Vura-Weis, J.; Wasielewski, M. R., Photoinitiated Charge Transport through  $\pi$ -Stacked Electron Conduits in Supramolecular Ordered Assemblies of Donor-Acceptor Triads. *Journal of the American Chemical Society* **2009**, *131* (33), 11919-11929.
104. Salikhov, K. M.; Bock, C. H.; Stehlik, D., Time development of Electron Spin Polarization in magnetically coupled, spin correlated radical pairs. *Appl Magn Reson* **1990**, *1* (2), 195-211.
105. Buckley, C. D.; Hunter, D. A.; Hore, P. J.; McLauchlan, K. A., Electron spin resonance of spin-correlated radical pairs. *Chemical Physics Letters* **1987**, *135* (3), 307-312.
106. Jin, S.; Ding, X.; Feng, X.; Supur, M.; Furukawa, K.; Takahashi, S.; Addicoat, M.; El-Khouly, M. E.; Nakamura, T.; Irle, S.; Fukuzumi, S.; Nagai, A.; Jiang, D., Charge Dynamics in

A Donor–Acceptor Covalent Organic Framework with Periodically Ordered Bicontinuous Heterojunctions. *Angewandte Chemie International Edition* **2013**, 52 (7), 2017-2021.

107. Jin, S.; Supur, M.; Addicoat, M.; Furukawa, K.; Chen, L.; Nakamura, T.; Fukuzumi, S.; Irle, S.; Jiang, D., Creation of Superheterojunction Polymers via Direct Polycondensation: Segregated and Bicontinuous Donor–Acceptor  $\pi$ -Columnar Arrays in Covalent Organic Frameworks for Long-Lived Charge Separation. *Journal of the American Chemical Society* **2015**, 137 (24), 7817-7827.

108. Franco, L.; Ruzzi, M.; Corvaja, C., Time-Resolved Electron Paramagnetic Resonance of Photoinduced Ion Pairs in Blends of Polythiophene and Fullerene Derivatives. *The Journal of Physical Chemistry B* **2005**, 109 (28), 13431-13435.

109. Behrends, J.; Sperlich, A.; Schnegg, A.; Biskup, T.; Teutloff, C.; Lips, K.; Dyakonov, V.; Bittl, R., Direct detection of photoinduced charge transfer complexes in polymer fullerene blends. *Physical Review B* **2012**, 85 (12), 125206.

110. Green, S.; Fox, M. A., Intramolecular Photoinduced Electron Transfer from Nitroxyl Radicals. *The Journal of Physical Chemistry* **1995**, 99 (40), 14752-14757.

111. Sekiguchi, S.; Kobori, Y.; Akiyama, K.; Tero-Kubota, S., Marcus Free Energy Dependence of the Sign of Exchange Interactions in Radical Ion Pairs Generated by Photoinduced Electron Transfer Reactions. *Journal of the American Chemical Society* **1998**, 120 (6), 1325-1326.

112. Pensack, R. D.; Guo, C.; Vakhshouri, K.; Gomez, E. D.; Asbury, J. B., Influence of Acceptor Structure on Barriers to Charge Separation in Organic Photovoltaic Materials. *The Journal of Physical Chemistry C* **2012**, 116 (7), 4824-4831.

113. Gélinas, S.; Rao, A.; Kumar, A.; Smith, S. L.; Chin, A. W.; Clark, J.; van der Poll, T. S.; Bazan, G. C.; Friend, R. H., Ultrafast Long-Range Charge Separation in Organic Semiconductor Photovoltaic Diodes. *Science* **2014**, 343 (6170), 512-516.

114. Bakulin, A. A.; Rao, A.; Pavelyev, V. G.; van Loosdrecht, P. H. M.; Pshenichnikov, M. S.; Niedzialek, D.; Cornil, J.; Beljonne, D.; Friend, R. H., The Role of Driving Energy and Delocalized States for Charge Separation in Organic Semiconductors. *Science* **2012**, 335 (6074), 1340-1344.

115. Savoie, B. M.; Rao, A.; Bakulin, A. A.; Gelinas, S.; Movaghar, B.; Friend, R. H.; Marks, T. J.; Ratner, M. A., Unequal Partnership: Asymmetric Roles of Polymeric Donor and Fullerene Acceptor in Generating Free Charge. *Journal of the American Chemical Society* **2014**, 136 (7), 2876-2884.

116. Lee, J.; Vandewal, K.; Yost, S. R.; Bahlke, M. E.; Goris, L.; Baldo, M. A.; Manca, J. V.; Voorhis, T. V., Charge Transfer State Versus Hot Exciton Dissociation in Polymer–Fullerene Blended Solar Cells. *Journal of the American Chemical Society* **2010**, 132 (34), 11878-11880.

117. Veldman, D.; İpek, Ö.; Meskers, S. C. J.; Sweelssen, J.; Koetse, M. M.; Veenstra, S. C.; Kroon, J. M.; van Bavel, S. S.; Loos, J.; Janssen, R. A. J., Compositional and Electric Field Dependence of the Dissociation of Charge Transfer Excitons in Alternating Polyfluorene Copolymer/Fullerene Blends. *Journal of the American Chemical Society* **2008**, 130 (24), 7721-7735.

118. Rao, A.; Chow, P. C.; Gelinas, S.; Schlenker, C. W.; Li, C. Z.; Yip, H. L.; Jen, A. K.; Ginger, D. S.; Friend, R. H., The role of spin in the kinetic control of recombination in organic photovoltaics. *Nature* **2013**, 500 (7463), 435-9.

119. Hilczer, M.; Tachiya, M., Unified Theory of Geminate and Bulk Electron–Hole Recombination in Organic Solar Cells. *J. Phys. Chem. C* **2010**, *114* (14), 6808-6813.
120. Coronado, E.; Epstein, A. J., Molecular spintronics and quantum computing. *Journal of Materials Chemistry* **2009**, *19* (12), 1670-1671.
121. Epstein, A. J., Organic-based magnets. Opportunities in photoinduced magnetism, spintronics, fractal magnetism, and beyond. *MRS Bulletin* **2003**, *28* (7), 492-499.
122. Vlasiouk, I.; Smirnov, S.; Kutzki, O.; Wedel, M.; Montforts, F.-P., Radical Induced Impeding of Charge Recombination. *J. Phys. Chem. B* **2002**, *106*, 8657-8666.
123. Buchachenko, A. L.; Berdinsky, V. L., Electron Spin Catalysis. *Chem. Rev.* **2002**, *102* (3), 603-612.
124. Mori, Y.; Sakaguchi, Y.; Hayashi, H., Spin Chemical Approach towards Long-Lived Charge-Separated States Generated by Photoinduced Intramolecular Electron Transfer in a Donor-Bridge-Acceptor System. *Bull. Chem. Soc. Jpn.* **2001**, *74* (2), 293-304.
125. Mori, Y.; Sakaguchi, Y.; Hayashi, H., Magnetic Field Effects on Chemical Reactions of Biradical Ion Pairs in Homogeneous Fluid Solvents. *J. Phys. Chem. A* **2000**, *104*, 4896-4905.
126. van Dijk, B.; Gast, P.; Hoff, A. J.; Dzuba, S. A., Control of Singlet-Precursor Radical Pair Lifetime by Manipulation of Spin-Selective Reaction Pathways. *J. Phys. Chem. A* **1997**, *101* (4), 719-724.
127. Hoff, A. J., Magnetic field effects on photosynthetic reactions. *Quarterly Reviews of Biophysics* **1981**, *14* (04), 599-665.
128. Steiner, U. E.; Ulrich, T., Magnetic field effects in chemical kinetics and related phenomena. *Chem. Rev.* **1989**, *89*, 51-147.
129. Cintolesi, F.; Ritz, T.; Kay, C. W. M.; Timmel, C. R.; Hore, P. J., Anisotropic recombination of an immobilized photoinduced radical pair in a 50- $\mu$ T magnetic field: a model avian photomagnetoceptor. *Chemical Physics* **2003**, *294* (3), 385-399.
130. Mi, Q.; Chernick, E. T.; McCamant, D. W.; Weiss, E. A.; Ratner, M. A.; Wasielewski, M. R., Spin Dynamics of Photogenerated Triradicals in Fixed Distance Electron Donor-Chromophore-Acceptor-TEMPO Molecules. *J. Phys. Chem. A* **2006**, *110* (23), 7323-7333.
131. Weiss, E. A.; Chernick, E. T.; Wasielewski, M. R., Modulation of Radical Ion Pair Lifetimes by the Presence of a Third Spin in Rodlike Donor-Acceptor Triads. *Journal of the American Chemical Society* **2004**, *126* (8), 2326-2327.
132. Blankenship, R. E.; Schaafsma, T. J.; Parson, W. W., Magnetic field effects on radical pair intermediates in bacterial photosynthesis. *Biochim. Biophys. Acta* **1977**, *461*, 297-305.
133. Weller, A.; Staerk, H.; Treichel, R., Magnetic-field Effects on Geminate Radical-pair Recombination. *Faraday Discuss. Chem. Soc.* **1984**, *78*, 271-278.
134. Miura, T.; Wasielewski, M. R., Manipulating Photogenerated Radical Ion Pair Lifetimes in Wirelike Molecules Using Microwave Pulses: Molecular Spintronic Gates. *Journal of the American Chemical Society* **2011**, *133* (9), 2844-2847.
135. Zhang, Y.; Basel, T. P.; Gautam, B. R.; Yang, X.; Mascaro, D. J.; Liu, F.; Vardeny, Z. V., Spin-enhanced organic bulk heterojunction photovoltaic solar cells. *Nat Commun* **2012**, *3*, 1043.
136. Wasielewski, M. R.; Bock, C. H.; Bowman, M. K.; Norris, J. R., Controlling the duration of photosynthetic charge separation with microwave radiation. *Nature* **1983**, *303*, 520-522.
137. Atkins, P. W.; Dobbs, A. J.; McLauchlan, K. A., Electron spin emission spectra from pairs of radicals. *Chem. Phys. Lett.* **1973**, *22* (1), 209-11.

138. Hoff, A. J.; Gast, P.; Dzuba, S. A.; Timmel, C. R.; Fursman, C. E.; Hore, P. J., The nuts and bolts of distance determination and zero- and double-quantum coherence in photoinduced radical pairs. *Spectrochim. Acta, Part A* **1998**, *54A* (14), 2283-2293.
139. Miura, T.; Scott, A. M.; Wasielewski, M. R., Electron Spin Dynamics as a Controlling Factor for Spin-Selective Charge Recombination in Donor-Bridge-Acceptor Molecules. *Journal of Physical Chemistry C* **2010**, *114* (48), 20370-20379.
140. Chernick, E. T.; Mi, Q.; Kelley, R. F.; Weiss, E. A.; Jones, B. A.; Marks, T. J.; Ratner, M. A.; Wasielewski, M. R., Electron Donor-Bridge-Acceptor Molecules with Bridging Nitronyl Nitroxide Radicals: Influence of a Third Spin on Charge- and Spin-Transfer Dynamics. *J. Am. Chem. Soc.* **2006**, *128* (13), 4356-4364.
141. Hore, P. J.; Hunter, D. A.; Mckie, C. D.; Hoff, A. J., Electron-Paramagnetic Resonance of Spin-Correlated Radical Pairs in Photosynthetic Reactions. *Chem. Phys. Lett.* **1987**, *137* (6), 495-500.
142. Santabarbara, S.; Kuprov, I.; Hore, P. J.; Casal, A.; Heathcote, P.; Evans, M. C. W., Analysis of the Spin-Polarized Electron Spin Echo of the [P700+A1-] Radical Pair of Photosystem I Indicates That Both Reaction Center Subunits Are Competent in Electron Transfer in Cyanobacteria, Green Algae, and Higher Plants. *Biochemistry* **2006**, *45* (23), 7389-7403.
143. Closs, G. L.; Forbes, M. D. E.; Norris, J. R., Spin-Polarized Electron-Paramagnetic Resonance-Spectra of Radical Pairs in Micelles - Observation of Electron Spin-Spin Interactions. *J. Phys. Chem.* **1987**, *91* (13), 3592-3599.
144. Hasharoni, K.; Levanon, H.; Greenfield, S. R.; Gosztola, D. J.; Svec, W. A.; Wasielewski, M. R., Mimicry of the Radical Pair and Triplet-States in Photosynthetic Reaction Centers with a Synthetic Model. *J. Am. Chem. Soc.* **1995**, *117* (30), 8055-8056.
145. Kobr, L.; Gardner, D. M.; Smeigh, A. L.; Dyar, S. M.; Karlen, S. D.; Carmieli, R.; Wasielewski, M. R., Fast Photodrivn Electron Spin Coherence Transfer: A Quantum Gate Based on a Spin Exchange J-Jump. *Journal of the American Chemical Society* **2012**, *134* (30), 12430-12433.
146. Zarea, M.; Carmieli, R.; Ratner, M. A.; Wasielewski, M. R., Spin Dynamics of Radical Pairs with Restricted Geometries and Strong Exchange Coupling: The Role of Hyperfine Coupling. *J. Phys. Chem. A* **2014**, *118* (24), 4249-4255.
147. Kobori, Y.; Sekiguchi, S.; Akiyama, K.; Tero-Kubota, S., Chemically Induced Dynamic Electron Polarization Study on the Mechanism of Exchange Interaction in Radical Ion Pairs Generated by Photoinduced Electron Transfer Reactions. *J. Phys. Chem. A* **1999**, *103*, 5416-5424.
148. Kanemoto, K.; Fukunaga, A.; Yasui, M.; Kosumi, D.; Hashimoto, H.; Tamekuni, H.; Kawahara, Y.; Takemoto, Y.; Takeuchi, J.; Miura, Y.; Teki, Y., Ultrafast photoexcitation dynamics of [small pi]-conjugated bodipy-anthracene-radical triad system. *RSC Advances* **2012**, *2* (12), 5150-5153.
149. Henstra, A.; Lin, T. S.; Schmidt, J.; Wenckebach, W. T., High dynamic nuclear polarization at room temperature. *Chemical Physics Letters* **1990**, *165* (1), 6-10.
150. Colvin, M. T.; Carmieli, R.; Miura, T.; Richert, S.; Gardner, D. M.; Smeigh, A. L.; Dyar, S. M.; Conron, S. M.; Ratner, M. A.; Wasielewski, M. R., Electron Spin Polarization Transfer from Photogenerated Spin-Correlated Radical Pairs to a Stable Radical Observer Spin. *J. Phys. Chem. A* **2013**, *117*, 5314-5325.

151. CRC, *CRC Handbook of Chemistry and Physics*. 70th ed.; CRC Press: Boca Raton, FL, 2008.
152. Young, R. M.; Dyar, S. M.; Barnes, J. C.; Juricek, M.; Stoddart, J. F.; Co, D. T.; Wasielewski, M. R., Ultrafast Conformational Dynamics of Electron Transfer in ExBox4+⊂Perylene. *J. Phys. Chem. A* **2013**, *117* (47), 12438-12448.
153. Ito, N.; Huang, W.; Richert, R., Dynamics of a supercooled ionic liquid studied by optical and dielectric Spectroscopy. *J. Phys. Chem. B* **2006**, *110* (9), 4371-4377.
154. MATLAB *MATLAB*, The MathWorks, Inc.: Natick, MA, 2010.
155. Henry, E. R.; Hofrichter, J., [8] Singular value decomposition: Application to analysis of experimental data. In *Methods in Enzymology*, Ludwig Brand, M. L. J., Ed. Academic Press: 1992; Vol. Volume 210, pp 129-192.
156. Zamis, T. M.; Parkhurst, L. J.; Gallup, G. A., A matrix series method for the integration of rate equations in a reaction network. An alternative to Runge-Kutta methods. *Computers & Chemistry* **1989**, *13* (3), 165-171.
157. Weiss, E. A.; Ahrens, M. J.; Sinks, L. E.; Ratner, M. A.; Wasielewski, M. R., Solvent Control of Spin-Dependent Charge Recombination Mechanisms within Donor–Conjugated Bridge–Acceptor Molecules. *Journal of the American Chemical Society* **2004**, *126* (31), 9510-9511.
158. Breslin, D. T.; Fox, M. A., Characterization of the excited-state reactivity of a persistent aryl-substituted allyl free radical. *J. Phys. Chem.* **1993**, *97* (50), 13341-7.
159. Kuhn, R.; Neugebauer, A., Über substituierte Bis-biphenylen-allyl-Radikale. *Monats. für Chemie* **1964**, *95* (1), 3-23.
160. Mi, Q. Dynamics and Coherence of Systems with Two and Three Unpaired Spins. Northwestern University, Evanston, Illinois, 2009.
161. Greenfield, S. R.; Svec, W. A.; Gosztola, D.; Wasielewski, M. R., Multistep Photochemical Charge Separation in Rod-like Molecules Based on Aromatic Imides and Diimides. *J. Am. Chem. Soc.* **1996**, *118* (28), 6767-6777.
162. Colvin, M. T.; Smeigh, A. L.; Giacobbe, E. M.; Conron, S. M. M.; Ricks, A. B.; Wasielewski, M. R., Ultrafast intersystem crossing and spin dynamics of zinc meso-tetraphenylporphyrin covalently bound to stable radicals. *J. Phys. Chem. A* **2011**, *115* (26), 7538-7549.
163. Gosztola, D.; Niemczyk, M. P.; Svec, W.; Lukas, A. S.; Wasielewski, M. R., Excited doublet states of electrochemically generated aromatic imide and diimide radical anions. *J. Phys. Chem. A* **2000**, *104* (28), 6545–6551.
164. Kimura, K.; Katsumata, S.; Sawada, K., Visible-light effects on electronic absorption band of some cation radicals produced by photoionization at 77.deg.K. *J. Phys. Chem.* **1972**, *76* (5), 639-41.
165. Dance, Z. E. X.; Mickley, S. M.; Wilson, T. M.; Ricks, A. B.; Scott, A. M.; Ratner, M. A.; Wasielewski, M. R., Intersystem crossing mediated by photoinduced intramolecular charge transfer: julolidine-anthracene molecules with perpendicular pi systems. *J. Phys. Chem. A* **2008**, *112* (18), 4194-4201.
166. Meyer, V.; Eaton, S. S.; Eaton, G. R., X-band Electron Spin Relaxation Times for Four Aromatic Radicals in Fluid Solution and Comparison with Other Organic Radicals. *Appl Magn Reson* **2014**, *45* (10), 993-1007.

167. Dyar, S. M.; Margulies, E. A.; Horwitz, N. E.; Brown, K. E.; Krzyaniak, M. D.; Wasielewski, M. R., Photogenerated Quartet State Formation in a Compact Ring-Fused Perylene-Nitroxide. *J. Phys. Chem. B* **2015**, *119*, 13560-13569
168. Astashkin, A. V.; Schweiger, A., Electron-spin transient nutation: a new approach to simplify the interpretation of ESR spectra. *Chem. Phys. Lett.* **1990**, *174*, 595-602.
169. Schweiger, A.; Jeschke, G., *Principles of pulse electron paramagnetic resonance*. 1 ed.; Oxford University Press, USA: Oxford, 2001; p 608.
170. Gardner, D. M.; Chen, H.-F.; Krzyaniak, M. D.; Ratner, M. A.; Wasielewski, M. R., Large Dipolar Spin-Spin Interaction in a Photogenerated U-Shaped Triradical. *J. Phys. Chem. A* **2015**, *119* (29), 8040-8048.
171. Colvin, M. T.; Giacobbe, E. M.; Cohen, B.; Miura, T.; Scott, A. M.; Wasielewski, M. R., Competitive Electron Transfer and Enhanced Intersystem Crossing in Photoexcited Covalent TEMPO-Perylene-3,4:9,10-bis(dicarboximide) Dyads: Unusual Spin Polarization resulting from the Radical-Triplet Interaction. *J. Phys. Chem. A* **2010**, *114*, 1741-1748.
172. Conti, F.; Corvaja, C.; Busolo, F.; Zordan, G.; Maggini, M.; Weber, S., Time-resolved EPR investigation of [70]fulleropyrrolidine nitroxide isomers. *Physical Chemistry Chemical Physics* **2009**, *11* (3), 495-502.
173. Rozenshtein, V.; Berg, A.; Stavitski, E.; Levanon, H.; Franco, L.; Corvaja, C., Electron Spin Polarization of Functionalized Fullerenes. Reversed Quartet Mechanism. *J. Phys. Chem. A* **2005**, *109* (49), 11144-11154.
174. Stoll, S.; Schweiger, A., EasySpin, a comprehensive software package for spectral simulation and analysis in EPR. *J. Magn. Reson.* **2006**, *178* (1), 42-55.
175. Salikhov, K. M.; Zech, S. G.; Stehlik, D., Light induced radical pair intermediates in photosynthetic reaction centres in contact with an observer spin label: Spin dynamics and effects on transient EPR spectra. *Mol. Phys.* **2002**, *100* (20), 1311-1321.
176. Salikhov, K. M.; van der Est, A. J.; Stehlik, D., The transient EPR spectra and spin dynamics of coupled three-spin systems in photosynthetic reaction centres. *Appl Magn Reson* **1999**, *16* (1), 101-134.
177. Hore, P. J.; Riley, D. J.; Semlyen, J. J.; Zwanenburg, G.; Hoff, A. J., Analysis of anisotropic electron spin polarization in the photosynthetic bacterium *Rhodospirillum rubrum*. Evidence that the sign of the exchange interaction in the primary radical pair is positive. *Biochim. Biophys. Acta, Bioenerg.* **1993**, *1141* (2-3), 221-30.
178. Zarea, M.; Ratner, M. A.; Wasielewski, M. R., Spin polarization transfer by the radical pair mechanism. *J. Chem. Phys.* **2015**, *143* (5), 054101/1-054101/10.
179. Blank, A.; Levanon, H., Triplet Radical Interaction. Direct Measurement of Triplet Polarization Transfer by Fourier Transform Electron Paramagnetic Resonance. *J. Phys. Chem. A* **2000**, *104* (4), 794-800.
180. Blank, A.; Levanon, H., Interaction between Polarized Triplets and Stable Radicals in Liquid Solutions. *J. Phys. Chem. A* **2001**, *105* (20), 4799-4807.
181. Steinfeld, J. I.; Francisco, J. S.; Hase, W. L., *Chemical Kinetics and Dynamics*. 2 ed.; Prentice Hall, Inc.: Upper Saddle River, NJ, 1999; p 287-321.
182. Kothe, G.; Weber, S.; Ohmes, E.; Thurnauer, M. C.; Norris, J. R., Transient EPR of Light-Induced Spin-Correlated Radical Pairs: Manifestation of Zero Quantum Coherence. *J. Phys. Chem.* **1994**, *98* (10), 2706-2712.

183. Levanon, H.; Norris, J. R., The photoexcited triplet-state and photosynthesis. *Chem. Rev.* **1978**, *78* (3), 185-198.
184. Kawai, A.; Hidemori, T.; Shibuya, K., Electron spin dynamics of triplet and doublet molecules in room temperature ionic liquids studied by a time-resolved EPR method. *Mol. Phys.* **2006**, *104* (10-11), 1573-1579.
185. Ishii, K.; Hirose, Y.; Kobayashi, N., Electron spin polarizations of phthalocyanatosilicon covalently linked to one TEMPO radical in the excited quartet and doublet ground states. *J. Phys. Chem. A* **1999**, *103*, 1986-1990.
186. Mori, Y.; Sakaguchi, Y.; Hayashi, H., Magnetic Field Effects on Chemical Reactions of Biradical Radical Ion Pairs in Homogeneous Fluid Solvents. *J. Phys. Chem. A* **2000**, *104* (21), 4896-4905.
187. Young, R. M.; Dyar, S. M.; Barnes, J. C.; Juríček, M.; Stoddart, J. F.; Co, D. T.; Wasielewski, M. R., Ultrafast Conformational Dynamics of Electron Transfer in ExBox4+*c* Perylene. *J. Phys. Chem. A* **2013**, *117* (47), 12438-12448.
188. Gosztola, D.; Yamada, H.; Wasielewski, M. R., Electric Field Effects of Photogenerated Ion Pairs on Nearby Molecules: A Model for the Carotenoid Band Shift in Photosynthesis. *J. Am. Chem. Soc.* **1995**, *117* (7), 2041-8.
189. Ardo, S.; Sun, Y.; Staniszewski, A.; Castellano, F. N.; Meyer, G. J., Stark Effects after Excited-State Interfacial Electron Transfer at Sensitized TiO<sub>2</sub> Nanocrystallites. *Journal of the American Chemical Society* **2010**, *132* (19), 6696-6709.
190. Debreczeny, M. P.; Svec, W. A.; Wasielewski, M. R., A molecular probe of the electric field produced by a photogenerated ion pair. *New J. Chem.* **1996**, *20* (7-8), 815-828.
191. Weiss, E. A.; Tauber, M. J.; Ratner, M. A.; Wasielewski, M. R., Electron spin dynamics as a probe of molecular dynamics: Temperature-dependent magnetic field effects on charge recombination within a covalent radical ion pair. *J. Am. Chem. Soc.* **2005**, *127* (16), 6052-6061.
192. Lauteslager, X. Y.; van Stokkum, I. H. M.; van Ramesdonk, H. J.; Brouwer, A. M.; Verhoeven, J. W., Conformational Dynamics of Semiflexibly Bridged Donor-Acceptor Systems Studied with a Streak Camera and Spectrotemporal Parametrization of Fluorescence. *J. Phys. Chem. A* **1999**, *103* (6), 653-659.
193. Scott, A. M.; Miura, T.; Ricks, A. B.; Dance, Z. E. X.; Giacobbe, E. M.; Colvin, M. T.; Wasielewski, M. R., Spin-Selective Charge Transport Pathways through p-Oligophenylene-Linked Donor-Bridge-Acceptor Molecules. *J. Am. Chem. Soc.* **2009**, *131* (48), 17655-17666.
194. Hasharoni, K.; Levanon, H.; Greenfield, S. R.; Gosztola, D. J.; Svec, W. A.; Wasielewski, M. R., Radical pair and triplet state dynamics of a photosynthetic reaction-center model embedded in isotropic media and liquid crystals. *J. Am. Chem. Soc.* **1996**, *118*, 10228-10235.
195. Zarea, M.; Ratner, M. A.; Wasielewski, M. R., Spin polarization transfer by the radical pair mechanism. *The Journal of Chemical Physics* **2015**, *143* (5), 054101.
196. Kawai, A.; Shibuya, K., Electron spin dynamics in a pair interaction between radical and electronically-excited molecule as studied by a time-resolved ESR method. *Journal of Photochemistry and Photobiology C: Photochemistry Reviews* **2006**, *7* (2-3), 89-103.
197. Ishii, K.; Hirose, Y.; Kobayashi, N., Electron Spin Polarizations of Phthalocyaninosilicon Covalently Linked to One TEMPO Radical in the Excited Quartet and Doublet Ground States. *The Journal of Physical Chemistry A* **1999**, *103* (13), 1986-1990.

198. Colvin, M. T.; Carmieli, R.; Gardner, D. M.; Co, D. T.; Smeigh, A. L.; Dyar, S. M.; Mickley Conron, S. M.; Ratner, M. A.; Wasielewski, M. R., Electron Spin Polarization Transfer from Spin Correlated Radical Pairs to a TEMPO Observer Spin: Dependence on the Exchange and Dipolar Interaction. *Manuscript in preparation* **2012**.
199. Blank, A.; Levanon, H., Triplet Radical Interaction. Direct Measurement of Triplet Polarization Transfer by Fourier Transform Electron Paramagnetic Resonance. *J. Phys. Chem. A* **2000**, *104* (4), 794-800.
200. Pellizzari, T.; Gardiner, S. A.; Cirac, J. I.; Zoller, P., Decoherence, Continuous Observation, and Quantum Computing: A Cavity QED Model. *Physical Review Letters* **1995**, *75* (21), 3788-3791.
201. Khaneja, N.; Glaser, S. J.; Bockett, R., Sub-Riemannian geometry and time optimal control of three spin systems: Quantum gates and coherence transfer. *Physical Review A* **2002**, *65* (3), 032301.
202. Engel, G. S.; Calhoun, T. R.; Read, E. L.; Ahn, T.-K.; Mancal, T.; Cheng, Y.-C.; Blankenship, R. E.; Fleming, G. R., Evidence for wavelike energy transfer through quantum coherence in photosynthetic systems. *Nature* **2007**, *446* (7137), 782-786.
203. Bennett, C. H.; Brassard, G.; Crépeau, C.; Jozsa, R.; Peres, A.; Wootters, W. K., Teleporting an unknown quantum state via dual classical and Einstein-Podolsky-Rosen channels. *Physical Review Letters* **1993**, *70* (13), 1895-1899.
204. Salikhov, K. M.; Golbeck, J. H.; Stehlik, D., Quantum teleportation across a biological membrane by means of correlated spin pair dynamics in photosynthetic reaction centers. *Appl Magn Reson* **2007**, *31* (1), 237-252.
205. Kandrashkin, Y. E.; Salikhov, K. M., Numerical Simulation of Quantum Teleportation Across Biological Membrane in Photosynthetic Reaction Centers. *Appl Magn Reson* **2009**, *37* (1), 549.
206. Braunschweiler, L.; Ernst, R. R., Coherence transfer by isotropic mixing: Application to proton correlation spectroscopy. *Journal of Magnetic Resonance (1969)* **1983**, *53* (3), 521-528.
207. Bodenhausen, G.; Kogler, H.; Ernst, R. R., Selection of coherence-transfer pathways in NMR pulse experiments. *Journal of Magnetic Resonance (1969)* **1984**, *58* (3), 370-388.
208. Karpiuk, J.; Grabowski, Z. R., Mechanism and kinetics of fluorescence quenching of aromatic hydrocarbons by a stable nitroxyl radical. *Chemical Physics Letters* **1989**, *160* (4), 451-456.
209. Kuzmin, V. A.; Tatikolov, A. S., Formation of triplets of aromatic hydrocarbons on quenching of excited singlet states by nitroxyl radicals. *Chemical Physics Letters* **1977**, *51* (1), 45-47.
210. Dyar, S. M.; Margulies, E. A.; Horwitz, N. E.; Brown, K. E.; Krzyaniak, M. D.; Wasielewski, M. R., Photogenerated Quartet State Formation in a Compact Ring-Fused Perylene-Nitroxide. *The Journal of Physical Chemistry B* **2015**.
211. Dane, E. L.; Maly, T.; Debelouchina, G. T.; Griffin, R. G.; Swager, T. M., Synthesis of a BDPA-TEMPO Biradical. *Organic Letters* **2009**, *11* (9), 1871-1874.
212. Jeschke, G.; Chechik, V.; Ionita, P.; Godt, A.; Zimmermann, H.; Banham, J.; Timmel, C. R.; Hilger, D.; Jung, H., DeerAnalysis2006—a comprehensive software package for analyzing pulsed ELDOR data. *Appl Magn Reson* **2006**, *30* (3), 473-498.

213. Ito, N.; Duvvuri, K.; Matyushov, D. V.; Richert, R., Solvent response and dielectric relaxation in supercooled butyronitrile. *The Journal of Chemical Physics* **2006**, *125* (2), 024504.
214. Kuhn, R.; Neugebauer, A., Über substituierte Bis-biphenylen-allyl-Radikale. *Monatshefte für Chemie* **1964**, *95* (1), 3-23.
215. Horiuchi, S.; Tokura, Y., Organic ferroelectrics. *Nat Mater* **2008**, *7* (5), 357-366.
216. Hall, D. A.; Maus, D. C.; Gerfen, G. J.; Inati, S. J.; Becerra, L. R.; Dahlquist, F. W.; Griffin, R. G., Polarization-Enhanced NMR Spectroscopy of Biomolecules in Frozen Solution. *Science* **1997**, *276* (5314), 930-932.
217. Bajaj, V. S.; Farrar, C. T.; Hornstein, M. K.; Mastovsky, I.; Vieregg, J.; Bryant, J.; Eléna, B.; Kreischer, K. E.; Temkin, R. J.; Griffin, R. G., Dynamic nuclear polarization at 9 T using a novel 250 GHz gyrotron microwave source. *Journal of Magnetic Resonance* **2003**, *160* (2), 85-90.
218. Saxena, S.; Freed, J. H., Two-Dimensional Electron Spin Resonance and Slow Motions. *The Journal of Physical Chemistry A* **1997**, *101* (43), 7998-8008.
219. Enkin, N.; Liu, G.; Gimenez-Lopez, M. d. C.; Porfyrakis, K.; Tkach, I.; Bennati, M., A high saturation factor in Overhauser DNP with nitroxide derivatives: the role of <sup>14</sup>N nuclear spin relaxation. *Physical Chemistry Chemical Physics* **2015**, *17* (17), 11144-11149.
220. Jones, J. A.; Hore, P. J., Spin-selective reactions of radical pairs act as quantum measurements. *Chemical Physics Letters* **2010**, *488* (1), 90-93.
221. Kothe, G.; Weber, S.; Ohmes, E.; Thurnauer, M. C.; Norris, J. R., Transient EPR of Light-Induced Spin-Correlated Radical Pairs: Manifestation of Zero Quantum Coherence. *The Journal of Physical Chemistry* **1994**, *98* (10), 2706-2712.
222. Zwanenburg, G.; Hore, P. J., EPR of spin-correlated radical pairs. Analytical treatment of selective excitation including zero-quantum coherence. *Chemical Physics Letters* **1993**, *203* (1), 65-74.
223. Murai, H., Spin-chemical approach to photochemistry: reaction control by spin quantum operation. *Journal of Photochemistry and Photobiology C: Photochemistry Reviews* **2003**, *3* (3), 183-201.
224. Iwasaki, Y.; Murai, H.; Maeda, K.; Azumi, T., Study on the coherent spin motion of the radical-ion pair formed in the laser photolysis of N,N,N',N'-tetramethyl-1,4-phenylenediamine in 2-propanol. *Chemical Physics* **1998**, *230* (2-3), 201-208.
225. Araki, Y.; Maeda, K.; Murai, H., Observation of two-spin controlling of a radical pair by pulsed irradiation of microwave monitored by absorption detected magnetic resonance. *Chemical Physics Letters* **2000**, *332* (5-6), 515-520.
226. Batchelor, S. N.; McLauchlan, K. A.; Shkrob, I. A., Time-resolved reaction yield detected magnetic resonance (RYDMR). *Chemical Physics Letters* **1991**, *181* (4), 327-334.
227. Veselov, A. V.; Melekhov, V. I.; Anisimov, O. A.; Molin, Y. N., The induction of quantum beats by the  $\Delta g$  mechanism in radical ion pair recombination. *Chemical Physics Letters* **1987**, *136* (3), 263-266.
228. Anisimov, O. A.; Bizyaev, V. L.; Lukzen, N. N.; Grigoryants, V. M.; Molin, Y. N., The induction of quantum beats by hyperfine interactions in radical-ion pair recombination. *Chemical Physics Letters* **1983**, *101* (2), 131-135.

229. Molin, Y. N.; Salikhov, K. M., Spin exchange interaction as a possible source of oscillations in recombination of spin-correlated radical pairs. *Chemical Physics Letters* **1993**, *211* (4), 484-490.
230. Krzyaniak, M. D.; Kobr, L.; Rugg, B. K.; Phelan, B. T.; Margulies, E. A.; Nelson, J. N.; Young, R. M.; Wasielewski, M. R., Fast photo-driven electron spin coherence transfer: the effect of electron-nuclear hyperfine coupling on coherence dephasing. *Journal of Materials Chemistry C* **2015**, *3* (30), 7962-7967.
231. Scott, A. M.; Miura, T.; Ricks, A. B.; Dance, Z. E. X.; Giacobbe, E. M.; Colvin, M. T.; Wasielewski, M. R., Spin-Selective Charge Transport Pathways through p-Oligophenylene-Linked Donor-Bridge-Acceptor Molecules. *Journal of the American Chemical Society* **2009**, *131* (48), 17655-17666.
232. Ramos, J.; M. Yartsev, V.; Golhen, S.; Ouahab, L.; Delhaes, P., Synthesis and characterization of an extended tetrathiafulvalene derivative coordinated to copper iodide and its charge-transfer and radical ion salts. *Journal of Materials Chemistry* **1997**, *7* (8), 1313-1319.
233. Grampp, G.; Kelterer, A.-M.; Landgraf, S.; Sacher, M.; Niethammer, D.; Telo, J. P.; Dias, R. M. B.; Vieira, A. J. S. C., ESR and ENDOR Investigations on Various Wurster's Radical Cations in Solution. Experimental Results, Theoretical Ab Initio, and DFT Calculations. *Monatshefte für Chemie / Chemical Monthly* **2005**, *136* (4), 519-536.
234. Young, R. M.; Dyar, S. M.; Barnes, J. C.; Juriček, M.; Stoddart, J. F.; Co, D. T.; Wasielewski, M. R., Ultrafast Conformational Dynamics of Electron Transfer in ExBox4+⊂Perylene. *The Journal of Physical Chemistry A* **2013**, *117* (47), 12438-12448.
235. Hasharoni, K.; Levanon, H.; Greenfield, S. R.; Gosztola, D. J.; Svec, W. A.; Wasielewski, M. R., Mimicry of the Radical Pair and Triplet States in Photosynthetic Reaction Centers with a Synthetic Model. *Journal of the American Chemical Society* **1995**, *117* (30), 8055-8056.
236. Tayebjee, M. J. Y.; Sanders, S. N.; Kumarasamy, E.; Campos, L. M.; Sfeir, M. Y.; McCamey, D. R., Quintet multiexciton dynamics in singlet fission. *Nat Phys* **2017**, *13* (2), 182-188.
237. Weiss, L. R.; Bayliss, S. L.; Kraffert, F.; Thorley, K. J.; Anthony, J. E.; Bittl, R.; Friend, R. H.; Rao, A.; Greenham, N. C.; Behrends, J., Strongly exchange-coupled triplet pairs in an organic semiconductor. *Nat Phys* **2017**, *13* (2), 176-181.
238. Burdett, J. J.; Bardeen, C. J., Quantum Beats in Crystalline Tetracene Delayed Fluorescence Due to Triplet Pair Coherences Produced by Direct Singlet Fission. *Journal of the American Chemical Society* **2012**, *134* (20), 8597-8607.
239. Basel, B. S.; Zirzmeier, J.; Hetzer, C.; Phelan, B. T.; Krzyaniak, M. D.; Reddy, S. R.; Coto, P. B.; Horwitz, N. E.; Young, R. M.; White, F. J.; Hampel, F.; Clark, T.; Thoss, M.; Tykwinski, R. R.; Wasielewski, M. R.; Guldi, D. M., Unified model for singlet fission within a non-conjugated covalent pentacene dimer. *Nature Communications* **2017**, *8*, 15171.
240. Lloyd, J. E., Bioluminescence and communication in insects. *Annual review of entomology* **1983**, *28* (1), 131-160.
241. Sancar, A., Structure and function of DNA photolyase. *Biochemistry* **1994**, *33* (1), 2-9.
242. Kataria, S.; Jajoo, A.; Guruprasad, K. N., Impact of increasing Ultraviolet-B (UV-B) radiation on photosynthetic processes. *Journal of Photochemistry and Photobiology B: Biology* **2014**, *137* (0), 55-66.

243. Rizzini, L.; Favory, J.-J.; Cloix, C.; Faggionato, D.; O'Hara, A.; Kaiserli, E.; Baumeister, R.; Schäfer, E.; Nagy, F.; Jenkins, G. I.; Ulm, R., Perception of UV-B by the Arabidopsis UVR8 Protein. *Science* **2011**, 332 (6025), 103-106.
244. Di, W.; Hu, Q.; Yan, Z.; Chen, W.; Yan, C.; Huang, X.; Zhang, J.; Yang, P.; Deng, H.; Wang, J.; Deng, X.; Shi, Y., Structural basis of ultraviolet-B perception by UVR8. *Nature* **2012**, 484 (7393), 214-219.
245. Christie, J. M.; Arvai, A. S.; Baxter, K. J.; Heilmann, M.; Pratt, A. J.; O'Hara, A.; Kelly, S. M.; Hothorn, M.; Smith, B. O.; Hitomi, K.; Jenkins, G. I.; Getzoff, E. D., Plant UVR8 Photoreceptor Senses UV-B by Tryptophan-Mediated Disruption of Cross-Dimer Salt Bridges. *Science* **2012**, 335 (6075), 1492-1496.
246. Wu, M.; Grahn, E.; Eriksson, L. A.; Strid, Å., Computational Evidence for the Role of Arabidopsis thaliana UVR8 as UV-B Photoreceptor and Identification of Its Chromophore Amino Acids. *Journal of Chemical Information and Modeling* **2011**, 51 (6), 1287-1295.
247. Thomas T.T, D.; Puthur, J. T., UV radiation priming: A means of amplifying the inherent potential for abiotic stress tolerance in crop plants. *Environmental and Experimental Botany* **2017**, 138, 57-66.
248. Roberts, J. A.; Kirby, J. P.; Nocera, D. G., Photoinduced Electron Transfer within a Donor-Acceptor Pair Juxtaposed by a Salt Bridge. *Journal of the American Chemical Society* **1995**, 117 (30), 8051-8052.
249. Katagiri, H.; Tanaka, Y.; Furusho, Y.; Yashima, E., Multicomponent Cylindrical Assemblies Driven by Amidinium-Carboxylate Salt-Bridge Formation. *Angewandte Chemie* **2007**, 119 (14), 2487-2491.
250. Corbellini, F.; Di Costanzo, L.; Crego-Calama, M.; Geremia, S.; Reinhoudt, D. N., Guest Encapsulation in a Water-Soluble Molecular Capsule Based on Ionic Interactions. *Journal of the American Chemical Society* **2003**, 125 (33), 9946-9947.
251. Cooke, G.; Duclairoir, F. M. A.; Kraft, A.; Rosair, G.; Rotello, V. M., Pronounced stabilisation of the ferrocenium state of ferrocenecarboxylic acid by salt bridge formation with a benzamidine. *Tetrahedron Letters* **2004**, 45 (3), 557-560.
252. Klajn, R., Immobilized azobenzenes for the construction of photoresponsive materials. In *Pure and Applied Chemistry*, 2010; Vol. 82, p 2247.
253. Ercole, F.; Davis, T. P.; Evans, R. A., Photo-responsive systems and biomaterials: photochromic polymers, light-triggered self-assembly, surface modification, fluorescence modulation and beyond. *Polymer Chemistry* **2010**, 1 (1), 37-54.
254. Voityuk, A. A.; Marcus, R. A.; Michel-Beyerle, M.-E., On the mechanism of photoinduced dimer dissociation in the plant UVR8 photoreceptor. *Proceedings of the National Academy of Sciences* **2014**, 111 (14), 5219-5224.
255. Jenkins, G. I., Structure and function of the UV-B photoreceptor UVR8. *Current Opinion in Structural Biology* **2014**, 29 (0), 52-57.
256. Zeng, X.; Ren, Z.; Wu, Q.; Fan, J.; Peng, P.-P.; Tang, K.; Zhang, R.; Zhao, K.-H.; Yang, X., Dynamic crystallography reveals early signalling events in ultraviolet photoreceptor UVR8. *Nature Plants* **2015**, 1.
257. Wu, M.; Strid, Å.; Eriksson, L. A., Photochemical Reaction Mechanism of UV-B-Induced Monomerization of UVR8 Dimers as the First Signaling Event in UV-B-Regulated Gene Expression in Plants. *The Journal of Physical Chemistry B* **2014**, 118 (4), 951-965.

258. Li, X.; Chung, L. W.; Morokuma, K.; Li, G., Theoretical Study on the UVR8 Photoreceptor: Sensing Ultraviolet-B by Tryptophan and Dissociation of Homodimer. *Journal of Chemical Theory and Computation* **2014**, *10* (8), 3319-3330.
259. Yu, H. T.; Colucci, W. J.; McLaughlin, M. L.; Barkley, M. D., Fluorescence quenching in indoles by excited-state proton transfer. *Journal of the American Chemical Society* **1992**, *114* (22), 8449-8454.
260. Chatteraj, M.; King, B. A.; Bublitz, G. U.; Boxer, S. G., Ultra-fast excited state dynamics in green fluorescent protein: multiple states and proton transfer. *Proceedings of the National Academy of Sciences* **1996**, *93* (16), 8362-8367.
261. Fang, C.; Frontiera, R. R.; Tran, R.; Mathies, R. A., Mapping GFP structure evolution during proton transfer with femtosecond Raman spectroscopy. *Nature* **2009**, *462* (7270), 200-204.
262. Brejc, K.; Sixma, T. K.; Kitts, P. A.; Kain, S. R.; Tsien, R. Y.; Ormö, M.; Remington, S. J., Structural basis for dual excitation and photoisomerization of the *Aequorea victoria* green fluorescent protein. *Proceedings of the National Academy of Sciences* **1997**, *94* (6), 2306-2311.
263. Weber, S.; Biskup, T.; Okafuji, A.; Marino, A. R.; Berthold, T.; Link, G.; Hitomi, K.; Getzoff, E. D.; Schleicher, E.; Norris, J. R., Origin of Light-Induced Spin-Correlated Radical Pairs in Cryptochrome†. *The Journal of Physical Chemistry B* **2010**, *114* (45), 14745-14754.
264. Hore, P. J.; Hunter, D. A.; McKie, C. D.; Hoff, A. J., Electron paramagnetic resonance of spin-correlated radical pairs in photosynthetic reactions. *Chemical Physics Letters* **1987**, *137*, 495-500.
265. Stehlik, D.; Bock, C. H.; Petersen, J., Anisotropic electron spin polarization of correlated spin pairs in photosynthetic reaction centers. *The Journal of Physical Chemistry* **1989**, *93* (4), 1612-1619.
266. Bittl, R.; Weber, S., Transient radical pairs studied by time-resolved EPR. *Biochimica et Biophysica Acta (BBA) - Bioenergetics* **2005**, *1707* (1), 117-126.
267. Wasielewski, M. R.; Gaines, G. L.; Wiederrecht, G. P.; Svec, W. A.; Niemczyk, M. P., Biomimetic modeling of photosynthetic reaction center function: long-lived, spin-polarized radical ion pair formation in chlorophyll-porphyrin-quinone triads. *Journal of the American Chemical Society* **1993**, *115* (22), 10442-10443.
268. Wasielewski, M. R.; Gaines, G. L.; O'Neil, M. P.; Svec, W. A.; Niemczyk, M. P., Photoinduced spin-polarized radical ion pair formation in a fixed-distance photosynthetic model system at 5 K. *Journal of the American Chemical Society* **1990**, *112* (11), 4559-4560.
269. Carbonera, D.; Di Valentin, M.; Corvaja, C.; Agostini, G.; Giacometti, G.; Liddell, P. A.; Kuciauskas, D.; Moore, A. L.; Moore, T. A.; Gust, D., EPR Investigation of Photoinduced Radical Pair Formation and Decay to a Triplet State in a Carotene-Porphyrin-Fullerene Triad. *Journal of the American Chemical Society* **1998**, *120* (18), 4398-4405.
270. Tang, J.; Thurnauer, M. C.; Norris, J. R., Electron spin echo envelope modulation due to exchange and dipolar interactions in a spin-correlated radical pair. *Chemical Physics Letters* **1994**, *219* (3-4), 283-290.
271. Dzuba, S. A.; Gast, P.; Hoff, A. J., ESEEM study of spin-spin interactions in spin-polarised P+QA<sup>-</sup> pairs in the photosynthetic purple bacterium *Rhodobacter sphaeroides* R26. *Chemical Physics Letters* **1995**, *236* (6), 595-602.

272. Zuclich, J., Triplet-State Electron Spin Resonance of the Aromatic Amino Acids and Proteins. *The Journal of Chemical Physics* **1970**, *52* (7), 3586-3591.
273. Hasharoni, K.; Levanon, H.; Greenfield, S. R.; Gosztola, D. J.; Svec, W. A.; Wasielewski, M. R., Mimicry of the radical pair and triplet states in photosynthetic reaction centers with a synthetic model. *Journal of the American Chemical Society* **1995**, *117*, 8055-8056.
274. Thurnauer, M. C.; Katz, J. J.; Norris, J. R., The triplet state in bacterial photosynthesis: Possible mechanisms of the primary photo-act. *Proceedings of the National Academy of Sciences* **1975**, *72* (9), 3270-3274.
275. Levanon, H.; Norris, J. R., The photoexcited triplet state and photosynthesis. *Chemical Reviews* **1978**, *78* (3), 185-198.
276. de Schoulepnikoff, L.; Mitev, V.; Simeonov, V.; Calpini, B.; van den Bergh, H., Experimental investigation of high-power single-pass Raman shifters in the ultraviolet with Nd:YAG and KrF lasers. *Appl. Opt.* **1997**, *36* (21), 5026-5043.
277. Haner, D. A.; McDermid, I. S., Stimulated Raman shifting of the Nd:YAG fourth harmonic (266 nm) in H<sub>2</sub>, HD, and D<sub>2</sub>. *Quantum Electronics, IEEE Journal of* **1990**, *26* (7), 1292-1298.
278. Coherent, I. Coherent Inc. COMPexPro high pulse energy UV laser up to 100 Hz. <http://www.coherent.com/products/index.cfm?1027/COMPexPro-Series> (accessed Feb. 22).
279. García de la Torre, J.; Huertas, M. L.; Carrasco, B., HYDRONMR: Prediction of NMR Relaxation of Globular Proteins from Atomic-Level Structures and Hydrodynamic Calculations. *Journal of Magnetic Resonance* **2000**, *147* (1), 138-146.
280. Beechem, J. M.; Brand, L., Time-Resolved Fluorescence of Proteins. *Annual Review of Biochemistry* **1985**, *54* (1), 43-71.
281. Heilmann, M.; Christie, J. M.; Kennis, J. T. M.; Jenkins, G. I.; Mathes, T., Photoinduced transformation of UVR8 monitored by vibrational and fluorescence spectroscopy. *Photochemical & Photobiological Sciences* **2015**, *14* (2), 252-257.
282. Nitschke, W.; Feiler, U.; Rutherford, A. W., Photosynthetic reaction center of green sulfur bacteria studied by EPR. *Biochemistry* **1990**, *29* (16), 3834-3842.
283. Malkin, R.; Bearden, A. J., Detection of a Free Radical in the Primary Reaction of Chloroplast Photosystem II. *Proceedings of the National Academy of Sciences* **1973**, *70* (2), 294-297.
284. Shida, T., *Electronic absorption spectra of radical ions*. Elsevier: 1988.
285. Kandori, H.; Borkman, R. F.; Yoshihara, K., Picosecond transient absorption of aqueous tryptophan. *The Journal of Physical Chemistry* **1993**, *97* (38), 9664-9667.
286. Bent, D. V.; Hayon, E., Excited state chemistry of aromatic amino acids and related peptides. III. Tryptophan. *Journal of the American Chemical Society* **1975**, *97* (10), 2612-2619.
287. Bellina, B.; Compagnon, I.; Houver, S.; Maître, P.; Allouche, A.-R.; Antoine, R.; Dugourd, P., Spectroscopic Signatures of Peptides Containing Tryptophan Radical Cations. *Angewandte Chemie International Edition* **2011**, *50* (48), 11430-11432.
288. Joly, L.; Antoine, R.; Allouche, A.-R.; Dugourd, P., Formation and Spectroscopy of a Tryptophan Radical Containing Peptide in the Gas Phase. *Journal of the American Chemical Society* **2008**, *130* (42), 13832-13833.
289. Miller, J. E.; Grădinaru, C.; Crane, B. R.; Di Bilio, A. J.; Wehbi, W. A.; Un, S.; Winkler, J. R.; Gray, H. B., Spectroscopy and Reactivity of a Photogenerated Tryptophan Radical in a

- Structurally Defined Protein Environment. *Journal of the American Chemical Society* **2003**, *125* (47), 14220-14221.
290. Choi, J.; Fujitsuka, M.; Tojo, S.; Majima, T., Folding Dynamics of Cytochrome c Using Pulse Radiolysis. *Journal of the American Chemical Society* **2012**, *134* (32), 13430-13435.
291. Chen, Y.; Barkley, M. D., Toward Understanding Tryptophan Fluorescence in Proteins. *Biochemistry* **1998**, *37* (28), 9976-9982.
292. Dergachev, A. Y.; Pati, B.; Moulton, P. F. In *Efficient Third-Harmonic Generation with a Ti:sapphire Laser*, Advanced Solid State Lasers, Boston, Massachusetts, 1999/01/31; Fejer, M. I. H.; Keller, U., Eds. Optical Society of America: Boston, Massachusetts, 1999; p PD3.
293. Ferguson, A. J.; Kopidakis, N.; Shaheen, S. E.; Rumbles, G., *J. Phys. Chem. C* **2008**, *112*, 9865.
294. Rava, R. P.; Spiro, T. G., Resonance enhancement in the ultraviolet Raman spectra of aromatic amino acids. *The Journal of Physical Chemistry* **1985**, *89* (10), 1856-1861.
295. Liu, Z.; Li, X.; Zhong, F. W.; Li, J.; Wang, L.; Shi, Y.; Zhong, D., Quenching Dynamics of Ultraviolet-Light Perception by UVR8 Photoreceptor. *The Journal of Physical Chemistry Letters* **2013**, *5* (1), 69-72.
296. Cloix, C.; Jenkins, G. I., Interaction of the Arabidopsis UV-B-Specific Signaling Component UVR8 with Chromatin. *Molecular Plant* **2008**, *1* (1), 118-128.
297. Recombinant Protein Production Core at Northwestern University. <http://rppc.mccormick.northwestern.edu/>.
298. Peters, K.; Richards, F. M., Chemical Cross-Linking: Reagents and Problems in Studies of Membrane Structure. *Annual Review of Biochemistry* **1977**, *46* (1), 523-551.
299. Fujiyama, T.; Sugimoto, K.; Sekiguchi, M., Novel compound and organic electronic device using such compound. 2006.
300. Sinks, L. E.; Wasielewski, M. R., Effects of Solvent and Structural Dynamics on Electron Transfer Reactions of 4-Aminonaphthalene-1,8-dicarboximide Donor-Acceptor Molecules in Nematic Liquid Crystals and Isotropic Solvents. *The Journal of Physical Chemistry A* **2003**, *107* (5), 611-620.
301. Mauck, C. M.; Young, R. M.; Wasielewski, M. R., Characterization of Excimer Relaxation via Femtosecond Shortwave- and Mid-Infrared Spectroscopy. *The Journal of Physical Chemistry A* **2017**, *121* (4), 784-792.

## APPENDIX A

# *Original Research Proposal:* Photophysical Investigation of the Dissociation Mechanism of the Plant Photoreceptor Protein UVR8

Full text of Appendix A available upon request: [noah.horwitz@gmail.com](mailto:noah.horwitz@gmail.com)

### Abstract

Experiments are proposed to interrogate the detailed chemical mechanism of the plant photoreceptor protein UVR8. UVR8 allows plants to mitigate damage from UV-B radiation. UVR8 relies on tryptophan residues in the protein structure for light absorption, and exists in the resting state as a dimer held together by salt bridge interactions. Upon absorption of UV-B light, UVR8 dissociates, and UVR8 monomers trigger biological changes in the cell. Dissociation mechanisms involving electron transfer, proton coupled electron transfer, and excited state proton transfer have been proposed in previous studies, but current evidence cannot distinguish between these mechanisms. We propose to study UVR8 by time-resolved electron paramagnetic resonance (EPR) and transient optical absorption for the first time, to search for key intermediates in each of the proposed mechanisms. We anticipate that these results will lead to a greater understanding of the mechanism of UVR8, and may also open the door to creating synthetic photoresponsive materials that mimic this protein.

## APPENDIX B

# Supplementary Organic Synthesis Information

## B.1 Chapter 2

### Compound 2.1

N-(4-amino-2,5-dimethylphenyl)-naphthalene-1,8-dicarboximide<sup>68</sup> (300 mg, 0.95 mmol, 1 eq.) and 1,4,5,8-naphthalenetetracarboxylic dianhydride (306 mg, 1.14 mmol, 1.2 eq.) were added to a flame-dried flask with pyridine (15 mL). This mixture was degassed by 3 pump-purge cycles and heated to reflux under N<sub>2</sub> for 16 h. 3-aminopentane (1.1 mL, 9.5 mmol, 10 eq.) was added and refluxing continued for 3 hours. Pyridine and excess 3-aminopentane were removed on a rotary evaporator and the resulting brown solid purified by column chromatography on SiO<sub>2</sub> in chloroform/tetrahydrofuran (93:7). Compound **2.1** was obtained as a pale yellow solid (116 mg, 19%). <sup>1</sup>H-NMR (499 MHz, CD<sub>2</sub>Cl<sub>2</sub>) δ 8.86 (d, J = 7.5 Hz, 2H), 8.80 (d, J = 7.6 Hz, 2H), 8.70 (dd, J = 7.1, 1.1 Hz, 2H), 8.36 (dd, J = 8.3, 1.1 Hz, 2H), 7.86 (dd, J = 8.2, 7.3 Hz, 2H), 7.29 (d, J = 4.0 Hz, 2H), 5.05 (tt, J = 9.5, 5.8 Hz, 1H), 2.30 – 2.20 (m, 2H), 2.19 (s, 6H), 2.00 – 1.91 (m, 2H), 0.93 (t, J = 7.5 Hz, 6H). <sup>13</sup>C-NMR (126 MHz, CD<sub>2</sub>Cl<sub>2</sub>) δ 164.34, 163.24, 136.25, 135.84, 135.38, 134.99, 134.94, 132.30, 131.98, 131.78, 131.76, 131.37, 129.11, 127.62, 127.53, 127.49, 126.76, 123.11, 58.58, 25.37, 17.49, 17.45, 11.50.

### Compound 2.6

N-(4-amino-2,5-dimethylphenyl)-4-bromonaphthalene-1,8-dicarboximide<sup>70</sup> (199 mg, 0.5 mmol, 1 eq.), N-(1-ethylpropyl)-naphthalene-1,8-dicarboxyanhydride-4,5-dicarboximide<sup>299</sup> (179 mg, 0.53 mmol, 1.05 eq.), and 1-butanol (10 mL) were added to a flame-dried flask and degassed by 3 pump-purge cycles. The mixture was heated to reflux under N<sub>2</sub> for 17h after which butanol

was removed on a rotary evaporator. The resulting solid was purified via column chromatography on SiO<sub>2</sub> in dichloromethane/acetone (96:4) to afford Compound **2.6** as a pale yellow solid (219 mg, 61%). <sup>1</sup>H-NMR (500 MHz, CDCl<sub>3</sub>) δ 8.90 – 8.77 (m, 4H), 8.75 (dd, J = 7.2, 1.1 Hz, 1H), 8.67 (dd, J = 8.5, 1.1 Hz, 1H), 8.51 (d, J = 7.8 Hz, 1H), 8.12 (d, J = 7.8 Hz, 1H), 7.92 (dd, J = 8.5, 7.3 Hz, 1H), 7.27 (s, 1H), 7.26 (presumed s, obscured by CHCl<sub>3</sub>), 5.07 (tt, J = 9.7, 5.8 Hz, 1H), 2.25 (m, 2H), 2.19 (s, 3H), 2.18 (s, 3H), 2.01 – 1.91 (m, 2H), 0.93 (t, J = 7.4 Hz, 6H). <sup>13</sup>C-NMR (126 MHz, CDCl<sub>3</sub>) δ 163.36, 163.32, 162.62, 135.27, 134.93, 134.49, 133.91, 133.30, 132.71, 131.86, 131.58, 131.43, 131.37, 131.12, 131.05, 130.97, 129.69, 128.40, 127.32, 127.23, 126.61, 123.33, 122.44, 58.41, 25.12, 17.52, 17.48, 11.44. MALDI-MS m/z [M]<sup>-</sup> 712.2 found, 713.1 expected.

### Compound 2.7

Compound **2.6** (100 mg, 0.14 mmol, 1 eq.), 4-aminophenyl boronic acid, pinacol ester (35 mg, 0.15 mmol, 1.05 eq.), K<sub>2</sub>CO<sub>3</sub> (162 mg, 1.12 mmol, 8 eq.), toluene (5 mL), ethanol (0.5 mL), and deionized water (1 mL) were added to a flask. This mixture was degassed by 3 pump-purge cycles and tetrakis(triphenylphosphine)palladium(0) (11 mg, 0.007 mmol, 0.05 eq.) was added. The mixture was degassed again by 3 pump-purge cycles and heated to reflux under N<sub>2</sub> overnight. The reaction mixture was partitioned between dichloromethane and NaCl brine and the organic layer separated and dried over Na<sub>2</sub>SO<sub>4</sub>. A small amount of SiO<sub>2</sub> was added to remove residual catalyst and the solution filtered and concentrated to an orange solid. Purification by column chromatography on SiO<sub>2</sub> in dichloromethane/acetone/triethylamine

(93:6:1) afforded Compound **2.7** as a dark yellow solid (102 mg, 70%).  $^1\text{H-NMR}$  (500 MHz,  $\text{CDCl}_3$ )  $\delta$  8.85 (d,  $J = 7.5$  Hz, 2H), 8.80 (d,  $J = 7.5$  Hz, 2H), 8.74 – 8.66 (m, 2H), 8.46 (dd,  $J = 8.4, 1.1$  Hz, 1H), 7.79 – 7.70 (m, 2H), 7.37 (d,  $J = 8.2$  Hz, 2H), 7.30 (s, 1H), 7.27 (s, obscured by  $\text{CHCl}_3$ ), 6.91 – 6.84 (m, 2H), 5.07 (ddd,  $J = 15.4, 9.6, 5.8$  Hz, 1H), 3.93 (s, 2H), 2.32 – 2.23 (m, 2H), 2.22 (s, 3H), 2.18 (s, 3H), 0.93 (t,  $J = 7.4$  Hz, 6H).  $^{13}\text{C-NMR}$  (126 MHz,  $\text{CDCl}_3$ )  $\delta$  164.19, 163.98, 162.63, 148.00, 147.18, 135.74, 135.40, 134.83, 134.31, 133.65, 131.75, 131.64, 131.59, 131.49, 131.31, 131.04, 130.54, 129.60, 128.80, 127.84, 127.33, 127.24, 126.79, 126.66, 123.02, 121.06, 115.18, 58.40, 25.12, 17.55, 17.49, 11.45. MALDI-MS  $m/z$   $[\text{M}]^-$  725.4 found, 726.2 expected.

## Compound 2.2

Compound **2.7** (39 mg, 0.055 mmol, 1 eq.), *N*-(2,6-diisopropylphenyl)-pyromellitic monoanhydride (25 mg, 0.061 mmol, 1.1 eq.), and glacial acetic acid (5 mL) were added to a flame-dried flask. This mixture was degassed by 3 pump-purge cycles and refluxed 17h under  $\text{N}_2$ , after which acetic acid was removed on a rotary evaporator. 56 mg of impure Compound **2.2** was obtained following chromatography on a short column of  $\text{SiO}_2$  in dichloromethane/acetone (96:4). Further purification by preparative TLC in dichloromethane/acetone/methanol (97:2:1) afforded pure Compound **2.2** as a pale yellow solid (extrapolated yield 38%).  $^1\text{H-NMR}$  (500 MHz,  $\text{CD}_2\text{Cl}_2$ )  $\delta$  8.87 (d,  $J = 7.5$  Hz, 2H), 8.80 (d,  $J = 8.4$  Hz, 2H), 8.79 – 8.78 (d,  $J = 7.5$  Hz, 1H), 8.77 – 8.76 (dd,  $J = 7.3, 1.3$  Hz, 1H), 8.54 (s, 2H), 8.46 (dd,  $J = 8.5, 1.0$  Hz, 1H), 7.92 – 7.84 (m, 2H), 7.84 – 7.73 (m, 4H), 7.55 (t,  $J = 7.8$  Hz, 1H), 7.37 (d,  $J = 7.8$  Hz, 2H), 7.34 (s, 1H),

7.31 (s, 1H), 5.06 (tt,  $J = 9.6, 5.8$  Hz, 1H), 2.71 (hept,  $J = 6.8$  Hz, 2H), 2.29 – 2.15 (m, 2H), 2.22 (s, 3H), 2.21 (s, 3H), 1.96 (ddd,  $J = 13.6, 7.4, 6.0$  Hz, 2H), 1.18 (d,  $J = 6.8$  Hz, 12H), 0.93 (t,  $J = 7.5$  Hz, 6H).  $^{13}\text{C}$ -NMR (126 MHz,  $\text{CDCl}_3$ )  $\delta$  166.15, 165.23, 163.93, 163.71, 162.60, 147.10, 146.03, 139.28, 137.59, 137.20, 135.54, 135.29, 134.86, 134.42, 132.01, 131.57, 131.42, 131.09, 130.97, 130.33, 129.39, 128.28, 127.47, 127.33, 127.25, 126.69, 126.63, 126.25, 124.38, 123.25, 122.49, 119.85, 58.41, 29.73, 25.13, 24.14, 17.58, 17.53, 11.45.

## B.2 Chapter 4

### 2-iodo-4-nitroaniline

Two solutions were prepared. Solution A consisted of iodine monochloride (6.6 mL at 30 °C, 130 mmol, 1 eq.; some precipitate of  $\text{I}_2$  formed),  $\text{H}_2\text{O}$  (60 mL), and 12M HCl (21 mL, 250 mmol, 1.9 eq.). Solution B was prepared from 4-nitroaniline (18.03 g, 130 mmol, 1 eq.; did not completely dissolve),  $\text{H}_2\text{O}$  (150 mL), and 12M HCl (6 mL, 70 mmol, 0.54 eq.). Solution B was placed in a flask under air and cooled to 0 °C in an icebath. Solution A was added slowly and the reaction mixture returned to room temperature and stirred overnight. The reaction mixture was filtered and the collected solid washed with  $\text{H}_2\text{O}$  to yield 2-iodo-4-nitroaniline as a yellow solid (32.87g, 95%).  $^1\text{H}$ -NMR (500 MHz, chloroform- $d$ )  $\delta$  8.56 (d,  $J = 2.5$  Hz, 1H), 8.10 – 8.00 (dd, 1H), 6.70 (d,  $J = 8.9$  Hz, 1H), 4.84 (s, 2H).

**2-bromo-6-iodo-4-nitroaniline**

2-Iodo-4-nitroaniline (32.87 g, 124.5 mmol, 1 eq.) and chloroform (350 mL) were added to a flask under air. N-bromosuccinimide (22.17 g, 124.5 mmol, 1 eq.) was added slowly and the reaction stirred at room temperature for 25 h. 350 mL H<sub>2</sub>O was added and the reaction mixture filtered to yield 2-bromo-6-iodo-4-nitroaniline as a yellow solid (38.44 g, 90%). <sup>1</sup>H-NMR (500 MHz, chloroform-d) δ 8.53 (d, J = 2.4 Hz, 1H), 8.37 (d, J = 2.4 Hz, 1H), 5.32 (s, 2H).

**1-bromo-3-iodo-5-nitrobenzene**

*Safety note: this reaction should not be scaled up due to the presence of a potentially explosive diazonium intermediate.*

2-Bromo-6-iodo-4-nitroaniline (10.01 g, 29.2 mmol, 1 eq.) and ethanol (200 mL) were added to a flask under air. 18M sulfuric acid (15.7 mL, 292 mmol, 10 eq.) was added slowly with stirring at room temperature and the reaction mixture heated to 60 °C. Sodium nitrite (6.04 g, 87.5 mmol, 3 eq.) was added in small portions. The flask was equipped with a reflux condenser and heated to reflux for 3h. The reaction mixture was poured over 500 mL of ice, causing an ivory solid to precipitate. This mixture was filtered and washed 3 times with H<sub>2</sub>O to yield 1-bromo-3-iodo-5-nitrobenzene as ivory crystals (9.21 g, 96%). <sup>1</sup>H-NMR (500 MHz, chloroform-d) δ 8.48 (apparent t, J = 1.7 Hz, 1H), 8.33 (apparent t, J = 1.9 Hz, 1H), 8.16 (apparent t, J = 1.6 Hz, 1H).

### 3-bromo-5-iodoaniline

*Safety note: heat is evolved when sodium hydroxide is added to the reaction mixture, which may cause boiling and spattering of the dichloromethane solution.*

1-Bromo-3-iodo-5-nitrobenzene (18.26 g, 55.69 mmol, 1 eq.), tin(II) chloride dihydrate (47.75 g, 212 mmol, 3.8 eq.), and ethanol (130 mL) were added to a flask equipped with a reflux condenser. The reaction mixture was deoxygenated by 3 pump-purge cycles and refluxed under nitrogen atmosphere for 1.5 h. The reaction mixture was transferred to a separatory funnel and dichloromethane was added. A cold, aqueous solution of sodium hydroxide (6M, 900 mL) was added slowly (light colored precipitate formed) and any heat evolved allowed to dissipate. The funnel was shaken with frequent venting until most of the solids had dissolved, and the organic layer was separated and dried over Na<sub>2</sub>SO<sub>4</sub>. Concentration of this solution on a rotary evaporator yielded 3-bromo-5-iodoaniline as light brown needles (16.30 g, 98%). <sup>1</sup>H-NMR (500 MHz, chloroform-d) δ 7.20 (m, 1H), 6.95 (m, 1H), 6.77 (m, 1H), 3.72 (s, 2H). <sup>13</sup>C-NMR (126 MHz, chloroform-d) δ 148.70, 129.44, 123.46, 122.48, 117.31, 94.94.

### 3-bromo-5-iodo-N,N-dimethylaniline

3-Bromo-5-iodoaniline (6.29 g, 21.1 mmol, 1 eq.) and acetonitrile (90 mL) were added to a flask. Formaldehyde (37% aqueous solution, 18 mL, 646 mmol, 30.6 eq.) and sodium cyanoborohydride (4.24 g, 67.5 mmol, 3.2 eq.) were added and the solution deoxygenated by 3 pump-purge cycles. Acetic acid (2.25 mL, 38 mmol, 1.8 eq.) was added dropwise while cooling the reaction mixture with an icebath to remove evolved heat. The mixture was stirred for 2 h at

room temperature, after which another aliquot of acetic acid (2.25 mL) was added and the mixture stirred for another 30 min. The reaction mixture was partitioned between diethyl ether (340 mL) and 1M potassium hydroxide (180 mL). The organic layer was collected, dried over  $\text{Na}_2\text{SO}_4$ , and concentrated to afford crude product as an oil with some immiscible liquid. The crude product was dissolved in hot hexanes and decanted from an insoluble liquid that remained in the flask. The soluble material was recrystallized from hexanes to afford 3-bromo-5-iodoaniline as an orange, crystalline solid (4.78 g, 69%).  $^1\text{H-NMR}$  (500 MHz, chloroform- $d$ )  $\delta$  7.14 (apparent t,  $J = 1.3$  Hz, 1H), 6.91 (dd, 1H), 6.75 (apparent t,  $J = 1.9$  Hz, 1H), 2.92 (s, 6H).  $^{13}\text{C-NMR}$  (126 MHz, chloroform- $d$ )  $\delta$  152.15, 126.92, 123.57, 119.69, 114.43, 95.30, 40.34.

### Compound 4.3

A flask was charged with 1,3-bis(diphenylene)-2-(4-bromophenyl)propene (3.01 g, 6.03 mmol, 1 eq.), bis(pinacolato)diboron (6.90 g, 27.14 mmol, 4.5 eq.), dry potassium acetate (1.8 g, 18 mmol, 3 eq.), and 1,4-dioxane (100 mL, distilled from lithium aluminum hydride). The solution was deoxygenated by 3 pump-purge cycles, after which [1,1'-bis(diphenylphosphino)ferrocene]dichloropalladium(II) (223 mg, 0.302 mmol, 5 mol %) was added and 3 more pump-purge cycles were performed. The reaction mixture was heated to 75 °C under nitrogen for 2d and partitioned between  $\text{H}_2\text{O}$  and dichloromethane. The organic layer was dried over  $\text{Na}_2\text{SO}_4$  and concentrated to a brown solid. Purification by column chromatography on  $\text{SiO}_2$  in dichloromethane afforded **4.3** as a pale yellow, crystalline solid (2.86 g, 88%).  $\text{I}_2$  was used to visualize boron-containing byproducts and residual bis(pinacolato)diboron on TLC.  $^1\text{H-NMR}$  (500 MHz, methylene chloride- $d_2$ )  $\delta$  8.48 – 8.41 (m,

1H), 7.89 (dt,  $J = 7.5, 0.9$  Hz, 1H), 7.75 (dt,  $J = 7.6, 1.0$  Hz, 1H), 7.69 (dt,  $J = 7.5, 1.0$  Hz, 2H), 7.62 (dq,  $J = 7.5, 1.0$  Hz, 2H), 7.48 (td,  $J = 7.5, 0.9$  Hz, 1H), 7.43 – 7.33 (m, 5H), 7.29 (td,  $J = 7.5, 1.2$  Hz, 2H), 7.22 (td,  $J = 7.5, 1.0$  Hz, 1H), 6.81 (ddd,  $J = 8.3, 7.3, 1.2$  Hz, 1H), 6.75 – 6.68 (m, 2H), 6.56 – 6.49 (m, 1H), 5.88 (dt,  $J = 8.0, 0.9$  Hz, 1H), 1.29 (s, 12H).  $^{13}\text{C}$ -NMR (126 MHz, methylene chloride- $d_2$ )  $\delta$  145.16, 144.48, 142.29, 141.97, 141.62, 140.14, 139.19, 139.05, 136.38, 134.34, 128.62, 128.25, 127.91, 127.88, 127.71, 127.38, 126.99, 126.45, 125.84, 125.60, 120.34, 120.26, 119.42, 84.19, 53.08, 25.11. MALDI-MS  $m/z$   $[\text{M}]^+$  544.72 found, 544.26 expected.

#### Compound 4.4

3-Bromo-5-iodo-*N,N*-dimethylaniline (3.26 g, 10 mmol, 1 eq.), **4.3** (5.44 g, 10 mmol, 1 eq.), and toluene (100 mL) were added to a flask equipped with a reflux condenser. Potassium carbonate (11.07 g, 80 mmol, 8 eq.), ethanol (10 mL), and  $\text{H}_2\text{O}$  (30 mL) were added and the solution deoxygenated by sparging with nitrogen for 15 min. Tetrakis(triphenylphosphine)palladium(0) (235 mg, 0.2 mmol, 2 mol %) was added and the solution sparged with nitrogen for an additional 15 min. The reaction mixture was heated to reflux for 2d and partitioned between  $\text{H}_2\text{O}$  and dichloromethane. The organic layer was dried over  $\text{Na}_2\text{SO}_4$  and evaporated to an orange solid. Recrystallization from dichloromethane/hexanes afforded pure **4.4** as a pale orange solid (1.86 g, 30%).  $^1\text{H}$ -NMR (500 MHz, methylene chloride- $d_2$ )  $\delta$  8.45 (d,  $J = 7.9$  Hz, 1H), 7.90 (d,  $J = 7.5$  Hz, 1H), 7.76 (dt,  $J = 7.6, 1.0$  Hz, 1H), 7.71 (dt,  $J = 7.7, 0.9$  Hz, 2H), 7.64 (dd,  $J = 7.7, 1.1$  Hz, 2H), 7.48 (td,  $J = 7.5, 0.9$  Hz, 1H), 7.42 – 7.33 (m, 3H), 7.30 (td,  $J = 7.4, 1.2$  Hz, 2H), 7.28 – 7.19 (m, 3H), 6.94 (t,  $J =$

1.5 Hz, 1H), 6.82 (ddd,  $J = 8.2, 7.3, 1.2$  Hz, 1H), 6.79 – 6.73 (m, 3H), 6.71 (dd,  $J = 2.5, 1.5$  Hz, 1H), 6.53 (s, 1H), 5.96 (dt,  $J = 8.1, 0.9$  Hz, 1H), 2.95 (s, 6H).  $^{13}\text{C}$ -NMR (126 MHz, methylene chloride- $d_2$ )  $\delta$  152.21, 144.89, 144.56, 142.99, 142.33, 141.62, 140.17, 139.65, 139.26, 139.05, 138.71, 136.81, 129.39, 128.64, 127.95, 127.89, 127.72, 127.43, 127.00, 126.70, 126.41, 125.82, 125.60, 123.85, 120.42, 120.27, 119.46, 117.92, 114.19, 109.73, 53.21, 40.64. MALDI-MS:  $m/z$   $[\text{M}]^+$  614.37 found, 615.16 expected.

### Compound 4.5a

*Note: BDPAH is deprotonated by the sodium tert-butoxide base used in this reaction. The resulting BDPA $^-$  is readily oxidized to the radical in air, so the base and starting material are only mixed under inert atmosphere, and the reaction is quenched with acetic acid prior to workup. Additionally, to prevent deprotonation of BDPAH during column chromatography and improve recovery of product, acetic acid had to be added to the eluent.*

Compound **4.4** (1.23 g, 2.0 mmol, 1 eq.), *N*-Boc-piperazine (522 mg, 2.8 mmol, 1.4 eq.), and tris(dibenzylideneacetone)dipalladium(0) (46 mg, 0.05 mmol, 5 mol % Pd) were added to a flame-dried pressure flask. The flask was loaded into a nitrogen atmosphere glovebox, and sodium tert-butoxide (692 mg, 7.2 mmol, 3.6 eq.) and toluene (20 mL) were added. Tri(*tert*-butyl)phosphine (1.0 M in toluene, 0.25 mL, 0.25 mmol, 0.125 eq., 2.5 L: Pd) was added and the flask was sealed and removed from the glovebox. Compound **4.4** became deprotonated to form a dark blue solution. The flask was heated to 100 °C overnight, after which acetic acid was added (10% in dichloromethane, ~9 mL) and the solution partitioned between dichloromethane and H<sub>2</sub>O. The organic layer was dried over Na<sub>2</sub>SO<sub>4</sub>, treated with a small amount of additional acetic

acid, and concentrated to a yellow-brown oil. This material was purified via column chromatography on SiO<sub>2</sub> in dichloromethane/acetone/acetic acid (96:4:0.25) to afford **4.5a** as light brown crystals (1.05 g, 73%). <sup>1</sup>H-NMR (500 MHz, methylene chloride-d<sub>2</sub>) δ 8.44 (d, J = 8.0 Hz, 1H), 7.90 (dd, J = 7.6, 1.2 Hz, 1H), 7.78 – 7.74 (m, 1H), 7.72 (dt, J = 7.6, 0.9 Hz, 2H), 7.65 (dd, J = 7.5, 1.1 Hz, 2H), 7.48 (td, J = 7.5, 0.9 Hz, 1H), 7.40 – 7.34 (m, 3H), 7.33 – 7.25 (m, 4H), 7.22 (td, J = 7.5, 1.0 Hz, 1H), 6.81 (ddd, J = 8.3, 7.4, 1.2 Hz, 1H), 6.77 – 6.72 (m, 2H), 6.54 (s, 1H), 6.41 (dt, J = 12.6, 1.7 Hz, 2H), 6.22 (t, J = 2.2 Hz, 1H), 5.97 (d, J = 8.0 Hz, 1H), 3.57 – 3.49 (m, 4H), 3.11 (m, 4H), 2.93 (s, 6H), 1.45 (s, 9H). <sup>13</sup>C-NMR (126 MHz, methylene chloride-d<sub>2</sub>) δ 175.21, 154.97, 153.34, 152.32, 145.16, 144.63, 142.33, 141.90, 141.61, 141.41, 140.13, 139.33, 139.08, 138.16, 136.83, 129.22, 128.59, 127.92, 127.84, 127.70, 127.41, 126.99, 126.73, 126.41, 125.87, 125.58, 120.42, 120.25, 119.43, 105.13, 104.53, 101.21, 79.85, 53.28, 50.34, 41.02, 28.52, 28.48, 20.65. ESI-MS: m/z [M+H]<sup>+</sup> 722.36 found, 722.37 expected.

### Compound 4.5b

0.2 mg of **4.5a** was dissolved in 1.5 mL THF. 10 mg MnO<sub>2</sub> was added and the mixture sonicated to disperse the MnO<sub>2</sub>. 1 μL of 1,8-diazabicyclo[5.4.0]undec-7-ene was added and the solution stirred in the dark for 15 min. The solution was run through a SiO<sub>2</sub> plug with THF eluent and used without further purification.

### Compound 4.6

Compound **4.5a** (48 mg, 0.067 mmol, 1 eq.), ethanol (8 mL), and 12 M HCl (111 μL, 1.33 mmol, 20 eq.) were added to a flask equipped with a reflux condenser. The reaction

mixture was heated to reflux for 1h. Ethanol was removed on a rotary evaporator and the remaining mixture partitioned between dichloromethane and 0.5 M sodium hydroxide. The organic layer was dried over Na<sub>2</sub>SO<sub>4</sub> and concentrated to a reddish orange, glassy solid, which was used without further purification (41 mg, *quant.*). ESI-MS: m/z [M+H]<sup>+</sup> 622.44 found, 622.32 expected.

#### **4-bromo-N-(2,5-dimethylphenyl)-1,8-naphthalimide**

4-Bromo-1,8-naphthalic anhydride (2.28 g, 8.22 mmol, 1 eq.), 2,5-dimethylaniline (6.6 mL, 51.6 mmol, 6 eq.), and ethanol (100 mL, 200 proof) were added to a flame-dried flask equipped with a reflux condenser. The reaction mixture was deoxygenated by 3 pump-purge cycles and refluxed overnight. Approximately half of the ethanol was removed on a rotary evaporator and the flask cooled to -20 °C in a freezer. The precipitated solid was collected by filtration and washed with cold ethanol to afford 4-bromo-N-(2,5-dimethylphenyl)-1,8-naphthalimide as a pale yellow solid (1.30 g, 42%). <sup>1</sup>H-NMR (500 MHz, chloroform-d) δ 8.71 (dd, J = 7.3, 1.2 Hz, 1H), 8.65 (dd, J = 8.5, 1.1 Hz, 1H), 8.47 (d, J = 7.8 Hz, 1H), 8.09 (d, J = 7.8 Hz, 1H), 7.90 (dd, J = 8.6, 7.3 Hz, 1H), 7.29 (d, J = 7.9 Hz, 1H), 7.24 – 7.17 (m, 1H), 7.06 – 6.98 (m, 1H), 2.37 (s, 3H), 2.12 (s, 3H). <sup>13</sup>C-NMR (126 MHz, chloroform-d) δ 163.58, 163.55, 137.04, 134.22, 133.80, 132.64, 132.60, 131.76, 131.36, 131.05, 131.02, 130.84, 130.26, 129.67, 128.98, 128.34, 123.40, 122.51, 21.08, 17.30. MALDI-MS: m/z [M]<sup>-</sup> 377.84 found, 379.02 expected.

**Compound 4.1a**

Compound **4.6** (41 mg, 0.067 mmol, 1 eq.), 4-bromo-*N*-(2,5-dimethylphenyl)-1,8-naphthalimide (32 mg, 0.080 mmol, 1.2 eq.), and 2-methoxyethanol (5 mL) were added to a flame-dried flask. The reaction mixture was refluxed for 2d after which the solvent was removed on a rotary evaporator. The resulting yellow-brown solid was purified by column chromatography on SiO<sub>2</sub> in dichloromethane/acetone/acetic acid (97:3:0.125) followed by preparative thin layer chromatography in dichloromethane/acetone/acetic acid (97:3:0.125) to afford **4.1a** as a yellow solid (19.3 mg, 32%). <sup>1</sup>H-NMR (500 MHz, methylene chloride-d<sub>2</sub>) δ 8.62 – 8.52 (m, 3H), 8.45 (d, J = 8.1 Hz, 1H), 7.90 (d, J = 7.3 Hz, 1H), 7.80 – 7.75 (m, 2H), 7.73 (d, J = 7.6 Hz, 2H), 7.66 (d, J = 7.4 Hz, 2H), 7.48 (t, J = 7.4 Hz, 1H), 7.43 – 7.26 (m, 9H), 7.26 – 7.18 (m, 2H), 7.01 (s, 1H), 6.83 (t, J = 8.2 Hz, 1H), 6.78 (d, J = 8.3 Hz, 2H), 6.55 (s, 2H), 6.46 (s, 1H), 6.34 (s, 1H), 5.99 (d, J = 8.0 Hz, 1H), 3.49 (m, 4.4 Hz, 8H), 2.98 (s, 6H), 2.38 (s, 3H), 2.08 (s, 3H). <sup>13</sup>C-NMR (126 MHz, methylene chloride-d<sub>2</sub>) δ 164.55, 164.05, 156.62, 153.13, 152.39, 145.13, 144.65, 142.35, 142.01, 141.61, 141.46, 140.17, 139.34, 139.08, 138.23, 137.17, 136.87, 135.60, 133.37, 133.00, 131.58, 131.06, 130.94, 130.82, 129.88, 129.62, 129.28, 128.62, 127.93, 127.86, 127.73, 127.43, 126.98, 126.80, 126.77, 126.43, 126.17, 125.88, 125.59, 123.86, 120.43, 120.27, 119.45, 117.27, 115.47, 104.84, 104.53, 100.90, 53.29, 50.41, 41.04, 21.00, 17.25. ESI-MS: m/z [M+H]<sup>+</sup> 921.4187 found, 921.4163 expected.

**Compound 4.1b (general procedure)**

0.2 mg of **4.1a** was dissolved in 1.5 mL THF. 10 mg MnO<sub>2</sub> was added and the mixture sonicated to disperse the MnO<sub>2</sub>. 1 μL of 1,8-diazabicyclo[5.4.0]undec-7-ene was added and the

solution stirred in the dark for 15 min. The solution was run through a SiO<sub>2</sub> plug with THF eluent and used without further purification. ESI-MS: m/z [M+H]<sup>+</sup> 920.4118 found, 920.4085 expected.

## B.3 Chapter 5

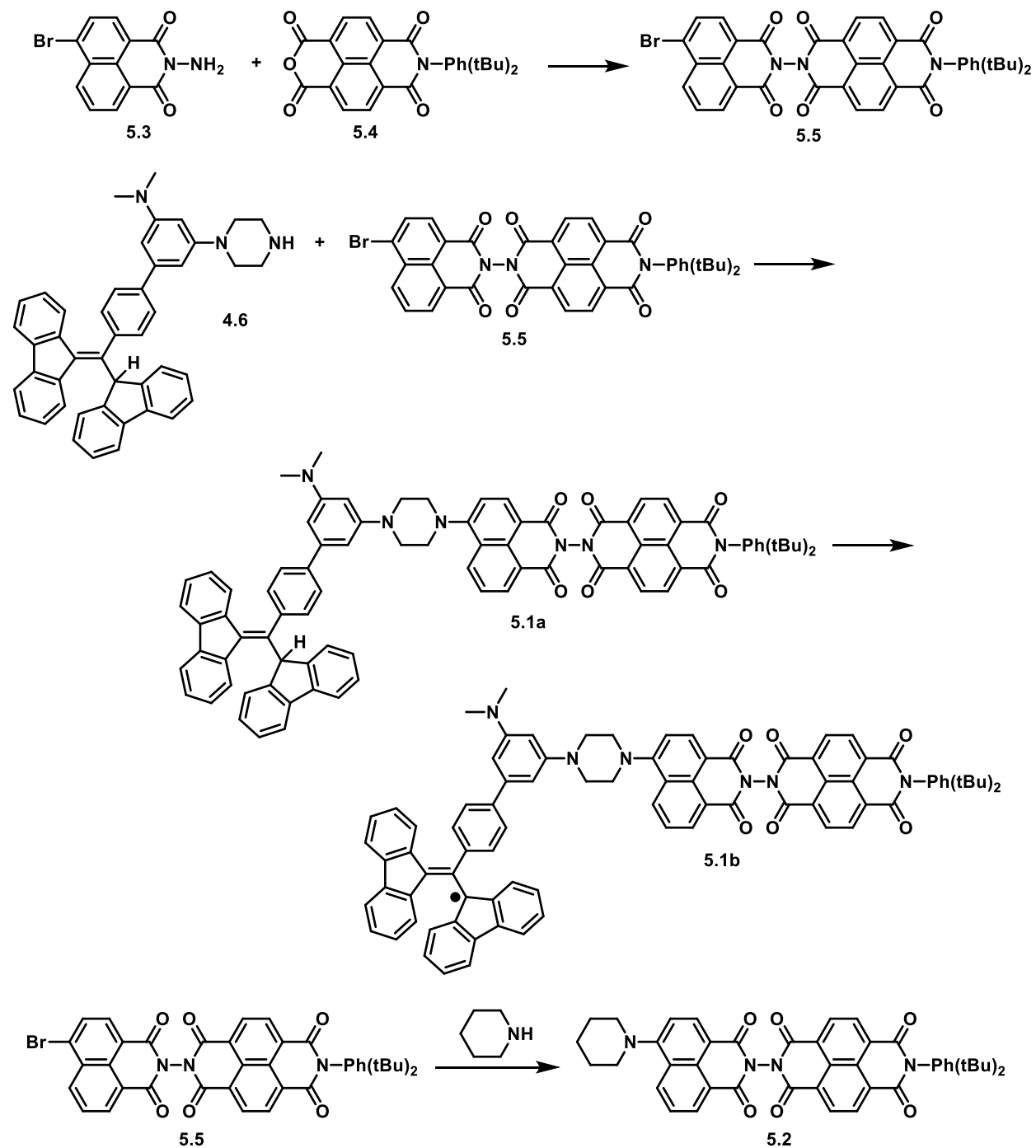


**Figure B.1.** Outline of synthetic route to final products **5.1a**, **5.1b**, and **5.2**. Compounds **5.3**, **5.4**, and **4.6** were synthesized as previously described.<sup>45, 70, 300</sup>

**Compound 5.5**

**5.3** (99 mg, 0.34 mmol, 1 eq.)<sup>300</sup> and **5.4** (171 mg, 0.38 mmol, 1.1 eq.)<sup>70</sup> were added to a flame-dried flask with 1-butanol (5 mL). The mixture was deoxygenated by three pump-purge cycles and heated to reflux under N<sub>2</sub> for 16h. Solvent was removed by rotary evaporation and the material purified by column chromatography on SiO<sub>2</sub> in dichloromethane/acetone (97:3). **5.5** was obtained as a pale yellow solid (146 mg, 59%). <sup>1</sup>H-NMR (500 MHz, CDCl<sub>3</sub>) δ 8.91 (d, J = 7.6 Hz, 2H), 8.88 (d, J = 7.5 Hz, 2H), 8.78 (ddd, J = 7.3, 3.9, 1.2 Hz, 1H), 8.75 (dt, J = 8.6, 1.3 Hz, 1H), 8.53 (dd, J = 7.8, 3.7 Hz, 1H), 8.15 (dd, J = 7.8, 3.2 Hz, 1H), 7.95 (ddd, J = 8.5, 7.3, 3.7 Hz, 1H), 7.62 (d, J = 8.6 Hz, 1H), 7.50 (dd, J = 8.5, 2.2 Hz, 1H), 7.04 (d, J = 2.2 Hz, 1H), 1.34 (s, 9H), 1.29 (s, 9H). MALDI-MS m/z [M]<sup>-</sup> 726.12 found, 727.12 expected.

**Compound 5.1a**

**5.5** (29 mg, 0.040 mmol, 1.1 eq.) and **4.6** (22 mg, 0.036 mmol, 1 eq.)<sup>45</sup> were combined in a flask with 2-methoxyethanol (5 mL). The mixture was deoxygenated by three pump-purge cycles and heated to reflux under N<sub>2</sub> for 2d. The solvent was removed on a rotary evaporator and the crude material partially purified by column chromatography on SiO<sub>2</sub> in dichloromethane/acetone/acetic acid (97:3:0.125). Pure product was obtained as a yellow-brown solid by preparative TLC on SiO<sub>2</sub> in dichloromethane/acetone/acetic acid (96:4:0.125). <sup>1</sup>H-NMR (500 MHz, CD<sub>2</sub>Cl<sub>2</sub>) δ 8.89 (d, J = 7.6 Hz, 2H), 8.86 (d, J = 7.6 Hz, 2H), 8.70 – 8.65 (m, 1H), 8.65 – 8.58 (m, 2H), 8.46 (d, J = 8.1 Hz, 1H), 7.91 (d, J = 7.7 Hz, 1H), 7.81 (dd, J = 8.5, 7.2 Hz, 1H), 7.79 – 7.75 (m, 1H), 7.75 – 7.71 (m, 2H), 7.71 – 7.60 (m, 3H), 7.53 (dd, J = 8.6, 2.3 Hz, 1H), 7.48 (t, J = 7.5 Hz, 1H), 7.43 – 7.28 (m, 8H), 7.23 (t, J = 7.5, 1H), 7.08 (d, J = 2.3 Hz, 1H),

6.84 (t,  $J = 8.2$  Hz, 1H), 6.78 (d,  $J = 8.3$  Hz, 2H), 6.55 (s, 2H), 6.46 (s, 1H), 6.34 (s, 1H), 6.00 (d,  $J = 8.0$  Hz, 1H), 3.58 – 3.46 (m, 8H), 2.99 (s, 6H), 1.35 (s, 9H), 1.27 (s, 9H). ESI-MS:  $m/z$   $[M+H]^+$  1269.5261 found, 1269.5273 expected.

### Compound 5.1b

A THF solution of **5.1a** with an optical density between 0.4 and 0.7 at 416 nm in a 2 mm path length, 0.6 mL cuvette was prepared. The sample was diluted to 1.5 mL with THF and 10 mg of  $MnO_2$  was added. The mixture sonicated to disperse the  $MnO_2$ . 1  $\mu$ L of 1,8-diazabicyclo[5.4.0]undec-7-ene was added and the mixture was briefly sonicated then stirred in the dark for 15 min. The mixture was run through a  $SiO_2$  plug with THF eluent, then solvent was evaporated under an  $N_2$  stream, affording **5.1b** as a reddish-orange solid. ESI-MS:  $m/z$   $[M+H]^+$  1268.5195 found, 1268.5195 expected.

### Compound 5.2

**5.5** (22 mg, 0.03 mmol, 1 eq.) and piperidine (4 mL, 40 mmol, 1300 eq.) were added to a flame-dried flask. The mixture was deoxygenated by three pump-purge cycles and heated to reflux under  $N_2$  for 80 minutes. Excess piperidine was removed on a rotary evaporator and the crude product purified on a short  $SiO_2$  column in dichloromethane/acetone (98:2). **5.2** was obtained as dark yellow solid (20 mg, 91%).  $^1H$ -NMR (500 MHz,  $CD_2Cl_2$ )  $\delta$  8.89 (d,  $J = 7.6$  Hz, 2H), 8.86 (d,  $J = 7.6$  Hz, 2H), 8.67 – 8.62 (m, 1H), 8.60 – 8.53 (m, 2H), 7.77 (ddd,  $J = 8.7, 7.2, 2.0$  Hz, 1H), 7.64 (d,  $J = 8.6$  Hz, 1H), 7.53 (dd,  $J = 8.5, 2.3$  Hz, 1H), 7.27 (dd,  $J = 8.2, 2.0$  Hz,

1H), 7.07 (d,  $J = 2.3$  Hz, 1H), 3.40 – 3.27 (m, 4H), 1.97 – 1.87 (m, 4H), 1.81 – 1.71 (m, 2H), 1.35 (s, 9H), 1.27 (s, 9H). ESI-MS:  $m/z$   $[M+H]^+$  733.3024 found, 733.3021 expected.

## B.4 Chapter 6

### Compound 6.3

Napthalene-1,4,5,8-tetracarboxylic dianhydride (268 mg, 1.0 mmol, 1 eq.) and DMF (10 mL) were added to a flame-dried flask. The mixture was degassed by three pump-purge cycles and heated to reflux under  $N_2$  for 55 min. Meanwhile, 4-amino-TEMPO (172 mg, 1.0 mmol, 1 eq.) and DMF (1 mL) were added to a small flask and deoxygenated by bubbling  $N_2$  for 10 min. This solution was then added dropwise to the initial flask, under  $N_2$ , causing the reaction mixture to become dark and transparent. This flask was then heated to reflux under  $N_2$  overnight. DMF was then removed on a rotary evaporator, and **5.3** (349 mg, 1.2 mmol, 1.2 eq.) and 2-methoxyethanol (5.5 mL) were added and the mixture degassed by three pump-purge cycles. This mixture was heated to reflux under  $N_2$  overnight. 2-methoxyethanol was removed on a rotary evaporator and the resulting solid purified by column chromatography on  $SiO_2$  (5% acetone/DCM eluent). **6.3** was obtained as a brown solid (144 mg, 21%).  $^1H$ -NMR (500 MHz,  $CDCl_3$ )  $\delta$  8.97 – 8.81 (broad m, 4H), 8.77 (dd,  $J = 11.5, 7.9$  Hz, 2H), 8.53 (d,  $J = 7.8$  Hz, 1H), 8.16 (d,  $J = 7.8$  Hz, 1H), 7.96 (t,  $J = 7.9$  Hz, 1H). MALDI-MS:  $[M]^-$  693.10 expected, 693.91 found.

### Compound 6.4

**4.6** (72 mg, 0.12 mmol, 1 eq.), **6.3** (80 mg, 0.12 mmol, 1 eq.), and 2-methoxyethanol (5 mL) were added to a flame-dried flask. This solution was degassed by three pump-purge cycles and heated to reflux under N<sub>2</sub> for 2 d. 2-methoxyethanol was then removed on a rotary evaporator and the resulting solid purified by preparative TLC on SiO<sub>2</sub> (5% acetone/0.125% acetic acid/DCM eluent). **6.4** was obtained as a yellow-brown solid (5 mg, ~1.5%) with a small impurity of **6.1**. <sup>1</sup>H-NMR (500 MHz, CD<sub>2</sub>Cl<sub>2</sub>) δ 8.99 – 8.72 (broad m, 4H), 8.73 – 8.54 (m, 3H), 8.45 (d, *J* = 8.0 Hz, 1H), 7.91 (d, *J* = 7.5 Hz, 1H), 7.81 (t, *J* = 7.8 Hz, 1H), 7.77 (d, *J* = 7.5 Hz, 1H), 7.73 (d, *J* = 7.5 Hz, 2H), 7.67 (d, *J* = 7.5 Hz, 2H), 7.48 (t, *J* = 7.4 Hz, 1H), 7.44 – 7.28 (m, 8H), 7.23 (t, *J* = 7.4 Hz, 1H), 6.84 (t, *J* = 7.6 Hz, 1H), 6.78 (d, *J* = 7.9 Hz, 2H), 6.55 (s, 2H), 6.47 (s, 1H), 6.34 (s, 1H), 6.00 (d, *J* = 7.9 Hz, 1H), 3.58 – 3.47 (m, 8H), 2.99 (s, 6H). MALDI-MS: [M]<sup>+</sup> 1234.49 expected, 1235.71 found.

### Compound 6.1

A solution of **6.4** was prepared in 0.6 mL THF with an optical density at 416 nm between 0.5 and 0.7 in a 2 mm cuvette. This solution was transferred to a vial and an additional 0.9 mL THF added with 10 mg MnO<sub>2</sub>. This mixture was sonicated to disperse the MnO<sub>2</sub>. 1 μL of DBU was added and the mixture sonicated again. The mixture was stirred in the dark for 15 minutes, after which it was passed through an SiO<sub>2</sub> plug with additional THF and evaporated under a stream of N<sub>2</sub>. **6.1** was obtained as a red-orange glassy solid and used immediately.

**Compound 6.5**

3-bromo-5-iodo-N,N-dimethylaniline (1.50 g, 4.6 mmol, 1 eq.), phenylboronic acid (562 mg, 4.6 mmol, 1 eq.), K<sub>2</sub>CO<sub>3</sub> (5.09 g, 36.8 mmol, 8 eq.), Pd(PPh<sub>3</sub>)<sub>4</sub> (263 mg, 0.23 mmol, 0.05 eq.), toluene (60 mL), ethanol (6 mL), and water (18 mL) were added to a flask. The mixture was degassed by three pump-purge cycles and heated to reflux under N<sub>2</sub> for 2 d. The reaction mixture was partitioned between DCM and water, and the organic layer was collected, dried over Na<sub>2</sub>SO<sub>4</sub>, filtered, and concentrated to an oil on a rotary evaporator. The crude product was purified by column chromatography on SiO<sub>2</sub> (50% DCM/hexanes eluent). **6.5** was obtained as a pale yellow oil (670 mg, 53%). <sup>1</sup>H-NMR (500 MHz, CDCl<sub>3</sub>) δ 7.58 – 7.52 (m, 2H), 7.43 (t, *J* = 7.6 Hz, 2H), 7.38 – 7.33 (m, 1H), 7.05 (s, 1H), 6.82 (s, 1H), 6.79 (s, 1H), 3.00 (s, 6H).

**Compound 6.6**

**6.5** (670 mg, 2.43 mmol, 1 eq.), N-Boc-piperazine (635 mg, 3.40 mmol, 1.4 eq.), Pd<sub>2</sub>(dba)<sub>3</sub> (56 mg, 0.061 mmol, 0.025 eq.), sodium t-butoxide (420 mg, 4.37 mmol, 1.8 eq.), and toluene (24 mL) were added to a flame-dried Schlenk tube. The mixture was degassed by three freeze-pump-thaw cycles and loaded into an N<sub>2</sub>-filled glovebox. Tri(*t*-butyl)phosphine (1 M in toluene, 0.3 mL, 0.3 mmol, 0.125 eq.) was added and the tube sealed and removed from the glovebox. The tube was heated to 100 °C for 18 h. The reaction mixture was poured directly onto a SiO<sub>2</sub> column and product was separated by chromatography (5% acetone/DCM eluent). **6.6** was recovered as a pale orange crystalline solid (440 mg, 47%). <sup>1</sup>H-NMR (500 MHz, CDCl<sub>3</sub>) δ 7.57 (d, *J* = 7.8 Hz, 2H), 7.41 (t, *J* = 7.6 Hz, 2H), 7.33 (t, *J* = 7.4 Hz, 1H), 6.53 (s, 1H),

6.51 (s, 1H), 6.29 (s, 1H), 3.63 – 3.54 (m, 4H), 3.23 – 3.14 (m, 4H), 3.00 (s, 6H), 1.48 (s, 9H).

MALDI-MS:  $[M]^+$  381.24 expected, 381.57 found.

### Compound 6.7

**6.6** (59 mg, 0.16 mmol, 1 eq.), ethanol (6.5 mL), and hydrochloric acid (12 M, 270  $\mu$ L, 3.2 mmol, 20 eq.) were added to a flask. The mixture was degassed by three pump-purge cycles and heated to reflux under  $N_2$  for 100 min. Ethanol was removed on a rotary evaporator and the resulting solid dissolved in DCM and 0.5 M NaOH aqueous solution. The organic layer was collected using a separatory funnel, dried over  $Na_2SO_4$ , filtered, and evaporated to yield **6.7** as a yellow oil (52 mg, quant.) containing some solvent.  $^1H$ -NMR (499 MHz,  $CDCl_3$ )  $\delta$  7.58 (dd,  $J = 8.2, 1.3$  Hz, 2H), 7.41 (t,  $J = 7.6$  Hz, 2H), 7.33 (t,  $J = 7.3$  Hz, 1H), 6.55 (t,  $J = 1.8$  Hz, 1H), 6.49 (t,  $J = 1.8$  Hz, 1H), 6.31 (t,  $J = 2.2$  Hz, 1H), 3.24 – 3.18 (m, 4H), 3.08 – 3.03 (m, 4H), 2.99 (s, 6H).

### Compound 6.2

**6.7** (17 mg, 0.061 mmol, 1.4 eq.), **6.3** (29 mg, 0.043 mmol, 1 eq.), and 2-methoxyethanol (5 mL) were added to a flame-dried flask. The resulting solution was degassed by three pump-purge cycles and heated to reflux under  $N_2$  for 2 d. 2-methoxyethanol was removed on a rotary evaporator and the resulting solid purified by preparative TLC on  $SiO_2$  (3% methanol/DCM eluent). **6.2** was isolated as a yellow-brown solid.  $^1H$ -NMR (500 MHz,  $CD_2Cl_2$ )  $\delta$  8.93 – 8.74 (broad m, 4H), 8.66 (ddd,  $J = 8.5, 5.5, 1.2$  Hz, 2H), 8.61 (d,  $J = 8.1$  Hz, 1H), 7.82 (dd,  $J = 8.5, 7.2$  Hz, 1H), 7.67 – 7.59 (m, 2H), 7.44 (dd,  $J = 8.3, 7.0$  Hz, 2H), 7.41 – 7.30 (m, 2H), 6.63 (s,

1H), 6.55 (s, 1H), 6.39 (s, 1H), 3.59 (dd,  $J = 6.7, 3.2$  Hz, 4H), 3.54 (d,  $J = 4.8$  Hz, 4H), 3.03 (s, 6H). MALDI-MS:  $[M]^-$  894.36 expected, 894.86 found.

### B.5 Chapter 7

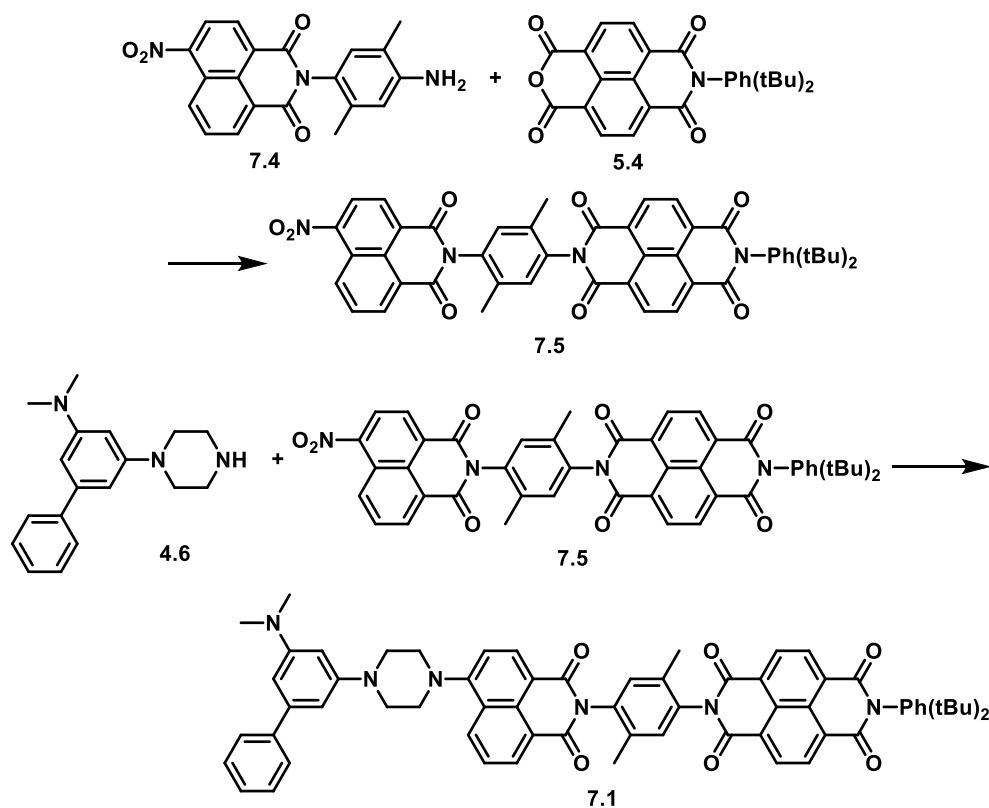


**Figure B.2.** Outline of synthetic scheme for 7.1. 7.4 was prepared as previously described.<sup>235</sup>

### Compound 7.5

7.4 (183 mg, 0.5 mmol, 1 eq.), 5.4 (341 mg, 0.75 mmol, 1.5 eq.), glacial acetic acid (10 mL), and a small scoop of p-toluenesulfonic acid monohydrate were added to a flame-dried flask. The reaction mixture was degassed by three pump-purge cycles and heated to 50 °C for 2

h under N<sub>2</sub>. The mixture was then refluxed under N<sub>2</sub> overnight. Acetic acid was removed on a rotary evaporator and the resulting light brown solid purified by column chromatography on SiO<sub>2</sub> (2.5% acetone/DCM eluent). **7.5** was isolated as a light yellow solid (322 mg, 80%). The yield was significantly reduced by a spill. <sup>1</sup>H-NMR (499 MHz, CDCl<sub>3</sub>) δ 8.92 (dd, *J* = 8.7, 1.1 Hz, 1H), 8.91 – 8.87 (m, 4H), 8.83 (dd, *J* = 7.3, 1.1 Hz, 1H), 8.79 (d, *J* = 7.9 Hz, 1H), 8.47 (d, *J* = 8.0 Hz, 1H), 8.07 (dd, *J* = 8.8, 7.3 Hz, 1H), 7.62 (d, *J* = 8.7 Hz, 1H), 7.50 (dd, *J* = 8.6, 2.2 Hz, 1H), 7.33 – 7.28 (m, 1H), 7.02 (dd, *J* = 7.5, 2.2 Hz, 1H), 2.24 – 2.19 (m, 6H), 1.35 – 1.33 (m, 9H), 1.29 (s, 9H).

### Compound 7.1

**6.7** (37 mg, 0.13 mmol, 1 eq.), **7.5** (105 mg, 0.13 mmol, 1 eq.), Na<sub>2</sub>CO<sub>3</sub> (16 mg, 0.14 mmol, 1.1 eq.), and DMSO (1.5 mL) were added to a flame-dried flask. This mixture was degassed by three pump-purge cycles and the flask kept under N<sub>2</sub>. The reaction mixture was heated under N<sub>2</sub> overnight, after which the DMSO was removed by heating under vacuum to afford a yellow-brown oil containing a little DMSO. The crude product was initially purified by chromatography on a short SiO<sub>2</sub> column (5% acetone/DCM eluent) and further purified by preparative TLC (10% acetone/DCM on SiO<sub>2</sub>). **7.1** was obtained as a yellow-brown glassy solid. <sup>1</sup>H-NMR (499 MHz, CD<sub>2</sub>Cl<sub>2</sub>) δ 8.92 (d, *J* = 7.5 Hz, 2H), 8.87 (d, *J* = 7.5 Hz, 2H), 8.69 (d, *J* = 7.2 Hz, 1H), 8.63 (t, *J* = 7.6 Hz, 2H), 7.82 (t, *J* = 7.9 Hz, 1H), 7.64 (t, *J* = 7.4 Hz, 3H), 7.54 (dd, *J* = 8.6, 2.3 Hz, 1H), 7.44 (t, *J* = 7.6 Hz, 2H), 7.38 (dd, *J* = 16.7, 7.7 Hz, 2H), 7.29 (d, *J* = 9.1 Hz, 2H), 7.10 – 7.03 (m, 1H), 6.64 (s, 1H), 6.55 (s, 1H), 6.40 (s, 1H), 3.65 – 3.56 (m, 4H), 3.56 –

3.49 (m, 4H), 3.03 (s, 6H), 2.23 – 2.17 (m, 6H), 1.35 (s, 9H), 1.28 (s, 9H). MALDI-MS:  $[M+H]^+$   
1033.46 expected, 1033.39 found.

# APPENDIX C

## Supplementary Information for Chapter 4

## C.1 Electrochemistry

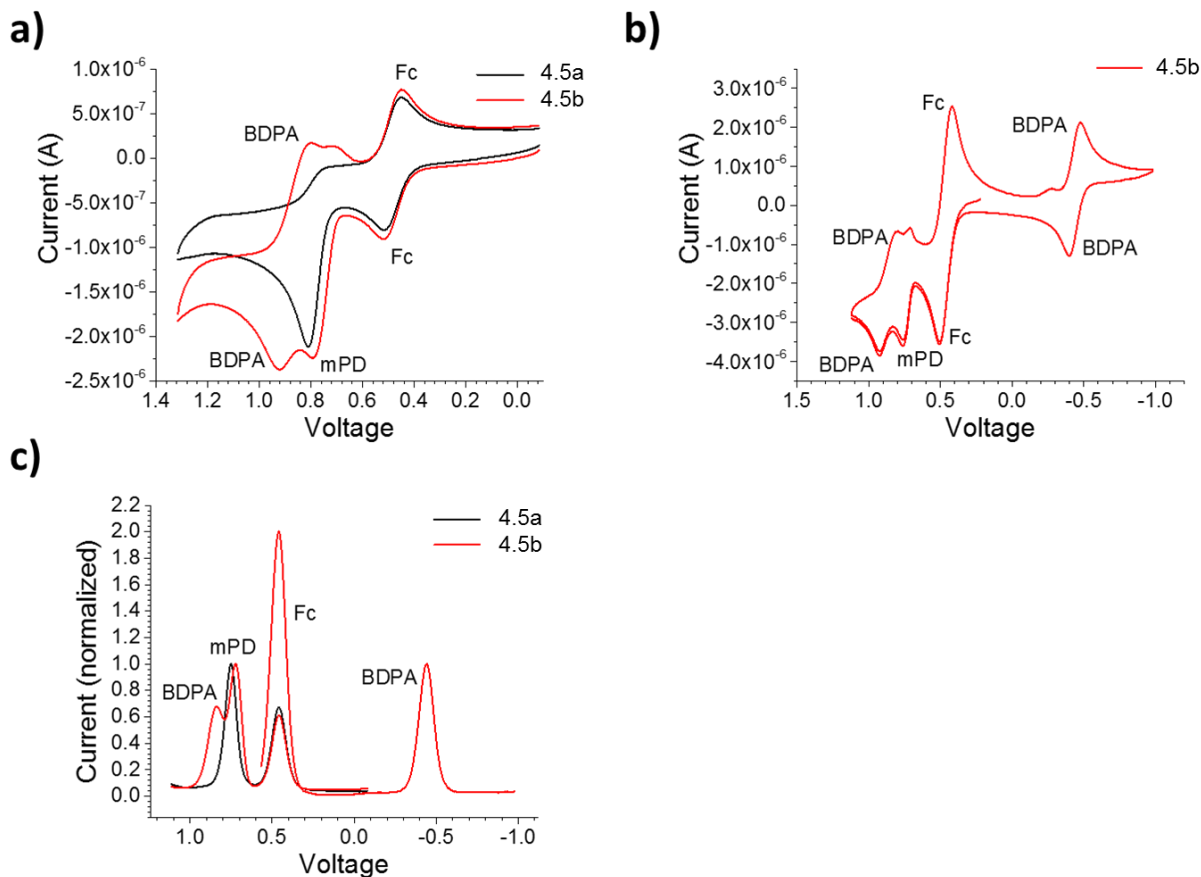


**Figure C.1.** a) Comparison of cyclic voltammograms (CVs) for **4.5a** and **4.5b**. b) CV for **4.5b** showing oxidation and reduction features. c) Differential pulse voltammograms for **4.5a** and **4.5b**.

## C.2 Reorganization Energy Calculations

The value of the total reorganization energy ( $\lambda$ ) is the sum of the internal ( $\lambda_I$ ) and solvent ( $\lambda_S$ ) reorganization energies. The values of  $\lambda_I$  for  $\text{mPD} \rightarrow \text{mPD}^{+\bullet}$  and  $\text{ANI} \rightarrow \text{ANI}^{\bullet}$  were calculated from the difference in energy of each radical ion in the neutral molecule geometry and

the corresponding energy of each radical ion in its relaxed geometry using the data in Table C.1. The values of  $\lambda_S$  were calculated using the Marcus expression,<sup>72</sup> which is based on the dielectric continuum model of the solvent:

$$\lambda_S = e^2 \left( \frac{1}{2r_D} + \frac{1}{2r_A} - \frac{1}{r_{DA}} \right) \left( \frac{1}{\epsilon_0} - \frac{1}{\epsilon_S} \right) \quad (1)$$

where  $e$  is the electronic charge,  $r_D$  and  $r_A$  are the radii of the donor and acceptor, respectively,  $\epsilon_S$  is the static dielectric constant, and  $\epsilon_0$  is the optical (high frequency) dielectric constant, which is approximated as the index of refraction squared. The radii of  $mPD^{+\bullet}$  and  $ANI^{\bullet-}$  are both approximately 4 Å, and  $r_{DA} = 9.0$  Å.

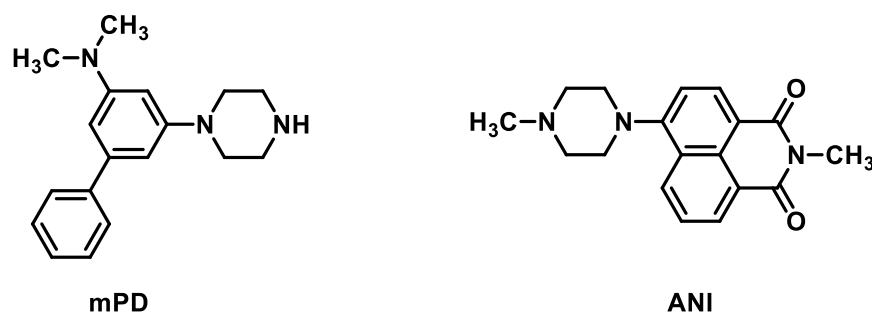


**Figure C.2.** Structures of molecular fragments for which energies were computed.

Compound	Energy (Hartree)
ANI neutral, optimized geometry	-1012.102124
ANI radical anion, neutral geometry	-1012.123317
ANI radical anion, optimized geometry	-1012.129645
mPD neutral, optimized geometry	-864.0000866
mPD radical cation, neutral geometry	-863.7720976
mPD radical cation, optimized geometry	-863.7790253

**Table C.1.** Energies of neutral and charged mPD and ANI obtained via DFT (B3LYP / 6-31G\* in vacuum)

Atom	X (Å)	Y (Å)	Z (Å)
C	0.095972137	-1.936652693	0.187049226
C	-1.086447385	-1.206354738	0.433199835
C	-1.070452261	0.190333101	0.586942115
C	1.305651084	-1.22899619	0.044965601
C	1.334278587	0.164574968	0.187371996
C	0.159251809	0.867605858	0.466761311
H	-2.030604638	-1.728479051	0.469900012
H	2.221701152	-1.744769247	-0.210263276
H	0.213678386	1.932009069	0.663763322
C	2.624950628	0.89356989	0.058872341
N	0.061474844	-3.325941039	0.070568697
N	-2.232674176	0.914541046	0.908944101
C	-3.474640799	0.240369092	1.275702837
C	-2.507745675	2.199884491	0.261119276
C	-3.439379154	2.023754822	-0.946574087
H	-1.575508317	2.667705328	-0.05582571
H	-2.992726369	2.863225312	0.990026578
C	-4.408895605	0.04898452	0.073536272
H	-3.992915748	0.877198956	2.006216387
H	-3.251901213	-0.708227	1.768843818
N	-4.675552541	1.367051748	-0.511670444
H	-2.897142189	1.451846518	-1.724315881
H	-3.692014037	3.00555369	-1.365168526
H	-5.308777088	1.27062722	-1.302437523
H	-5.359327905	-0.387925305	0.403677256
H	-3.941553542	-0.653277309	-0.642880388
C	-1.218315079	-4.007310494	0.014568149
H	-1.824811829	-3.725230008	-0.862970223
H	-1.809697329	-3.79970141	0.914035805
H	-1.047475669	-5.085401304	-0.022714796
C	1.221030319	-4.018499866	-0.46447834
H	1.481246063	-3.697420874	-1.486321966
H	1.018520708	-5.091466317	-0.483869631
H	2.100344677	-3.860919898	0.171248601
C	3.815032451	0.357655355	0.579858792
C	2.691251164	2.138777159	-0.588957438
C	3.900045693	2.822603452	-0.711654521
C	5.025004839	1.039491156	0.456901596
C	5.073769827	2.275809945	-0.189678542
H	5.93058027	0.607847555	0.875884323
H	3.781374907	-0.591225527	1.107829679
H	1.78698192	2.559561832	-1.019748588

H	6.016522921	2.807964886	-0.285333191
H	3.926875162	3.781014301	-1.224113853

**Table C.2.** Optimized coordinates for neutral mPD.

Atom	X (Å)	Y (Å)	Z (Å)
C	0.105809987	-2.020024789	0.103355038
C	-1.09888144	-1.327590476	0.3104292
C	-1.110647718	0.076232413	0.407863112
C	1.325549521	-1.267011143	-0.007390191
C	1.342342157	0.128382267	0.098159167
C	0.133229926	0.793959421	0.307983896
H	-2.02882368	-1.872418011	0.321878041
H	2.260748468	-1.781175102	-0.184640309
H	0.157306881	1.860288574	0.488385863
C	2.620134874	0.878290425	0.010630016
N	0.143477581	-3.377480853	-0.019102406
N	-2.25804079	0.778981272	0.657789987
C	-3.510949685	0.147582886	1.094188553
C	-2.463770802	2.186805294	0.277646242
C	-3.538393038	2.262681793	-0.825769653
H	-1.53748543	2.627628288	-0.084060911
H	-2.806111356	2.737292062	1.160487999
C	-4.570526789	0.232568131	-0.016391177
H	-3.870912414	0.717126495	1.958933745
H	-3.328552542	-0.875346447	1.417199383
N	-4.758508965	1.638279468	-0.340554813
H	-3.127708698	1.79185459	-1.738851035
H	-3.734137977	3.316532811	-1.047386692
H	-5.5336828	1.778450828	-0.982294229
H	-5.51180425	-0.183641133	0.356073412
H	-4.241135636	-0.383016628	-0.874683808
C	-1.080980775	-4.15558479	0.149486514
H	-1.79144311	-3.96460839	-0.665687546
H	-1.565069379	-3.913045571	1.102382291
H	-0.836392604	-5.216894874	0.151554755
C	1.38112592	-4.085288107	-0.363711519
H	1.808090732	-3.706049568	-1.297701452
H	1.152043148	-5.140627548	-0.504776813
H	2.128224339	-4.003158299	0.434102341
C	3.786366558	0.379138888	0.613698686
C	2.68410179	2.100853005	-0.678072685

C	3.884077348	2.804395377	-0.76319773
C	4.984516089	1.085886677	0.530420143
C	5.036910107	2.299208232	-0.158675296
H	5.875279179	0.693347429	1.011756111
H	3.749298248	-0.54771924	1.179999909
H	1.799614283	2.486321363	-1.178634284
H	5.971535832	2.848062136	-0.224615465
H	3.92115791	3.742293843	-1.309395391

**Table C.3.** Optimized coordinates for mPD radical cation.

Atom	X (Å)	Y (Å)	Z (Å)
C	-5.241439806	2.176547343	1.001050593
C	-3.98653119	2.492271153	0.475879719
C	-3.112656043	1.404622184	0.095007319
C	-3.506477917	0.062515851	0.393445368
C	-4.770524923	-0.203907266	0.978431049
C	-5.626596615	0.851340837	1.243098861
C	-5.192928377	-1.581311572	1.297536697
H	-6.594858247	0.633235957	1.681946453
H	-5.920916756	2.971352403	1.285129536
N	-3.580803154	3.813616267	0.257224981
C	-2.642581185	-1.013634089	0.062143707
C	-1.44251503	-0.779613851	-0.586402802
C	-1.086011808	0.530722533	-0.951459076
C	-1.904693048	1.595562183	-0.623802181
H	-0.80843646	-1.626808873	-0.825925644
H	-0.169846915	0.704714176	-1.508267697
H	-1.640536933	2.594142994	-0.952597921
N	-4.272239246	-2.603211443	0.994066897
O	-6.278852346	-1.841146202	1.802107975
C	-3.026165209	-2.410091836	0.387312002
O	-2.305180412	-3.370440301	0.144865865
C	-4.635226413	-3.988367323	1.30650554
H	-5.598415745	-3.970151497	1.811240844
H	-3.869497403	-4.433937148	1.945607433
H	-4.697349555	-4.576327505	0.386758081
C	-4.572818142	4.881738876	0.116734251
C	-2.343639478	4.322537519	0.872838695
C	-4.83506754	5.648977391	1.418919429
H	-5.49725655	4.464081344	-0.288264052
H	-4.178881616	5.593720481	-0.621471646

H	-5.353604377	4.998294548	2.151585039
H	-5.49853984	6.497240597	1.209674673
N	-3.57644529	6.162734959	1.955532349
C	-2.630356615	5.072527891	2.179010385
H	-1.857696075	5.00899618	0.166789075
H	-1.665111108	3.492772261	1.071549281
C	-3.783671604	6.955380463	3.158659473
H	-1.692396078	5.494812384	2.560367651
H	-3.000775959	4.35292495	2.938091351
H	-4.457171163	7.790928919	2.938549568
H	-2.826980225	7.368590575	3.496194917
H	-4.220557607	6.373715685	3.993945968

**Table C.4.** Optimized coordinates for neutral ANI.

Atom	X (Å)	Y (Å)	Z (Å)
C	-5.168754806	2.216723015	1.094020412
C	-3.942609699	2.49505154	0.459977474
C	-3.105577091	1.408493175	0.039493486
C	-3.504203176	0.060647343	0.370479332
C	-4.741242844	-0.174021197	1.032903276
C	-5.572347129	0.917541493	1.362655854
C	-5.162429085	-1.520137123	1.374468732
H	-6.516484625	0.711054067	1.855702611
H	-5.817186454	3.035860661	1.390094549
N	-3.501657448	3.831889537	0.184000996
C	-2.661673013	-1.028595493	0.008922064
C	-1.45341544	-0.795955266	-0.689943568
C	-1.099253863	0.495754989	-1.047277401
C	-1.904828676	1.58886067	-0.697133474
H	-0.838622426	-1.653475385	-0.94297316
H	-0.183786235	0.669990088	-1.611782935
H	-1.640089379	2.587519947	-1.028587433
N	-4.269944185	-2.552938641	1.013638843
O	-6.23079053	-1.786450467	1.956024243
C	-3.039349372	-2.388985678	0.346864944
O	-2.355425639	-3.397100692	0.090476318
C	-4.633915737	-3.922749165	1.352280326
H	-5.572826686	-3.880063066	1.902074196
H	-3.844686531	-4.382365976	1.955146344
H	-4.746109372	-4.525363401	0.444214269
C	-4.478869249	4.897352044	0.023606518

C	-2.324326223	4.315211589	0.909986258
C	-4.819480434	5.657225685	1.320243164
H	-5.389427924	4.481129388	-0.416838414
H	-4.067957989	5.633877564	-0.686240441
H	-5.413442698	5.013629989	1.997795176
H	-5.439257392	6.532391377	1.077698632
N	-3.598398094	6.127973658	1.978944448
C	-2.68400643	5.008486801	2.228412525
H	-1.792054176	5.042775278	0.277140128
H	-1.654428939	3.472972588	1.094425347
C	-3.900742266	6.855445441	3.197794347
H	-1.774622923	5.407261762	2.699200751
H	-3.123128731	4.268747069	2.927460239
H	-4.544399282	7.714223275	2.969178993
H	-2.97252488	7.233269896	3.643788255
H	-4.417972932	6.238511622	3.96127378

**Table C.5.** Optimized coordinates for ANI radical anion.

### C.3 Electron Transfer Reaction Free Energy Calculations

The one-electron oxidation potentials for mPD, ANI, and BDPA are given in Table 1 in the main text. The ion pair energies in a given solvent were calculated using the method outlined in Greenfield et al.<sup>161</sup> using eq. C.2,

$$\Delta G_F = \Delta G_I + \text{sign}(E_I - E_F) + \frac{e^2}{\epsilon_S} \left( \frac{q^2}{r_I} - \frac{1}{r_F} \right) \quad \text{if } |E_F| > |E_I|, \text{ then sign} = (-)$$

$$\text{if } |E_I| > |E_F|, \text{ then sign} = (+) \quad (\text{C.2})$$

where  $\Delta G_I$  and  $\Delta G_F$  are the energies above ground state for the initial and final ion pairs, respectively,  $E_I$  and  $E_F$  are the redox potentials for the initial and final ions, respectively, between which the electron is transferred,  $r_I$  and  $r_F$  are the initial and final ion pair distances,

respectively,  $e$  is the electronic charge,  $q = 0.7$  is the fraction of charge transferred in the excited singlet state of ANI (which is considered the initial ion pair because of its high charge transfer character),<sup>161</sup> and  $\epsilon_s$  is the static dielectric constant of the solvent. The internal charge transfer distance within ANI is  $r_I = 3.3 \text{ \AA}$ <sup>161</sup> and the mPD<sup>+</sup>-ANI<sup>•</sup> distance is  $r_F = 9.0 \text{ \AA}$ . The free energies for the initial charge separation ( $\Delta G_{CS}$ ), charge recombination to the singlet ground state ( $\Delta G_{CRS}$ ), and charge recombination to <sup>3\*</sup>ANI ( $\Delta G_{CRT}$ ) were then determined using eqs. C.3-C.5, where  $E_S = 2.80 \text{ eV}$  and  $E_T = 2.05 \text{ eV}$  are the lowest excited singlet and triplet state energies of ANI, respectively.

$$\Delta G_{CS} = \Delta G_F - E_S \quad (\text{C.3})$$

$$\Delta G_{CRS} = -\Delta G_F \quad (\text{C.4})$$

$$\Delta G_{CRT} = \Delta G_F - E_T \quad (\text{C.5})$$

### C.4 Transient Absorption Spectroscopy

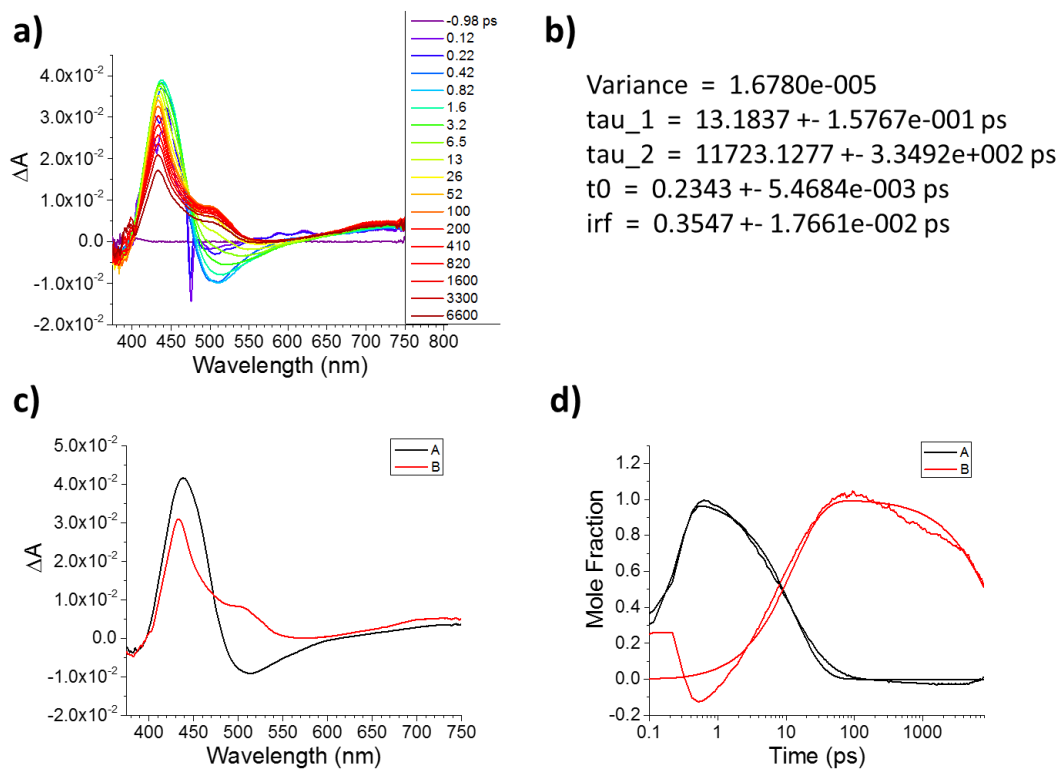


**Figure C.3.** 4.1a in benzene at 295 K, 414 nm exc., fsTA. a) fsTA spectra; b) fitting parameters; c) fitted species spectra; d) fitted kinetics.

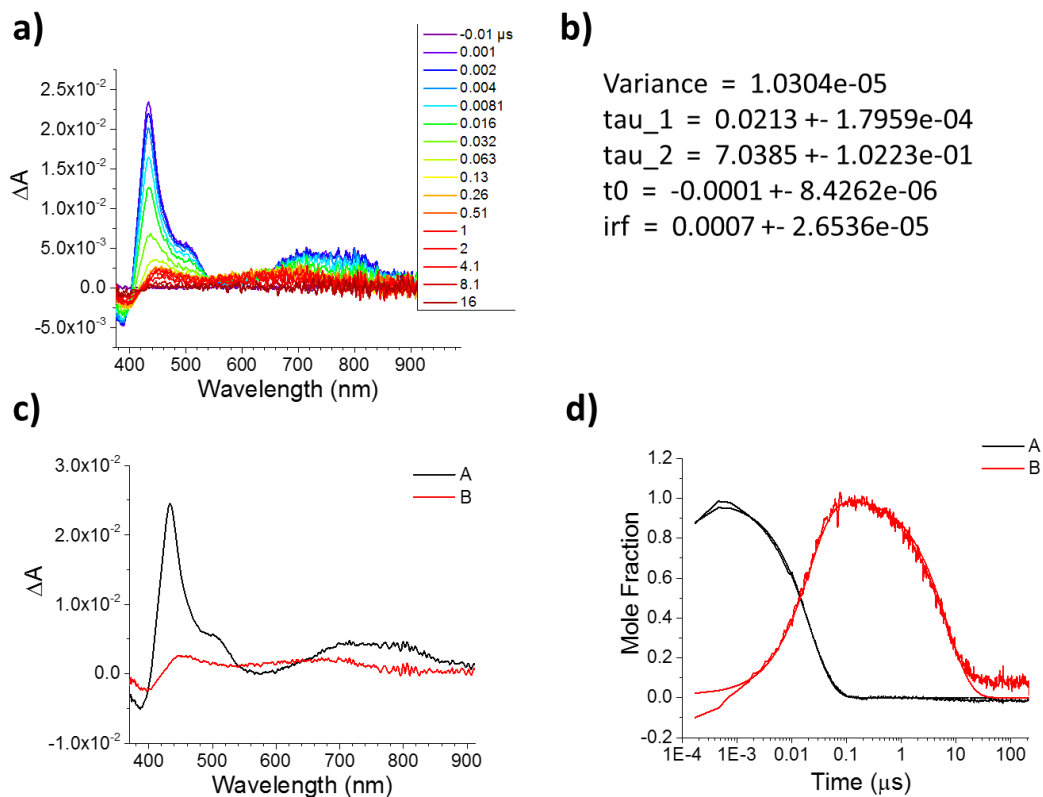


**Figure C.4.** **4.1a** in benzene at 295 K, 414 nm exc., nsTA. a) nsTA spectra; b) fitting parameters; c) fitted species spectra; d) fitted kinetics.

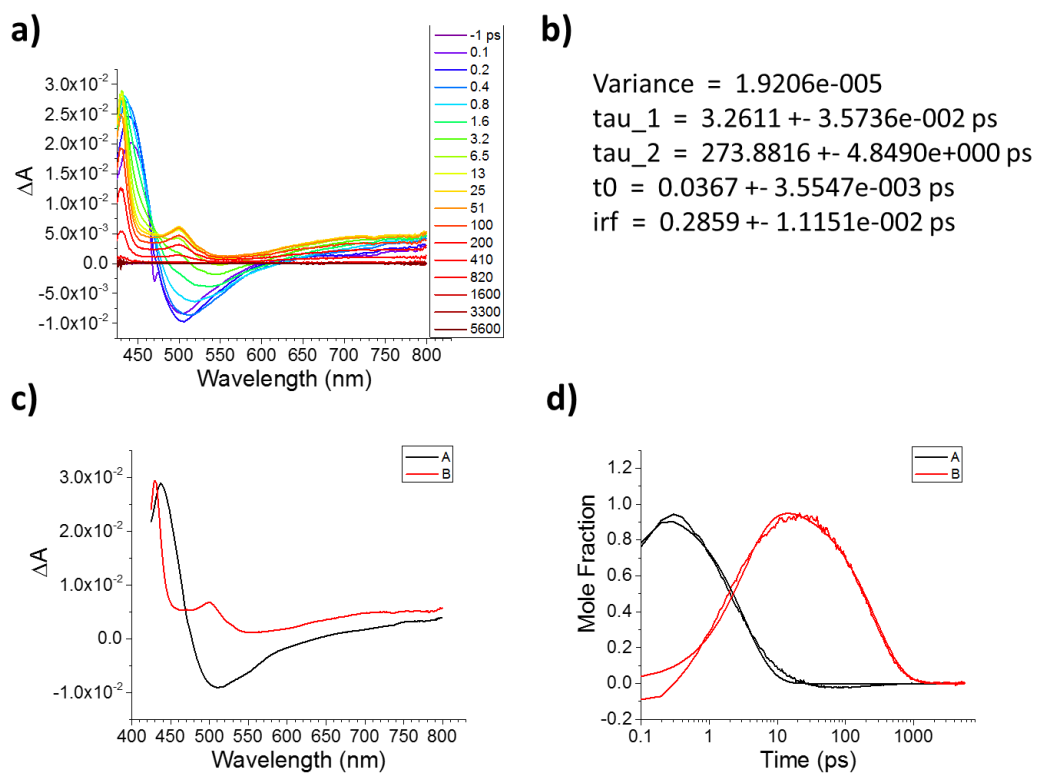


**Figure C.5.** 4.1a in THF at 295 K, 414 nm exc., fsTA. a) fsTA spectra; b) fitting parameters; c) fitted species spectra; d) fitted kinetics.

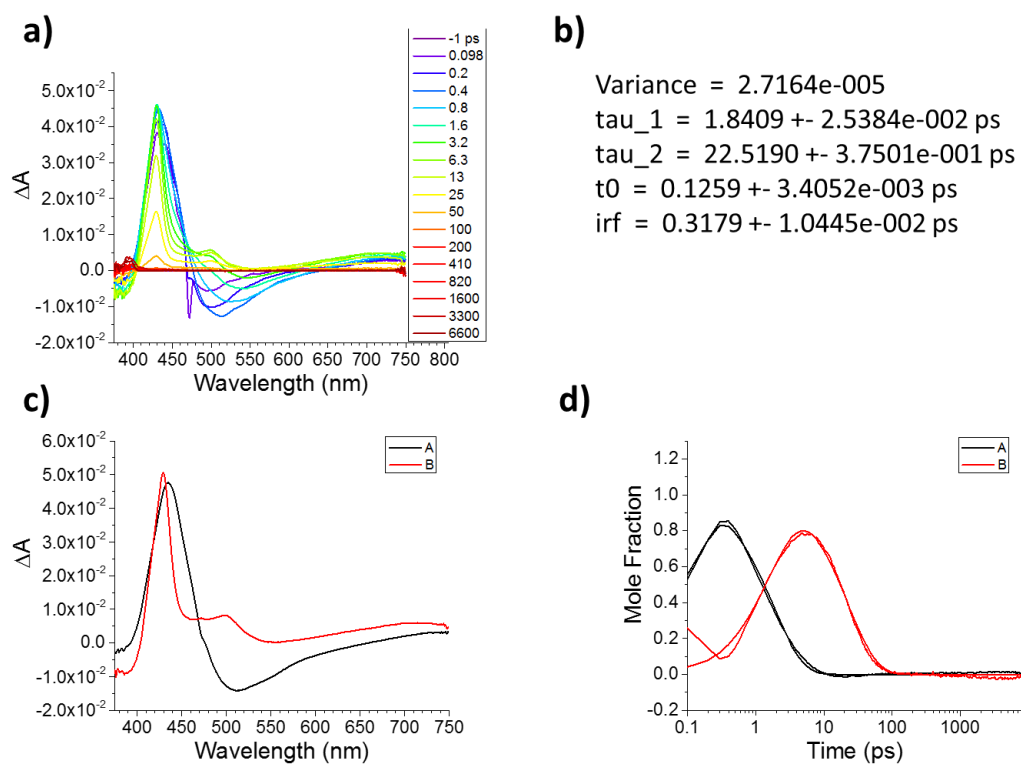


**Figure C.6.** **4.1a** in PrCN at 295 K, 414 nm exc., fsTA. a) fsTA spectra; b) fitting parameters; c) fitted species spectra; d) fitted kinetics.

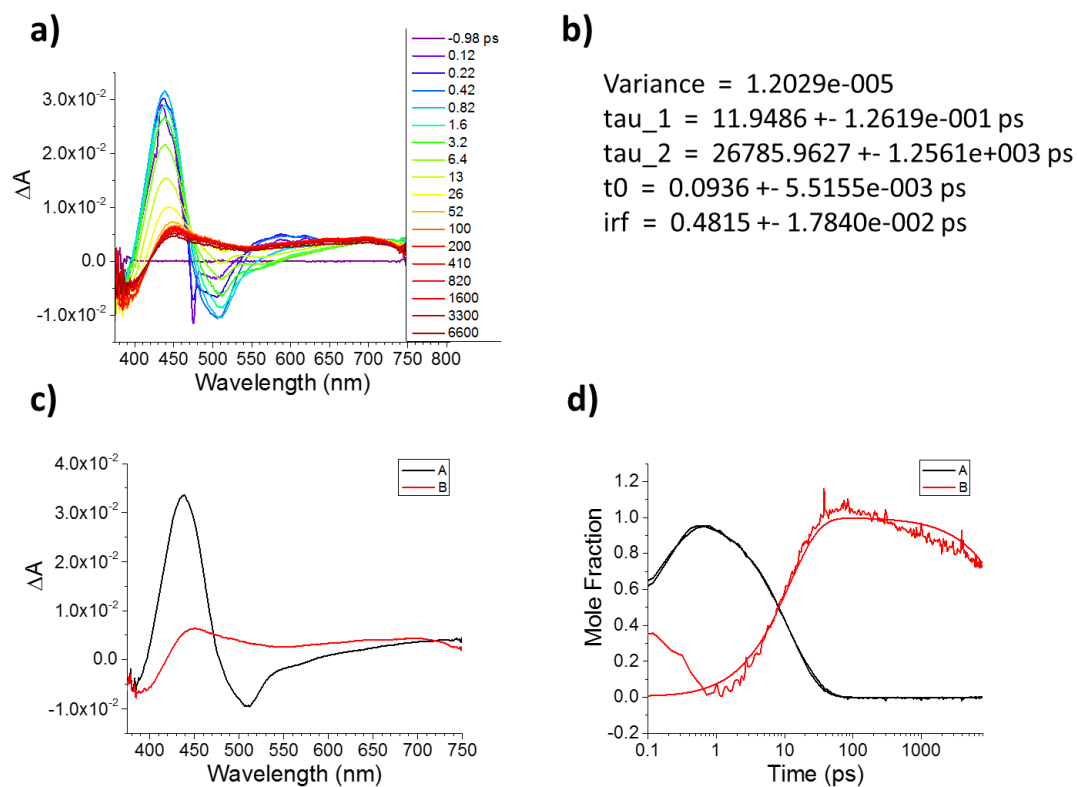


**Figure C.7.** **4.1b** in benzene at 295 K, 414 nm exc., fsTA. a) fsTA spectra; b) fitting parameters; c) fitted species spectra; d) fitted kinetics.

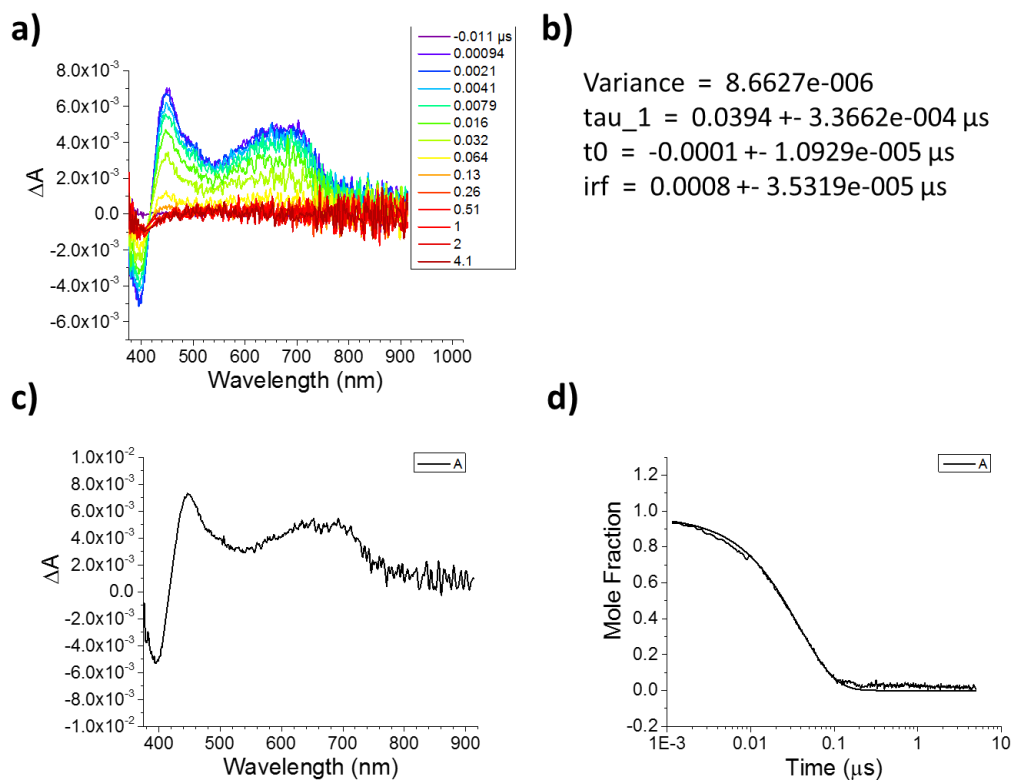


**Figure C.8.** **4.1b** in benzene at 295 K, 414 nm exc., nsTA. a) nsTA spectra; b) fitting parameters; c) fitted species spectra; d) fitted kinetics.

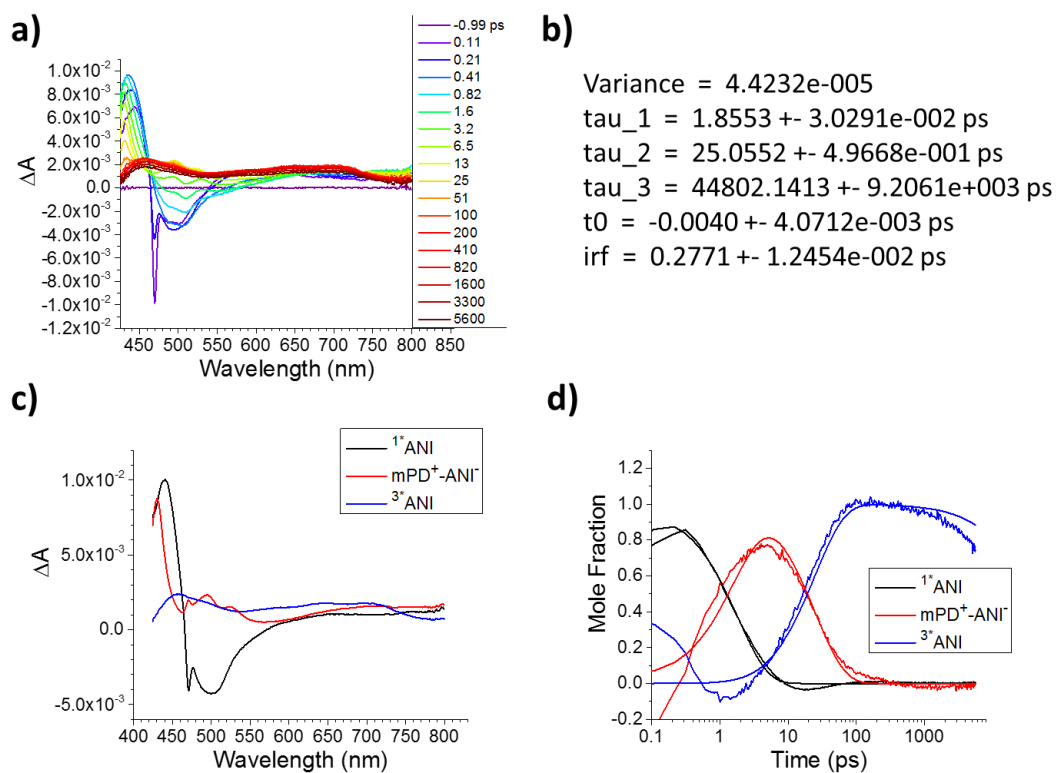


**Figure C.9.** 4.1b in THF at 295 K, 414 nm exc., fsTA. a) fsTA spectra; b) fitting parameters; c) fitted species spectra; d) fitted kinetics.

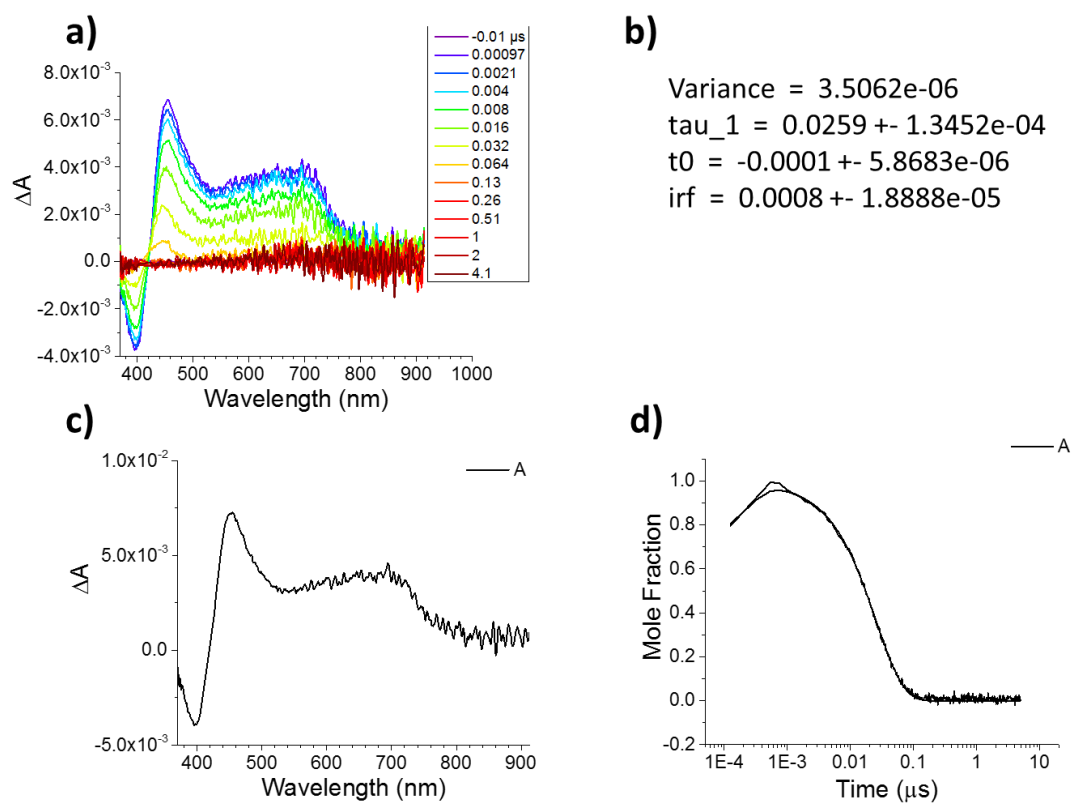


**Figure C.10.** 4.1b in THF at 295 K, 414 nm exc., nsTA. a) nsTA spectra; b) fitting parameters; c) fitted species spectra; d) fitted kinetics.

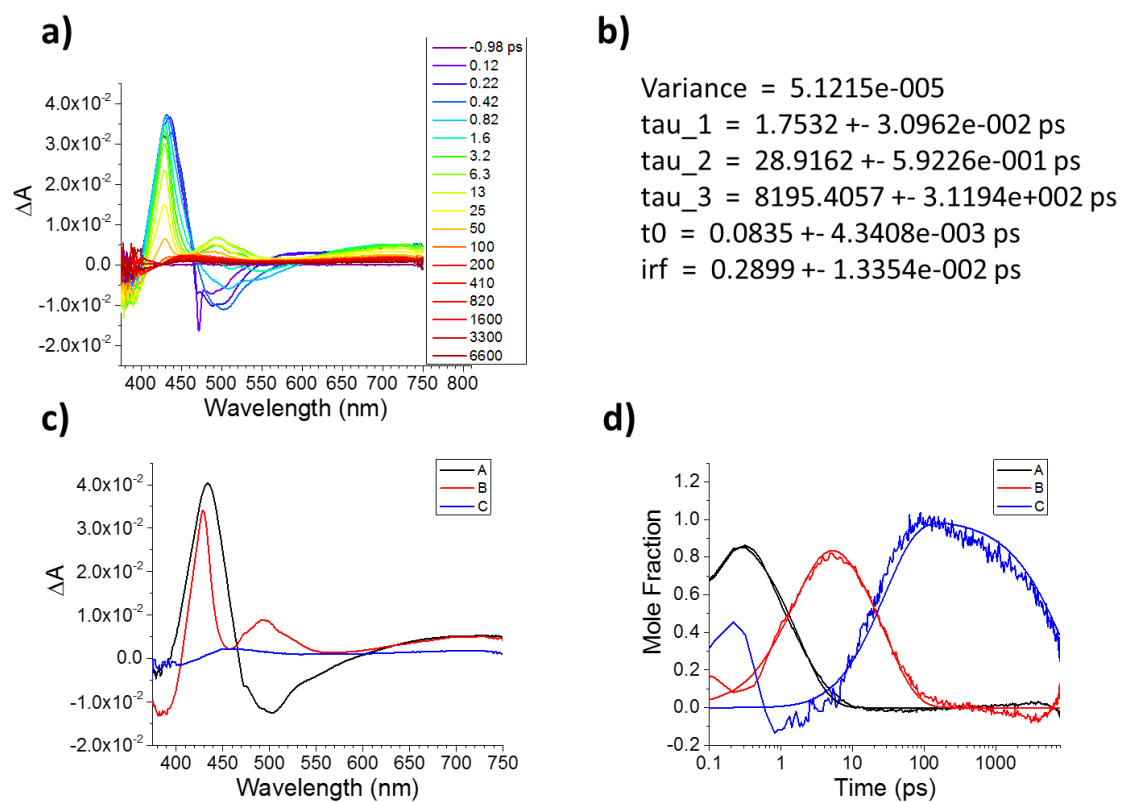


**Figure C.11.** 4.1b in PrCN at 295 K, 414 nm exc., fsTA. a) fsTA spectra; b) fitting parameters; c) fitted species spectra; d) fitted kinetics.

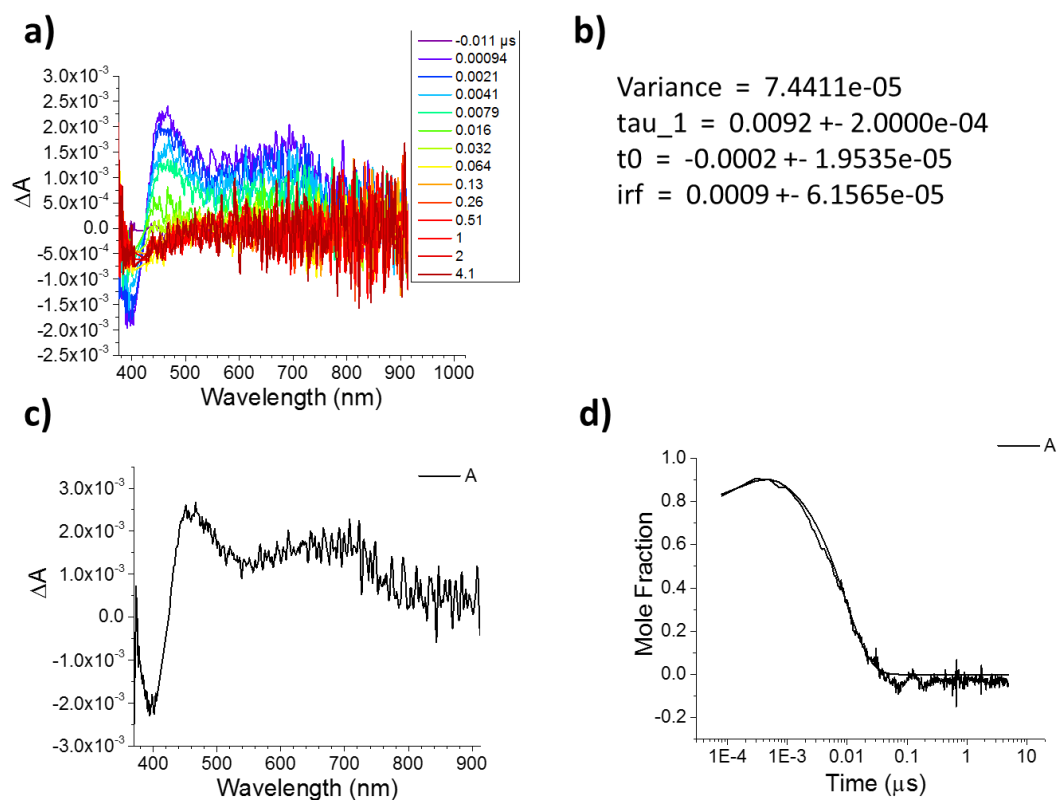


**Figure C.12.** 4.1b in PrCN at 295 K, 414 nm exc., nsTA. a) nsTA spectra; b) fitting parameters; c) fitted species spectra; d) fitted kinetics.

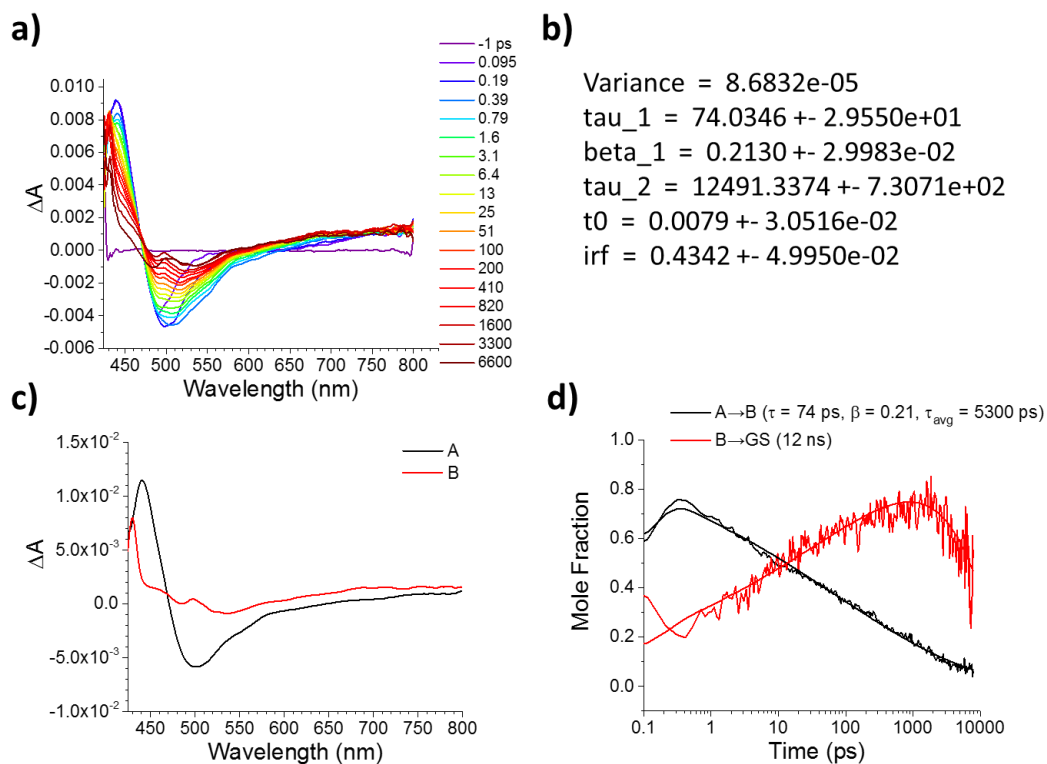


**Figure C.13.** 4.1a in PrCN at 105 K, 414 nm exc., fsTA. a) fsTA spectra; b) fitting parameters for model with stretched exponential decay between A and B; c) fitted species spectra; d) fitted kinetics.

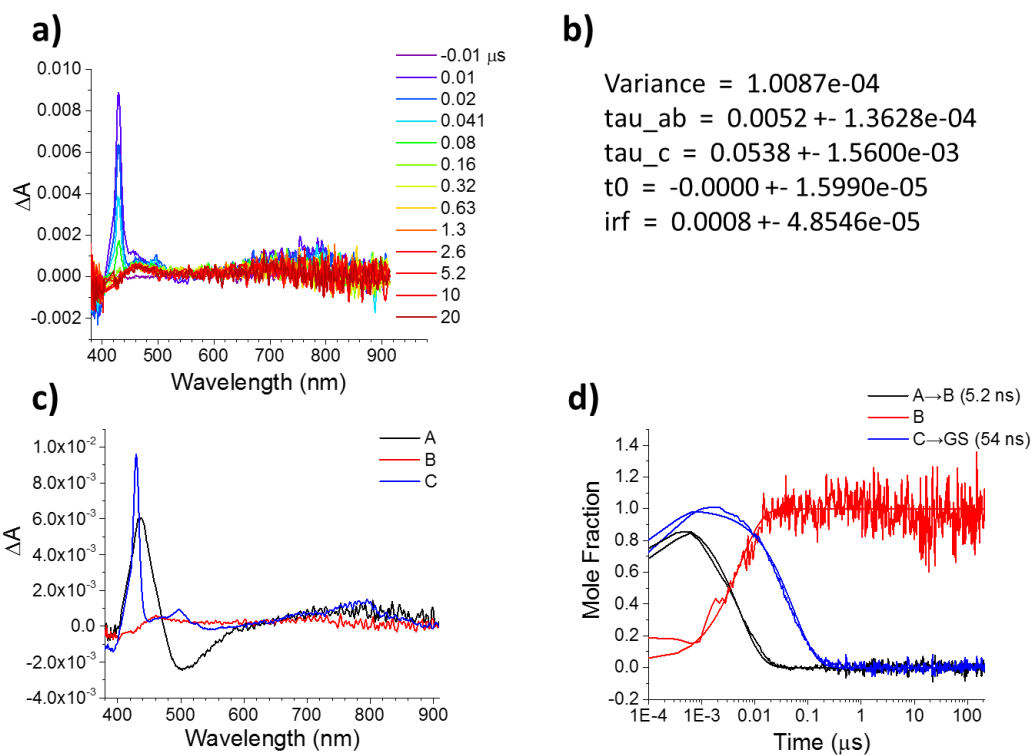


**Figure C.14.** 4.1a in PrCN at 105 K, 414 nm exc., nsTA. a) nsTA spectra; b) fitting parameters; c) fitted species spectra; d) fitted kinetics.

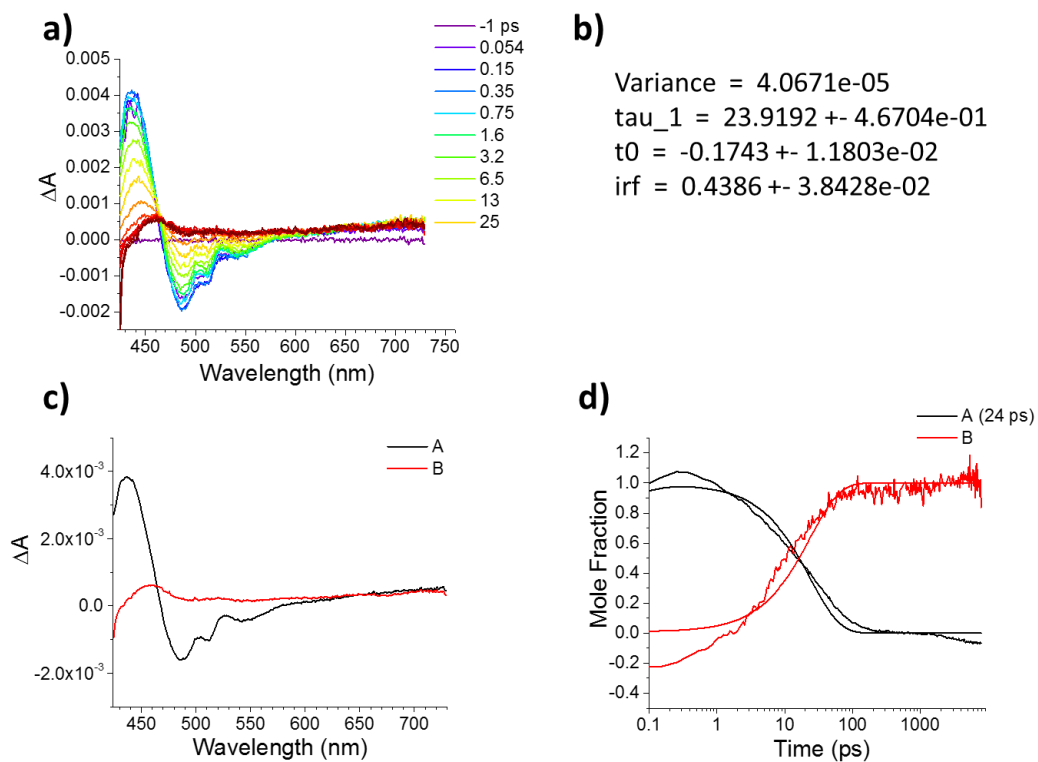


**Figure C.15.** 4.1b in PrCN at 105 K, 414 nm exc., fsTA. a) fsTA spectra; b) fitting parameters; c) fitted species spectra; d) fitted kinetics.

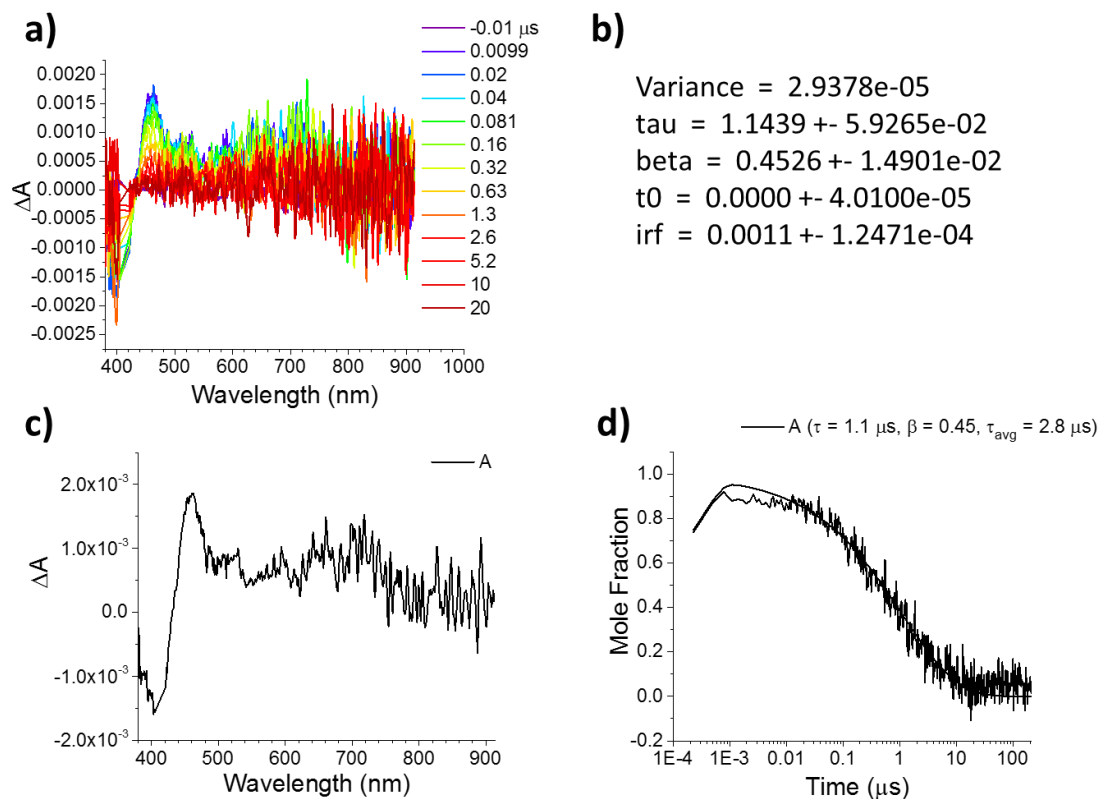


**Figure C.16.** 4.1b in PrCN at 105 K, 414 nm exc., nsTA. a) nsTA spectra; b) fitting parameters; c) fitted species spectra; d) fitted kinetics.

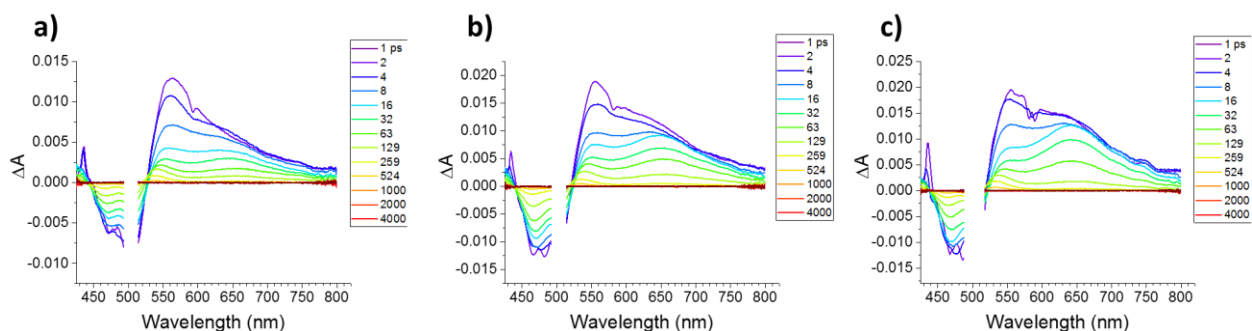


**Figure C.17.** 4.1b in a) benzene, b) THF, and c) PrCN at 295 K, 502 nm exc., fsTA. Scattered excitation light near 500 nm has been removed from the spectra.

### C.5 Magnetic Field Effects on Transient Absorption Spectra

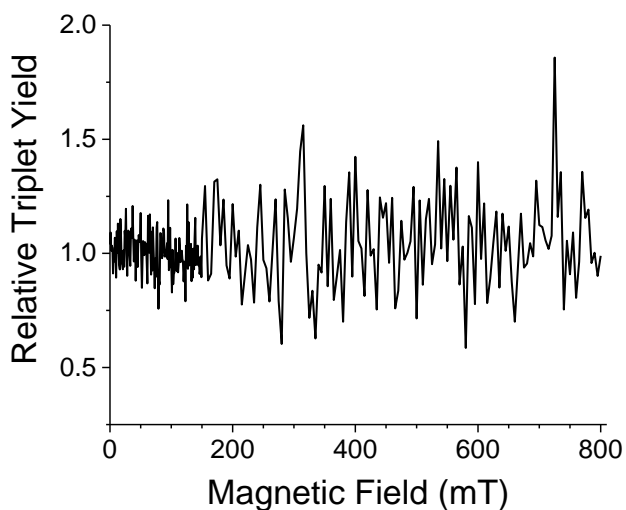


**Figure C.18.** Magnetic field effect on  $^3\text{ANI}$  yield in **4.1a** following 416 nm excitation, measured at room temperature in an air-free toluene solution. Triplet yield is reported relative to the average value over several measurements at zero field.

### C.6 EPR Spectroscopy

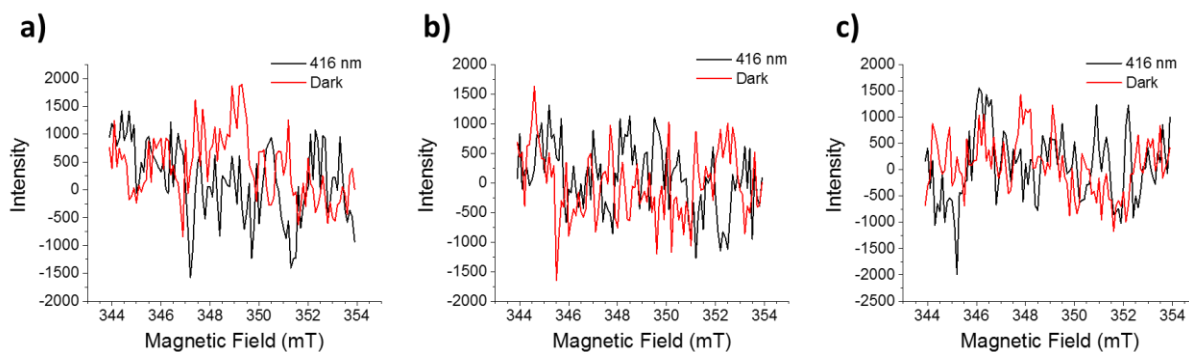


**Figure C.19.** Echo-detected EPR spectra of **4.1a** in a) benzene, b) THF, and c) PrCN at 295 K with 416 nm excitation.

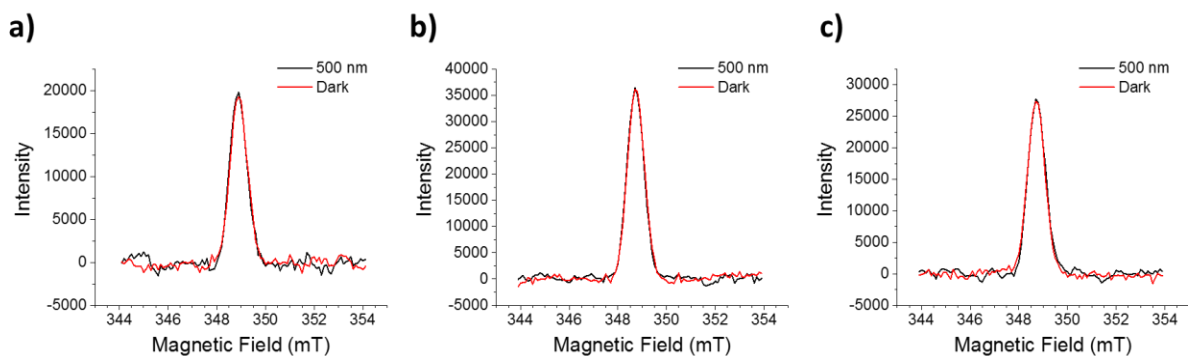


**Figure C.20.** Echo-detected EPR spectra of **4.1b** in a) benzene, b) THF, and c) PrCN at 295 K with 500 nm excitation selective for BDPA.

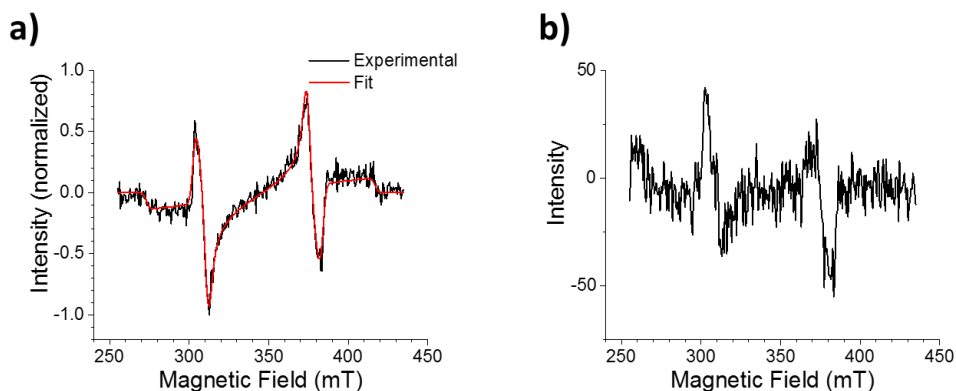


**Figure C.20.** Echo-detected EPR spectra of **4.1b** in a) benzene, b) THF, and c) PrCN at 295 K with 500 nm excitation selective for BDPA.

Parameter	Fitted value
D (MHz)	2000
E (MHz)	90
Gaussian broadening, FWHM (mT)	1.6
Triplet sublevel populations: $T_x$ , $T_y$ , $T_z$	0.61, 0.22, 0.29
% Spin orbit ISC	100%
% Radical pair (S- $T_0$ mixing) ISC	0%

**Table C.6.** Fitting parameters for BDPAH-mPD-<sup>3\*</sup>ANI spectrum from **4.1a** in toluene (Figure C.21a).

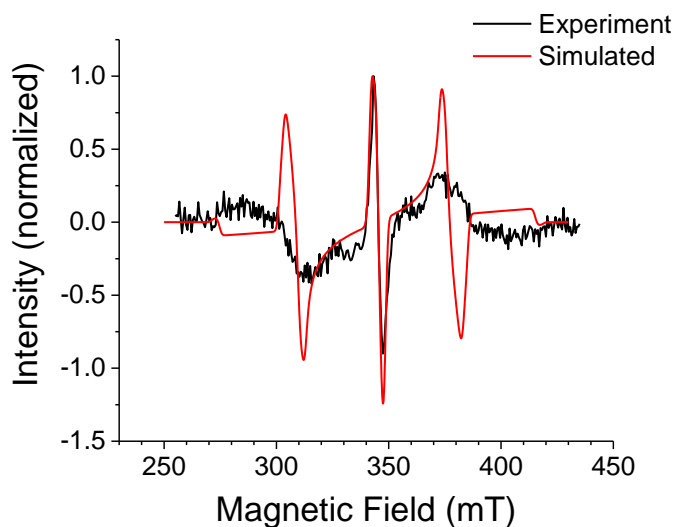


**Figure C.22.** Simulation of the EPR spectrum from a system with weak coupling between  $S = \frac{1}{2}$  and  $S = 1$  species, compared to the spectrum of **4.1b** at 105 K in PrCN at 472 ns after excitation.

Parameter	Value
$^{3*}$ ANI D (MHz)	2000
$^{3*}$ ANI E (MHz)	90
$J_{\text{radical-triplet}}$ (MHz)	0
$D_{\text{radical-triplet}}$ (MHz)	50
Gaussian broadening, FWHM (mT)	1.6

**Table C.7.** Simulation parameters for Figure C.22. Hyperfine coupling was not treated explicitly and is assumed to contribute to the broadening.

## APPENDIX D

### Supplementary Information for Chapter 5

## D.1 Reorganization Energy Calculations

The value of the total reorganization energy ( $\lambda$ ) is the sum of the internal ( $\lambda_I$ ) and solvent ( $\lambda_S$ ) reorganization energies. The values of  $\lambda_I$  for  $\text{mPD} \rightarrow \text{mPD}^{+\bullet}$  and  $\text{NDI} \rightarrow \text{NDI}^{\bullet}$  were calculated from the difference in energy of each radical ion in the neutral molecule geometry and the corresponding energy of each radical ion in its relaxed geometry using the data in Table D.1. Values for mPD and  $\text{mPD}^{+\bullet}$  ( $\lambda_I = 0.19$  eV) are reproduced here from earlier work.<sup>45</sup> The values of  $\lambda_S$  was calculated using the Marcus expression,<sup>72</sup> which is based on the dielectric continuum model of the solvent:

$$\lambda_S = e^2 \left( \frac{1}{2r_D} + \frac{1}{2r_A} - \frac{1}{r_{DA}} \right) \left( \frac{1}{\epsilon_0} - \frac{1}{\epsilon_S} \right) \quad (\text{D.1})$$

where  $e$  is the electronic charge,  $r_D$  and  $r_A$  are the radii of the donor and acceptor, respectively,  $\epsilon_S$  is the static dielectric constant, and  $\epsilon_0$  is the optical (high frequency) dielectric constant, which is approximated as the index of refraction squared. The radii of  $\text{mPD}^{+\bullet}$  and  $\text{NDI}^{\bullet}$  are both approximately 4 Å, and  $r_{DA} = 15.8$  Å.

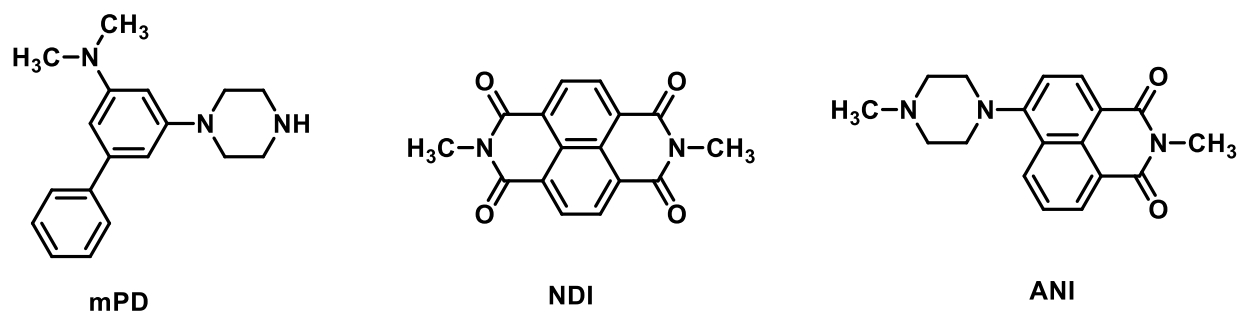


**Figure D.1.** Structures of molecular fragments for which energies were computed.

Compound	Energy (Hartree)
NDI neutral, optimized geometry	-1026.2261289146
NDI neutral, anion geometry	-1026.2201823743 ( $\lambda_I = 0.16$ eV from anion)
NDI radical anion, neutral geometry	-1026.2946664635
NDI radical anion, optimized geometry	-1026.3007218803 ( $\lambda_I = 0.16$ eV from neutral)
NDI triplet, neutral geometry	-1026.1419574989
NDI triplet, anion geometry	-1026.1484631298
NDI triplet, optimized geometry	-1026.1526371790 ( $\lambda_I = 0.11$ eV from anion)
ANI neutral, optimized geometry	-1012.1021235262
ANI neutral, cation geometry	-1012.0964370274 ( $\lambda_I = 0.15$ eV from cation)
ANI radical cation, neutral geometry	-1011.8437735418
ANI radical cation, optimized geometry	-1011.8506061012 ( $\lambda_I = 0.19$ eV from neutral)
mPD neutral, optimized geometry	-864.0000865731
mPD neutral, cation geometry	-863.9950575752 ( $\lambda_I = 0.14$ eV from cation)

**Table D.1.** Energies of neutral and charged mPD and NDI obtained via DFT (B3LYP / 6-31G\* in vacuum). Vibrational frequencies were calculated for all optimized structures and no imaginary frequencies were found.

Atom	X (Å)	Y (Å)	Z (Å)
N	3.53688	-0.00971	-0.00734
C	2.89553	1.23727	0.01201
C	2.89098	-1.25803	-0.02416
C	1.40923	1.2304	0.01533
O	3.55021	2.26888	0.02552
C	1.40333	-1.235	-0.02054
O	3.52311	-2.30332	-0.04078
C	0.69708	-2.42758	-0.03652
C	0.71029	-0.00048	-0.00103
C	-0.71051	0.00336	0.00216
C	0.71041	2.42688	0.03445
C	-0.6973	2.43046	0.03753
C	-0.71063	-2.424	-0.03322
C	-1.40355	1.23789	0.02153
H	1.25074	-3.3603	-0.05176
H	-1.26952	-3.35376	-0.04571
C	-1.40944	-1.22752	-0.01407
C	-2.89575	-1.23439	-0.01052
C	-2.89121	1.26091	0.0248
H	-1.25096	3.36318	0.05256
H	1.2693	3.35664	0.04713
O	-3.55043	-2.26601	-0.02361

N	-3.5371	0.01259	0.00871
C	-5.00569	-0.01513	0.01136
O	-3.52341	2.30617	0.04062
H	-5.36262	-0.5533	0.89254
H	-5.35572	1.0142	0.02267
C	5.00547	0.01803	-0.00997
H	5.35551	-1.0113	-0.02063
H	5.36551	0.53886	0.88025
H	5.36248	0.55554	-0.89155
H	-5.36579	-0.53528	-0.87924

**Table D.2.** Optimized coordinates for neutral NDI.

Atom	X (Å)	Y (Å)	Z (Å)
N	3.51043	-0.00878	-0.00771
C	2.87253	1.24656	0.01127
C	2.86773	-1.2671	-0.02443
C	1.41434	1.23447	0.01371
O	3.5621	2.27438	0.02578
C	1.40914	-1.23894	-0.02116
O	3.53428	-2.31019	-0.03992
C	0.68486	-2.45073	-0.03677
C	0.71733	-0.00037	-0.00242
C	-0.71758	0.00321	0.00038
C	0.69764	2.45005	0.03251
C	-0.68512	2.45357	0.03514
C	-0.69789	-2.4472	-0.03395
C	-1.40939	1.24179	0.01912
H	1.24746	-3.37857	-0.05134
H	-1.26574	-3.37205	-0.04599
C	-1.4146	-1.23161	-0.01551
C	-2.8728	-1.24367	-0.01276
C	-2.86797	1.26998	0.02232
H	-1.24772	3.38142	0.04968
H	1.26549	3.37489	0.045
O	-3.56239	-2.27151	-0.02456
N	-3.51067	0.01165	0.00569
C	-4.97057	-0.01504	0.00848
O	-3.53437	2.31317	0.0389
H	-5.33574	-0.55443	0.88779
H	-5.31424	1.01748	0.01824

C	4.97026	0.01773	-0.00944
H	5.31388	-1.01473	-0.02509
H	5.33838	0.5365	0.88096
H	5.3357	0.56248	-0.88526
H	-5.33874	-0.53933	-0.87857

**Table D.3.** Optimized coordinates for NDI radical anion.

Atom	X (Å)	Y (Å)	Z (Å)
N	3.52329	-0.00983	-0.00701
C	2.87988	1.23455	0.01185
C	2.87445	-1.2548	-0.02353
C	1.41248	1.22401	0.01501
O	3.53214	2.27733	0.02536
C	1.40596	-1.22865	-0.01986
O	3.50349	-2.3118	-0.04017
C	0.67494	-2.46876	-0.03607
C	0.71562	-0.00061	-0.0009
C	-0.71585	0.00333	0.0022
C	0.68961	2.46784	0.03444
C	-0.67517	2.47149	0.0374
C	-0.68984	-2.46512	-0.03296
C	-1.40619	1.23138	0.02109
H	1.24599	-3.38999	-0.0509
H	-1.26611	-3.38329	-0.04509
C	-1.4127	-1.22129	-0.0136
C	-2.88011	-1.23181	-0.01042
C	-2.87468	1.25753	0.02442
H	-1.24621	3.39272	0.05215
H	1.26588	3.386	0.0467
O	-3.53238	-2.27459	-0.02346
N	-3.52351	0.01256	0.00843
C	-4.99144	-0.01421	0.01095
O	-3.50377	2.31452	0.04051
H	-5.34887	-0.55187	0.89232
H	-5.34053	1.0156	0.02168
C	4.99122	0.01692	-0.00958
H	5.34033	-1.01287	-0.01989
H	5.35158	0.53803	0.88042
H	5.34867	0.55411	-0.89125
H	-5.3518	-0.53485	-0.87933

**Table D.4.** Optimized coordinates for triplet NDI.

Atom	X (Å)	Y (Å)	Z (Å)
C	-0.83634	-1.41306	-0.67244
C	-1.09664	-0.0434	-0.59156
C	0.02177	0.854	-0.40303
C	1.3211	0.30268	-0.17237
C	1.5253	-1.10012	-0.21029
C	0.45298	-1.93002	-0.48933
C	2.8574	-1.68799	0.02931
H	0.62443	-3.00101	-0.52495
H	-1.65397	-2.10776	-0.824
N	-2.38512	0.4809	-0.74417
C	2.42218	1.16906	0.05393
C	2.25838	2.54266	0.01
C	0.99897	3.08986	-0.29297
C	-0.09082	2.26473	-0.50038
H	3.123	3.1741	0.18569
H	0.88602	4.16656	-0.38029
H	-1.0444	2.69825	-0.77928
N	3.90078	-0.78135	0.30026
O	3.0633	-2.89554	0.00196
C	3.77213	0.61194	0.31889
O	4.7487	1.31637	0.54466
C	5.24089	-1.3138	0.56224
H	5.16975	-2.39905	0.56065
H	5.59933	-0.94887	1.52747
H	5.93642	-0.97577	-0.21071
C	-3.42001	-0.28326	-1.44401
C	-2.97522	1.3212	0.3114
C	-4.3371	-1.07579	-0.50382
H	-2.94864	-0.93818	-2.18018
H	-4.04061	0.43923	-1.99165
H	-3.77563	-1.90335	-0.02532
H	-5.14818	-1.52754	-1.08829
N	-4.92261	-0.18	0.49155
C	-3.87547	0.5043	1.24575
H	-3.57515	2.10936	-0.16267
H	-2.18135	1.79203	0.89148
C	-5.85338	-0.87705	1.36707
H	-4.34868	1.18228	1.96682
H	-3.25002	-0.20727	1.82345
H	-6.65044	-1.33333	0.76983

H	-6.31244	-0.1628	2.0592
H	-5.37353	-1.67585	1.96587

**Table D.5.** Optimized coordinates for neutral ANI.

Atom	X (Å)	Y (Å)	Z (Å)
C	-0.71041	-1.50134	-0.84361
C	-1.04871	-0.13728	-0.61245
C	0.02751	0.81287	-0.3634
C	1.34355	0.29402	-0.15674
C	1.60595	-1.09201	-0.2864
C	0.58122	-1.96567	-0.66046
C	2.9724	-1.6527	-0.06329
H	0.81422	-3.01936	-0.76978
H	-1.49034	-2.22001	-1.06137
N	-2.36046	0.23809	-0.60703
C	2.42341	1.17086	0.10064
C	2.22689	2.54471	0.10152
C	0.95856	3.06142	-0.19409
C	-0.12013	2.21422	-0.42738
H	3.07299	3.19406	0.29941
H	0.81464	4.13562	-0.2528
H	-1.07262	2.65326	-0.69942
N	3.97967	-0.74429	0.25433
O	3.17136	-2.85364	-0.15781
C	3.79638	0.63951	0.34975
O	4.72625	1.3767	0.62507
C	5.34441	-1.24703	0.49212
H	5.33167	-2.32525	0.35309
H	5.65484	-0.99423	1.50803
H	6.03239	-0.77588	-0.21245
C	-3.40977	-0.49594	-1.33404
C	-2.91815	1.22241	0.33816
C	-4.40861	-1.15823	-0.36859
H	-2.95858	-1.21486	-2.01537
H	-3.94285	0.24969	-1.93437
H	-3.89663	-1.9763	0.17527
H	-5.21792	-1.60434	-0.95515
N	-4.95494	-0.15109	0.5174
C	-3.91805	0.51075	1.27915
H	-3.43536	2.00834	-0.22191

H	-2.11765	1.65814	0.93142
C	-6.10428	-0.59081	1.30419
H	-4.37107	1.26986	1.92493
H	-3.34861	-0.18485	1.92546
H	-6.87759	-0.97425	0.63229
H	-6.51746	0.26264	1.84946
H	-5.85105	-1.38047	2.03198

**Table D.6.** Optimized coordinates for ANI radical cation.

## D.2 Electron Transfer Reaction Free Energy Calculations

The one-electron redox potentials for mPD, ANI, and NDI have been reported previously.<sup>45, 78</sup> The ion pair energies in a given solvent were calculated using the method outlined in Greenfield et al.<sup>78</sup> using eq D.2,

$$\Delta G_F = \Delta G_I + \text{sign}(E_I - E_F) + \frac{e^2}{\epsilon_S} \left( \frac{q^2}{r_I} - \frac{1}{r_F} \right) \quad \text{if } |E_F| > |E_I|, \text{ then sign} = (-)$$

$$\text{if } |E_I| > |E_F|, \text{ then sign} = (+) \quad (D.2)$$

where  $\Delta G_I$  and  $\Delta G_F$  are the energies above ground state for the initial and final ion pairs, respectively,  $E_I$  and  $E_F$  are the redox potentials for the initial and final ions, respectively, between which the electron is transferred,  $r_I$  and  $r_F$  are the initial and final ion pair distances, respectively,  $e$  is the electronic charge,  $q = 0.7$  is the fraction of charge transferred in the excited singlet state of ANI (which is considered the initial ion pair because of its high charge transfer character),<sup>78</sup> and  $\epsilon_S$  is the static dielectric constant of the solvent. For mixed solvents,  $\epsilon_S$  was estimated as the average of the  $\epsilon_S$  values of the component solvents weighted by their mole fractions. The internal charge transfer distance within ANI is  $r = 3.3 \text{ \AA}$ ,<sup>78</sup> the ANI<sup>+</sup>-NDI<sup>•</sup>

distance is  $r = 6.8 \text{ \AA}$ , and the mPD<sup>+</sup>-NDI<sup>-</sup> distance is  $r = 15.8 \text{ \AA}$ . The free energies for the initial charge separation ( $\Delta G_{CS1}$ ), charge shift ( $\Delta G_{CS2}$ ), charge recombination to the singlet ground state ( $\Delta G_{CRS}$ ), and charge recombination to <sup>3</sup>\*NDI ( $\Delta G_{CRT}$ ) were then determined using eqs D.3-D.6, where  $E_S = 2.80 \text{ eV}$  and  $E_T = 2.03 \text{ eV}$  are the lowest excited singlet state energy of ANI and lowest triplet state energy of NDI, respectively.

$$\Delta G_{CS1} = \Delta G_1 - E_S \quad (\text{D.3})$$

$$\Delta G_{CS2} = \Delta G_2 - \Delta G_1 \quad (\text{D.4})$$

$$\Delta G_{CRS} = -\Delta G_2 \quad (\text{D.5})$$

$$\Delta G_{CRT} = E_T - \Delta G_2 \quad (\text{D.6})$$

## D.3 Transient Absorption Spectroscopy

### D.3.1 Global Fitting of Transient Absorption Data

Factoring of the two-dimensional (signal vs time & frequency) data set by Singular Value Decomposition (SVD) is performed as implemented in the MATLAB software package.<sup>154</sup> This factoring produces an orthonormal set of basis spectra that describe the wavelength dependence of the species and a corresponding set of orthogonal vectors that describe the time-dependent amplitudes of the basis spectra.<sup>155</sup> These kinetic vectors are then fit using the global analysis method described below.

We globally fit the dataset to a specified kinetic model and use the resultant populations to deconvolute the dataset and reconstruct species-associated spectra. We use a first-order kinetic model with rate matrix  $K$ , detailed in Appendix D.3 for each fit.

The MATLAB program solves the differential equations numerically using the Runge-Kutta algorithm, then convolutes the solutions with a Gaussian instrument response function (IRF) with width  $w$  (FWHM), before employing a least-squares fitting to find the parameters which result in matches to the kinetic data. Reported error bounds reflect error estimates from individual fits, rather than the standard deviation of parameters across multiple runs. The assumption of a uniform instrument response across the frequency domain and a fixed time-zero ( $t_0$ ) are implicit in global analysis.

Once the fit parameters are established, they are fed directly into the differential equations, which were solved for the populations of the states in the kinetic model—e.g.,  $A(t)$ ,  $B(t)$ ,  $C(t)$ , and  $D(t)$ . Finally, the raw data matrix (with all the raw data) is deconvoluted with the populations as functions of time to produce the spectra associated with each species.

### D.3.2 Femtosecond Transient Absorption Spectroscopy

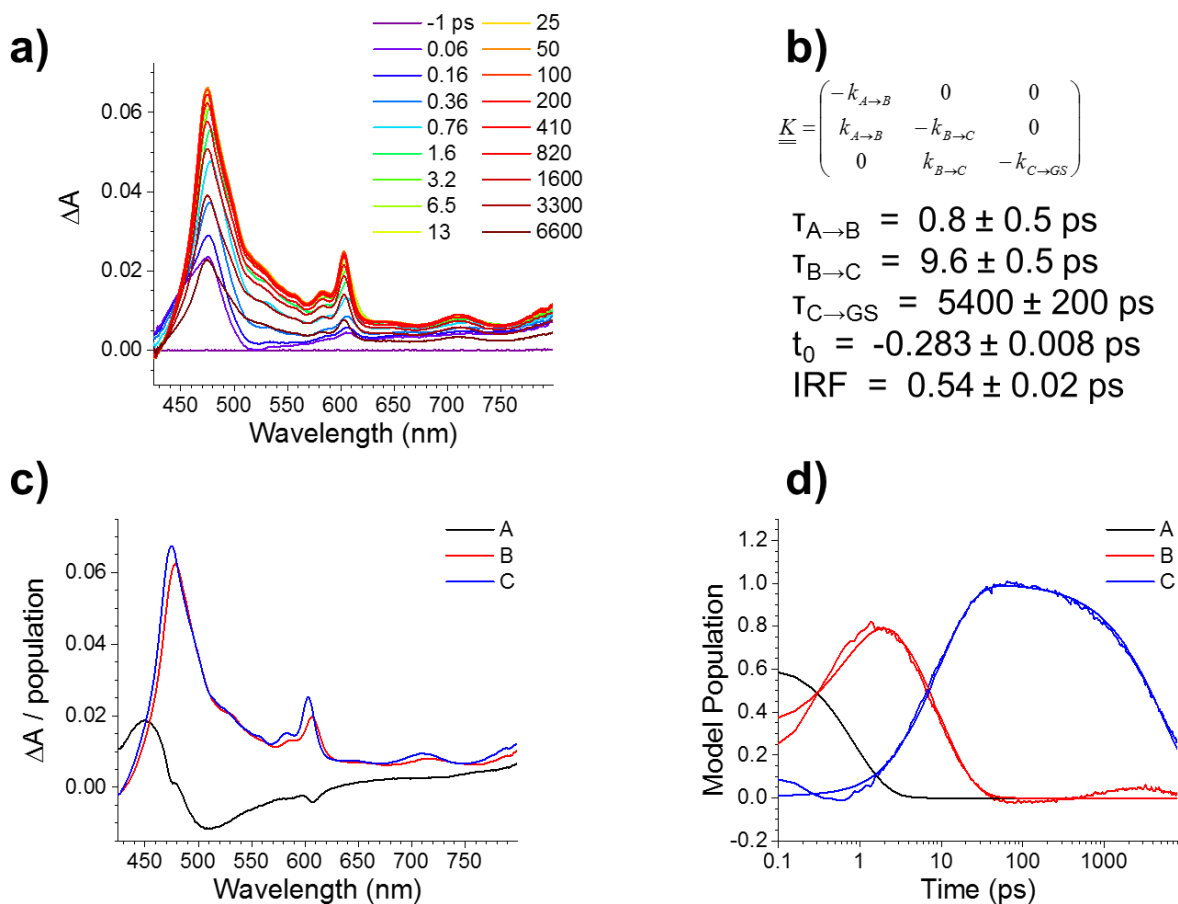


**Figure D.2.** Femtosecond transient absorption spectra (a) of **5.2** in airfree toluene following excitation at 414 nm. Spectra were fitted to a species-associated kinetic model (b). Species spectra (c) and populations over time (d) are shown.

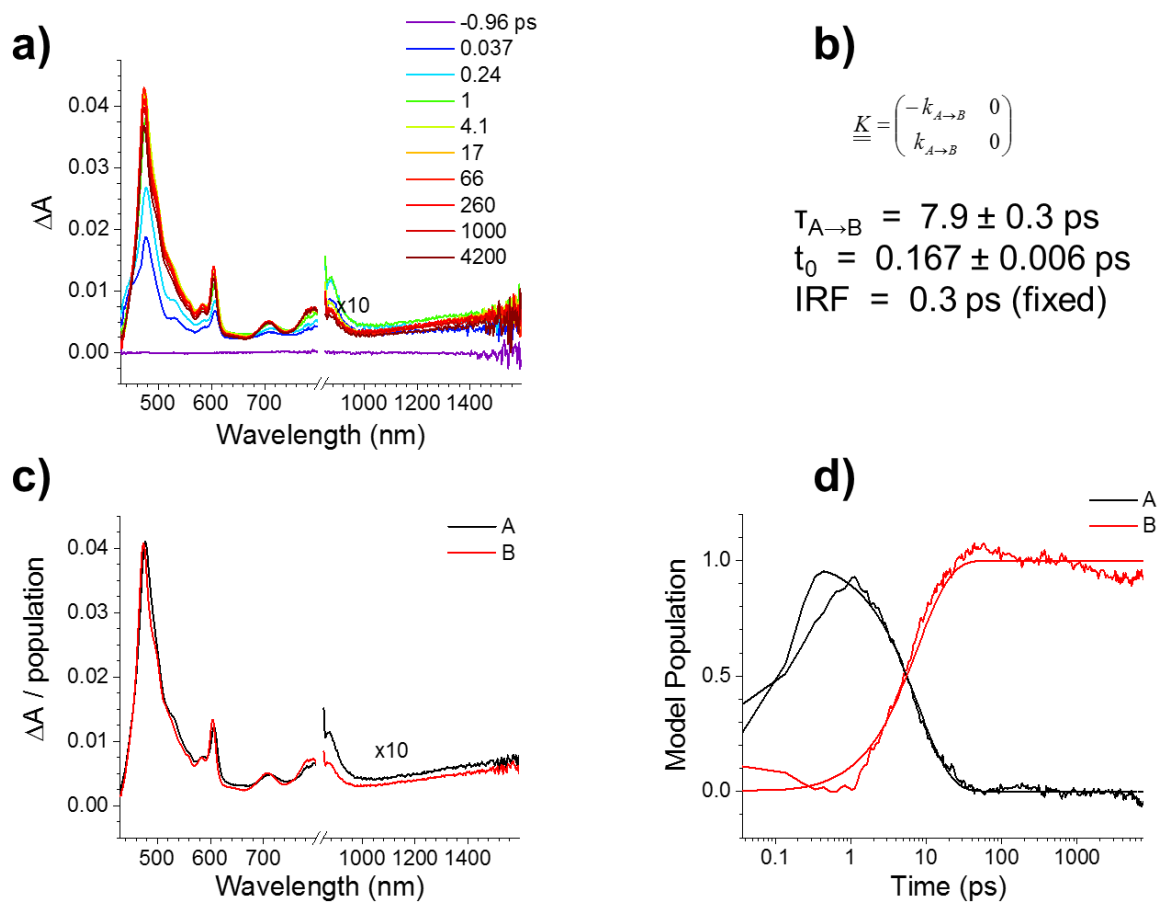


**Figure D.3.** Femtosecond transient absorption spectra (a) of **5.1a** in airfree benzene following excitation at 414 nm. Spectra were fitted to a species-associated kinetic model (b). Species spectra (c) and populations over time (d) are shown.

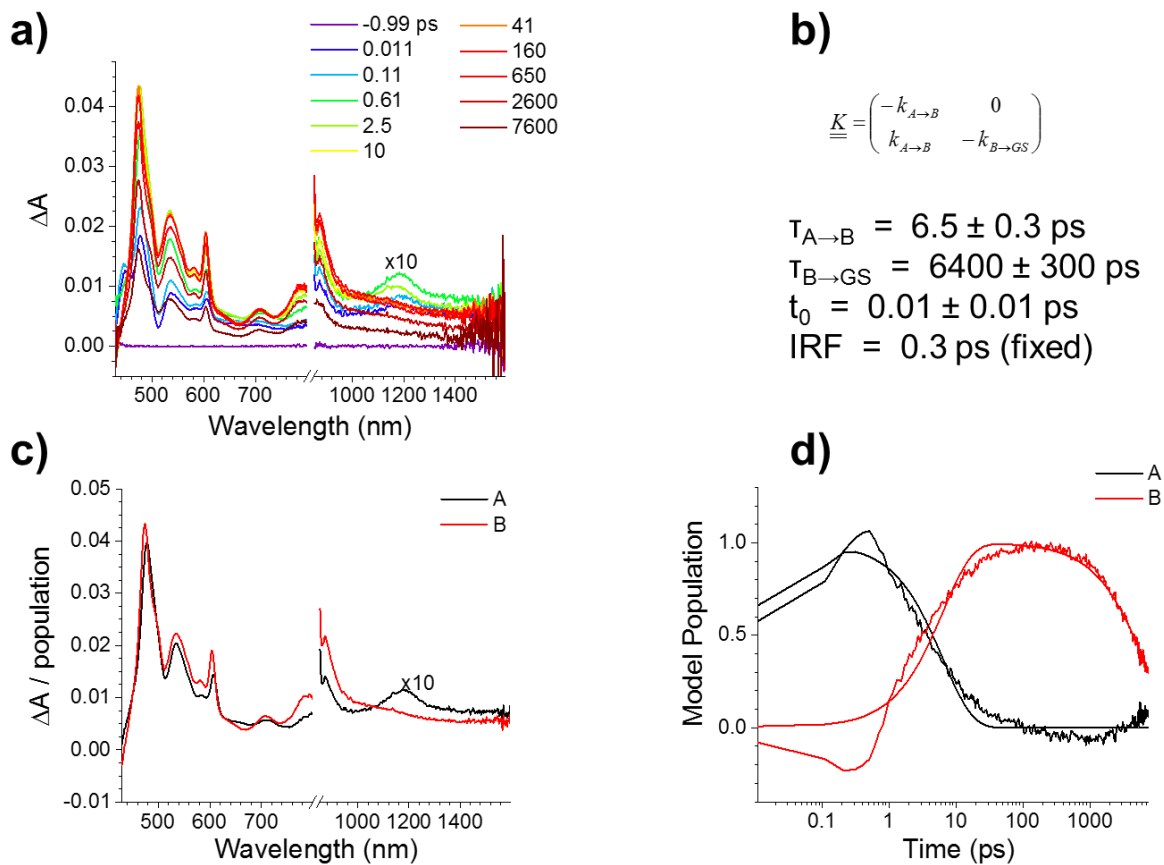


**Figure D.4.** Femtosecond transient absorption spectra (a) of **5.1b** in airfree benzene following excitation at 414 nm. Spectra were fitted to a species-associated kinetic model (b). Species spectra (c) and populations over time (d) are shown.

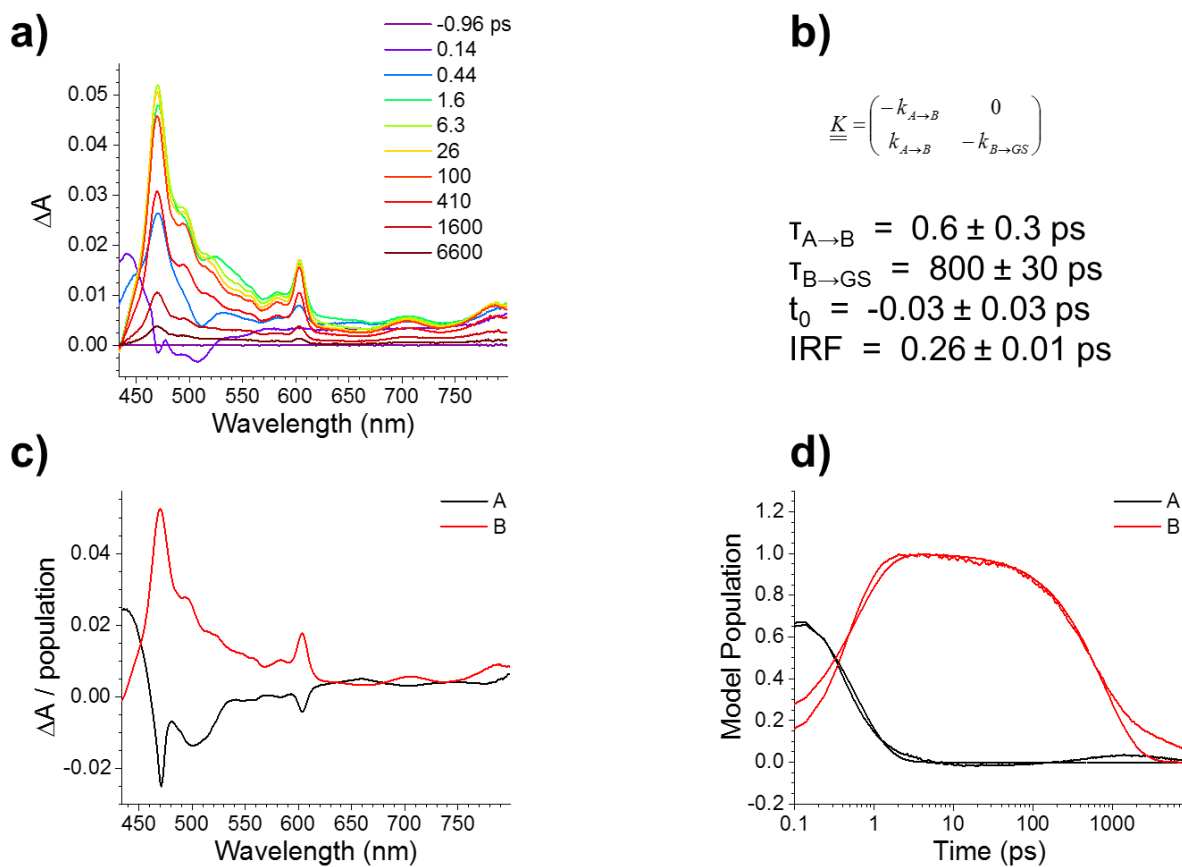


**Figure D.5.** Femtosecond transient absorption spectra (a) of **5.1b** in airfree tetrahydrofuran following excitation at 414 nm. Spectra were fitted to a species-associated kinetic model (b). Species spectra (c) and populations over time (d) are shown. Sharp features in the fitted spectrum of species A are artifacts due to the similarity of the charge separation rate and the instrument response function.

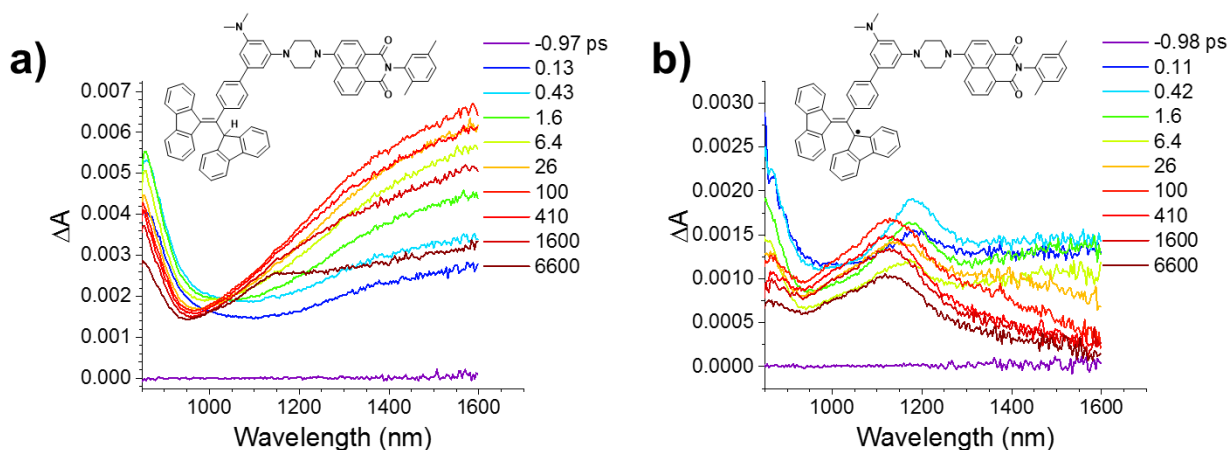


**Figure D.6.** Femtosecond transient absorption spectra in the NIR region (a) of **4.1a** in airfree toluene and (b) **4.1b** in airfree THF, following excitation at 414 nm. These compounds have previously been shown to form  $\text{mPD}^{+\bullet}$  upon photoexcitation. The  $\text{mPD}^{+\bullet}$  feature near 1600 nm is clearly visible in (a), and possibly present in (b).

### D.3.3 Femtosecond Shortwave Infrared Transient Absorption Spectroscopy

The details of the transient shortwave infrared (SWIR) spectroscopy apparatus have been described previously.<sup>301</sup> The probe is generated with the signal or idler beam from mid-IR TOPAS-C (Light Conversion), centered at a given wavelength and overlapped with the pump beam (414 nm, 1  $\mu\text{J}/\text{pulse}$ ) at the sample, contained in a liquid IR cell (Harrick Scientific) enclosed between two  $\text{CaF}_2$  windows with a 500  $\mu\text{m}$  Teflon spacer. The transmitted probe after the sample is then dispersed on a grating with 150 l/mm density. A reference beam corrects for probe fluctuations. The resulting difference spectrum has a small  $\leq 100$  nm window of transmitted probe due to the bandwidth of the SWIR signal or idler. Each time the probe wavelength is moved, the pump beam is adjusted to maximize overlap with the probe. To constitute a full spectrum from the series of  $\leq 100$  nm slices, spectra are combined in Surface Explorer (Ultrafast Systems). Further manual stitching is sometimes required due to data noise from stitch artifacts and atmospheric absorption. Asterisks denote artifacts. All samples were

measured in air free solvents (benzene or tetrahydrofuran) at 295 K following excitation at 414 nm.

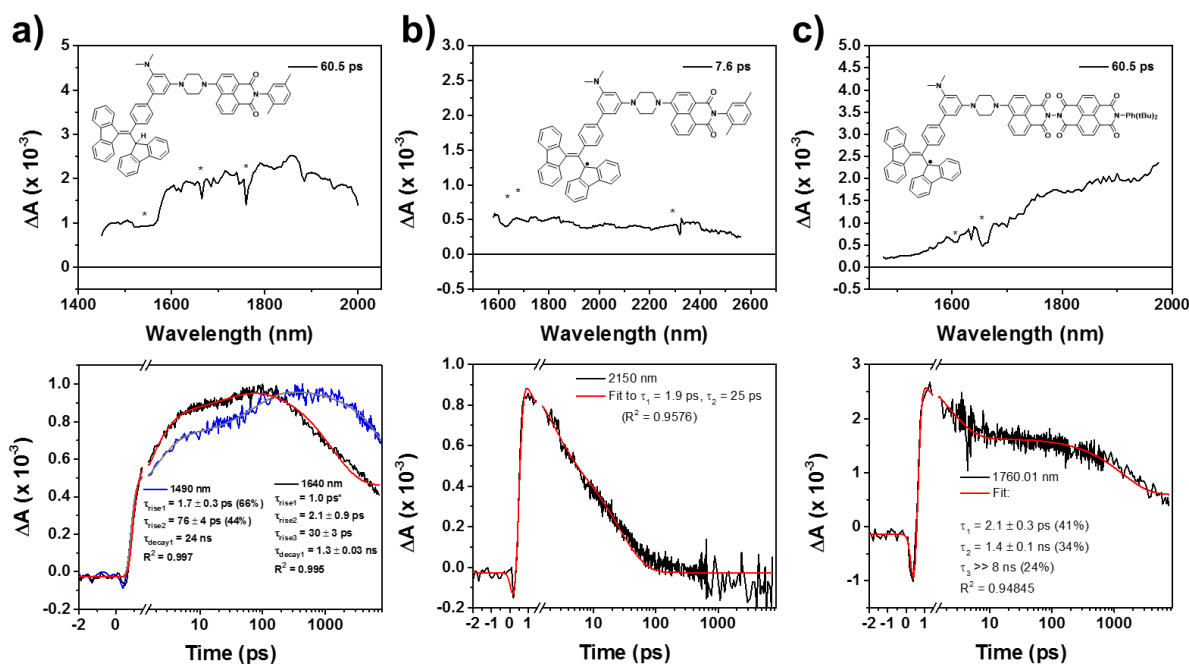


**Figure D.7.** Shortwave infrared transient absorption spectra (top) and kinetics (bottom) of (a) **4.1a** in benzene, (b) **4.1b** in tetrahydrofuran, and (c) **5.1b** in benzene.

All of the samples studied show some transient absorption features in the shortwave infrared (SWIR) region. A band is clearly visible in data from **4.1a**, where the edge of the band was also detected in the NIR region, and in **5.1b**, where the band appears to have redshifted. The feature is less well resolved in **4.1b**, possibly due to degradation of the sample during the several hours required for measurement. The deviation of the kinetics of this data from the visible TA is also likely due to some sample degradation during the measurement.

### D.3.4 Nanosecond Transient Absorption Spectroscopy

Some nanosecond transient absorption data was fit at single wavelengths by a model consisting of a biexponential decay and a Gaussian IRF. The following equation was used for these fits:

$$\begin{aligned} \Delta A(t) = & A_1/2 * \exp\left(\left(\frac{\text{FWHM}}{2 * \sqrt{\ln(2)}}\right)^2 - (4 * (t-t_0) * \tau_1) / (4 * \tau_1^2)\right) * (1 + \text{erf}\left(\frac{(t-t_0) / (\text{FWHM} / (2 * \sqrt{\ln(2)})) - ((\text{FWHM} / (2 * \sqrt{\ln(2)})) / (2 * \tau_1))}{\sqrt{2}}\right)) \\ & + A_2/2 * \exp\left(\left(\frac{\text{FWHM}}{2 * \sqrt{\ln(2)}}\right)^2 - (4 * (t-t_0) * \tau_2) / (4 * \tau_2^2)\right) * (1 + \text{erf}\left(\frac{(t-t_0) / (\text{FWHM} / (2 * \sqrt{\ln(2)})) - ((\text{FWHM} / (2 * \sqrt{\ln(2)})) / (2 * \tau_2))}{\sqrt{2}}\right)) \end{aligned}$$

Where  $A_1$  and  $\tau_1$  are amplitude and time constant for the first decay component,  $A_2$  and  $\tau_2$  are amplitude and time constant for the second decay component, and FWHM is the full width at half maximum of the Gaussian IRF.

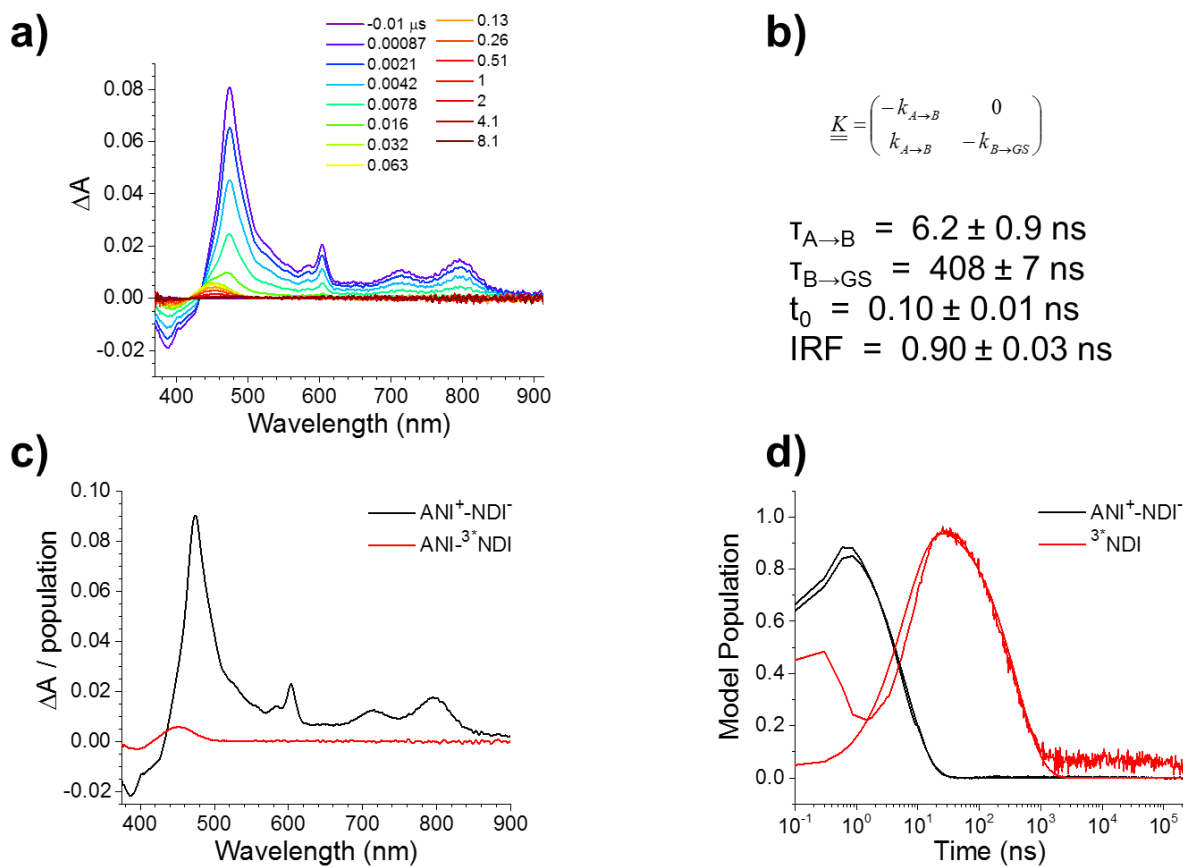


**Figure D.8.** Nanosecond transient absorption spectra (a) of **5.2** in airfree toluene following excitation at 414 nm. Spectra were fitted to a species-associated kinetic model (b). Species spectra (c) and populations over time (d) are shown.

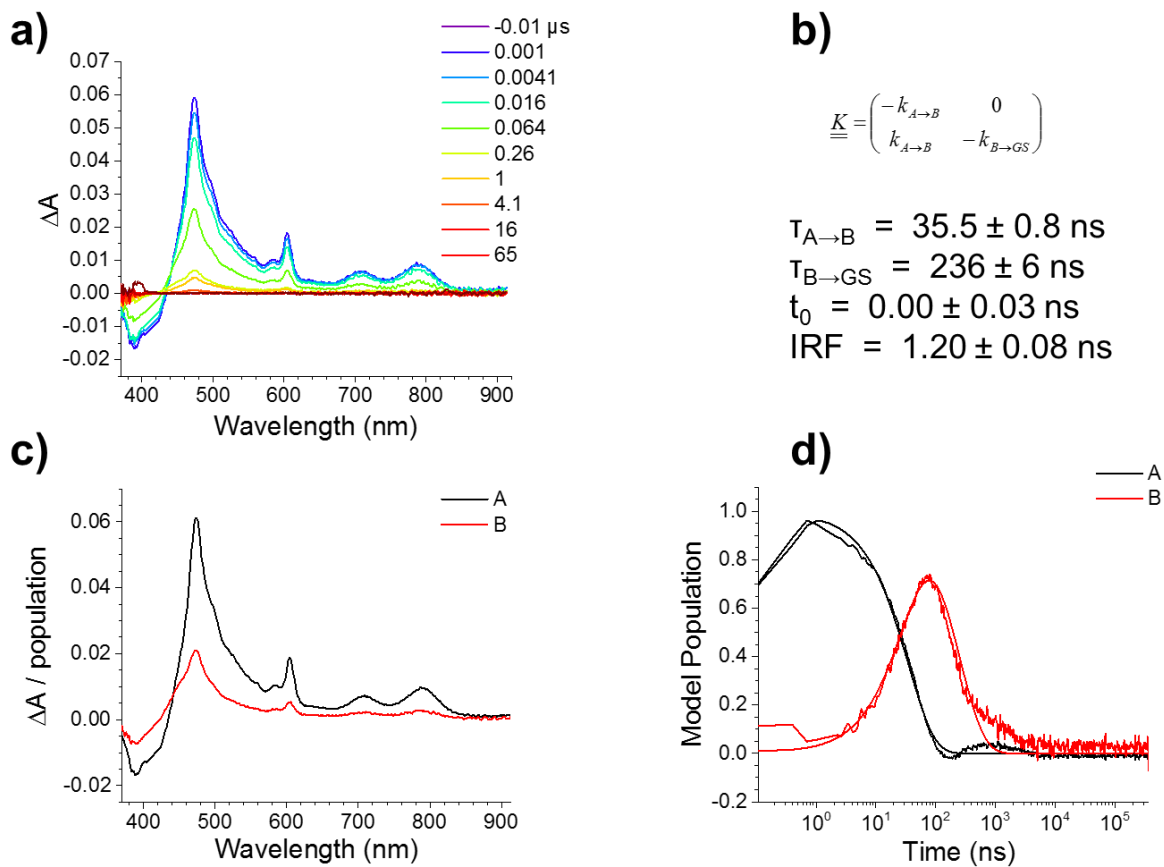


**Figure D.9.** Nanosecond transient absorption spectra (a) of **5.1a** in airfree benzene following excitation at 414 nm. Fitting to a species-associated kinetic model (b) including recombination to triplet was attempted. Species spectra (c) and populations over time (d) are shown.

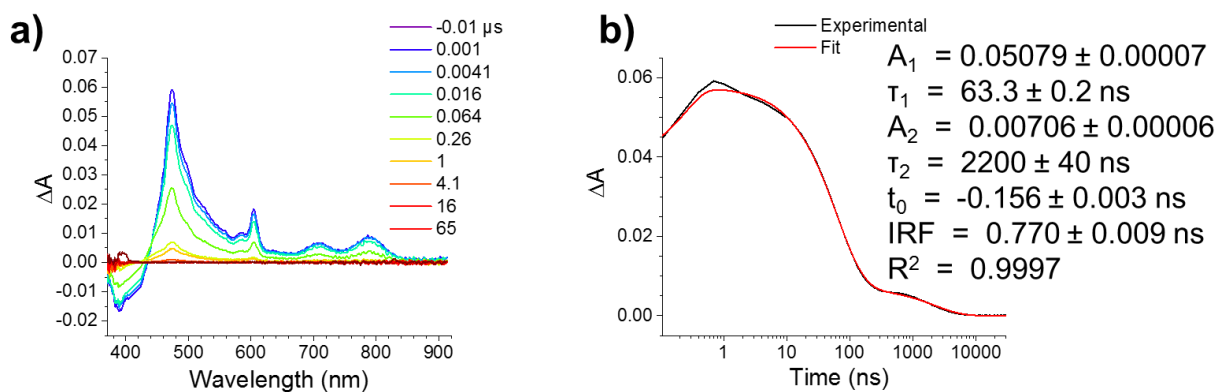


**Figure D.10.** Nanosecond transient absorption spectra (a) of **5.1a** in airfree benzene following excitation at 414 nm. A kinetic trace at 476 nm was fitted to a biexponential decay with a Gaussian IRF (b).

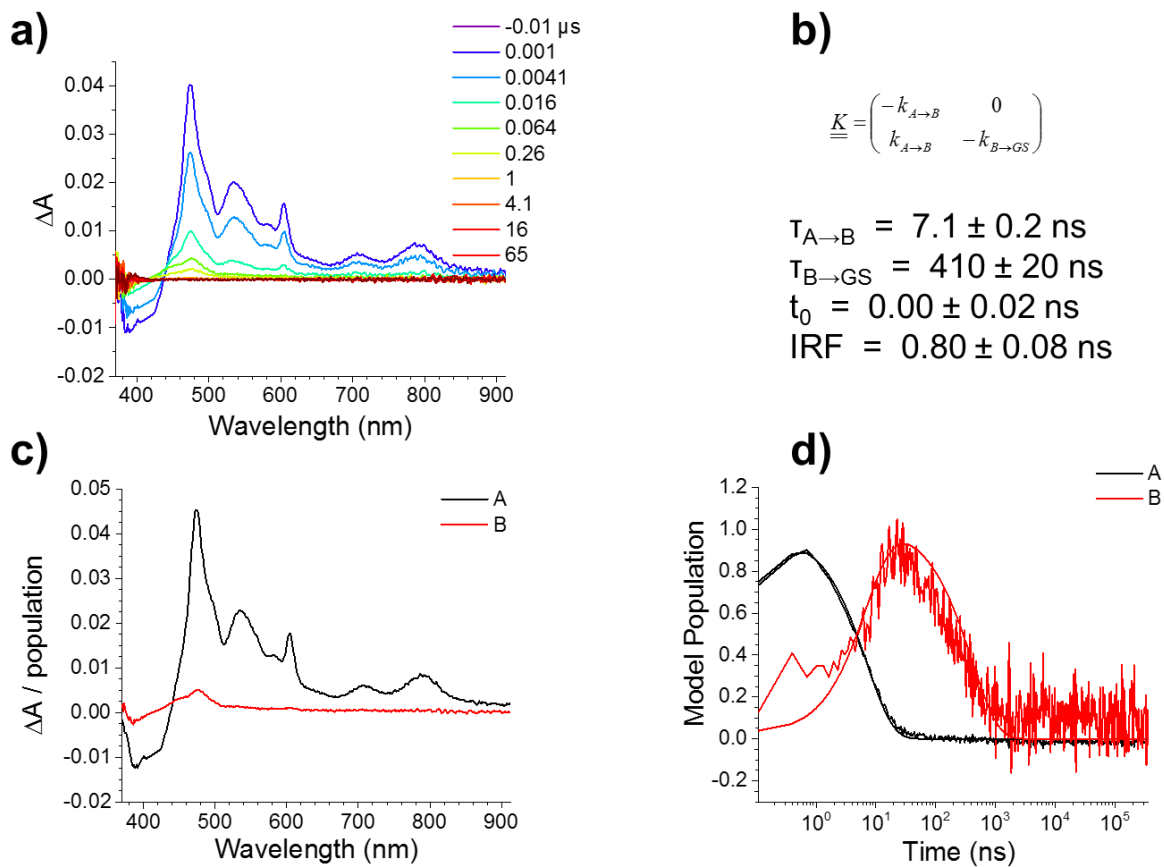


**Figure D.11.** Nanosecond transient absorption spectra (a) of **5.1b** in airfree benzene following excitation at 414 nm. Fitting to a species-associated kinetic model (b) including recombination to triplet was attempted. Species spectra (c) and populations over time (d) are shown.

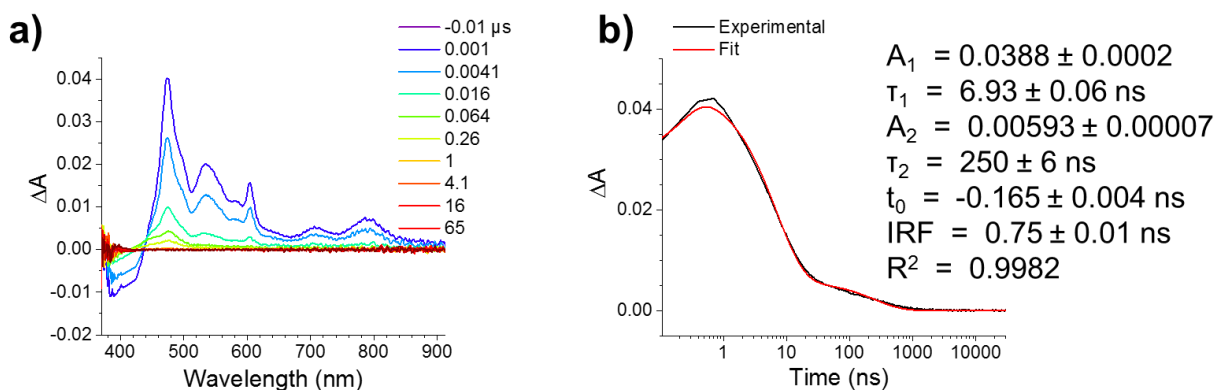


**Figure D.12.** Nanosecond transient absorption spectra (a) of **5.1b** in airfree benzene following excitation at 414 nm. A kinetic trace at 476 nm was fitted to a biexponential decay with a Gaussian IRF (b).

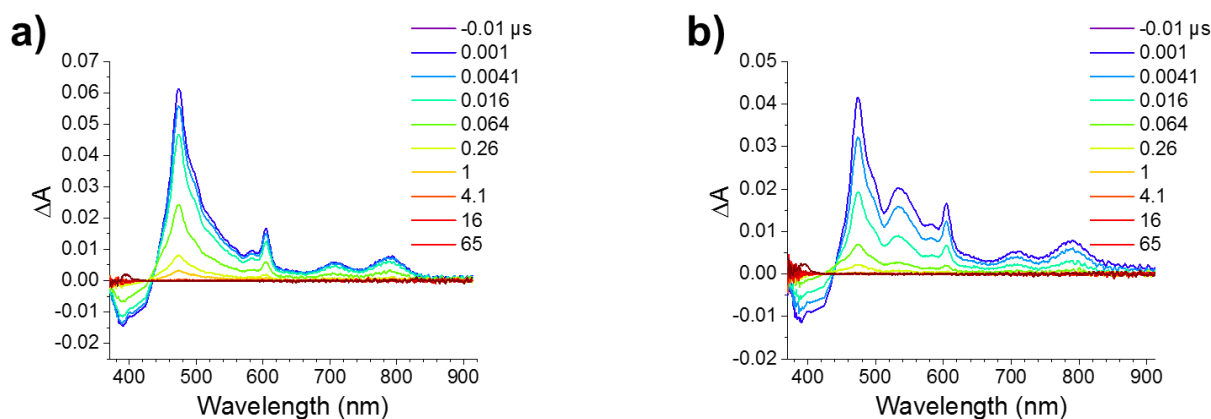


**Figure D.13.** Nanosecond transient absorption spectra of (a) **5.1a** and (b) **5.1b** in airfree 10% fluorobenzene/benzene (v/v), at 295 K following excitation at 414 nm. These data were fit using the basis spectrum deconvolution described below.

### D.3.5 Nanosecond Transient Absorption Basis Spectrum Deconvolution

Nanosecond transient absorption spectra at each time point were fitted to a linear combination of two normalized basis spectra. The fitted contributions of these two components as a function of time are presented. The linear least-squares fitting was performed using the following MATLAB code

```

sp = [rp, trip];
k = (sp'*sp)\(sp'*tadata(2:end,2:end));
resid = tadata(2:end,2:end)-sp*k;

```

where *rp* and *trip* are the reference spectra of the ion pair and  $^3\text{NDI}$  from Figure D.14. *tadata* is a matrix containing the transient absorption wavelengths in the first column, the transient absorption delays across the first row, and the transient absorption spectra in the rest of the matrix. *k* is a matrix containing the fitted contributions of the ion pair and  $^3\text{NDI}$  at each time delay. *resid* is a matrix containing the fit residuals, used to assess the quality of the fits as shown in Figure D.15.

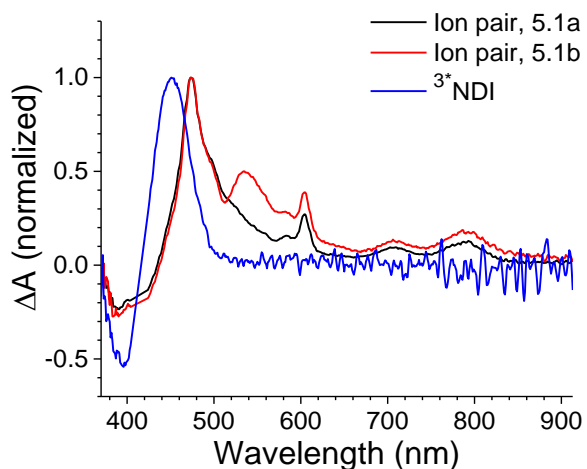


**Figure D.14.** Normalized triplet and radical ion pair basis spectra used in the nanosecond transient absorption fitting procedure.

### D.3.6 Fitted Transient Absorption Data

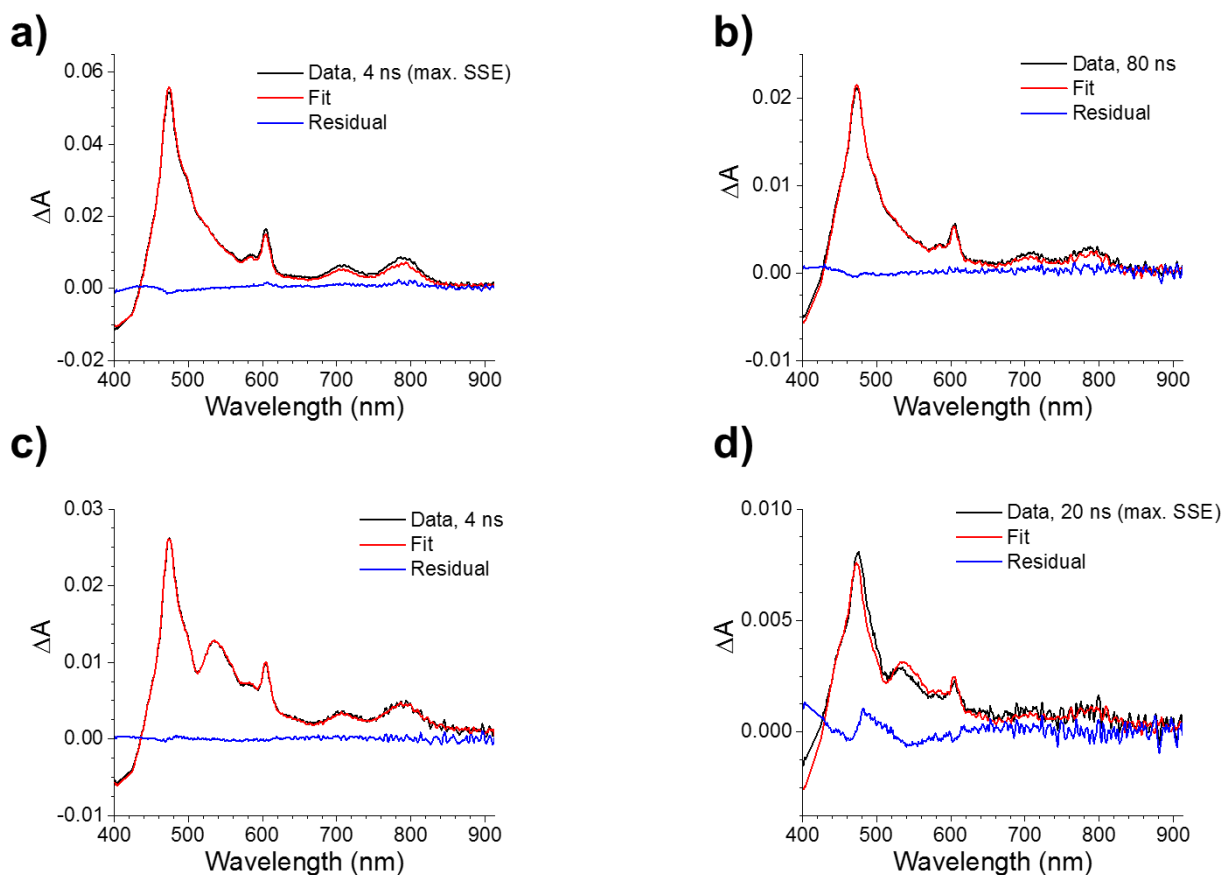


**Figure D.15.** Individual nanosecond transient absorption spectra with fits and residuals, used to check goodness of fit: **5.1a** in benzene at 4 ns (a) and 80 ns (b) after pump pulse; **5.1b** in benzene at 4 ns (c) and 20 ns (d). (a) and (d) are the time points with the largest residuals (as sum of squared errors) in their respective datasets. The relatively large residual in (d) near the BDPA ground state absorption is due to a change in the Stark shift features that may be related to conformational change over time.

### D.3.7 Nanosecond Transient Absorption Spectroscopy: Magnetic Field Effects

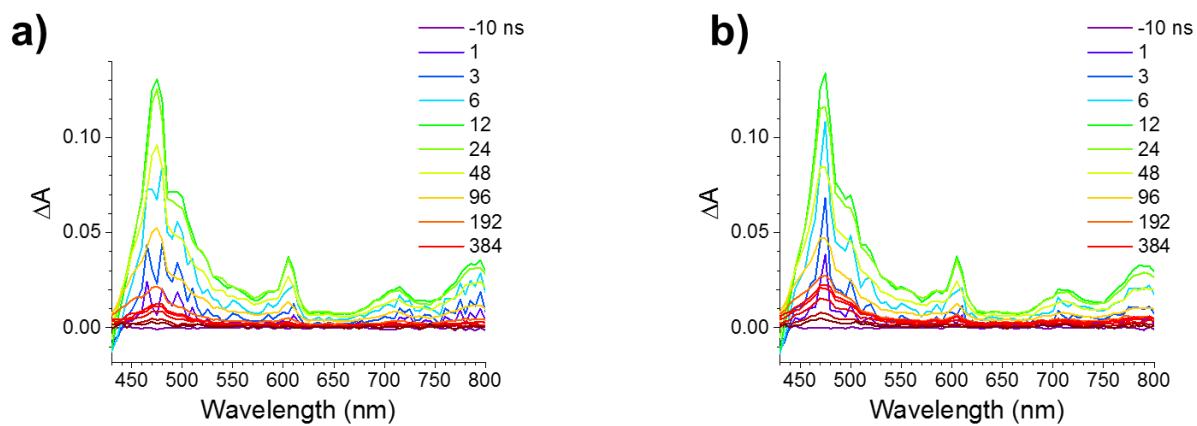


**Figure D.16.** Nanosecond transient absorption spectra of **5.1a** in airfree toluene at 295 K following excitation at 416 nm with (a) 0 mT and (b) 19 mT applied magnetic field.

## D.4 Electron Paramagnetic Resonance Spectroscopy

### D.4.1 Echo-detected Field-swept Spectra

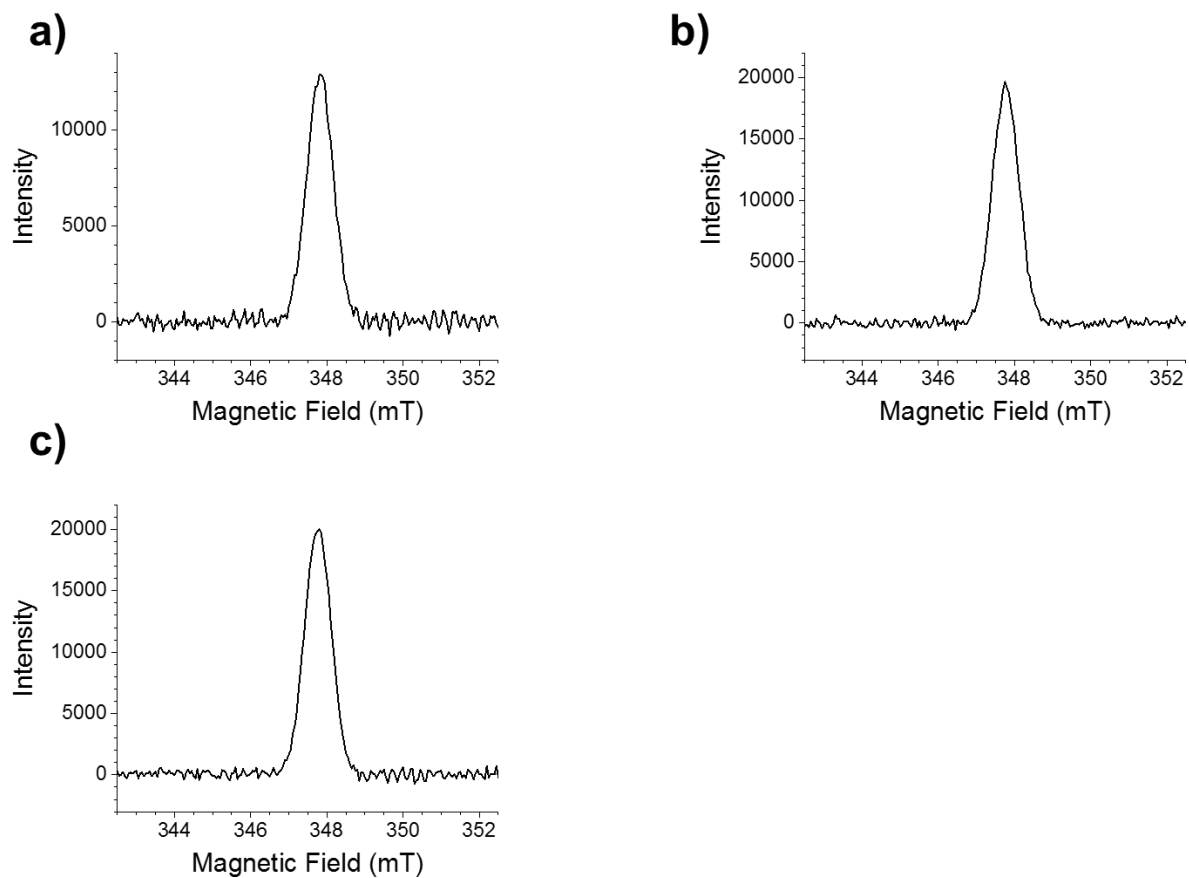


**Figure D.17.** Echo-detected EPR spectra of **5.1b** in (a) benzene, (b) 5% fluorobenzene/95% benzene (v/v), and (c) 10% fluorobenzene/90% benzene (v/v) at 295 K.

### D.4.2 Transient Continuous Wave Spectra

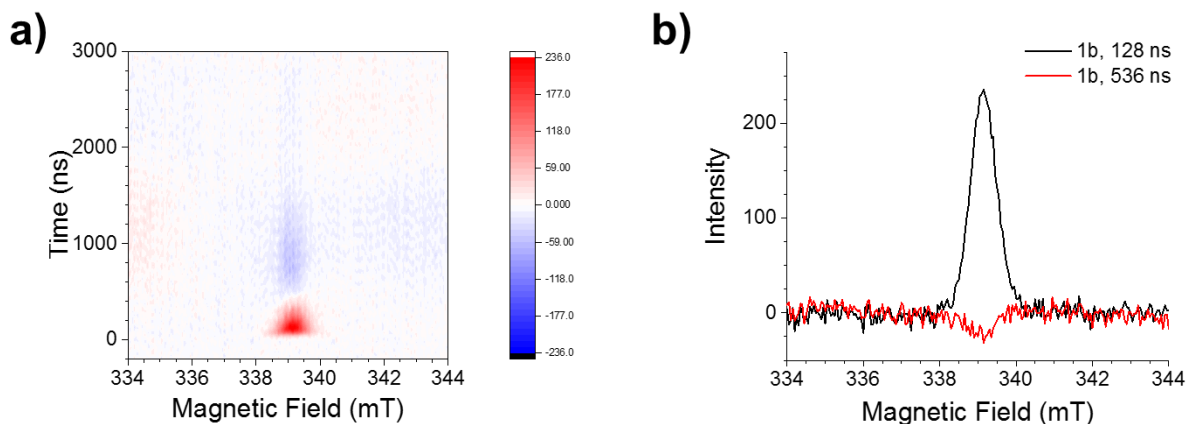


**Figure D.18.** Transient continuous wave detected EPR spectra of **5.1b** in toluene at 295 K following excitation at 416 nm. (a) Contour plot showing initial positive then negative polarization of BDPA'. (b) Two time points showing that positive and negative features are confined to the BDPA' line.

### D.4.3 $T_1$ and $T_2$ measurements

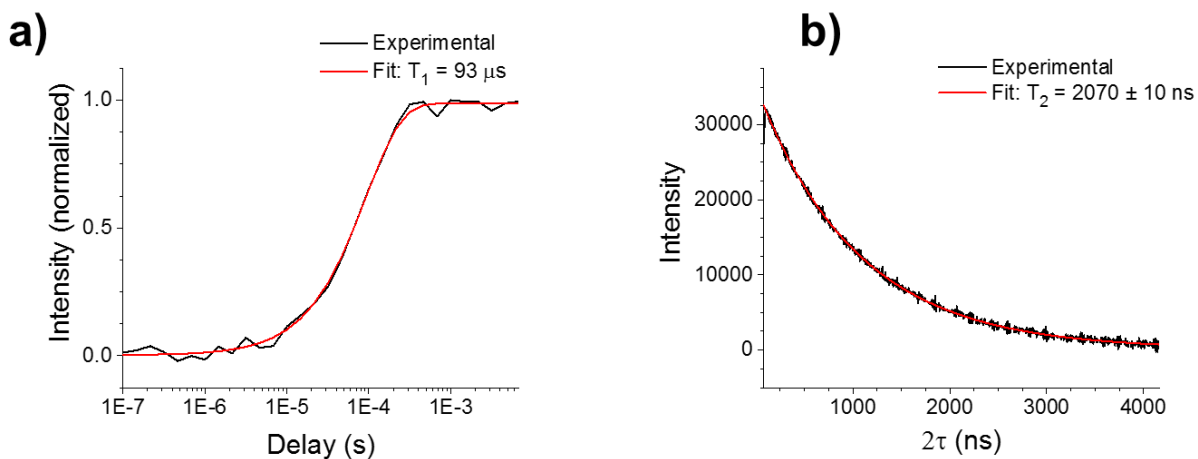


**Figure D.19.** Saturation recovery measurement of  $T_1$  (a) and  $T_2$  measurement (b) for **5.1b** in benzene at 295 K.

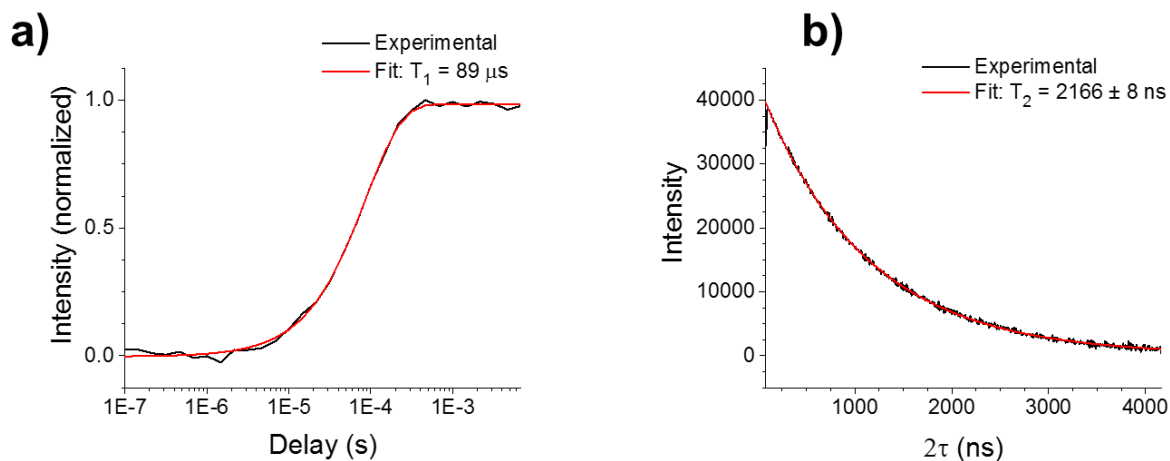


**Figure D.20.** Saturation recovery measurement of  $T_1$  (a) and  $T_2$  measurement (b) for **5.1b** in 5:95 fluorobenzene:benzene at 295 K.

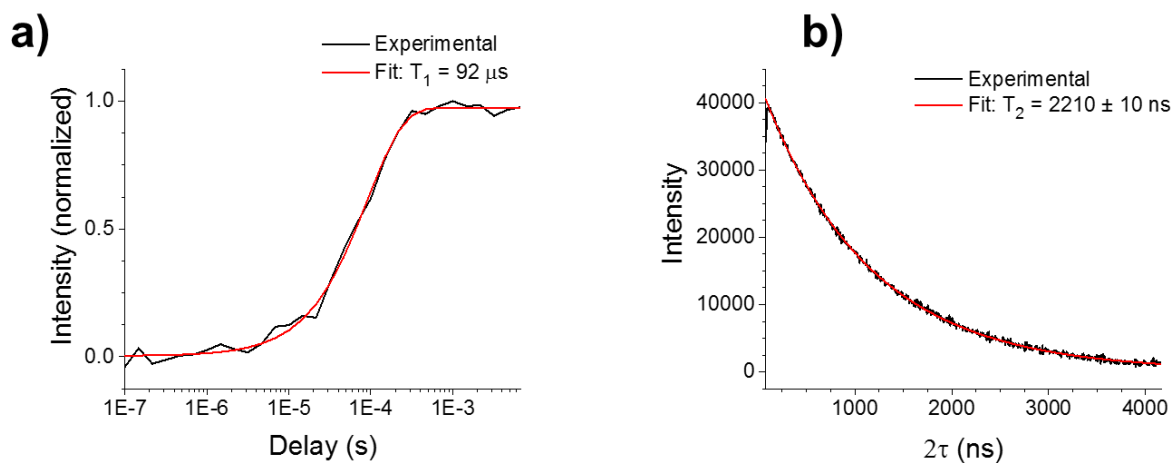


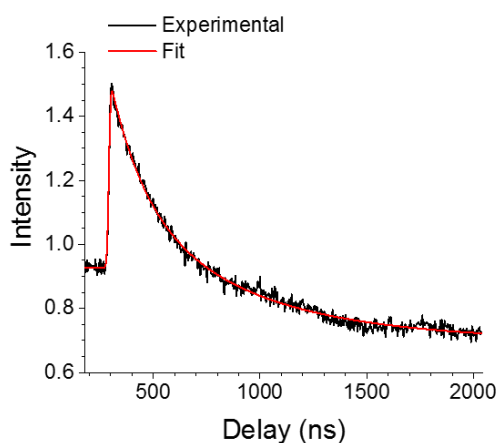
**Figure D.21.** Saturation recovery measurement of  $T_1$  (a) and  $T_2$  measurement (b) for **5.1b** in 10:90 fluorobenzene:benzene at 295 K.

#### D.4.4 Fits to Polarization Transfer Kinetics

Transient EPR kinetics were fit by a model consisting of a biexponential decay and a Gaussian IRF, with a baseline before the laser pulse and an offset at late times. The EPR signal as a function of time was fit to the following equation:

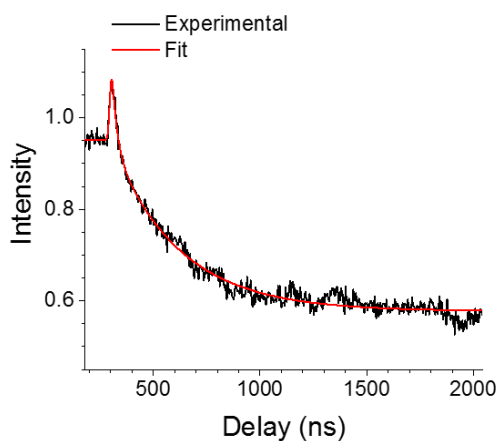
$$\begin{aligned}
S(t) = & \text{Baseline} + A_1/2 * \exp\left(\left(\frac{\text{FWHM}}{2 * \sqrt{\ln(2)}}\right)^2 - \frac{4 * (t - t_0) * \tau_1}{4 * \tau_1^2}\right) * \left(1 + \operatorname{erf}\left(\frac{t - t_0}{\text{FWHM}/(2 * \sqrt{\ln(2)})}\right)\right) - \\
& \left(\frac{\text{FWHM}}{2 * \sqrt{\ln(2)}}\right) / (2 * \tau_1) + A_2/2 * \exp\left(\left(\frac{\text{FWHM}}{2 * \sqrt{\ln(2)}}\right)^2 - \frac{4 * (t - t_0) * \tau_2}{4 * \tau_2^2}\right) * \left(1 + \operatorname{erf}\left(\frac{t - t_0}{\text{FWHM}/(2 * \sqrt{\ln(2)})}\right)\right) - \\
& \left(\frac{\text{FWHM}}{2 * \sqrt{\ln(2)}}\right) / (2 * \tau_2) + \text{Shelf}/2 * \left(1 + \operatorname{erf}\left(\frac{2 * (\ln(2))^{1/2} * (t - t_0)}{\text{FWHM}}\right)\right)
\end{aligned}$$

Where Baseline is the intensity before  $t_0$ , Shelf is the late-time offset,  $A_1$  and  $\tau_1$  are amplitude and time constant for the first decay component,  $A_2$  and  $\tau_2$  are amplitude and time constant for the second decay component, and FWHM is the full width at half maximum of the Gaussian IRF. For these fits, the FWHM was fixed at the length of the  $\pi/2$  microwave pulse used in the EPR experiments, 16 ns. Data shown in the main text Figure 7 have been shifted in time by the fitted  $t_0$  values.



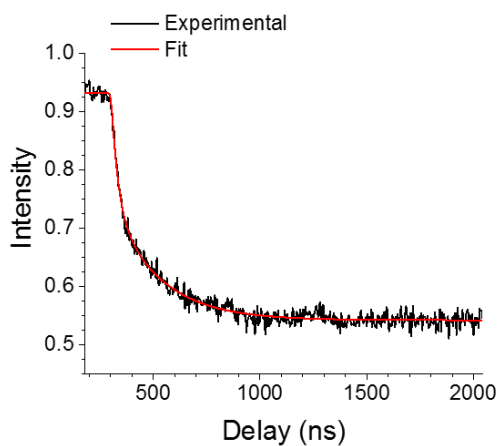
$$\begin{aligned}
A_1 &= 0.38 \pm 0.05 \\
\tau_1 &= 160 \pm 20 \text{ ns} \\
A_2 &= 0.46 \pm 0.05 \\
\tau_2 &= 590 \pm 70 \text{ ns} \\
t_0 &= 291.4 \pm 0.3 \text{ ns} \\
\text{IRF} &= 16 \text{ ns (fixed)} \\
\text{Baseline} &= 0.928 \pm 0.003 \\
\text{Shelf} &= -0.229 \pm 0.008 \\
R^2 &= 0.9908
\end{aligned}$$

**Figure D.22.** EPR signal of **5.1b** in benzene as a function of time following excitation at 416 nm, with kinetic fit.



$$\begin{aligned}
 A_1 &= 0.23 \pm 0.02 \\
 \tau_1 &= 24 \pm 4 \text{ ns} \\
 A_2 &= 0.375 \pm 0.007 \\
 \tau_2 &= 316 \pm 9 \text{ ns} \\
 t_0 &= 296 \pm 1 \text{ ns} \\
 \text{IRF} &= 16 \text{ ns (fixed)} \\
 \text{Baseline} &= 0.952 \pm 0.003 \\
 \text{Shelf} &= -0.375 \pm 0.003 \\
 R^2 &= 0.9831
 \end{aligned}$$

**Figure D.23.** EPR signal of **5.1b** in 5% fluorobenzene/benzene as a function of time following excitation at 416 nm, with kinetic fit.



$$\begin{aligned}
 A_1 &= 0.2 \pm 0.2 \\
 \tau_1 &= 30 \pm 5 \text{ ns} \\
 A_2 &= 0.20 \pm 0.03 \\
 \tau_2 &= 220 \pm 10 \text{ ns} \\
 t_0 &= 300 \pm 40 \text{ ns} \\
 \text{IRF} &= 16 \text{ ns (fixed)} \\
 \text{Baseline} &= 0.932 \pm 0.002 \\
 \text{Shelf} &= -0.390 \pm 0.002 \\
 R^2 &= 0.9894
 \end{aligned}$$

**Figure D.24.** EPR signal of **5.1b** in 10% fluorobenzene/benzene as a function of time following excitation at 416 nm, with kinetic fit.